In situ Raman Spectroscopy Study of Oxidation of Nanostructured Carbons

A Thesis

Submitted to the Faculty

of

Drexel University

by

Sebastian Osswald

in partial fulfillment of the

requirements for the degree

of

Doctor of Philosophy

January 2009

Dedications

To my parents Hans-Juergen and Gerda Osswald

For their never-ending love and support

ACKNOWLEDGEMENTS

First and foremost I would like to thank my Ph.D. advisors Dr. Yury Gogotsi and Dr. Peter Scharff, who dedicated time and patience to teach me how to become a successful researcher. Their support and encouragement have accompanied me throughout the entire Ph.D. study. I could not imagine having better advisors and mentors.

I would also like to thank my committee members Dr. John E. Fischer, Dr. Reinhard Schweitzer-Stenner, Dr. Christopher Li, and Dr. Jonathan Spanier for their time and thoughtful advice. I am also grateful to Dr. Michel Barsoum for his participation in my thesis proposal and preliminary defense committee.

Special thanks go to Dr. Gleb Yushin, Dr. Vadym Mochalin, Dr. Mickael Havel, Dr. Cristelle Portet, Dr. Ranjan K. Dash and Dr. Uwe Ritter for their guidance and assistance.

My thanks also go to the Nanomaterials Group at Drexel University, especially Kris Behler, John Chmiola, and Dr. Davide Mattia for experimental help and valuable discussions; Holly Burnside and Shirin Karsan for proof-reading my manuscripts and the administrative support, and to the chemistry group at Ilmenau University of Technology. It has been a great pleasure working with them side by side during the past three years.

I also wish to thank the faculty and staff of the Materials Science and Engineering Department and College of Engineering, in particular Judy Trachtman, Dorilona Rose, Andrew Marx, and Keiko Nakazawa, who have always been of great help.

Many thanks to Dr. Julie Mostov and Dr. Bahram Nabet for putting forward the dual Ph.D. program and enabling the collaboration between Drexel University and Ilmenau University of Technology.

I am grateful to the assistance of Dr. Zhorro Nikolov in the Centralized Research Facility (CRF) and to the financial support of Arkema and NanoBlox Inc., USA.

Many thanks to all my friends in the United States and Germany, in particular Ashley Friedrich, Rene Mueller, and James Paganda.

Finally, I would like to thank my girlfriend, Ellen, for her patience and for proofreading this thesis.

TABLE OF CONTENTS

LIST OF TABLES

LIST OF FIGURES

ABSTRACT

In situ Raman Spectroscopy Study of Oxidation of Nanostructured Carbons
Sebastian Osswald
Advisors: Dr. Yury Gogotsi and Dr. Peter Scharff

The ability to synthesize carbon nanostructures, such as fullerenes, carbon nanotubes, nanodiamond, and mesoporous carbon; functionalize their surface; or assemble them into three-dimensional networks has opened new avenues for material design. Carbon nanostructures possess tunable optical, electrical or mechanical properties, making them ideal candidates for numerous applications ranging from composite structures and chemical sensors to electronic devices and medical implants.

Unfortunately, current synthesis techniques typically lead to a mixture of different types of carbon rather than a particular nanostructure with defined size and properties. In order to fully exploit the great potential of carbon nanostructures, one needs to provide purification procedures that allow a selective separation of carbon nanostructures, and methods which enable a control of size and surface functionalization. Oxidation is a frequently used method for purification of carbon materials, but it can also damage or destroy the sample.

In situ Raman spectroscopy during heating in a controlled environment allows a time-resolved investigation of the oxidation kinetics and can identify the changes in material structure and composition, thus helping to accurately determine optimal purification conditions. However, while carbon allotropes such as graphite and diamond show unique Raman signals and allow a fast and straightforward identification, the interpretation of Raman spectra recorded from nanostructures containing mixtures of sp, sp^2 and sp^3 bonded

carbon is more complex and the origin of some peaks in Raman spectra of nanocarbons is not yet fully understood.

In this study we applied *in situ* Raman spectroscopy to determine conditions for selective oxidation of carbon nanostructures, such as nanodiamond, nanotubes, carbide-derived carbon and carbon onions; accurately measure and control the crystal size; and improve the fundamental understanding of effects of temperature, quantum confinement and surface chemistry on Raman spectra of nanocrystalline materials.

Thermogravimetric analysis, X-ray diffraction and high-resolution transmission electron microscopy were used to complement Raman spectroscopy in order to facilitate the analysis and the interpretation of the results.

This work has improved our understanding of oxidation of carbon materials, especially selectivity of the oxidation process to different carbon structures in a broad temperature range. The results of this study have been used to develop simple and environmentally friendly procedures for purification and surface functionalization of carbon nanoparticles and nanoporous materials.

1 INTRODUCTION

Carbon is the basis of all life on earth, and without a doubt one of the most versatile elements known to man. More than ten million carbon compounds are known today, many times more than that of any other element.[1] The main reason why carbon is such a diverse element is the fact that it can form bonds with a large number of other elements, both metals and non-metals. In addition, carbon itself exists in several allotropes.[2] Its flexible electron configuration allows carbon to form three hybridization states which lead to different types of covalent bonding.[3] The most representative macroscopic forms of carbon are graphite and diamond. In 1985, Kroto et al. discovered a third carbon allotrope, the fullerenes[4]. While their experiments aimed at understanding the mechanisms by which long chained carbon molecules are formed in interstellar space, their results opened a new era in science - the beginning of nanotechnology.

Today nanotechnology includes the synthesis, characterization and application of a variety of nanostructured materials.[5] Efforts on investigate these materials were intensified during the last decade. Characterization techniques such as high resolution transmission electron microscopy (HRTEM), scanning tunneling microscopy (STM) and atomic force microscopy (AFM) were further developed, allowing researchers to overcome the limitations of optical microscopy and study materials at the atomic scale. As a result, a variety of new carbon structures and morphologies were found to exist, including carbon nanotubes (CNT)[6], carbon onions[7], nanodiamond (ND)[8,9], diamondoids[10] and ordered and disordered nanoporous carbon, all showing unique and promising characteristics. Between 1995 and 2006, the number of research papers dedicated to a "nano" topic increased from 3,000 to 40,000 per year.[11] Today, the economic potential of carbon nanostructures exceeds all

expectations and is still growing rapidly, with applications ranging from composite materials[12,13] to electronic devices[14-16], optics[17-19], chemical sensors[20-22] and biomedical components[23-26].

The physical and chemical properties of nanostructures differ significantly from that of bulk materials of the same composition. For example, a decrease in the crystal size results in an increase in the surface/volume ratio, which is exceptionally high when entering the lower nanometer range. As a result, properties are primarily determined by the shape of the crystals and their surfaces[23]. Therefore, controlling both the size of nanostructures as well as their surface chemistry appears to be crucial.

Current synthesis techniques such as chemical vapor deposition[24], arc discharge[25], laser ablation[26], or detonation[27] typically lead to a mixture of different types of carbon rather than a particular nanostructure with defined properties. In order to fully exploit the great potential of carbon nanostructures, one needs to provide purification procedures that allow for a selective separation of carbon nanostructures, and methods which enable size control and surface functionalization.

2 LITERATURE REVIEW

2.1 Carbon Nanomaterials

The most stable carbon phase on the macroscale is graphite. Diamond is a metastable phase at atmospheric pressure and moderate temperatures. However, the high activation energy needed for a phase transition from diamond into graphite (0.4 eV/atom) requires high temperatures[2,3] and allows diamond to survive under ambient conditions.

When entering the nanoscale, a third parameter needs to be considered – the crystal size.[28] For carbon clusters of only a few nanometers, one has to adjust the expression for Gibbs free energy, and contributions from the surface need to be considered in addition to the bulk free energy. This results in changes in the phase diagram.[29-31] The stability of the same structure at the nanoscale may be different from that in bulk.[29] For example, it was found that carbon clusters with $< 10^4$ atoms show liquid-like behavior at temperatures far below the melting point of the bulk material, and are subject to frequent surface reconstructions.[30]

Planar graphite (graphene) becomes the most stable form of carbon for crystals above approximately 10 nm. Fullerenes are believed to be the energetically preferred form for cluster sizes less than 1.9 nm .[31] In between, carbon onions, buckydiamonds and ND are thermodynamically favored. Barnard et al. calculated that as the size of the crystals is increased, the most stable carbon form at the nanoscale changes from fullerenes to carbon onions, to buckydiamond, to ND, and finally to graphitic carbon (**Figure 2.1**).[29,32] Fullerenes are spherical molecules which, in contrast to graphite (sp^2) or diamond (sp^3), exhibit intermediate hybridization. The best known fullerene is C_{60}, a highly symmetric molecule

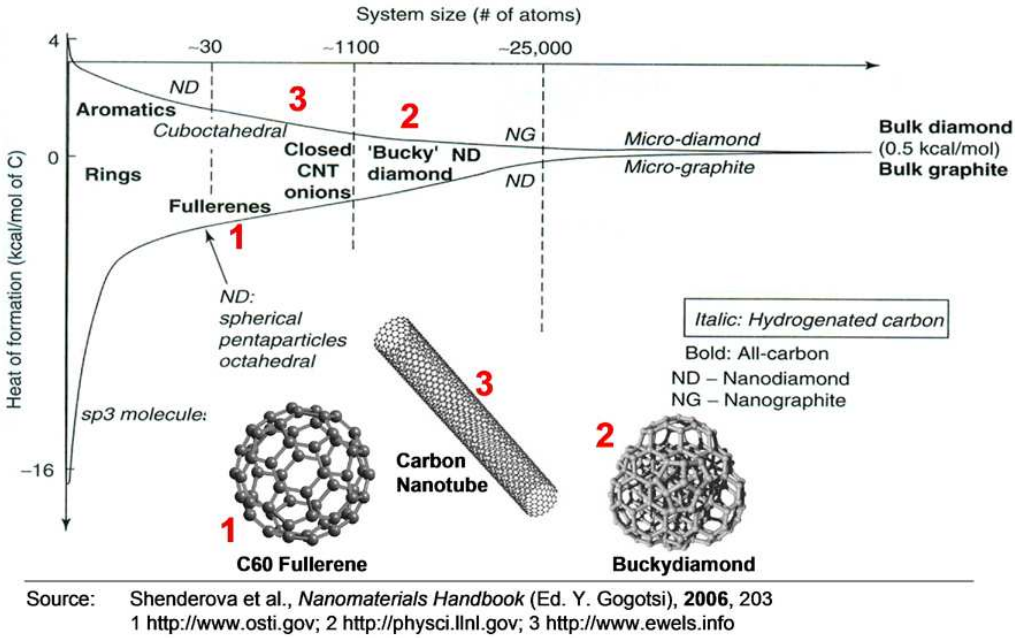

Figure 2.1: Structure and stability of different carbon nanomaterials. Decrease in size increases the surface/volume ratio and contributions from surface atoms become significant. Minimizing Gibbs free energy thus lead to new shapes and novel carbon structures, such as fullerenes, carbon nanotubes and nanodiamonds.

consisting of 60 carbon atoms arranged in 12 pentagons and 20 hexagons, where each carbon atom has equilibrated sp^2 and sp^3 character. Carbon onions are closely related to the fullerenes, consisting of an arrangement of closed, concentrically nested graphitic shells.[33]

Due to a large number of unsatisfied surface atoms and a large surface/volume ratio, ND exhibits a very high surface reactivity compared to other carbon nanostructures. [29] The smallest ND crystals experience extensive surface reconstruction with phase transitions from sp^3 to sp^2 bonding. As a result, the diamond core becomes partially encapsulated in a graphitic shell (**Figure 2.1**), leading to a structure known as buckydiamonds.[34,35] However, the surface termination strongly affects the energetics of nanoparticles and can inhibit surface reconstruction or phase changes. For example, a whole class of hydrogen-terminated diamondoid molecules exists in the 1-2 nm size range.[10]

Experiments showed that various nanostructures can exist simultaneously, depending on the ambient conditions (**Figure 2.1**).[36] The rather small differences in stability of carbon nanomaterials allow phase transformation of, for example, ND into carbon onions and vice versa.[10,37,38] A direct crossover from fullerenes to CNTs and vice versa has also been described.[39] CNTs are hollow structures consisting of one, two or more concentric tubes. Each tube can be imagined as a one-atomic hexagonal layer of graphite (graphene) rolled into a cylinder.

Nanoporous materials, consisting of interconnected cells or networks, are also considered carbon nanostructures. Of special interest are carbide-derived carbons (CDC) produced by high-temperature chlorination of carbides due to the ability to control and fine-tune pore size and pore volume.[40]

2.1.1 Carbon Nanotubes

CNTs are classified into single-walled (SWCNTs) and multi-walled carbon nanotubes (MWCNTs). SWCNTs consist of a single graphene layer rolled up into a hollow cylinder whereas MWCNTs are comprised of two, three or more concentrically arranged cylinders. CNTs can be understood as individual molecules or quasi-one-dimensional crystals with translational periodicity along the tube axis. Their diameters range from 0.4 nm to tens of nanometers, with lengths reaching several hundred micrometers or more. Their ends are open or capped by hemispherical fullerenes. One further distinguishes between metallic and semi-conducting CNTs. While MWCNTs are metallic, approximately 2/3 of all possible SWCNTs are semi-conducting and only 1/3 are metallic.[41] The properties of CNTs, e.g. electronic band structure or phonon density of states, depend on the diameter and the

helicity Θ (chiral angle) of the nanotube. The atomic structure of an individual SWCNT is exactly defined by the (n,m) nomenclature[49,50] also know as Hamada indices[42]. SWCNTs with (n,0) and (n,n) indices are called achiral nanotubes and referred to as "zigzag" ($\Theta = 0°$) and "armchair" ($\Theta = 30°$) nanotubes, respectively.

The electronic structure of CNTs can be derived from the electronic properties of 2D-graphite (graphene), but additional confinement effects must be taken into account. All armchair SWCNTs are metallic. SWCNTs where n-m is not an integer multiple of 3 are semi-conducting nanotubes with band gap energies between 0.3 and 1.0 eV. SWCNTs where n-m is an integer multiple of 3 are quasi-metallic nanotubes with band gap energies below ~0.02 eV. While the σ bonds are responsible for the strong in-plane correlation between atoms in the graphene that result in the unique mechanical properties of the cylindrical tubes, only π-electrons, which are close to the Fermi level, determine the characteristic optical and electronic properties of CNTs.

Although CNTs consist of merely carbon atoms, they originally have two areas of different reactivity: the highly-reactive fullerene-like tube ends and the less-reactive hexagonal cylindrical tube walls.[43] Carbon bonds at the tips are under higher strain due to their larger curvature and provide an area of enhanced reactivity.[43]

Double-wall carbon nanotubes (DWCNTs)[44] are the most basic members of the MWCNT family. These tubes consist of two concentric cylindrical graphene layers and their size is comparable to that of SWCNTs. The special role of DWCNTs should be emphasized, as they are the link between SWCNTs and the more complex and less-studied MWCNTs, and therefore of great interest for a fundamental understanding of these novel nanostructures. DWCNTs are also of great importance from an industrial standpoint.

Activation and functionalization of SWCNTs break carbon-carbon bonds, thus leading to defects in the tube structure and a degradation of their mechanical and electrical properties. In the case of DWCNTs, only the outer wall is modified and the inner tube remains unchanged.

CNTs exhibit remarkable properties.[48-50] They were found to possess extraordinary mechanical strength with an elastic modulus (Young's modulus) up to ~ 1-2 TPa (more than 5 times than that of steel), and a shear modulus at the order of ~ 1-5 GPa.[51-53] Therefore, CNTs show an extremely high stiffness along the nanotube axis, but are easy to bend perpendicular to the axis. CNTs were reported to carry electric currents[45] up to 10^9 A/cm^2, and theoretical calculations using molecular dynamics simulations suggested a thermal conductivity of up to 6,000 W/(m·K)[46], many times more than that of copper or diamond.

There exists a wide range of potential applications for CNTs including composite materials, transistors, diodes and field emission displays.[14,17,47,48]. While some of them have already been realized on an industry scale, others still require extensive preparation.

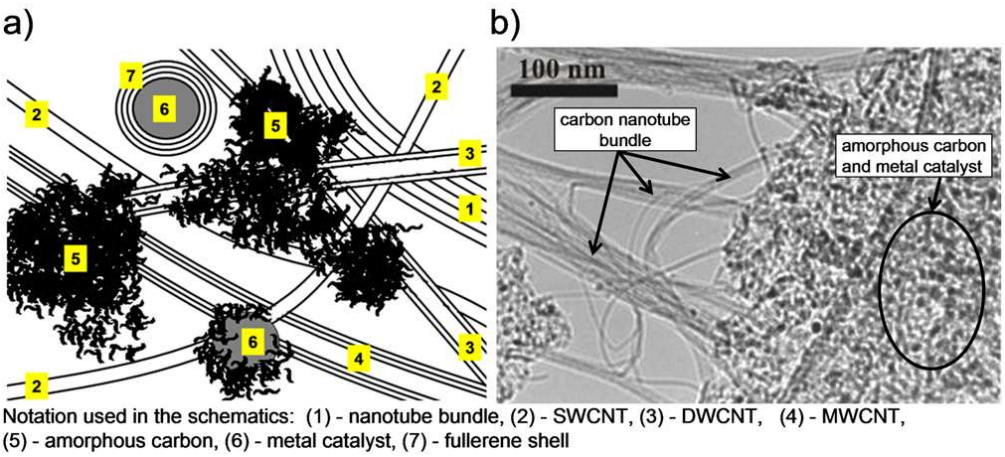

Figure 2.2: Composition of CNT samples. (a) Schematic of as-produced CNT sample showing common impurities such as catalyst particles and/or amorphous carbon, and simultaneous presence of SWCNTs, DWCNTs and MWCNTs. (b) HRTEM image of a DWCNT sample showing CNT bundles and a large number of catalyst particles surrounded by amorphous carbon.

Although SWCNTs have been of particular interest due to their small diameter and well defined properties, MWCNTs are becoming more and more attractive from a practical standpoint. Their relatively low production costs and availability in large quantities are two important advantages over SWCNTs.

Different methods have been proposed for CNT synthesis, including catalytic chemical vapor deposition (CVD), laser ablation or arc discharge. Unfortunately, the presence of catalytic particles and amorphous carbon in as-produced CNT samples (**Figure 2.2**) still hinders a large number of potential applications. Other major difficulties are the co-existence of metallic and semi-conducting CNTs, bundling of small diameter CNTs, and variations in tube size, number of walls and amount of defects (**Figure 2.2**).

2.1.2 Nanocrystalline Diamond

Nanocrystalline or ultra-dispersed diamond, often simply referred to as "nanodiamond" (ND), is another very promising carbon nanomaterial. Despite its discovery in the early 1960s in the former Soviet Union[49], ND has received much less attention compared to CNTs. However, over that past few years interest in ND has been quickly increasing.[8,18] ND can be produced either as thin films using CVD techniques or as powder via detonation of carbon-containing explosives such as trinitrotoluene (TNT) and hexogen in a steel chamber.[9,27,48,59] While ND films are undoubtedly attractive as biocompatible, smooth, and wear resistant coatings, it is the ND powder that has the potential to achieve truly widespread use on a scale comparable to that of CNTs. In this work the term "nanodiamond" refers to ND powders produced by the detonation synthesis.

ND powders are composed of aggregates of primary particles with an average size of ~ 5 nm, each consisting of a diamond core partially or completely covered by layers of graphitic and/or amorphous carbon.

A new wave of recent interest in ND stems from the expectation that these nanocrystals might be able to combine an active surface, featuring a variety of chemically reactive moieties, with the favorable properties of macroscopic diamonds. Such properties include the diamonds' extreme hardness and Young's modulus, chemical stability, biocompatibility, high thermal conductivity, and electrical resistivity, to name a few. Moreover, ND is one of few nanomaterials produced in large commercial quantities. A simple production process using expired munitions as the energy and carbon source for the detonation synthesis results in moderate material costs, leading to numerous applications.

Currently, ND is used in composite materials[60,61], as an additive in cooling fluids[50], lubricants[51], and electroplating baths[8]. However, a large number of other potential applications, including drug delivery, stable catalyst support, transparent coatings for optics,

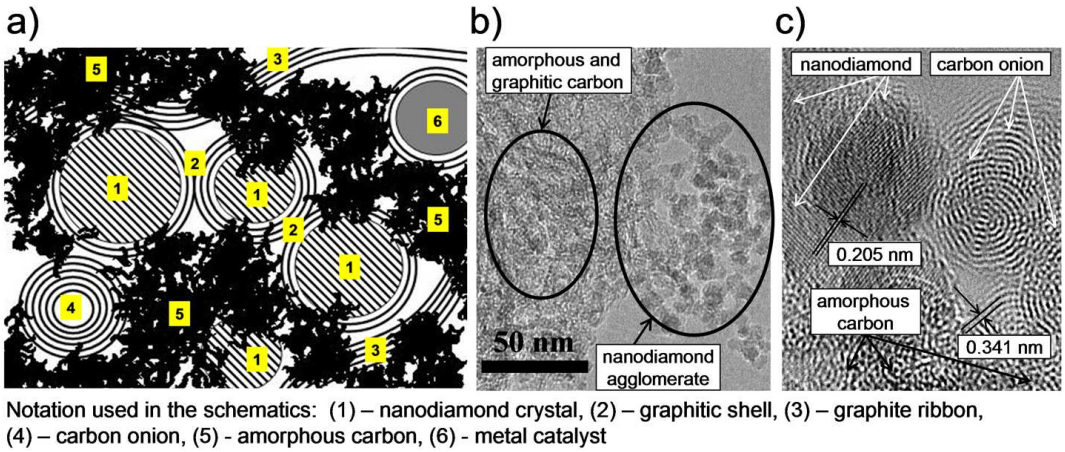

Figure 2.3: Composition of detonation ND. (a) Schematic of ND detonation soot showing coexistence of different nanostructures. HRTEM images of as-produced ND showing b) large amounts of sp^2 carbon and agglomerates of ND crystals and c) presents of carbon onion, ND and amorphous carbon.

and others still remain under-explored. Most of these applications are hindered by the current inability of the manufacturers to provide ND with well-controlled surface chemistry, as well as the absence of a process that would achieve this control in a research laboratory.

The raw diamond-bearing soot obtained during detonation synthesis consists of ND particles, non-diamond carbon, as well as metals, metal oxides and other impurities coming from the detonation chamber or the explosives used (**Figure 2.3**). Up to this in time, the purification treatment remains the most complicated and expensive stage of the ND production.[8]

2.1.3 Nanoporous Carbon

Nanoporous carbon materials consisting of interconnected cells and networks are also considered as nanostructures. Porous carbons with nano-sized pores and a high specific surface area are of great technological importance, and are commonly used for a variety of applications including gas separation and storage, water/air filtration, catalyst supports, as well as electrodes in lithium-ion batteries and supercapacitors, to name a few.[52-55]

Various nanoporous carbon materials, including activated carbons, aerogels, templated carbons, carbon nanotubes, and more recently, carbide-derived carbons (CDC)[40], have been studied and can be produced on an industrial scale. Unfortunately, all of these carbons, with the exception of CDC, offer limited control over the porosity.

Although activated carbons are widely used and considered the most powerful conventional adsorbents, little control over the pore structure has been achieved, in spite of extensive studies and improvements in the activation processes[56-58]

CDCs are produced by extraction of metal from metal carbides using techniques such as vacuum decomposition, leaching in supercritical water or high temperature treatments in halogens. These techniques lead to films and powders that contain mainly amorphous and graphitic carbon, but also carbon nanotubes, fullerenes, carbon onions and nanodiamond, depending on the synthesis conditions.[59-63]

In particular, high temperature treatments in chlorine were found to lead to a uniform extraction of metals.[64] The chlorination process allows a high control over pore size and surface area, which is crucial for key technologies such batteries, supercapacitors, selective

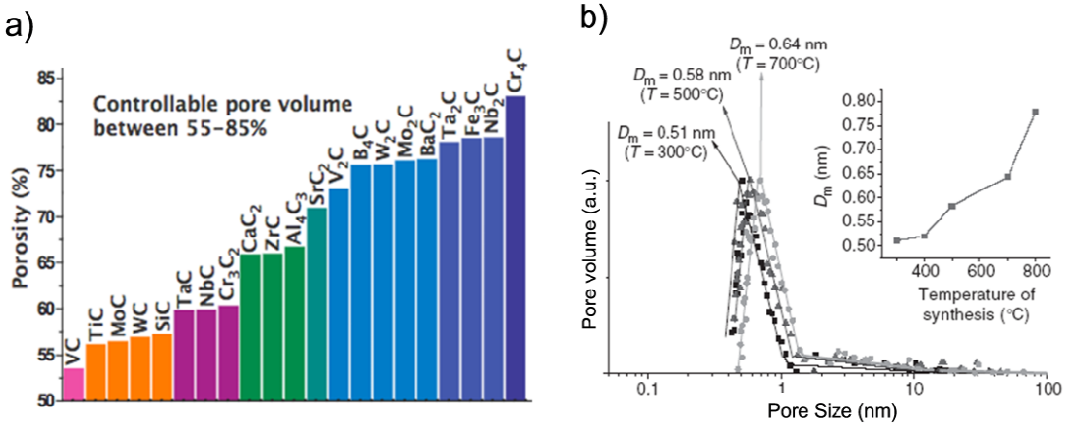

Figure 2.4: (a) Theoretical pore volume of CDC produced from different carbide precursors. The pore volume increases with increasing metal/carbon ratio. (b) Changes of average pore size as function of chlorination temperature. Increasing graphitization and ribbon formation at higher chlorination temperatures shift the average pore a size towards higher values. Graphs obtained from Ref. 40.

adsorption, and gas storage.[65-67] CDCs synthesized by chlorination are characterized by a narrow pore-size distribution with an average pore-size between 0.4 and 3 nm (micropores) that can be tuned with subnanometer accuracy.[40,68]

Porosity control (e.g. average pore size, size distribution, pore shape, specific surface area) is achieved by selecting an appropriate host carbide lattice and optimizing the

chlorination process. Depending on the carbide precursor and the corresponding metal/carbon ratio (stoichiometry), pore volumes up to 80% can be achieved (**Figure 2.4**a).[40] The pore size of a specific carbide can be controlled by adjusting the synthesis conditions (**Figure 2.4**b).[69] Higher chlorination temperatures lead to enhanced graphitization and formation of ribbons and turbostratic graphite, thus shifting the average pore size towards higher values (**Figure 2.4**b).[69]

A wide variety of carbon structures have been observed in CDC samples. The structure of CDC depends on the processing conditions. Turbostratic and amorphous carbons, spherical, polyhedral and tubular structures, graphite or diamond can be present in CDC, depending on process parameters.

Therefore, while carbons produced by chlorination of metal carbides are generally considered as amorphous or disordered carbons, both structure and composition of the samples can vary largely and depend strongly on the synthesis conditions. CDCs can contain different mixtures of sp^3, sp^2 and even sp^1 sites, as well as other non-carbon species such as hydrogen. In the case of highly amorphous materials such as CDC, the sp^3, sp^2 and sp^1 hybridization energies of carbon-carbon bonds may be slightly different compared to diamond, graphite and carbines, respectively, due to variations in bond length, bond angle and chemical environment in a disordered carbon network.

Figure 2.5 shows the ratio between sp^2 and sp^3 sites of different CDCs, determined by electron energy lost spectroscopy (EELS). CDCs synthesized at ≤ 700 °C are highly amorphous. Graphitization typically starts at ~ 800 °C, with a sharp increase in ordering around 900 - 1000 °C. Higher chlorination temperatures lead to graphitization and ribbon formation, but the sp^2/sp^3 ratio remains almost unchanged between 700 - 1100 °C (**Figure 2.5**a). While someone could expect that the sp^2 content in CDCs increases with temperature,

EELS studies reveal that the chlorination temperature does not significantly affect the bond hybridization.

Figure 2.5b shows the ratio between sp^2 and sp^3 sites for CDCs synthesized using different carbide precursors.[70] The carbides are arranged according to the mean distance between carbon atoms in the carbide structure, with VC having the smallest carbon-carbon (C-C) distance. The lowest relative sp^2 content is found in CDCs derived from carbides with a short C-C distance such as VC and TiC.[70] Carbides with larger C-C distances lead to CDCs with higher sp^2 contents (**Figure 2.5**b). The lower sp^2 content in VC-CDC and TiC-CDC results from a smaller unit-cell volume. The carbon atoms have lower freedom for rearrangement and the structure get locked during the synthesis.

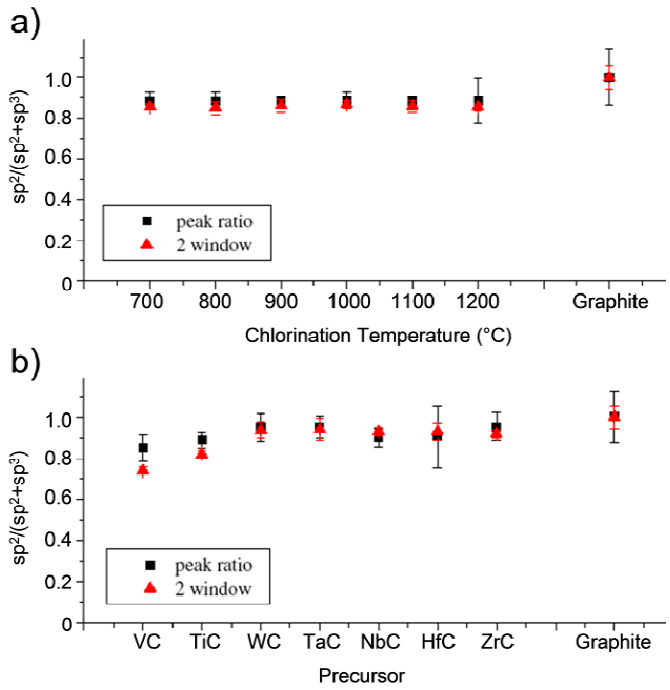

Figure 2.5: Ratio between sp^2 and sp^3 sites of TiC-CDC chlorinated at different temperatures (a) and different CDCs synthesized at 1000 °C, as determined by electron energy loss spectroscopy (EELS). Data obtained from Ref. 70. The ratios were calculated using two methods which are described in Ref. 70.

Since CDCs chlorinated without addition of hydrogen contain mainly sp^2 sites (~ 90%), structure and ordering of sp^2 phases dominate the properties of the material. In summary, structure and properties of CDCs vary largely and depend strongly on both carbide precursor and chlorination conditions.

2.2 Oxidation of Carbon Nanomaterials

The oxidation of carbon materials such as coal, charcoal or graphite has been investigated for decades, and is well known as a powerful route to modify the physical and chemical properties of carbon materials. While the reaction of oxygen with carbon surfaces is one of the simplest reactions involving elemental carbon, it is also one of the most important reactions for a wide range of technological applications, such as heterogeneous oxidation catalysis, carbon activation, spacecraft engineering, fuel-efficiency, emission control, and surface functionalization, to mention a few. Until recently, carbon-oxygen reactions had two main functions: (1) increasing surface area and porosity of a material by removing carbon atoms from the surface (activation), and (2) formation of organic functional groups on the carbon surface (functionalization). However, during the recent years, researchers have recognized the great potential of carbon-oxygen reactions for nanotechnology and took advantage of another important function: the selectivity of the oxidation process towards different forms of carbon.

The large number of existing oxidation methods can be classified into dry chemistry (gas-based) and wet chemistry (liquid-based) approaches. Liquid phase oxidation involves treatments in concentrated or diluted acids (e.g. HNO_3, H_2SO_4, H_3PO_4) and/or bases (e.g. NaOH, KOH).[70-74] One advantage of liquid phase oxidation is the ability to control the

Table 2.1: Comparison of dry chemistry- and wet chemistry-based oxidation of carbon materials.

	Wet Chemistry	*Dry chemistry*
Reactant	*acid:* HNO_3, H_2SO_4, H_3PO_4 *base:* KOH, NaOH	*gas:* air, O_2, O_3, CO_2, H_2O vapor
Advantages	☺ very homogeneous ☺ high selectivity with respect to sp^2 and sp^3 carbon	☺ high process control using *in situ* characterization ☺ fast and inexpensive ☺ easy to scale up
Disadvantages	☹ require extensive washing and corrosion-resistant equipment ☹ environmentally harmful and expensive waste disposal ☹ little process control during treatment: high sample loss/reduced selectivity	☹ require high temperatures *and/or* ☹ use of toxic/aggressive substances or supplementary catalysts

purification process and reaction rates by adjusting the concentrations of reactants. Simultaneous dissolution of metal impurities in parallel to oxidation of non-diamond carbon phase is also possible. At the same time liquid phase oxidation techniques suffer from many disadvantages (**Table 2.1**). Despite being effective oxidation reactants, acids and bases are environmentally harmful and require corrosion-resistant equipment in order to run the process and to store and transport aggressive oxidizers. In some cases, oxidation with acids, salts or oxides introduces foreign elements and leads to additional impurities, such as nitrogen- and sulfur-containing compounds, chlorine, chromium, etc., which alter the intrinsic characteristics of the carbon material and need to be removed in additional purification steps. Especially heavy metal compounds cannot be ignored and result in a costly waste disposal process.

To overcome the disadvantages of liquid oxidizers, some alternative purification techniques have been elaborated. Dry chemistry approaches are based on high-temperature

reactions in gases such as air, oxygen, carbon dioxide or ozone.[71-77] A comparison of both oxidation methods is shown in **Table 2.1**.

While oxidation has been used extensively to modify and activate macroscopic forms of carbon on an industrial scale, most of the studies reported in literature provide only a qualitative description of the oxidation kinetics, and lack a fundamental understanding of the physical and chemical processes occurring at the nanoscale. The various types of carbon used in these studies were often simply referred to as "coke" or "carbon soot", even though they are characterized by distinct differences in crystal structure and surface terminations. Therefore, a comparison of available data is difficult and interpretation of the results may lead to ambiguous conclusions.

The structural diversity of carbon at the nanoscale exceeds that of all other materials. Detailed information on the nature of the material and the structure-dependency of the oxidation kinetics is thus crucial for providing the required selectivity. While some nanomaterials such as carbon nanotubes have been studied extensively and are generally well understood, other nanostructures such as ND or CDC have received much less attention. In order to study their properties and open avenues for new applications, one has to provide a material of high purity and defined composition.

Although oxidation has been used to purify carbon materials, oxygen-carbon reactions have been shown to drastically alter physiochemical properties such as wettability and adsorption characteristics. Moreover, oxidation can easily induce damage to carbon materials or even destroy the sample under improper conditions. This is of particular importance in the case of carbon nanostructures. Thermogravimetric analysis (TGA), which measures changes of mass during oxidation processes, has been widely used to determine the

purification conditions.[78-80] However, TGA does not provide information on what type of carbon is removed from the sample or to what extent nanostructures are damaged.

In order to successfully apply oxidation methods to carbon nanomaterials, one has to systematically study their interactions with gases and liquids, monitor changes in structure and composition, and simultaneously follow the reaction kinetics of the different carbon nanostructures. This has been partially achieved for carbon nanotubes[81-83], but remains a major challenge for other forms of carbon including ND and CDC.

2.2.1 Oxidation of Carbon

The interaction of oxygen with carbon materials is of great technological importance, and therefore one of the most studied reactions. The reaction of oxygen with carbon surfaces has two main steps: (1) activation of molecular oxygen at the carbon surface (physisorption) and (2) stabilization of the activated oxygen by formation of covalent bonds with the carbon atoms (chemisorption).

During the last decades graphite has been of particular interest since it can be used in extreme environments, such as in nuclear reactors, as it is one of the purest materials that retains its proprieties even at very high temperatures. However, since the emergence of nanotechnology, graphite has received increasing attention as a model material for carbon nanostructures. Twodimensional graphite layers (graphene) are the basic modules for fullerenes, carbon nanotubes and carbon black, and have been used to explain a large number of the novel properties of these nanomaterials. The interactions between the basal planes in graphite were used to explain bundling effects in CNT samples and analyze wall-wall interactions in carbon onions and MWCNTs. Therefore, most of the properties of

carbon nanomaterials, including thermal stability and chemical reactivity, are closely-related to the graphitic structure. Study of the basic reactions between oxygen and graphitic surfaces will improve the understanding of carbon nanomaterials and their oxidation behavior.

The following chapter summarizes the main steps of the oxidation mechanism in general and discusses the reaction kinetics of graphite and other carbon materials.

2.2.1.1 Reactions between Oxygen and Carbon

The reaction of molecular oxygen with carbon can be described by the following three basic equations (related to 1 mol of O_2):

$$C(s) + O_2(g) = CO_2(g) \tag{2-1}$$

$$2C(s) + O_2(g) = 2CO(g) \tag{2-2}$$

$$2CO(g) + O_2(g) = 2CO_2(g)\,. \tag{2-3}$$

We also need to consider the so-called Boudouard equation as an intermediate state:

$$C(s) + CO_2(g) = 2CO(g)\,. \tag{2-4}$$

The temperature-dependent standard Gibbs energy change ($\Delta G°$) for each reaction is shown in **Figure 2.6**[84] and given by:

$$\Delta G° = \Delta H - T\Delta S\,, \tag{2-5}$$

where T is the temperature and ΔH and ΔS are the enthalpy and entropy of the reaction, respectively. Enthalpy can be understood as a measure of the energy in a chemical bond. Tightly bound molecules have higher heat energy. The enthalpy change ΔH for reactions 2-1, 2-2, 2-3 and 2-4 can be calculated using Hess's law and are -393.5, -221.0, -565.9 and +172.5 kJ/mol, respectively. Thus reactions 2-1, 2-2 and 2-3 are exothermic, while the Boudouard

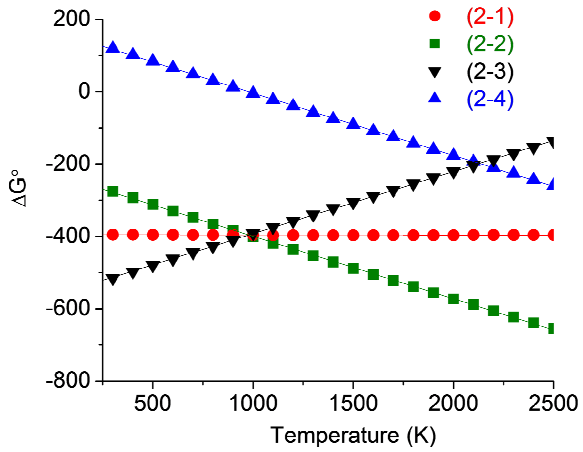

Figure 2.6: Standard Gibbs free energy change of equations 2-1, 2-2, 2-3, and 2-4 as a function of the temperature. Below the interception point at ~1000 K formation of CO_2 is thermodynamically favored. Data obtained from Ref. 84.

reaction is endothermic. The entropy is a measure of the disorder in a system. Molecules distributed randomly have high entropy, whereas ordered molecules have low entropy. Spontaneous reactions are characterized by a negative $\Delta G°$. The more negative $\Delta G°$, the higher the yield of reaction products. A positive $\Delta G°$ does not predicate that a reaction is improbable, but that the yield of reaction products is rather low. The Gibbs energies of equation 2-1, 2-2 and 2-3 intersect at approximately 1000 K (**Figure 2.6**).

To the right of the interception point, $\Delta G°$ of reaction 2-2 passes below the others, suggesting the formation of CO to be the dominant process. To the left of the interception point, at temperatures below 1000 K, formation of CO_2 is thermodynamically favored.[84,85] Since the Gibbs free energy change of equation 2-1 has a large negative value, the reaction occurs with a large driving force even at low oxygen partial pressures, and is the predominant process in the oxidation regime of interest (chemical regime). The rate of carbon oxidation in reaction 2-1 is equal to the rate of formation of CO_2 according to:

$$-\frac{d[C]}{dt} = -\frac{d[O_2]}{dt} = \frac{d[CO_2]}{dt} = k[O_2]^n, \qquad (2\text{-}6)$$

where [C] and [O_2] are the initial concentration of carbon and oxygen, respectively; [CO_2] is the concentration of carbon dioxide formed during the reaction, k is the reaction rate, and the index n characterizes the order of the reaction. The reaction rate k is temperature-dependent following the Arrhenius equation:

$$\ln k = \ln A - \frac{E_a}{R} \cdot \frac{1}{T}, \tag{2-7}$$

where E_a is the activation energy of the oxidation (in kJ/mol), T is the temperature (in K), R is the universal gas constant, and A is a pre-exponential constant often referred to as frequency factor. The activation energy can be understood as a measure of the energy that is required for the oxygen-carbon to occur. The frequency factor reflects the probability of a molecule to become activated. Therefore it is also a measure of the total number of molecules that possess the activation energy.

Reaction rates can be determined by directly measuring the concentration of the reaction products (CO_2) or determining the decrease in the concentration of the reactants (C).[86] In this work, we will study the reaction kinetics by analyzing the weight loss of the carbon materials during oxidation using TGA. The change in weight is indirectly related to the reactivity of carbon and its activation energy. The relationship between weight loss and activation energies will discussed in the following chapter.

2.2.1.2 Mechanism and Reaction Kinetics

The oxidation mechanism consists of several individual steps, of which each can become the rate controlling process of the reaction. A typical, non-catalyzed oxidation is subject to the following reaction steps:

1. Transport of oxygen to the graphite surface
2. Adsorption of oxygen onto the graphite surface (physisorption)
3. Formation of oxygen-carbon bonds (chemisorption)
4. Breaking of carbon-carbon bonds
5. Desorption of reaction products from the graphite surface
6. Transport of reaction products away from the graphite surface

The contribution of each step to the total oxidation reaction depends on the environmental conditions, and can be controlled by temperature, partial pressure of the oxidant, active surface area, amount of catalyst impurities and surface functionalities, diffusion constants and defect concentration.

Depending on the oxidation temperature, one typically distinguishes among three main reactions regimes. At low temperatures (low oxidation rates), the concentration of the oxidant is essentially the same everywhere in the sample (chemical regime). The reaction rates are largely determined by the intrinsic reactivity of a carbon material, while different parts of the structure may react at different rates. The chemical regime ranges from approximately 300 to 600 °C, and rate controlling processes are steps (2) to (5).

The second regime is characterized by diffusion control, with reaction rates thus being determined by steps (1) and (6). The diffusion of oxidants and reactants is strongly affected by the pore structure of a material, especially at the nanoscale. The third regime is dominated by mass transfer. The reaction rate is so high that nearly all of the oxidant is consumed at the outer surface of the material. The reaction is controlled by steps (1) and (6), which are strongly dependent upon the partial pressure of the oxidant.

In this study, oxidation reactions occur mainly in the chemical regime and are therefore, in a first approximation, independent from the diffusion of oxidants and reactants. The rate

controlling steps are physisorption (2) and chemisorption of oxygen (3), and the breaking of the carbon-carbon bonds (4).

Using low-temperature thermal desorption spectroscopy, Ulbricht et al. showed that the binding energy of oxygen on defect-free graphitic surfaces ranges between 0.12 and 0.19 eV.[87] In their experiments, the reaction of molecular oxygen with graphitic surfaces did not produce any reactants such as carbon monoxide or carbon dioxide, suggesting the dominant interaction to be of van der Waals type.[87] Their assumption was confirmed by density functional theory calculations, which revealed the absence of any kind of charge transfer between the oxygen molecules and the carbon surface as a result of the energy mismatch between the unoccupied states of molecular oxygen and the valence band of graphite.[88]

Therefore, any reaction between oxygen and graphitic surfaces requires a transformation of unoccupied states. Physisorption onto defective sites such as edges or vacancies lowers the energy of the unoccupied states in oxygen molecules, and allows oxidation (chemisorption) of graphitic materials at temperatures below 600 °C (chemical regime).[87] Only temperatures above 700 °C facilitate the removal of carbon atoms from defect-free basal planes.[89]

Two different reaction mechanisms have been proposed for the oxidation of graphitic surfaces[90]: the Eley-Rideal mechanism[91] (ERM) and the Langmuir-Hinshelwood mechanism[87] (LHM). The latter consists of two distinct steps: (1) physisorption of oxygen on the graphitic surface, and (2) diffusion of the physisorbed species to the defective sites, where carbon-oxygen bonds are formed. The ERM process is characterized by a direct collision of oxygen molecules with the surface.[91] Both the physics of reaction mechanism and the adsorption energies are dependent on the structure of the graphitic surface.[91] For

example, former studies suggested that the oxidation of graphite follows the LHM, which includes physisorption of oxygen and diffusion to defective sites[91], while chemisorption on CNTs occurs mainly due to the direct collision of oxygen molecules with defective sites and edge atoms[88]. More recent studies using scanning tunneling microscopy showed that reaction kinetics at the atomic level appear to be quite complex because both size and shape of the defects strongly affect the oxidation mechanism, leading to energetically different adsorption sites.[92]

For carbon materials, the weight loss during oxidation in the chemical regime ($T < 600$ °C) reads:

$$\frac{dm}{dt} = k \cdot m^n , \tag{2-8}$$

where m is the sample weight, t is the oxidation time and k is the reaction rate for a constant temperature (isothermal reactions).[93] The index n is used to account for particle shape and/or surface area available for oxidation. For example, oxidation reactions that are characterized by a contracting volume or a contracting area apply $n = 2/3$ and $n = 1/2$, respectively. In case of formal phase boundary reactions we assume $n = 1$.[80]

The measured weight loss during oxidation is commonly expressed as weight fraction α defined by:

$$\frac{d\alpha}{dt} = \frac{d(\frac{m_0 - m}{m})}{dt} = k(1-\alpha)^n , \tag{2-9}$$

where m_0 and m are the initial sample weight and sample weight at time t, respectively, and k is the reaction rate. Using equation 2-7 and 2-9 one can estimate the activation energy for the oxidation reaction by determining the slope of the Arrhenius curve. Changes in the slope indicate the presence of different reaction mechanisms. At low temperatures reactions are

controlled by the chemical process itself, while at elevated temperatures (T > 600 °C) oxidation reactions are increasingly dominated by the diffusion of gaseous species. The critical temperature that separates both steps depends on several factors, including surface area and pore structure of materials[94], and has been neither well defined nor exactly determined.[85] Other critical factors are the partial pressure of the oxidizing gases, the gas flow used during the experiments, and mechanical stress applied to the material.[85]

Diffusion controlled oxidation mechanisms have been studied by several groups.[95] However, in the case of carbon nanomaterials, size and surface-effects are dominant and therefore of particular importance for diffusion processes. In this work, oxidation reaction occurs mainly in the temperature range between 300 and 500 °C (chemical regime), and diffusion is therefore considered as negligible.

2.2.1.3 Oxidation of Graphite in Air

The solid-gas reaction between molecular oxygen and graphite is technologically and scientifically important and one of the most studied reactions.[96-98] The reaction mechanism has been described using both ERM[91] and LHM[87]. In the following discussion we assume the latter to be the dominant process and restrict ourselves to a two-dimensional graphite layer (basal plane).

The oxidation of oxygen on the graphite layer proceeds through two distinct steps[99]:

1. Physisorption of molecular oxygen onto the basal plane, and
2. Diffusion of molecular oxygen to defective sites.

As mentioned above, physisorption of oxygen onto the basal plane is of van der Waals type and occurs without any charge transfer (**Figure 2.7**a).[87] The diffusion of physisorbed oxygen to defective sites lowers the kinetic barrier of oxygen-graphite reaction, enabling a charge transfer. There exist various types of defects which are energetically different. In general, one distinguishes between vacancies and edge sites (armchair, zigzag) as illustrated in **Figure 2.7**b.

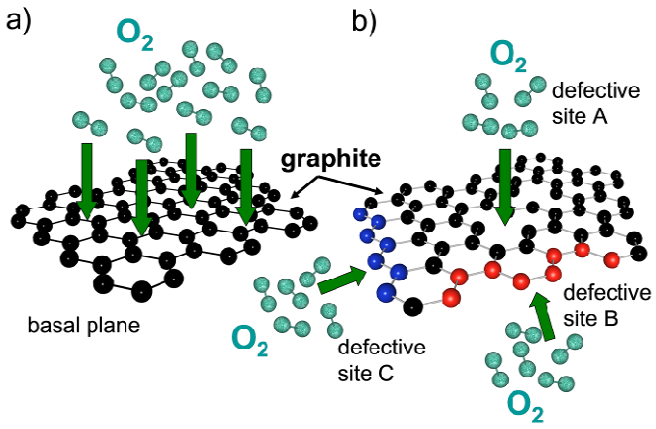

Figure 2.7: Reaction of molecular oxygen with graphite layer. (a) Physisorbtion of oxygen on the basal plane. (b) Chemisorption of oxygen at defective sites: vacancies (site A), armchair (site B) and zigzag edges (site C).

The presence of a defects leads to a reduction of the adsorbed oxygen at the surface and formation of various activated oxygen species, as O^-, O^{2-}, O_2^{2-} and O_2^-. The O^{2-} ion is the most stable surface species and preferentially formed according to:

$$O_2(ads) + C_{defect} + 2e^- = O_2^{2-}(ads) \quad (2\text{-}10)$$

$$O_2^{2-}(ads) + 2e^- = 2O^{2-}(ads) \quad (2\text{-}11)$$

The oxide ions then lead to the formation of oxygen-carbon surface groups:

$$O^{2-}(ads) + C_{defect} = CO(ads) + 2e^-. \quad (2\text{-}12)$$

The most common surface functionalities formed during the oxidation of graphite are carboxyl and carbonyl groups. The nature of the functional group formed depends on the temperature and the reactivity of the defective site, which is different for different types of defects. The decomposition of carboxylic acids and lactones occurs at low temperatures (< 300 °C) and leads mainly to desorption of carbon dioxide, whereas phenols and quinones favor formation of carbon monoxide, but decompose only at temperatures above 600 °C. The exact decomposition/desorption temperatures depends on the carbon material used and may vary in literature.

2.2.1.4 Oxidation of Carbon Nanomaterials

Although much progress has been made in both synthesis and purification of carbon nanomaterials, samples still contain nanostructures of different size, shape and composition.

As-produced carbon nanomaterials are composed of mixtures of CNTs, fullerenes, carbon onions, amorphous carbon and graphite, which are structurally different and possess different reactivity. Even within a category, significant variation may exist. Since the oxidation kinetics are closely related to structural features, reaction rates and activation energies are expected to differ for the distinct carbon forms, which is an important issue for oxidation-based purification or surface functionalization. In analogy to graphite or carbon soot, oxidation of a carbon nanostructure can be described by a first order reaction, with respect to the carbon component (equation 2-6).

Therefore, depending on the temperature, the oxidation of carbon nanomaterials can be understood as an overlap of several first-order oxidation reactions resulting from different nanostructures present in the sample. The resistance against oxidation increases with the

level of graphitization and is lowest for amorphous carbon. While CNTs are highly graphitized, curvature effects lower the activation energy, compared to that of graphite or graphene. A generally accepted oxidation model for CNTs has been proposed by Ayajan et al, wherein the fullerene-like caps are oxidized first, followed by a layer-by-layer gasification of the outer walls.[100] The oxidation of the fullerene-like CNT caps was found to be preferential to oxidation of CNT sidewalls due to the larger curvature.[101] However, Shimada et al. revealed that defects within the wall-structure (e.g. vacancies, dislocations, cracks) significantly lower the activation energy and may be more reactive than the pentagonal defects of the caps.[102] In case of MWCNTs, activation energies ranging from 225 up to 292 kJ/mol have been measured[86,103] and were in good agreement with theoretical data[104] Oxidation studies on SWCNT samples showed activation energies of 119 - 183 kJ/mol, depending on the fitting procedure used during data analysis.[80,86] It should also be mentioned that the obtained data represents an average value, resulting from many individual CNTs

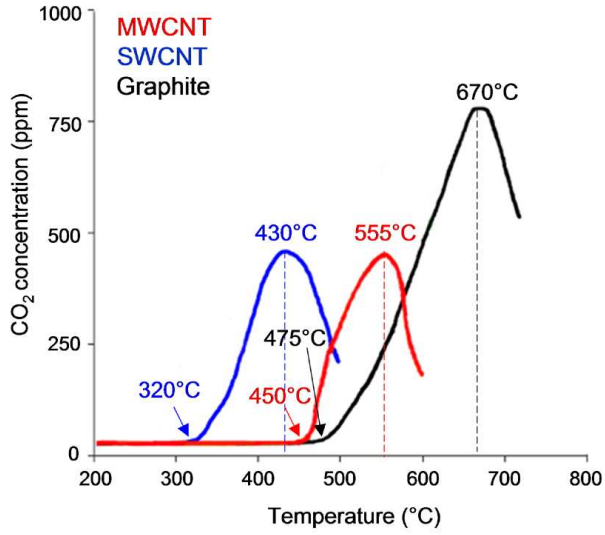

Figure 2.8: CO_2 evolution profiles measured during oxidation of SWCNTs and MWCNTs in comparison with graphite using a heating rate of 2 °C/min. Data obtained from Ref. 86.

within the broad diameter distributions of most CNT samples. **Figure 2.8** shows the CO_2 evolution profiles of SWCNTs and MWCNTs in comparison to graphite. It can be seen that the resistance of SWCNTs towards oxidation is lower than for the larger MWCNTs and bulk graphite. The corresponding activation energies are 120.6, 291.8 and 265.4 kJ/mole.[86] The frequency factors of MWCNTs ($6.6 \cdot 10^{14}$) and graphite ($2.1 \cdot 10^{12}$) were found to be similar and much higher compared to SWCNTs ($7.7 \cdot 10^{5}$).[86]

However, the values of the activation energies depend on the analysis method used. In addition, concentration of defects, homogeneity and morphology of the sample, presence of catalyst particles, and other synthesis-related factors must be taken into consideration during the analysis of the measured data and interpretation of the results. Therefore, literature data on activation energies of carbon nanomaterials vary widely.

2.2.1.5 Catalytic Reactions

In many experiments, the energy required for the oxidation of carbon materials is significantly lower than the activation energy predicted by theoretical calculations.[105] The process of lowering the activation energy by providing alternative reaction pathways is called catalysis.[106] Catalysts interact with the reactants (O_2) and form an intermediate state (typically oxides), which subsequently forms the reaction product (CO_2). The main advantage of the catalytic reactions is that the alternative route has a lower activation energy compared to the non-catalyzed reaction (**Figure 2.9**) and, for a given temperature, more molecules possess the energy needed to reach the activated state.[106] Thus, catalysts enable reactions that would be thermodynamically impossible in their absence, or serve to accelerate oxidation reactions several orders of magnitude. The catalyst itself is not consumed during the reaction and may

participate in multiple catalytic cycles.[106] Therefore, even small amounts of catalysts in the sample can significantly affect the oxidation reaction.

A large number of different inorganic materials, ranging from noble metals to salts and oxides of alkali and alkaline earth metals, were found to catalyze the reaction of carbon with gaseous reactants such as O_2 or CO_2 at elevated temperatures. The common property of these materials is that they are able to form several oxidation states in the temperature regime of the oxidation process. Although catalytic reactions are not fully understood and

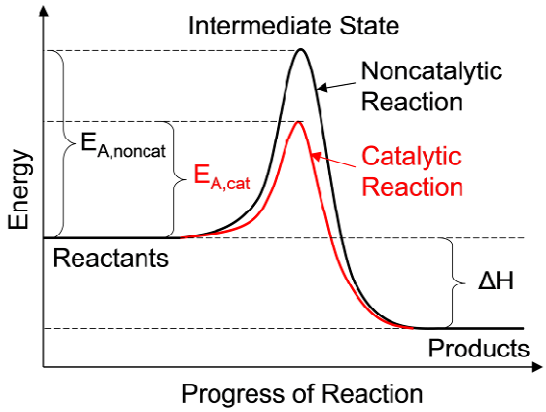

Figure 2.9: Energetics of catalytic and non-catalytic reactions. The presence of catalysts such as iron lowers the activation energy for carbon oxidation by using alternative reaction pathways.

the subject of ongoing research, it is generally agreed that catalytic processes result from oxidation/reduction cycles on the carbon surface. A simple catalytic process involving carbon (C), molecular oxygen (O_2) and a metal (Me) may follow two steps: the oxidation of the metal according to

$$Me + \tfrac{1}{2} O_2 = MeO\,, \tag{2-13}$$

and reduction of the metal oxide (MeO) by the carbon:

$$MeO + C = CO + Me\,. \tag{2-14}$$

The effects of catalysts on the oxidation temperature can be significant. For example, lead (Pb), copper (Cu), silver (Ag), iron (Fe), platinum (Pt), and nickel (Ni) were found to lower the ignition temperature of graphite powder from 740 to 382, 570, 585, 593, 602 and 613 °C, respectively. In all cases, the concentration of the metal in the sample was < 0.2 wt%.[107] While catalysts are widely used for large scale production of chemicals and play an important role in biological processes, they are consider as impurities in the case of carbon nanomaterials as they alter their properties and limit the number of potential applications.

2.2.2 Purification of Carbon Nanomaterials

2.2.2.1 Carbon Nanotubes

Most of the common CNTs synthesis methods include the usage of metal catalysts such as Fe, Co or Mg to maximize the CNT yield.[48,108-110] The as-produced raw material is thus often a mixture of CNTs, catalyst particles, amorphous carbon, and defective or damaged tubes. Furthermore, the final product usually contains tubes with a different number of walls and a wide diameter distribution, which can vary largely between several synthesis methods.[25,26,48,108-110] In particular, the presence of metal catalyst and amorphous carbon in as-produced samples may impair many potential applications. Unfortunately, there exists no single purification process which would remove all impurities and separate one class of CNTs from other types.

Removal of amorphous carbon and most catalyst particles has been achieved using acids such as HCl, HNO_3 or H_2SO_4.[53,73,74,91-94] Vacuum annealing at high temperatures has also

been reported to successfully remove metal impurities, amorphous carbon and defects from the CNT samples.[111] Oxidation in air and carbon dioxide was found to selectively remove amorphous carbon, highly damaged or small-diameter CNTs.[112-116] However, in most cases, the observed weight losses are very high and can exceed 90% after purification due to a lack of process control.

An accurate control of the purification process is needed to determine ideal oxidation conditions that lead to removal of impurities without loss of, or damage to valuable nanotubes. This is hard to realize for acid purification or high-temperature vacuum annealing, but feasible for oxidation treatments using gases such as air, oxygen or carbon dioxide.

2.2.2.2 Nanodiamond

The raw diamond-bearing soot obtained during detonation synthesis consists of ND agglomerates, non-diamond carbon, as well as metals, metal oxides and other impurities coming from the detonation chamber or the explosives used. Most producers employ liquid phase oxidizers such as HNO_3, $HClO_4$, H_2SO_4, H_2O_2, or aqueous and acidic solutions of $NaClO_4$, CrO_3, or $K_2Cr_2O_7$ to selectively remove amorphous and graphitic carbon from ND powders.[18,117] The treatments are based on different reactivity of diamond and non-diamond species towards oxidation, while oxidation time and temperature depend on the reactant used and the desired ND grade.[18,117]

In addition several dry chemistry techniques, including catalyst assisted oxidation[118], oxidation using boric anhydride as an inhibitor of diamond oxidation[119] and ozone-enriched air oxidation[120] have successfully been used to remove non-diamond phases from ND

powders. Catalyst-assisted oxidation in air consists of air bubbling through a water suspension of ND in the presence of catalysts favoring the oxidation of non-diamond carbon.[118] The need for the catalyst to selectively oxidize non-diamond carbon is the main disadvantage of this technique. Chiganov et al. used boric anhydride as an inhibitor of diamond phase oxidation during ND purification in air at elevated temperatures (300 - 550 °C).[119] Ozone-enriched air oxidation is based on blowing an ozone-air mixture through the detonation soot at temperatures between 150 and 400 °C.[120] However, the purity that has been achieved using the described methods is still insufficient. Moreover, similar to acid-based purification, they also require the use of either toxic and aggressive substances, or supplementary catalysts, which result in an additional contamination or a significant loss of the diamond phase.

Table 2.2 compares structure and composition of the ND powder mainly used in this study before (UD50) and after purification (UD90, UD98).[121] Black UD50 is the unpurified raw detonation soot containing mainly non-diamond carbon structures, such as amorphous carbon, carbon onions and graphite ribbons. The black color of the powder is related to the high content of sp^2 carbon (> 70%). UD90 and UD98 are purified by a multi-stage acid treatment using sulfuric (H_2SO_4) and nitric (HNO_3) acid. The denotation soot is immersed in concentrated acid, stirred and cooked for several hours at elevated temperatures. After cooling, the ND powders are washed in water until neutral (pH ~ 7) and centrifuged to extract the diamond crystals from the aqueous solution.

While these techniques are widely used, they do not provide sufficient purity, leading to the dark-grey color of commercially available ND powders (**Table 2.2**).[121] However, acid purification remains the most complicated and expensive stage in the ND production cycle and is crucial for all applications.

Table 2.2: Properties of as-produced and purified ND (Ref. 121).

	After Detonation	After Purification	
	UD50	UD90	UD98
Optical photograph	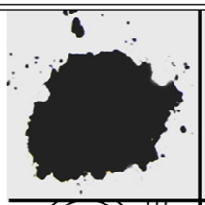	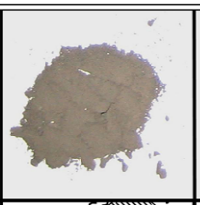	
Schematics of carbon structures present in the samples	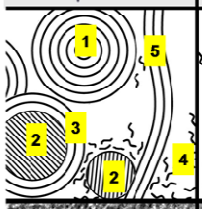	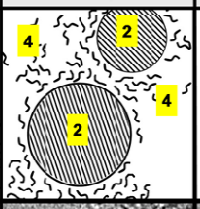	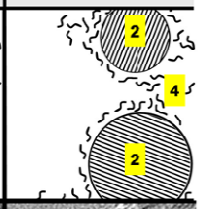
HRTEM image	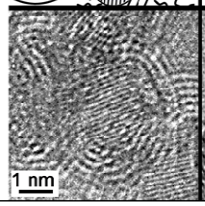	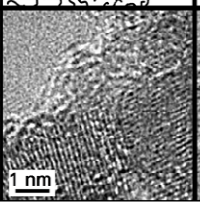	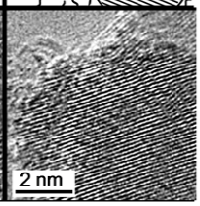
sp^3 carbon content	23%	70%	81%
Ash content	3.1 wt%	2.0 wt%	1.3 wt%
Fe content	1.3 wt%	0.7 wt%	0.2 wt%
BET-SSA	460 m^2/g	367 m^2/g	350 m^2/g

Notation in the schematics: (1) - carbon onion, (2) – nanodiamond, (3) - fullerenic shell, (4) - amorphous carbon, (5) – graphite ribbon

While the process is simple, inexpensive, environmentally friendly, and scalable, selective removal of non-diamond carbon in the ND soot by air oxidation would be very attractive. However, thus far it has not been considered feasible.[119] Chiganov et al. pointed out that the major part of non-diamond carbonaceous content (~ 60 wt.%) could be removed by air oxidation, but remaining graphitic carbon could not be destroyed selectively without considerable loss of the diamond phase.[119] Unfortunately, no experimental details (i.e. temperature and time of treatment), which led him to this conclusion, were reported. Cataldo et al. studied the oxidation of ND in an air flow and found that the ND sample is stable towards oxidation at temperatures below 450 °C, but burns quite suddenly above

450 °C.[122] However, no changes in content of diamond and non-diamond carbon were reported.

2.2.3 Functionalization of Carbon Nanostructures

A large number of potential applications are hindered by the tendency of carbon nanoparticles to agglomerate. For example, carbon nanotubes usually form large bundles, resulting in poor solubility, and are therefore difficult to handle.[123-125] In order to improve the solubility, the surface of carbon nanotubes has been functionalized.[126-129] Existing methods can generally be divided into two groups, depending on whether attached groups are introduced to the tips or to the sidewalls of a carbon nanotube. One can further distinguish between covalent and non-covalent functionalization.[43] The easiest way to covalently attach chemical groups (e.g., carboxylic groups) can be achieved by oxidation.[130]

Oxidation reactions in air[131], ozone[132] or nitric (HNO_3)[133] and sulfuric (H_2SO_4)[134] acid create defect sites in the wall structure, resulting in the formation of carboxyl and carbonyl groups on the surface of the nanotubes. These groups can then be used as sites for further functionalization.[135,136] Other techniques involve amidation[137,138] or fluorination[139,140]. Surface functionalization was also successfully used for the separation of metallic and semiconducting carbon nanotubes[141] as well as for diameter dependent length separation[142] of SWCNTs.

Dispersion of strongly bonded agglomerates is also a major issue limiting the use of ND. A large number of potential applications including biomedical imaging, drug delivery, and biocompatible and biodegradable composite materials are hindered by the current inability of manufacturers to provide ND with a well-controlled surface chemistry.[18] While being very

uniform in size, ND particles differ greatly in terms of their surface terminations, carbon phase composition, and the content of non-carbon impurities. To a large extent, this is the result of different purification procedures.

Similar to carbon nanotubes, functionalization has been used to modify and control the surface chemistry of ND particles.[143-145] Chen et al. annealed ND at 800 °C in an Ar atmosphere and observed a reduced agglomeration of ND crystals.[146] The graphitization of ND led to the removal of surface functional groups because graphene layers, which are formed during annealing, have a smaller number of active sites for functional group attachment compared to diamond-like carbon. Eremenko et al. observed an almost complete (> 95%) removal of surface functional groups at 800 °C in either Ar or H_2 atmosphere.[147] Thus, literature data show that when treated in an inert atmosphere, ND undergoes progressive graphitization at temperatures equal or higher than 800 °C. This treatment can be used to remove all functionalities from the surface of ND, and therefore it can be considered as a universal way to create a non-functionalized material for subsequent functionalization or specific applications. A concept for graphitization-based deagglomeration of ND has been proposed by Xu et al.[148] The graphitized surface of ND crystals has almost no functionalities. Thus, the interactions between crystals become weaker, and agglomerates are easier to break into smaller aggregates. Afterwards, graphitic shells were removed by air oxidation at 450 °C.

Spitsyn et al. studied solid-gas interactions of ND with hydrogen, chlorine, ammonia and carbon tetrachloride at high temperatures.[149] They found that ND treated in a mixture of Ar/CCl_4 gas showed a significant decrease in water adsorption as compared to, for example, ozone-purified ND.[149] The lower hydrophilicity results from an increase in the number of C-Cl bonds accompanied by a decrease in the amount of oxygenated functional groups on the

surface of ND.[150] Annealing in hydrogen[149] or NH_3[151] results in a strong decrease of C=O bonds and a significant increase in the number of C-H groups.

Liu et al. have recently reported on the fluorination of ND and subsequent reactions of the reactive fluoro-ND to produce hydrocarbon-, carboxy- and amino-terminated ND powders.[152] They have shown that a mixture of F_2/H_2 reacts with nanodiamond even at temperatures as low as 150 °C.[152] Fluorinated ND has also been used as precursor for subsequent reactions with alkyllithium reagents and diamines[153].

Oxidation using various reactants has been used to facilitate surfactant interactions and to enhance dispersibility.[154,155] Surface functionalization of ND via atom transfer radical polymerization, where organic polymers of choice can be grown directly on ND, has also been reported.[143]

These results show that gas treatment techniques can be used for purification and functionalization of ND. However, many previous studies used powders of different quality and purity, complicating comparison and interpretation of the published data. Moreover, many aspects of high temperature gas treatment of ND are still poorly understood.

2.2.4 Activation of Porous Carbon Materials

Carbon activation has been investigated for decades and is well known as a powerful route to modify the properties (porosity, microstructure, surface chemistry, electrical conductivity, etc.) of carbon materials.[156] Different methods have been developed including chemical activation using molten NaOH and KOH[157,158] or hot acids (HNO_3, H_2SO_4, H_3PO_4)[159] and physical activation in air, CO_2, or steam.[71-73,75-77,160] The properties of activated carbons strongly depend on the activation process and choice of conditions. Even minor

changes in the reaction conditions (e.g., temperature, concentration, and time) for the same reagent can lead to significant differences in pore texture, surface chemistry and microstructure.[161,162]

CDCs can be manufactured with a large variety of porosities, depending on synthesis conditions such as the carbide precursor, chlorination temperature, time and annealing procedure. Although large pore volumes can be achieved by using precursors with large metal/carbon ratios, pore growth and structure collapse occur when precursors with low carbon contents are used.[163] Practically, it is also more suitable to use low cost precursors such as TiC or SiC which produce about ~ 55% of porosity in case of conformal transformation. Since chemically CDC is similar to other porous carbons, methods of activation that are used for other carbon materials may be applied to CDC.

Activation procedures that maximize pore volume and surface area of different carbon materials lead to a simultaneous broadening of the pore size distribution (PSD), which can limit the control over the porosity. In most cases, the required activation conditions depend on the nature of the initial carbon, its porosity, degree of graphitization, and surface chemistry.[73] Of the potential activation techniques, physical activation is particularly advantageous due to its use of inexpensive gaseous reactants and process simplicity. Physical activation in CO_2, steam or air has been widely studied for different activated carbons.[72,162,164] CO_2 is a relatively mild oxidizer, which leads to a better control over the development of microporosity during activation compared to other reagents such as steam, O_2 or air.[71,75,77,160] On the other hand, air activation is a low energy/low cost process because of the higher reactivity, requiring a lower activation energy as compared to CO_2 or steam.[73,164,165] However, the process is more difficult to control.

Oxidation in air and CO_2 are therefore potentially suitable to control and modify the porosity of the most common and low-cost CDCs, such as TiC-CDC[166] or SiC-CDC[167], in order to achieve the desired pore volume or size. However, very little has been reported on activation of CDC, although CDC heating in nitrogen, air, CO_2 and water vapor was described in an early patent as a method of residual chlorine removal.[168] Activation of CDC by infiltration with water and fast heating was also mentioned, but no detailed studies of the activation process parameters on CDC structure and properties have been published.

2.3 Raman Spectra of Carbon Nanostructures

In solid-state physics, lattice vibrations are fundamental characteristics of crystals and determine a large number of their thermal, mechanical, and transport properties. The quantized energy of a vibrational mode (normal mode) is described by a phonon, and depends on the both the crystal structure and its environment. In analogy to photons (quantum of light), phonons are quasi-particles and can be understood as wave packets with particle-like properties. Atomic mass, bond order and geometry, the presence of substituents or hydrogen bonding all affect the lattice vibrations and thus the phonon energies of a crystal.

Solids with more than one atom per unit cell exhibit two types of phonons: acoustic phonons and optical phonons.[169] Acoustic phonons correspond to uniform displacements of the entire crystal. Modes where the atoms of the unit cell move out-of-phase are referred to as optical phonons. One further distinguishes between transverse and longitudinal modes. In the case of transverse modes, atoms move perpendicular to the propagation direction of the wave, whereas for longitudinal modes, the displacement of atoms coincides with the

direction of the wave. A three-dimensional crystal with N atoms per unit cell possesses $3N$ phonon modes: 3 acoustic modes (1 longitudinal, 2 transverse) and $3N$-3 optical modes (N-1 longitudinal, $2N$-2 transverse).[169] Information about the phonon modes of a crystal, their energy dispersion, and interaction with electrons or quasi-particles are essential for understanding the properties of a material.

Raman spectroscopy is a non-destructive but powerful tool used to study the vibrational modes of solids and provides deep insight into the physical processes that take place. The Raman process includes absorption and emission of light as well as inelastic scattering of electrons by phonons. By measuring the energy difference between the incident and Raman scattered light, one obtains a precise measure of the vibrational energies of a material.

Raman spectroscopy is commonly performed using lasers as excitation source. Lasers provide intense, highly collimated and monochromatic light, allowing for higher spatial resolution and measurement of relatively small vibration frequencies. Although the laser spot size of a conventional Raman spectrometer is in the order of 1 - 2 μm, Raman spectroscopy is suitable for the characterization of nanostructures such as CNTs and ND, because the spectral information originates from chemical bonds and thus the atomic level. The potential of Raman spectroscopy for characterization of carbon nanostructures ranges from a fast identification of different carbon phases and determination of the crystal structure, to estimates on structural disorder, sample temperature, lattice strains and crystal size.

2.3.1 Inelastic Light Scattering and Raman Effect

If a medium is irradiated by monochromatic light (intensity I_L, frequency ω_L), most of the radiation is either absorbed or transmitted, following the laws of reflection and

refraction. Only a small fraction ($10^{-4} \cdot I_L$) of the incident photons is scattered equally in all directions. When the incoming laser radiation interacts with a molecule or a solid, electron orbitals are disturbed periodically with the frequency ω_L of the incident wave. The resulting oscillation of the electron cloud leads to a periodic separation of charges and causes a temporary polarization of the bonds. The induced dipole moment is then manifested as a source of electromagnetic waves, thereby leading to the emission of scattered light with the frequency ω_S. Scattering events occur in less than 10^{-14} seconds and result from inhomogeneities, which can be of static or dynamic nature. Crystalline defects, such as dislocations, are static scatterers and lead to elastic light scattering, also known as Rayleigh Scattering ($\omega_S = \omega_L$).[170] Atomic and molecular vibrations represent dynamic inhomogeneities and result in inelastic scattering of light ($\omega_S \neq \omega_L$).

C.V. Raman and K.S. Krishnan[171] were the first who described the inelastic scattering of light by molecular vibrations. In their experiments they observed a very small portion of light ($10^{-9} \cdot I_L$) with new frequencies $\omega_S = \omega_L \pm \omega_{vib}$, where ω_{vib} was determined by the vibrational properties of the medium (**Figure 2.10**a). Unlike direct light-absorption, the measured scattering did not require incident photons to match the energy difference between two electronic states and was thus independent from the excitation wavelength. Their discovery was awarded with the Nobel Prize (1930) and became known as the Raman effect.

A theoretical description of the Raman effect was first accomplished by classical electrodynamics and later completed using quantum mechanics. Both approaches consider an oscillating electric dipole $\vec{\mu}$, induced in a molecule by the electromagnetic field $\vec{E}$ of the incident light wave, to be the main origin of the scattered radiation. The induced dipole is

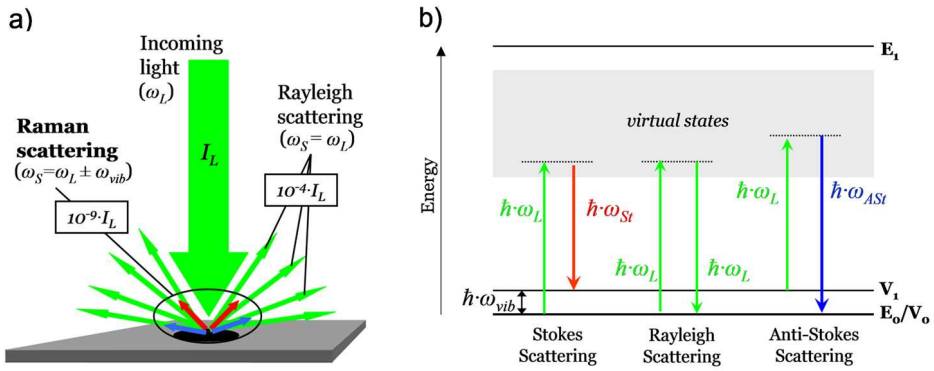

Figure 2.10: Elastic (Rayleigh scattering) and inelastic scattering (Raman scattering) of light. (a) The incoming monochromatic light (ω_L) interacts with the electron clouds of the molecules: approximately 10^{-4} of the photons are scattered elastically ($\omega_S=\omega_L$) and only 10^{-9} of the incident photons have new frequencies ($\omega_L \pm \omega_{vib}$). (b) Raman process in the energy transfer model.

dependent on the polarizability α and given by $\vec{\mu} = \vec{\alpha} \cdot \vec{E}$ The polarizability $\vec{\alpha}$ indicates how tightly the electrons are bound to the nuclei. For Raman scattering to occur, $\vec{\alpha}$ must vary for different molecular orientations ($d\vec{\alpha} / d\vec{r} \neq 0$). This is always the case for both heteronuclear and homonuclear diatomic molecules. If a vibration does not significantly change the polarizability ($d\vec{\alpha} / d\vec{r} = 0$) then the intensity of the Raman signal is low. For example, Raman scattering of highly polar molecules such as H_2O is relatively weak. O-H bonds posses an uneven distribution of the electron density and are inherently highly polar. Hence, the polarizability is low and the external field can not induce large changes in the dipole moment $\vec{\mu}$. Strong Raman scatterers such as carbon-carbon double bonds (C=C), with an evenly distributed electron density, exhibit large changes in the polarizability. The π-orbitals of C=C bonds are easily distorted and bending or stretching of the bonds cause a substantial change in the electron density and thus the induced-dipole moment.

Depending on the frequency ω_S of the Raman scattered light, one further distinguishes between Stokes ($\omega_{St} = \omega_L - \omega_{vib}$) and Anti-Stokes ($\omega_{ASt} = \omega_L + \omega_{vib}$) scattering (**Figure**

2.10b). In each case, the incident light excites an electron into a higher "virtual" energy state, followed by the relaxation of the electron to a lower energy level and emission of a Raman scattered photon. Stokes and Anti-Stokes features represent the energy difference (ΔE) between the incident and Raman scattered photon, and are therefore a direct measure of the vibrational energies (E_{vib}) of a crystal (**Figure 2.10**b). The energy difference ΔE in wavenumbers (cm^{-1}), commonly referred to as Raman shift ν, can be calculated according to

$$\nu = \frac{1}{\lambda_L} - \frac{1}{\lambda_{St\,/\,ASt}} = \frac{2\pi}{c}(\omega_L - \omega_{St\,/\,ASt}), \tag{2-15}$$

where c is the speed of light in vacuum, and λ_L and $\lambda_{St/ASt}$ are the wavelengths of the incident and Raman scattered photons, respectively. A plot of the intensity of the scattered light versus the energy difference (Raman shift) is called Raman spectrum, and may appear as shown in **Figure 2.11**. Stokes and Anti-Stokes lines are equally displaced from the Rayleigh line, since in both cases a vibrational quantum of equal energy ($\Delta E = E_{vib} = \hbar \cdot \omega_{vib}$) is gained or lost.

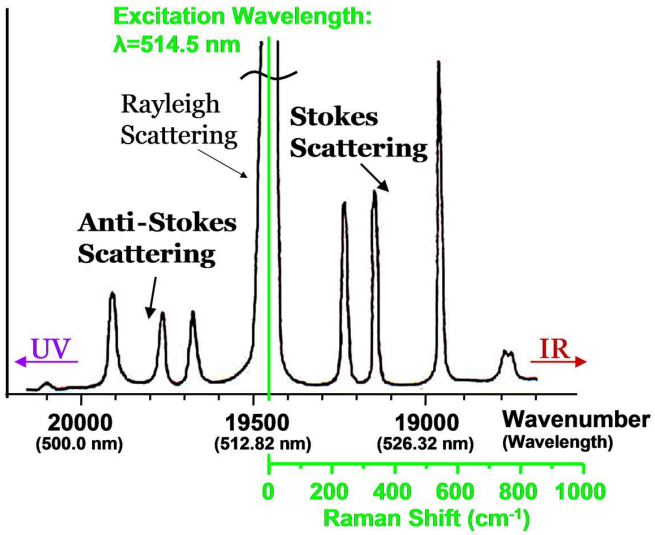

Figure 2.11: Typical Raman spectrum showing Rayleigh, Stokes and Anti-Stokes scattering. Peak positions are given in Raman shift and refer to the energy difference between the incoming and Raman scattered light.

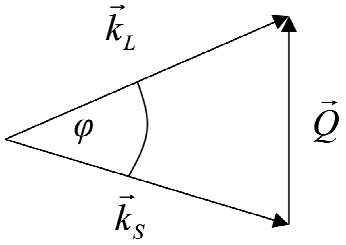

Figure 2.12: Definition of the scattering wave vector Q in the Raman process. The angle between the incoming wave vector k_L and the scattered wave vector k_S is defined as φ.

In ambient conditions, the intensity of Stokes scattering is significantly higher compared to Anti-Stokes scattering (**Figure 2.11**). Anti-Stokes scattering requires a molecule to be vibrationally excited prior to irradiation. Since the thermal population of vibrational excited states follows/obeys the Boltzmann distribution, the probability of Anti-Stokes scattering to occur is low at room temperature. Hence, in conventional Raman spectroscopy, only the more intense Stokes lines are measured.

In the following section $\vec{k}_L$ and $\vec{k}_S$ describe the wave vector of the incoming and the Raman scattered light, respectively (**Figure 2.12**). The scattering wave vector $\vec{Q}$ is given by

$$\vec{Q} = \vec{q} \pm \vec{G}\,, \tag{2-16}$$

where $\vec{q}$ is the phonon wave vector and $\vec{G}$ is the reciprocal lattice vector of the crystal. Like all physical processes, inelastic light scattering must satisfy energy and momentum conservation:

$$\vec{k}_L = \vec{k}_S + \vec{Q} \tag{2-17}$$

$$\hbar\omega_L = \hbar\omega_S \pm \hbar\omega_{vib}\,. \tag{2-18}$$

According to, the magnitude of the scattering wave vector $\vec{Q}$ reads

$$\left|\vec{Q}\right| = Q = \left|\vec{k}_L\right|^2 + \left|\vec{k}_S\right|^2 - 2 \cdot \left|\vec{k}_L\right| \cdot \left|\vec{k}_S\right| \cdot \cos\varphi, \tag{2-19}$$

where φ defines the angle between the incoming ($\vec{k}_L$) and the Raman scattered ($\vec{k}_S$) wave vector. In the case of inelastic light scattering in solids, phonon energies are typically two orders of magnitude smaller compared to the photon energies of the incoming and Raman scattered light. Thus, assuming $\left|\vec{k}_L\right| = \left|\vec{k}_S\right|$, we can approximate equation 2-19 by:

$$\left|\vec{Q}\right| = Q \approx 2 \cdot k_L \cdot \sin\frac{\varphi}{2}. \tag{2-20}$$

$\left|\vec{Q}\right| = Q$ is largest for φ=180° leading to $Q = 2 \cdot k_L$. The magnitude of the wave vector of incoming light $\vec{k}_L$ is given by

$$\left|\vec{k}_L\right| = k_L = 2\pi \cdot n / \lambda, \tag{2-21}$$

where n and λ are the refractive index of the medium and the wavelength of exciting laser, respectively. The extension of the Brillouin zone (BZ) in a solid (range of phonon wave vectors) can be calculated according to $\left|\vec{k}_{BZ}\right| = \pi / a$, where a is the lattice constant of the crystal. For example, the wave vector $\left|\vec{k}_L\right|$ of a Nd:YAG laser (λ=590 nm) in diamond (n = 2.42, a = 0.3567 nm) is on the order of ~ 0.025 nm^{-1}. In contrast, $\left|\vec{k}_{BZ}\right|$ (for diamond) is about 8.8 nm^{-1} and thus two orders of magnitude larger than the maximum scattering wave vector $\vec{Q} = 2 \cdot \vec{k}_L$. Therefore, conventional Raman analysis (first order scattering) of solids using visible laser excitation can only probe phonons close to the Γ-point of the BZ, also known as "$\vec{q} \approx 0$" selection rule. However, in higher-order Raman scattering processes, the

$\vec{q} \approx 0$ selection rule can also be fulfilled by two phonons with large but opposite wave vector, such that $\vec{q}_1 + \vec{q}_2 \approx 0$.

Unfortunately, Raman scattering is a relatively weak process and the number of Raman scattered photons is quite small. Several variations of Raman spectroscopy have been developed including surface-enhanced Raman spectroscopy[172], resonant Raman spectroscopy[173] or confocal Raman microscopy. The purpose of these modified Raman techniques is to enhance the intensity, sensitivity and selectivity, and improve the spatial resolution during the measurements.

2.3.2 Resonant Raman Spectroscopy

2.3.2.1 Resonance Effect

Conventional Raman spectroscopy is generally performed using green (500 - 550 nm) or red (620 - 750 nm) lasers. It was found that if the wavelength of the incident laser radiation coincides with an electronic transition (absorption) of the excited molecule, the Raman intensity of vibrations associated with the transition is enhanced by several orders of magnitude (10^2 - 10^4), compared to non-resonant Raman scattering.[173,174] This resonance enhancement is very useful for improving the detection limit and the selectivity of Raman spectroscopy. In addition, Raman spectroscopy upon resonance provides deep insight into the electronic properties of a material.

The concept of non-resonant, (single-) resonant and multiple-resonant Raman scattering is shown in **Figure 2.13**. The solid lines indicate real eigenstates of the system; the dotted lines correspond to intermediate "virtual" states. In a non-resonant Raman process (**Figure**

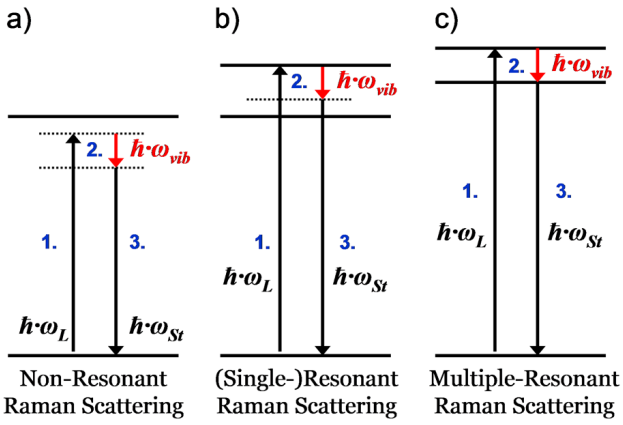

Figure 2.13: Concept of non-resonant Raman scattering (a), (single-) resonant (b), and multiple-resonant Raman scattering (c). The solid and dotted lines indicate real eigenstates and virtual states, respectively. A non-resonant process does not involve real eigenstates and both intermediate electronic states are virtual states. If one (b) or more (c) transitions are real, the Raman process resonant.

2.13a) real eigenstates are not involved: the incoming photon ($\hbar\cdot\omega_L$) is absorbed and excites an electron into a virtual state by creating an electron-hole pair (1.). The electron is then scattered to a lower virtual level by emitting a phonon of the energy $\hbar\cdot\omega_{vib}$ (2.), and finally recombining with the hole by emitting the Raman shifted photon with the energy $\hbar\cdot\omega_{St}$ (3.). In (single-) resonant Raman scattering (**Figure 2.13**b), one of the intermediate states of the electron is an eigenstate of the system. The wavelength of the incoming laser radiation is adjusted such that the incident or the Raman-scattered (not shown) photons match the energy gap between two real electronic states. Mulitple-resonant Raman processes (**Figure 2.13**c) involve two or more transitions between real eigenstates of the system.

The resonance effect does not occur at a single, sharp wavelength. Enhancement factors up to 10 have been observed, even when the energy of the laser was several hundred wavenumbers lower than the energy needed for an electronic transition.[175] In many cases, this is enough to drown out a particular Raman signal from other non-resonant vibrations

and provide the required selectivity. For example, if the incoming laser matches the energy of a π-π^* transition, the Raman intensity of C=C stretching modes is resonantly enhanced, while all other vibrational modes remain unaffected.

The transition energies and thus the resonance conditions differ from one material to another and depend on the atomic structure of the unit cell, bond order and geometry, and the crystal size.[169] Changes in the environment, e.g. dry sample versus wet sample, can also affect the resonance conditions. In addition, other factors such as temperature, strain, external electric/magnetic fields and bundling or aggregation were found to shift resonance energies, as well.[173,176,177]

Since their discovery in 1991, CNT samples have been analyzed using conventional Raman spectroscopy. However, it was not until 1997 that the great potential of RRS for CNT characterization was recognized.

Rao et al. showed that the dependence of the Raman spectrum on the excitation energy results from the diameter-selective enhancement of Raman scattering of different CNTs.[178] Pimenta et al. successfully applied RRS to differentiate between semiconducting and metallic CNTs.[179] Other studies revealed that resonance effects can even used to even determine structure and properties of individual CNTs.[180] Ever since then, innumerable studies have employed RRS in order to identify the atomic structure of CNTs and obtain information about their optical and electronic properties.[126,127]

However, Raman spectra of other carbon nanomaterials were found to show a similar dependence on the excitation wavelength. For example, ND powders consist of agglomerated particles, each comprising a diamond core partially or completely covered by layers of graphitic and/or amorphous carbon. Depending on the purity of the sample, the content of non-diamond phases can be as high as 70% (see section 2.2.2.2). The Raman

analysis of samples containing mixtures of different carbon species is difficult. In case of ND powders, a correct interpretation of Raman spectra acquired using visible lasers is hindered by the resonance enhancement of sp^2 species. For the most common 514 nm laser excitation, the Raman scattering cross sections of diamond (sp^3) is ~ 50 times smaller than that of graphite (sp^2)[181] and ~ 233 times smaller than that of sp^2 amorphous carbon[182]. Diamond-like sp^3 carbon has a higher energy gap (4 - 5 eV) compared to sp^2 carbon (~ 2 eV), and the resonant enhancement takes place in different wavelength ranges. The intensity ratio between diamond and non-diamond phases is very low in the visible range, but increases as the wavelength decreases into the UV. Therefore, while visible lasers are most suitable for analyzing the sp^2 carbon content and the graphitic shells surrounding the diamond core, an accurate characterization of the diamond phase in ND powders requires use of UV laser excitation.

2.3.2.2 Multiwavelength Analysis

The great potential of RRS for characterization of carbon nanostructures stems from the sensitivity of their optical and electronic properties to the atomic structure. For example, depending on the chirality and the (n,m) indices, CNTs can exhibit metallic or semi-metallic behavior when $n-m = 3 \cdot k$ (k = integer), whereas other CNTs that differ only slightly in structure are semiconducting, featuring a wide range of band gap energies (**Figure 2.14**a).[183,184] These novel electronic properties result from the quasi-onedimensionality of CNTs and the chirality-dependent quantization of their allowed eigenstates. The one-dimensional character of CNTs leads to sharp peaks in the electronic density of states (DOS), also known as van Hove singularities (**Figure 2.14**a).[185]

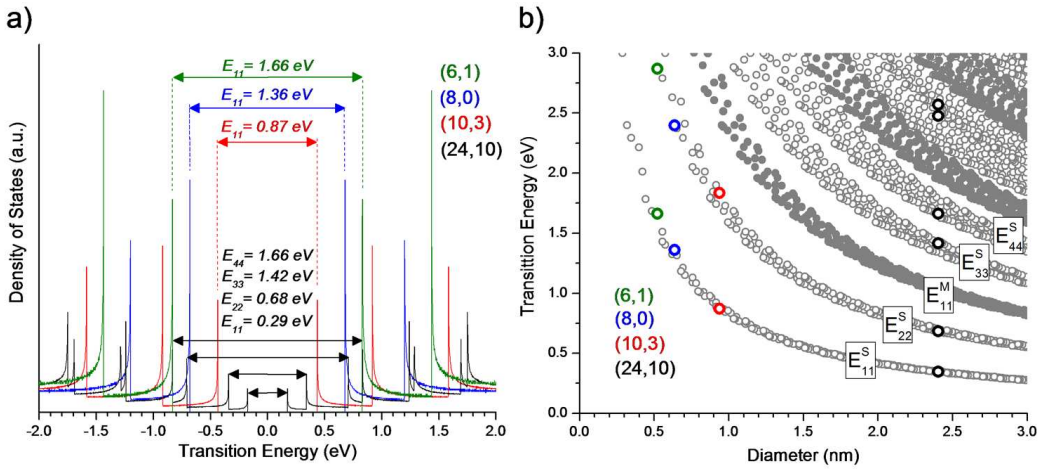

Figure 2.14: (a) Density of states of four different semiconducting CNTs. Bandgap energies range from 0.29 eV (24,10) to 1.66 eV (6,1) leading to differences in resonant conditions. (b) Transition energies of CNT as a function of diameter (Kataura plot). Closed symbols indicate metallic tubes; open circles are semiconducting tubes. E_{11}^S and E_{22}^S represent the first and second van Hove transitions in semiconducting tubes, respectively. Data obtained from Ref. 183.

Transitions between the corresponding van Hove singularities on opposite sites of the Fermi level (valence and conduction bands) dominate the absorption and emission properties of CNTs, and are the origin of the strong resonant enhancement of CNTs. The transition energies E_{ii} between the valence and conduction bands of the same symmetry, with i=1,2,3,… (index i numbers the valence and conduction subbands involved in the transition) are inverse proportional[186,187] to the tube diameter d and each set of E_{ii} values (e.g. E_{11}, E_{22}, E_{33},…) is specific to an individual (n,m) CNT. The E_{ii} energies of four different semiconducting CNTs are shown in **Figure 2.14**a. All possible transitions of CNTs (metallic and semiconducting) with diameters less than 3 nm and gap energies between 0 and 3 eV were plotted against the diameter d, in what is called the Kataura plot[188] (**Figure 2.14**b).

Tuning the laser energy through one of the E_{ii} transitions fulfills the resonance condition for a given phonon mode. The measured profile has two contributions: resonance with the incoming laser light ($E_{ii} = \hbar \cdot \omega_L$), and resonance with Raman scattered photons ($E_{ii} = \hbar \cdot \omega_L \pm$

$\hbar \cdot \omega_{vib}$), leading to an intensity maximum around $E_{ii} \pm \hbar \cdot \omega_{vib}$. Therefore, optimizing the resonance conditions by tuning the excitation wavelength allows a determination of the transition energies E_{ii} and the related structure of individual CNTs.[189] If the structure of a CNT is known, the information on optical transition energies can be used to selectively enhance the Raman scattering from a single CNT.

Many important biological species such as porphyrins[190], metallo-porphyrins[183] or carotenoids[191] show strong enhancement in the visible spectral range. Other molecules such as protein or DNA, which are frequently used for functionalization of nanoparticles, are in resonance upon UV laser excitation.[192] In order to resonantly enhance Raman signals of different molecules in solution or on the surface of nanostructures, and to achieve a high selectivity, one has to provide different excitation wavelengths or tunable lasers.

The Raman scattering cross section σ (non-resonant) is inversely proportional to the fourth power of the excitation wavelength λ_L according to[193]

$$\sigma \propto \left[\frac{1}{\lambda_L} - \frac{1}{\lambda_{vib}} \right]^4 . \qquad (2\text{-}22)$$

Therefore, selecting a shorter excitation wavelength can enhance the Raman intensity and improve the signal-to-noise. On the other hand, shorter excitation wavelengths increase the risk of fluorescence and photo-degradation of the samples due to the higher photon energy. Selecting the right excitation wavelength is crucial, especially during Raman analysis of composites materials and samples that contain different species. For example, while molecules embedded in a composite may be resonantly enhanced using UV laser excitation, strong fluorescence from the surrounding matrix can completely overshadow the Raman

signal and inhibit a characterization of the sample. Crystal defects and impurities in solids lead to similar problems.

The vibrational energy of a molecule is constant and independent from the excitation wavelength. Thus, the Raman shift is constant with respect to the wavenumber, but not the wavelength. As a consequence, the difference in wavelength between incoming and Raman scattered light is smaller for shorter excitation wavelengths, and separating elastically scattered (Rayleigh scattering) and Raman scattered light becomes more difficult, especially for small Raman shifts. On the other hand, longer excitation wavelengths (near IR) are inappropriate for Raman measurements at elevated temperatures due to the increasing intensity of thermal radiation (black body radiation) overlapping with the Raman signal.

In summary, meeting resonance conditions is essential for strong Raman scattering. However, selecting the optimal excitation wavelength depends on several factors, such as sample composition, fluorescence behavior, expected Raman shift and measurement temperature.

2.3.3 Raman Spectrum of Carbon Nanotubes

The vibrational modes of a SWCNT can be derived from the phonon structure of 2D graphite (graphene) by applying a zone folding procedure that considers the one-dimensionality of CNTs and a chirality-dependent confinement.

A graphene sheet has two atoms per unit cell, leading to 6 phonon branches: 3 acoustic modes and 3 optical modes (**Figure 2.15**a and b). The phonon structure of CNTs (**Figure 2.15**c and d) is more complex and shows a significant larger number of vibrational modes. The total number of distinct phonon branches in SWCNTs is $3(N'+2)$, where N' is the

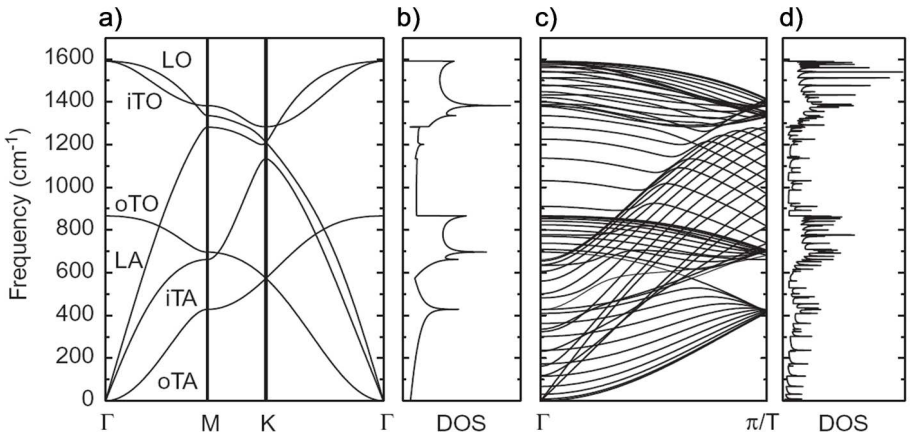

Figure 2.15: (a) Phonon dispersion relations of graphene showing 3 acoustic branches: out-of-plane transverse acoustic (oTA), in-plane transverse acoustic (iTA), longitudinal acosic (LA); and 3 optical branches: out-of-plane transverse optical (oTO), in-plane transverse optical (iTO), longitudinal optical (LO), and (b) corresponding phonon density of states. Phonon structure (c) and phonon density of states (d) of a (10,10) SWCNT calculated from 2D graphite using the zone folding approach. Plot obtained from Ref 195.

number of hexagons per unit cell.[194] For example, the phonon dispersion relations of a (10,10) armchair SWCNT exhibit 66 distinct phonon branches (**Figure 2.15**c) and a large number of van Hove singularities in the phonon density of states (**Figure 2.15**d).[195] Therefore, Raman spectra of CNTs show many size- and chirality-dependent features. However, only the most prominent and well-understood first and second-order Raman bands will be discussed. Similar to graphite, CNTs show a strong Raman peak around 1500-1600 cm^{-1} (G band) and a disorder or defect-induced feature between 1300 and 1400 cm^{-1} (D band) (**Figure 2.16**).

The G band originates from the tangential in-plane stretching vibrations of the carbon-carbon bonds within the graphene sheets. The D band is a double-resonance Raman mode, resulting from a one-phonon second-order Raman process, and can be understood as a measurement of structural disorder coming from tube edges and defects in the wall structure.[196]

In addition, CNTs show a unique, size-dependent Raman feature (100 - 400 cm^{-1}), called radial breathing mode (RBM) (**Figure 2.16**). The RBM is the real signature of the presence of CNTs and defined by a collective, in-phase vibration of all carbon atoms in the radial direction.[196] While large MWCNTs do not show any noticeable RBM signal, their Raman spectra contain an additional peak around ~1615 cm^{-1}, called D' band (not shown). Similar to the D band, D' is a double-resonance Raman feature, induced by disorder. The second-order Raman spectrum is dominated by 2D, an overtone of the D band, often labeled as G' or D* band.[196]

The following sections discuss differences between SWCNTs, DWCNTs and MWCNTs with respect to shape and intensity distribution of their Raman spectra, and summarize the properties of the above-mentioned Raman bands and how they are used for CNTs characterization.

2.3.3.1 First- and Second-Order Raman Scattering

The number of phonons involved in a Raman process can be one, two, or more, which is called one-phonon, two-phonon and multi-phonon Raman scattering, respectively (**Figure 2.17**). One further distinguishes between one-phonon, first-order and one-phonon, second-order Raman scattering. In graphene (2D graphite), optical transitions occur at the corner of the BZ, in the vicinity of the K point. The diagonal solid lines (black) in **Figure 2.17**a-c express two linear bands (valence and conduction band) that cross at the K point, as an approximation to the band structure of graphene. The upper row shows resonances with incoming photons, the lower row shows resonances with Raman scattered photons. In first-

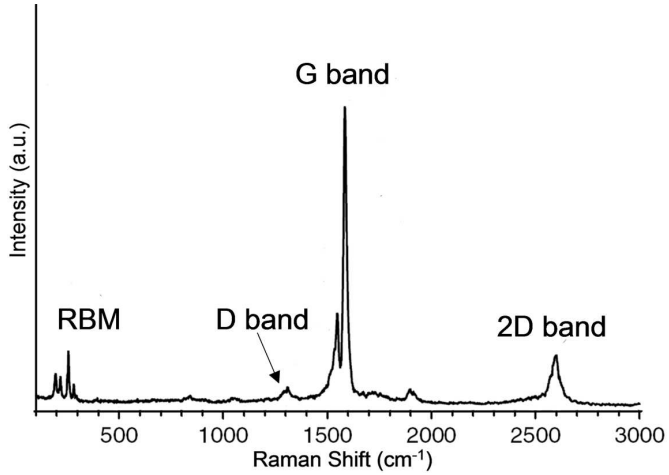

Figure 2.16: Raman spectrum of SWCNTs showing the radial breatig mode (RBM), the graphitic G band and the disorder-induced double-resonant D band. The higher frequency range is dominated by 2D. The spectrum was obtained from Ref. 206 and was recorded using 633 nm laser excitation.

order Raman scattering (**Figure 2.17**a), only one phonon ($\vec{q} = 0$) participates in a scattering event and contributes to the Raman spectrum (see section 2.3.1).

Raman processes consisting of one-phonon and additional defect-scattering (elastic) are considered as one-phonon, second-order Raman scattering (**Figure 2.17**b): the electron absorbs an incoming photon at a $\vec{k}$ state, scatters to a $\vec{k} + \vec{q}$ state by emitting a phonon with wave vector $\vec{q}$, is scattered back elastically (dashed line) by a defect (no energy transfer) to a state $\vec{k}$, and finally recombines with a hole at a $\vec{k}$ state. Since the phonon energy is much smaller than the energy needed for the electronic transition, we can assume that during the Raman process an electron scatters from a state $\vec{k}$ to another state $\vec{k}$ of equal energy ($\vec{k} = \vec{k}_L = \vec{k}_S$). Defect-induced second-order Raman scattering is discussed in detail in section 2.3.3.3.

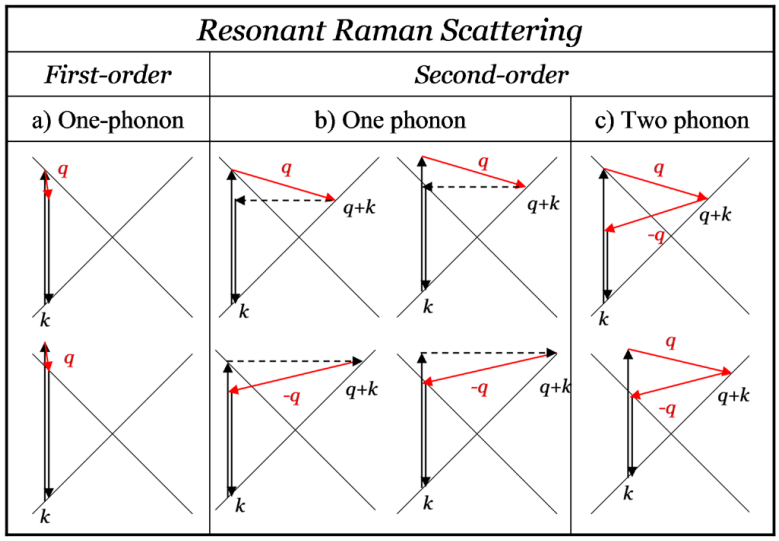

Figure 2.17: Comparison of first-order and second-order resonant Raman scattering. The diagonal solid lines indicate two linear electronic bands that cross at the K point in analogy to graphene. (a) Single-resonant scattering, where only the first transition is resonant. (b) Double-resonant scattering by one phonon and a defect. (c) Double-resonant scattering similar to (b) involving two phonons of opposite wave vector. The upper row indicates resonance with the incoming, the lower row with the scattered laser light.

Two-phonon Raman scattering (no defect-scattering) is a second-order Raman process (**Figure 2.17**c). In that case, two phonons of opposite wave vector $\vec{q}$ and $-\vec{q}$ are involved in the scattering event, satisfying both energy and momentum conservation. The two contributing phonons can (1) originate from the same vibrational mode (overtone mode), or (2) result from different vibrations (combination mode). Both cases are discussed in the following chapter.

Scattering processes that contain only elastic scattering events (change in momentum, but no energy transfer) are referred to as Rayleigh scattering and outside the scope of this work.

2.3.3.2 G band and RBM

The G band is the most intense peak in the Raman spectrum of CNTs and is often used for the characterization of CNT samples.[194] The "G" comes from graphite, since the G band of CNTs is closely related to the Raman active in-plane mode of graphite (E_{2g}) where the two atoms of the graphene unit cell are vibrating tangential against each other, giving rise to a single Lorentzian peak at ~ 1582 cm^{-1} (**Figure 2.18**a).

Unlike graphite, the G band of SWCNTs (**Figure 2.18**c and d) consists of two main components, one centered at ~ 1590 cm^{-1} and the other one around 1570 cm^{-1}, called G^+ and G^-, respectively, each consisting of three separate Raman modes (A_{1g}, E_{1g}, and E_{2g}). The G^+ feature is associated with tangential vibrations along the tube axis (LO modes). In contrast, the G^- feature results from tangential vibrations along the circumferential direction of the CNTs (TO modes) and is softened due to the curvature of the tubes. For simplicity, both Raman features can be fit using only two peaks, one for G^+ and one for G^-,

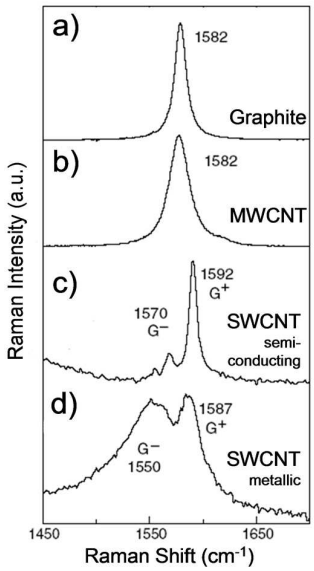

Figure 2.18: G band of a) graphite (HOPG), b) MWCNTs, c) a semiconducting and d) a metallic SWCNT, respectively. The G band of SWCNTs is split into G- and G+ bands due to chirality- and size-dependent confinement. Graph obtained from Ref. 194.

respectively. However, metallic and semiconducting SWCNTs differ with respect to line shape and peak width of the G^- band (**Figure 2.18**c and d). While both G^+ and G^- exhibit Lorentzian line shapes (FWHM ~ 5-15 cm^{-1}) for semiconducting SWCNTs, metallic SWCNTs show a significantly broadened and asymmetric G^- feature and only G^+ can be fitted using Lorentzian line shapes (**Figure 2.18**c and d). The asymmetric broadening can be account for by using a Breit-Wigner-Fano line. Earlier studies suggested the line shape can be attributed to the coupling between phonons and optical plasmons (collective oscillations of free electrons in metallic SWCNTs).[197,198] However, recent studies indicate that the coupling results from resonances between phonons and electron-hole pairs (eigenstates) and that the assignment of axial and circumferential vibrations may be reversed for metallic CNTs.[199,200] While G^+ does not show any diameter dependence, the frequency of the G^- band decreases with decreasing tube diameter (**Figure 2.19**). The diameter-dependence can be used to determine the tube size and distinguish between metallic and semiconducting SWCNTs, since the frequency shift is much larger for metallic SWCNTs than for semiconducting SWCNTs (**Figure 2.19**).[175,201]

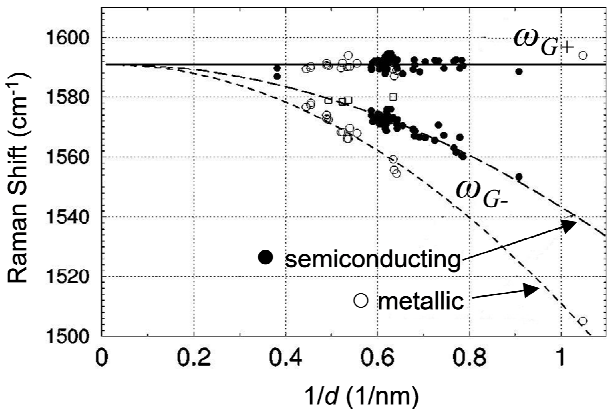

Figure 2.19: G^+ and G^- for metallic (open circles) and semiconducting (filled circles) SWCNTs as a function of the tube diameter. Graph obtained from Ref. 175

It should be noted that while for isolated semiconducting SWCNTs the line width (FWHM) of both G^+ and G^- is between 5 and 15 cm^{-1}, semiconducting SWCNTs in bundles may show a broadened G^- band due to its diameter-dependence and concurrent contributions from tubes of different size.[175,194,202] For isolated metallic SWCNTs, the line width of the G^+ is comparable to that of semiconducting SWCNTs. While larger metallic SWCNTs (d > 2 nm) show almost the same value for both G^+ and G^-, small-diameter SWCNTs (metallic) exhibit G^- line widths (FWHM) > 70 cm^{-1}.[175,202] Effects of doping[203], pressure[204], strain[205] and surface functionalization[206] on peak position, line shape and intensity of the different G band components have also been studied.

As shown in section 2.3.2, the energy of the exciting laser determines which of the CNTs in a sample are resonantly enhanced. Changes in the excitation energy modify the resonance conditions and promote the enhancement of different SWCNTs. Since the splitting between G^+ and G^- depends on both chirality and diameter of a tube (**Figure 2.19**), resonant enhancement of different SWCNTs leads to changes in the Raman spectrum of the sample. Until recently, this has been the common interpretation of the observed laser-energy dependence of the G band in SWCNT samples.[178,180]

However, studies on isolated SWCNTs revealed that some components in the G band of an individual SWCNT also show a laser-energy dependence.[207] This is not expected for a one-phonon first order Raman process, but can be explained by a double-resonance Raman scattering. Double-resonant processes and resulting Raman features are discussed in section 2.3.5. Differentiating between single-resonance and double-resonance contributions for samples that contain SWCNTs of various diameters and chiralities is difficult, and may lead to ambiguous conclusions. Both Raman processes lead to changes in position, shape and intensity of the G band, although for different physical reasons. Thus, it is important to

understand that the Raman signal of SWCNT samples is very complex and is averaged over thousands of individual tubes with properties that are yet not fully understood.

DWCNTs and TWCNTs are the smallest members of the MWCNT family and show G band features comparable to that of SWCNTs.[208] Although less pronounced, the splitting between G^+ and G^- is evident.[208] However, larger diameter distributions and additional inner tube – outer tube interactions complicate the analysis of the G band characteristics and related CNT properties.

Most MWCNT samples show very broad diameter distributions ranging from 10 up to 100 nm, and even the smallest inner-tube diameters are usually well above 2 nm. Therefore, curvature effects and confinement-related changes that distinguish the Raman spectra of SWCNTs from that of graphite, are less pronounced for MWCNTs, becoming weaker with increasing number of walls.[209] The splitting of the G band is negligible and smeared out due to the overlapping Raman signal of various tube diameters within an individual MWCNT, in addition to ensembles of different MWCNTs commonly present in commercial samples (**Figure 2.18**b).[210] Due to the different contributions, the G band of MWCNTs predominantly exhibits a weak asymmetric line shape, with a peak maximum close to that of graphite (1582 cm^{-1}) (**Figure 2.18**b). However, isolated MWCNTs with very small inner-tube diameters were found to show a distinct splitting of the G band, which, in some cases, is even more pronounced than for SWCNTs.[211] While the Raman spectrum of SWCNTs has been studied extensively, MWCNTs received much less attention but are expected to exhibit some new Raman features.

The RBMs (**Figure 2.16** and **Figure 2.20**a) are considered as a clear indicator for the presence of CNTs, since this Raman feature is unique to CNTs and is not observed for other carbon materials. As suggested by the name, the RBM is a bond-stretching, out-of-

plane mode, where all carbon atoms vibrate simultaneously in the radial direction. The RBM frequencies ω_{RBM} (cm^{-1}) are between 100 and 400 cm^{-1} and were found to be inversely proportional to the tube diameter d through the relation

$$\omega_{RBM} = \frac{A}{d}, \tag{2-23}$$

where A = 248 cm^{-1} is a constant, determined experimentally for isolated SWCNTs on a Si/SiO_2 substrate.[180] Equation 2-23 has been modified in order to account for bundling effects and reads

$$\omega_{RBM} = \frac{A}{d} + B \tag{2-24}$$

where B is an additional constant assigned to tube-tube interactions. For bundled SWCNTs (d = 1.3 - 1.7 nm), A = 234 cm^{-1} and B = 10 cm^{-1} have been reported. Other groups have found slightly different values for A and B depending on sample composition and experimental conditions[212-214] which is in agreement with theoretical calculations[215-217]. It should be noted that for SWCNTs with diameters $1 < d < 2$ nm equation 2-23 and 2-24 give similar results. However, for small diameter SWCNTs ($d < 1$ nm) equation 2-23 and 2-24 do not hold due to chirality-dependent distortions of the CNTs lattice, and an additional chirality-related term has been proposed.[218,219]

DWCNTs, TWCNTs or higher-order MWCNTs with very small inner-tube diameters ($d < 2$ nm) also exhibit size-dependent RBM features.[208,220,221] The van der Waals forces between outer and inner tubes are comparable to SWCNT-SWCNT interactions in bundles and do not significantly affect the breathing vibrations of individual tubes in the diameter range $1 < d < 2$ nm. The RBM signal from larger MWCNTs is usually very weak and, in addition, suffers from the broad diameter distribution of most MWCNT samples.

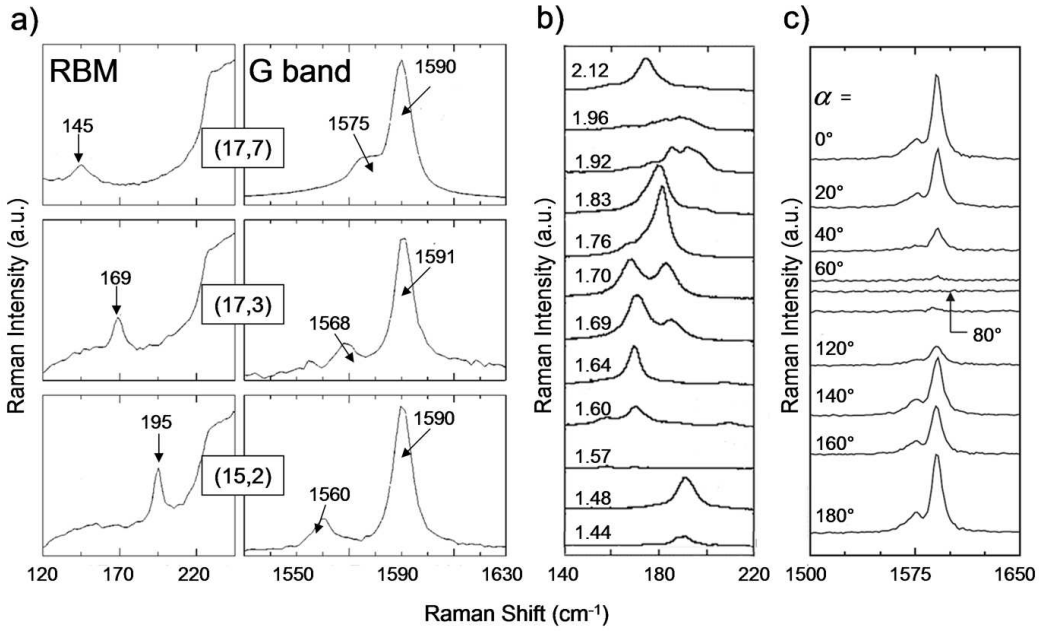

Figure 2.20: (a) RBM and corresponding G band of three isolated SWCNTs using 514 nm excitation wavelength (2.41 eV). (b) RBM Raman spectra of a SWCNT sample using different excitation energies. (c) Polarization dependence of the G band of an isolated semiconducting SWCNT. Incident and scattered light are polarized parallel to each other. α is the angle between the incident light and the nanotube axis. Data obtained from Ref. 175 (a), 222 (b) and 194 (c).

In analogy to the G band, the RBM spectrum of CNT samples contains contributions from different tubes that fulfill the resonance condition. Therefore, using multi-wavelength analysis (**Figure 2.20**b) one can characterize the diameter-distribution of the sample and, in combination with the Kataura plot (**Figure 2.14**a), determine the (*n*,*m*) indices of individual SWCNTs (**Figure 2.20**a).[175,194,222]

The intensity of both G band and RBM mode of a CNT were found to depend on the polarization of the incident radiation.[175,194,222] The largest Raman intensity is generally observed for laser light polarized along the CNT axis, while for cross-polarized light (perpendicular to the tube axis) almost no Raman signal is detected (**Figure 2.20**c). The angular dependence of the Raman modes can be described by $I(\alpha) \sim \cos^2 \alpha$, where I is the

Raman intensity and α ($0° \leq \alpha \leq 180°$) is the angle between the electric field vector $\vec{E}$ of the incident wave and the CNT axis (**Figure 2.20**c).[223] The decrease in the Raman intensity for cross-polarized light has several explanations: (1) for an individual SWCNT the resonance conditions for both polarization directions are different and can not be enhanced at the same time using a fixed laser energy;[224,225] (2) there exist different symmetry selection rules for parallel and perpendicular polarized light with respect to the E_2 and A modes[210,226]; (3) the "antenna effect", where the electric field $\vec{E}$ perpendicular to the tube axis induces charges on the opposing sides of the wall, leading to a depolarization field that reduces $\vec{E}$.[225,227]

The angular-dependence of the Raman intensity is very useful for analyzing the alignment of CNTs in a composite material or determining the direction of individual CNTs for electronic device applications.

2.3.3.3 Double-Resonant Raman Features

Most carbon materials exhibit several Raman features whose frequencies change with changing laser excitation wavelength (energy). The dispersive nature of some phonon modes has attracted much attention and is still subject to ongoing research and discussions. A prominent example for this unusual behavior is the disorder-induced D band and its second-order overtone 2D, observed in the Raman spectra of amorphous and graphitic carbon materials (**Figure 2.16**). In the case of graphite, the frequency shift was found to be as high as ~ 50 and ~ 100 cm^{-1}/eV for the D and 2D bands, respectively. [228]

The D band was known experimentally for more than three decades before its origin and characteristics could be explained. In the "molecular" picture, the D band results from the breathing vibrations of aromatic rings in the honeycomb lattice. However, its frequency and

the energy-dependence could not be explained using the fundamental understanding of Raman scattering in the solids at that time. In 1970, Tuinstra et al. analyzed the phonon structure of graphite and showed that the intensity ratio between the D band and G band was dependent on the crystal size.[229] Eleven years later, Vidano et al. recorded the Raman spectrum of graphite using different excitation energies and, for the first time, reported an up-shift of the D band with increasing laser energy.[230] The third and final puzzle piece was added by Wang et al., who related the intensity of the D band in graphitic materials to any kind of defects and disorder in general.[231] Additional studies confirmed these observations and revealed a similar energy-dependence for other Raman features.[228,232,233] However, up to that point, all attempts to explain the unusual behavior had failed.

In 2000, Thomsen et al. identified the D mode as a one-phonon second-order Raman feature resulting from a defect-induced double-resonant process.[234] As discussed in section 2.3.3.1, in a second-order double-resonance Raman process the electron absorbs a photon at a state $\vec{k}$, scatters to a state $\vec{k}+\vec{q}$, scatters back to a state $\vec{k}$, and recombines with a hole by emitting a photon. Although, second-order scattering is typically much less intense than a resonant first-order process, if one of the two scattering events corresponds to a real electronic transition (in addition to the incoming or outgoing resonance), the Raman intensity significantly increases and becomes comparable to that of the first-order process.[196] In the case of a defect-induced second-order Raman process, one of the two scattering events consists of elastic scattering by a defect.[234] The defect relaxes the $\vec{q}=0$ selection rule, and allows larger non-zone center phonons with $\vec{q}=0$ to contribute to the Raman spectra. For Stokes scattering, there are, in total, four different double-resonance Raman processes

(**Figure 2.17**b).[235] A double-resonance process requires two out of the three intermediate states to be resonant. As a consequence, $\vec{k}+\vec{q}$ is always a real electronic state.[185,235]

In order to scatter an electron from a state $\vec{k}$ to a state $\vec{k}+\vec{q}$, it requires either a phonon with wave vector $\vec{q}_{KK'}$ that scatters an electron from K to K' (or K' to K) (**Figure 2.21**a), or a phonon with wave vector $\vec{q}_{KK}$ that scatters an electron close to the K (or K') point (**Figure 2.21**b), which is called inter-valley and intra-valley scattering, respectively.[235] However, only inter-valley scattering resulting from optical phonons (TO) close to the K point ($\vec{q}_{KK'}$~K) contributes to the D band intensity (**Figure 2.21**c). LO phonons with smaller wave vectors ($\vec{q}_{KK}$ << $\vec{q}_{KK'}$) scatter electrons in the vicinity of the Γ point via an intra-valley process, giving rise to a Raman peak at ~ 1620 cm^{-1}, called D' peak (**Figure 2.21**c).[236] The D' mode, which does not exist in pure graphite, is observed with a high

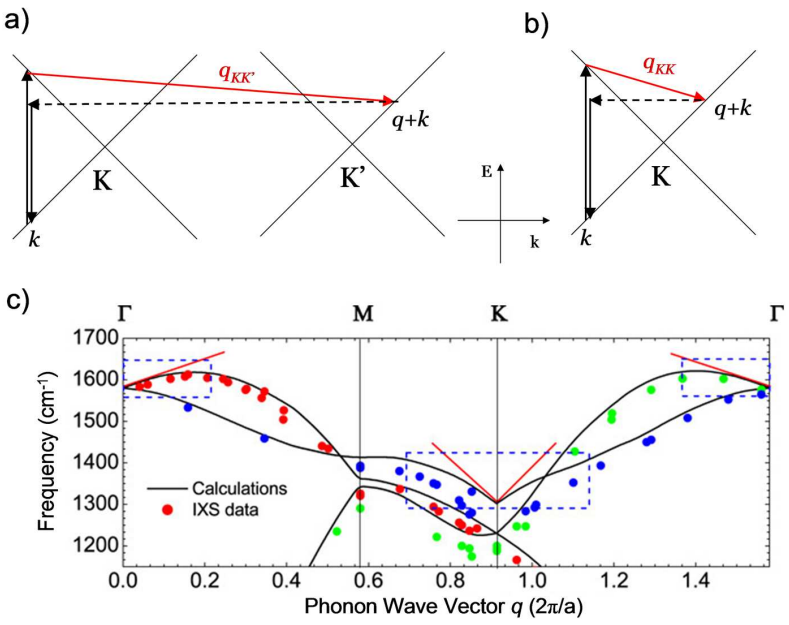

Figure 2.21: (a) Inter-valley scattering process from K to K', giving rise to the disorder-induced double-resonant D band. (b) Intra-valley scattering close to the K point leads to the D' band (c) Phonon density of states of graphite. The D band at ~ 1350 cm^{-1} results from phonons close to the K point D' band (~ 1620 cm^{-1}) originates from the vicinity of the zone center (Γ point) data obtained from Ref. 236.

intensity in intercalated graphite compounds, and has been assigned to the in-plane vibrations of the outer parts of graphite domains.[237,238]

The observed energy-dependence of the D band in graphite results from the unusual phonon dispersion at the K point (**Figure 2.21**c). Due to electron-phonon coupling, the phonon structure of metallic systems is closely related to the shape of Fermi surface. In graphite, valence and conductions bands touch each other at the K point and the band gap becomes zero (semi-metal). The corresponding anomalous behavior of the phonon modes (at the K point) is called Kohn anomaly, which appear as sharp kinks in the dispersion relations. Graphite has two distinct Kohn anomalies at the Γ (LO mode) and K (TO) points (**Figure 2.21**c).

Measurements on individual SWCNTs revealed that the D band in the Raman spectra of CNTs is well described by a double-resonance process similar to graphite. However, as discussed above, the reduced dimensionality of CNTs results in a strong confinement of electrons and phonons, leading to a larger number of discrete phonon energies and van Hove singularities in the phonon density of states.[239-241] Therefore, there exist some distinct differences between defect-induced Raman features in graphite and CNTs. For example, semiconducting CNTs show no Kohn anomalies and therefore do not contribute to the D band signal.[242] On the other hand, metallic CNTs exhibit much stronger Kohn anomalies than graphite and, in some cases, show D band intensities comparable to that of the G band.[223]

While successfully explaining many physical properties, the zone folding of graphene may not be a very accurate description of the complex phonon structure of CNTs. In the case of CNTs, peak position, shape and intensity of the D band are very sensitive to diameter and chirality, due to the unique relation between structural and electronic

properties.[243,244] In the case of bulk samples, however, the D band represents the average over many individual CNTs, similar to the G band.

The intensity ratio between D and G band (I_D/I_G) is often used to evaluate the disorder in carbon materials or estimate the amount of defects in the graphitic walls[245]. Tuinstra et al. proposed to use I_D/I_G as a qualitative probe for the size of graphite microcrystals.[229] Their approach has been modified by several authors[232,246] and was also applied to carbon nanomaterials[247]. A quantitative description of the D band intensity in graphene was recently derived by Sato et al.[248] It should be mentioned that the crystallite size estimated by Raman spectroscopy corresponds to homogeneous vibrational domains, not the particle size. These graphitic domains are defined by a surface, which can be understood as a defect interphase between different grains, thus contributing to the D band intensity. The approach of Tuinstra et al. relies on the assumptions that, the intensity of the G band is completely independent of the defect concentration and that I_D/I_G does not depend on other effects. However, several studies revealed that some components of the G band show characteristics of a defect-induced double-resonance process, suggesting the elastic scattering by a defect. The presents of the defect-induced D' band around 1620 cm^{-1} can further complicate the analysis of I_D/I_G. In the case of CNTs, the absence of the D mode could indicate either a low defect concentration or the exclusive presence of metallic CNTs. Therefore, the interpretation of the D and G bands in the Raman spectra of carbon nanostructures is not always straightforward. In order to get reliable information on the defect concentration it is necessary to analyze another second-order Raman feature, historically named G'.[233,249]

The G' band (~ 2700 cm^{-1}) is the dominant feature in the second-order Raman spectrum of CNTs and has been identified as the second-order mode of the D band. Therefore, it

became more common to refer to it as 2D. Unlike the D band, 2D results from a two-phonon scattering process and is therefore almost free from defect contributions. While for most carbon materials the 2D band can be fitted using one Lorentzian peak, individual SWCNTs sometimes exhibit a two-peak structure. Although a similar splitting occurs in bulk graphite, the physical origin is quite different. In the case of SWCNTs, the doublet is due to resonances with two different van Hove singularities of the same tube, occurring independently for the incident and Raman scattered photon[239,241], whereas for graphite the splitting is ascribed to interlayer coupling[250].

Similar to other Raman peaks such as RBM or G band, changes in the 2D band can be used for materials characterization. For example, using boron-doped MWCNTs, Maultzsch et al. demonstrated that, in some cases, I_D/I_G is an inappropriate measure for defect concentrations, and suggested to use intensity ratio between the D band and 2D instead. Shifts in the 2D band position have successfully been used to determine functional groups attached to the surface of SWCNTs and study charge transfer effects.[203,251]

2.3.4 Raman Spectrum of Nanodiamond

The first-order Raman spectrum of a defect-free, single-crystal diamond with grain sizes above ~20 μm (considered as bulk diamond) displays only one, triply degenerated Raman peak (one transversal and two longitudinal optical phonons) at 1332 cm^{-1}, with a full-width at half-maximum (FWHM) of approximately 1 - 3 cm^{-1} [252-254], corresponding to the vibrations of the two interpenetrating cubic lattices.[255-257] The Raman spectrum of bulk diamond has been extensively studied during the last decades[258-260] and effects of stress[261,262], temperature[255], and defects such as dopants, vacancies or dislocations[263,264] are well known.

However, while the Raman analysis of bulk diamond is relatively straightforward, the interpretation of Raman scattering spectra recorded from nanometer-sized diamond crystals is more complex and yet not fully understood.

The Raman spectrum of ND contains additional peaks as a result of grain boundaries and a large number of structural defects both at the surface and in the diamond core. Moreover, unlike bulk diamond, shape and intensity of different Raman peaks were found to be different for various excitation wavelengths and depend on both the size and surface chemistry of the nanocrystals.[265-269]

ND crystals with a diameter of 5 nm have more than 20% of the total number of atoms on the surface. With further decrease of particle size, this value drastically increases, and properties become strongly affected by the surface. Although there has been tremendous progress in science computing, first principles predictions of Raman spectra for ND are still restricted to crystal size below 1 nm.[270] A correct prediction of the Raman spectrum of a complex 5 nm ND particle is yet not possible. Therefore, experimental Raman spectroscopy studies remain the main characterization tool for carbon nanomaterials and are essential for a better understanding of carbon nanomaterial properties and their successful application.

In the case of ND, most of the recent work and earlier studies, focus mainly on the diamond features in the Raman spectra, limiting the use of Raman spectroscopy to simple identification of the diamond phase.[260,265-269,271-273] One of the main reasons is the poor understanding of surface contributions and other non-diamond features in Raman spectra of ND.

The following section gives an overview of the Raman features generally observed in the Raman spectra of ND films and powders. Phonon confinement effects and surface

contributions are of particular interest and will be discussed separately in sections 2.3.4.2 and 2.3.4.3, respectively.

2.3.4.1 First-Order Raman Spectrum of Nanodiamond

The Raman spectra of ND samples reported in literature vary significantly in shape and number of peaks, and are strongly dependent on the synthesis conditions. One generally distinguishes between ND films, grown using CVD techniques, and powders produced via detonation methods. However, even within each category, Raman spectra can have wide variation.

The Raman spectrum of ND film recorded using 514 nm laser excitation wavelength is shown in **Figure 2.22**a.[274] The spectrum shows a small diamond peak around 1332 cm^{-1} and four additional Raman features at 1150, 1350, 1450 and 1580 cm^{-1}. The peak at 1350 and 1580 cm^{-1} correspond to the D and G bands of sp^2 carbon, respectively. The origin of the

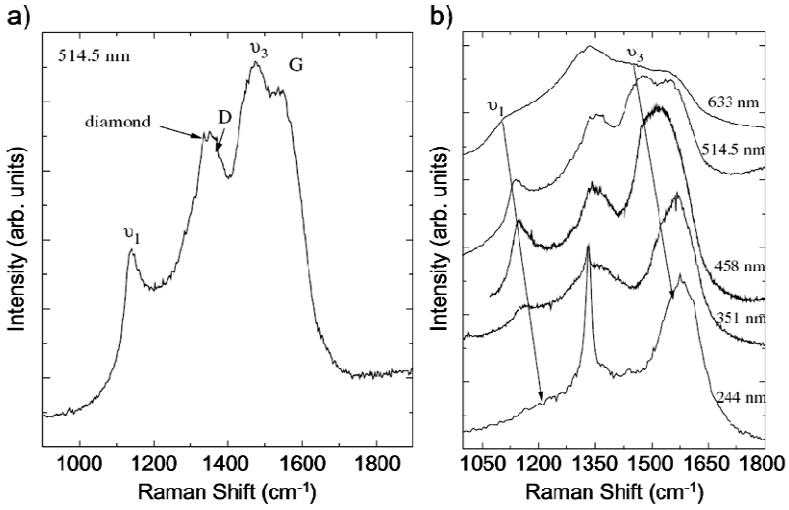

Figure 2.22: Raman spectra of ND films recorded using most common 514 nm laser excitation wavelength (a) and multi-wavelength analysis in the range 244 – 633nm. Graphs obtained from Ref. 274.

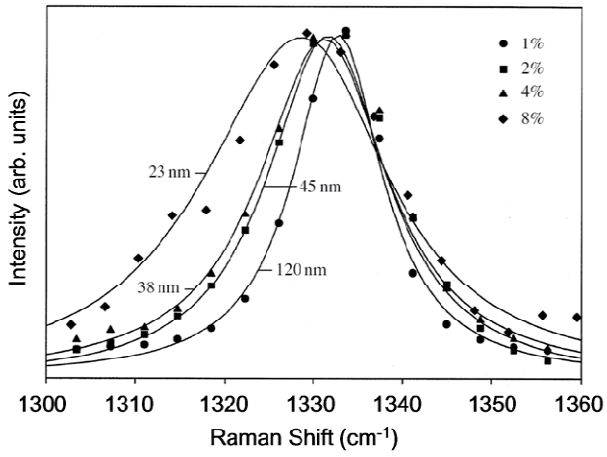

Figure 2.23: Diamond Raman peaks of ND films with different crystal sizes recorded using 244 nm UV laser excitation. Solid lines represent theoretical Raman spectra calculated using the phonon confinement model. Symbols correspond to experimental data. Graph obtained from Ref. 259.

Raman peaks around 1150 and 1450 cm^{-1} has been debated extensively during the recent years. While the assignment of these features still remains controversial, it is believed that both peaks result from polyacetylene groups at the surface of the ND crystals.[274] Possible contributions of functional groups, defects and other non-diamond species to the Raman spectrum of ND will be discussed in section 2.4.2.3.

The relative intensity of the diamond peak increases with deceasing excitation wavelength, as expected (**Figure 2.22**b). The resonance enhancement of sp^2 carbon is dominant in the visible spectral range, but decreases under UV excitation. Moreover, it was found that the diamond peak is broadened and shifted towards lower frequencies with decreasing crystal size. The observed changes in line-shape and peak position have successfully been explained by the phonon confinement model (PCM) and are in agreement with calculated data (**Figure 2.23**).[259] The PCM, which relates frequency and line-width of the diamond peak with the crystal size, will be discussed in detail in section 2.3.4.2.

While most of the former studies focus primarily on the characterization of CVD grown ND films, in this work we investigate the Raman spectra of ND powders produced by detonation synthesis.

The Raman spectrum of ND powder shows a broadened (FWHM > 36 cm^{-1}) and downshifted (~ 1325 cm^{-1}) diamond peak, with respect to the single crystal diamond (1332 cm^{-1}), with a shoulder at ~ 1250 cm^{-1} (**Figure 2.24**).[259,275,276] These changes are a result of the confined phonons in the small crystals that lead to the relaxation of the $\vec{q} = 0$ selection rule (see section 2.3). The small shoulder at ~ 1250 cm^{-1} is believed to originate from highly amorphous diamond[277], due to a strong maximum in the phonon DOS[278] in this frequency range. The presence of this peak at a relatively high intensity may indicate a considerable amount of amorphous material in the ND samples.[279,280] It is worth noting that ND samples (either film or powder) may show very weak or no Raman peak at ~ 1332 cm^{-1} due to the presents of larger of amounts of sp^2 bonded carbon and their larger Raman scattering cross-section, even under the UV excitation.

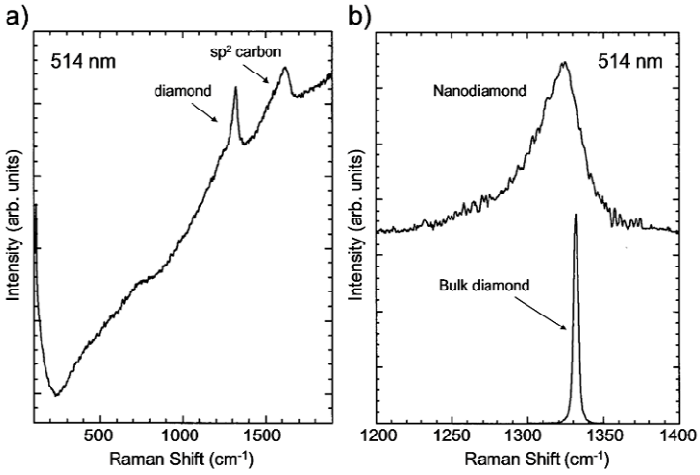

Figure 2.24: a) The Raman spectrum of ND powder shows only a weak diamond peak around ~1325 cm^{-1} and contributions from non-diamond phases such as sp^2 carbon. b) The diamond peak is asymmetrically broadened and shifted towards lower frequencyies compared to bulk diamond. The Raman spectrum in b) was baseline corrected. Data obtained from Ref. 175.

The broad bands around 1350 - 1400 cm^{-1} and 1500 - 1800 cm^{-1} are assigned to the D and G bands of graphitic carbon. As discussed in section 2.1.2, ND powders often contain significant amounts of amorphous carbon, as well as carbon onions and graphite ribbons. Unfortunately, this assignment does not hold for purified ND samples with diamond contents > 95% (see section 2.3.4.3).

Some ND powders show additional Raman features, including a broad peak around 500 - 800 cm^{-1} [277] and a weak Raman band at ~ 1090 cm^{-1}.[277] The position of the ~ 1090 cm^{-1} peak coincides well with the T peak of amorphous diamond.[281] Another possible contribution to this peak may come from surfaces modes, as suggested by Prawer et al.[277]

In-depth understanding of Raman spectra has led to the extension of this technique from simple carbon allotrope detection (fingerprinting) to analysis of the dimensions and ordering of graphene, graphite and nanotubes. However, in case of ND powders, Raman spectroscopy is still mainly used only for detecting the diamond phase due to the poor understanding of the Raman spectrum.

2.3.4.2 Phonon Confinement in Nanocrystals

A monoatomic solid such as diamond has two atoms per unit cell, leading to three optical and three acoustic phonon modes.[282] The phonons propagate into the crystal lattice with an energy dispersion that depends on the wave vector in the Brillouin zone. As a consequence of momentum conservation and because the Brillouin zone of an infinite perfect crystal is much larger ($\left|\vec{k}_{BZ}\right| \approx 10^8$ cm^{-1}) than the largest possible scattering vector using conventional Raman spectroscopy ($\left|\vec{k}_S\right| \approx 5 \cdot 10^4$ cm^{-1}), only phonon modes from the

center of the Brillouin zone ($|\vec{q}| = |\vec{k}_{BZ}| / |\vec{k}_{BZ}| \approx 0$) can contribute to the first-order Raman spectrum.[283,284]

However, in finite crystals, phonons are confined as a result of defects or grain boundaries and the $\vec{q} = 0$ selection rule is released. Thus, a significant decrease in crystal size affects the lattice vibrations of a material and thus the Raman spectrum.

Several models have been developed in order to relate the observed changes in the Raman spectrum to the crystal size of a material, such as the phonon confinement model[279,280] (PCM) and the elastic sphere model[285,286] (ESM). A general overview on existing confinement models was recently given by Arora et al.[287] The PCM describes the wave vector uncertainty of optical phonons propagating in nanocrystals. A weighting function accounts for contributions from phonons away from the center of the Brillouin zone.

The wave vector uncertainty associated with a vibration is given by:[288]

$$\Delta\vec{q} \sim \frac{\pi}{L}, \tag{2-25}$$

where $\vec{q}$ is the phonon wave vector and L the size of the crystal. It should be noted that relation 2-25 is only valid for weak phonon localization and not for completely confined phonons.[287] The largest possible phonon wave vector is defined by the size of Brillouin zone according to

$$|\vec{q}| = \frac{\pi}{a}, \tag{2-26}$$

where a is the lattice constant of the crystal. For example, a 20 nm diamond crystal (a = 0.3567 nm) would cause an uncertainty of $\Delta\vec{q}$ = 2% with respect to the phonon wave vector of the zone center vibration. An exact determination of the vibration dynamics in

nanostructures is currently restricted to crystals sized below 1 nm because of limited calculation power in molecular dynamics simulations.

Richter et al.[280] and Nemanich et al.[279] first and independently investigated how the uncertainty of the wave vector will affect the Raman lines and suggested a model (PCM) that correlates the observed changes with the crystal size. The wave function (plane-wave) of a phonon in an infinite crystal with the wave vector $\vec{q}_0$ is given by:

$$\Phi(\vec{q}_0,\vec{r}) = u(\vec{q}_0,\vec{r}) \cdot e^{-i\vec{q}_0\vec{r}}, \tag{2-27}$$

where $u(\vec{q}_0,\vec{r})$ has the periodicity of the diamond lattice. The wave function of the confined phonon can be expressed according to:

$$\Psi(\vec{q}_0,\vec{r}) = W(r,L) \cdot \Phi(\vec{q}_0,\vec{r}), \tag{2-28}$$

where W(r, L) is the weighting function accounting for the confinement and L indicates the crystal size (in units of a). With $\Psi(\vec{q}_0,\vec{r}) = \Psi'(\vec{q}_0,\vec{r}) \cdot u(\vec{q}_0,\vec{r})$ one can further write:

$$\Psi'(\vec{q}_0,\vec{r}) = W(r,L) \cdot e^{-i\vec{q}_0\vec{r}}. \tag{2-29}$$

A plane-wave-like phonon cannot exist within the nanocrystals because the phonon cannot propagate beyond the boundary. Therefore, the wave function of the phonon must decay to a very small value at the crystal boundary. Richter et al. suggested a Gaussian confinement function $W(r, L) \approx \exp(-\alpha r^2/L^2)$ with $\alpha = 2$. The parameter α determines how fast the wave function decays as one approaches the crystal boundary. While the Gaussian confinement has been extensively used, other values of α, such as $\alpha = 8\pi^2$ or $\alpha = 9.67$, have also been applied. $\Psi'(\vec{q}_0,\vec{r})$ can be expressed as a Fourier series

$$\Psi'(\vec{q}_0,\vec{r}) = \int d^3q \cdot C(\vec{q}_0,\vec{q}) \cdot e^{i\vec{q}\cdot\vec{r}}, \tag{2-30}$$

where $C(\vec{q}_0, \vec{q})$ are the Fourier transform coefficients of the confinement function $W(r, L)$ given by:

$$C(\vec{q}_0, \vec{q}) = \frac{1}{(2\pi)^3} \cdot \int d^3 r \cdot \Psi'(\vec{q}_0, \vec{r}) \cdot e^{-i\vec{q}_0 \cdot \vec{r}}$$
$$= \frac{1}{(2\pi)^3} \cdot \int d^3 r \cdot W(r, L) \cdot e^{-i(\vec{q} - \vec{q}_0) \cdot \vec{r}} \qquad (2\text{-}31)$$

Assuming $\vec{q}_0 = 0$ for one phonon, zone-center Raman scattering the first order Raman line can be constructed by superimposing Lorentzian lines (infinite crystal) centered at the wavenumber ω, weighted by the uncertainty of the wave vector according to

$$I(w) \cong \int \frac{d^3 q \cdot |C(0, \vec{q})|^2}{[\omega - \omega(\vec{q})]^2 - (\Gamma_0 / 2)^2}, \qquad (2\text{-}32)$$

where $\omega(\vec{q})$ and Γ_0 are the phonon dispersion relation and the natural line width of the zone-center Raman line, respectively. The predicted line is asymmetrically broaden and is shifted to lower wavenumbers as L decreases. The proposed model was successfully used to describe confinement effects in various materials such as Si[289-291], SiC(ref), BN[279] and GaAs[292,293].

Ager et al. were the first who tried to relate confinement-induced changes in the Raman spectrum of diamond to the crystal size.[275] Following the approach of Richter et al. they estimated the crystal size by reducing the three-dimensional integration in equation 2-32 to a one-dimensional integration over a spherical Brillouin zone using an averaged one-dimensional dispersion curve of the form $\omega(q) = A + B\ cos(q\pi)$, where A = 1241.25 cm^{-1} and B = 91.25 cm^{-1}.

Assuming a Gaussian confinement function $W(r, L) \approx \exp(-ar^2/L^2)$ with $a = 8 \cdot \pi^2$ they calculated the Raman intensity according to

$$I(w) \cong \int_0^1 \frac{\exp(-\vec{q}^{\,2}L^2/4) \cdot 4\pi\vec{q}^{\,2}}{\left[\omega - \varpi(\vec{q})\right]^2 - (\Gamma/2)^2} dq \,. \qquad (2\text{-}33)$$

However, their results showed rather poor agreement with experimental data. In contradiction to the confinement model, they observed an up-shift of the diamond peak with decreasing crystal size, suggesting other mechanisms such as stress affecting the Raman line[294,295]. Studies of the effects of uniaxial stress on diamond showed some distinct changes in line shape and position as a function of the stress direction.[262,272] Diamond films grown by CVD techniques using substrates such as Si or Al_2O_3 are subjected to internal stresses induced by the mismatch of the crystal lattices. Confinement effects and stress-induced changes both affect the Raman spectrum of ND films, thus limiting the potential of confinement-based size characterization.[272,275] Yoshikawa et al.[276] focused their analysis on ND powders synthesized by detonation of trinitrotoluene (TNT). Using the approach of Ager et al. and an averaged one-dimensional dispersion curve of the form $\omega(q) = A + B\cos(q\pi)$, where A = 1193.75 cm^{-1} and B = 139.25 cm^{-1}, they modeled the Raman line of a 5.5 nm diamond particle. Unlike Ager et al, they assumed the linewidth Γ to be dependent on the particle size L (in nm) following the relationship $\Gamma = \alpha + \beta/L$. The parameters α and β were determined experimentally by measuring the size-dependent peak broadening of different microcrystalline diamond films, and given by α =2.990 cm^{-1} and β=145.74. The parameter α represents the FWHM of bulk diamond, but includes an experimental error due to spectrometer related line-broadening, while β reflects the material-related size-dependency

of Γ. Although their results are in better agreement with experimental data compared to ND films, the accuracy is still unsatisfactory.

2.3.4.3 Contribution of Surface Functional Groups

The Raman spectrum of ND show several characteristic features in addition to the diamond peak as shown in section 2.3.4.1. In the case of ND films, four peaks centered at 1150, 1350, 1480 and 1550 cm^{-1} are generally observed. While the Raman peaks at 1350 cm^{-1} and 1550 cm^{-1} have been ascribed to the D and G bands of graphitic and amorphous sp^2 carbon, the assignment of the peaks at ~ 1150 and ~ 1480 cm^{-1} has lead to a long-lasting debate during the last decade and remains somewhat controversial. For many years, both peaks were considered as evidence for the presence of ND and interpreted as "fingerprint" of the nanocrystalline diamond phase. Most authors believed that the peak at 1150 cm^{-1} was a direct result of the relaxation of the $\vec{q} = 0$ selection rule and corresponded to a maximum in the phonon DOS. Ferrari and Robertson argued that the frequency of this Raman mode is too low to be ascribed to sp^3 carbon. In their studies they revealed the dispersive nature of both bands, and suggested the bands' origin to be trans-polyacetylene groups formed at the ND surface during CVD synthesis. Although one would expect rather sharp bands from molecular species, it is now generally believed that both bands result from trans-polyacetylen surface groups. While microcrystalline diamond films are grown using similar techniques, contribution of surface functionalities are negligible. However, with a dramatic increase in the surface to volume ratio at the lower end of the nanoscale, nanocrystalline films are increasingly dominated by surface effects and contributions of functional groups become non-negligible.

ND powders are synthesized by detonation techniques and formation of trans-polyacytelen surface groups is not expected. On the other hand, taking into account the rich surface chemistry of ND powders, contributions of other surface species to the Raman spectra are very likely. For example, the broad peak between 1500 and 1800 cm^{-1} is commonly labeled as the "G band" and ascribed to the in-plane vibrations of graphitic carbon. However, this peak significantly differs from the G band of graphitic materials both in shape and position.[296, 297] Therefore sometimes it is sometimes assigned to a mixed sp^2/sp^3 carbon structure [298], or is referred to as a peak of "sp^2 carbon" [299] or "sp^2 clusters" [265] without any explanation regarding the structure (amorphous, graphitic etc.). While these assignments hold for as-produced ND powders with high contents of sp^2 carbon, they cannot explain the existence of a similar feature in the Raman spectra of purified ND powders with diamond contents > 95%. There have also been attempts to relate this peak to localized interstitial C=C pairs within the diamond lattice also known as "dumb-bell defects" [260,266]. Such defects were formed during deep ion implantation in natural type-IIa diamond.

However, with plenty of various functional groups exposed on ND surface, the broad band(s) between 1500 and 1800 cm^{-1} may result from overlapping Raman signals of sp^2 carbon species, surface groups such as OH, COOH, and C=C pairs embedded inside the diamond core. In this case, the peak position, intensity, width and shape may all be influenced by the interplay of these contributions, i.e. they may vary for different types of ND. Taking into account the rich surface chemistry of ND, the lack of systematic studies on the contribution of functional groups into the Raman spectrum of ND is surprising.

2.3.5 Raman Spectra of Nanoporous and Amorphous Carbon

2.3.5.1 Activated Carbon and Carbon Black

The composition of porous carbon nanomaterials can vary largely, due to different mixtures of sp^3, sp^2, and sp^1 sites. In particular, clustering and orientation of the sp^2 sites are crucial because graphitization and ribbon formation mainly determine physical properties of carbons with high sp^2 contents.[268]

Figure 2.25 compares the Raman spectra of two commercially available nanoporous carbons (carbon black[300] and activated carbon[301]) with that of a highly amorphous carbon film[302]. Carbon black (**Figure 2.25**a) is produced by incomplete combustion of petroleum products such as coal tar, and contains mainly graphitic nanocrystals with an average size of 30-80 nm, depending on the synthesis conditions.[300,303] The Raman spectra of most carbon blacks can be well fitted using two Lorentzian lines at ~1360 and ~1600 cm^{-1} and a broad Gaussian band between 1540 and 1550 cm^{-1}.[268,300] The Raman peak at ~1360 corresponds to the disorder-induced D band is associated with a double-resonance process as discussed in

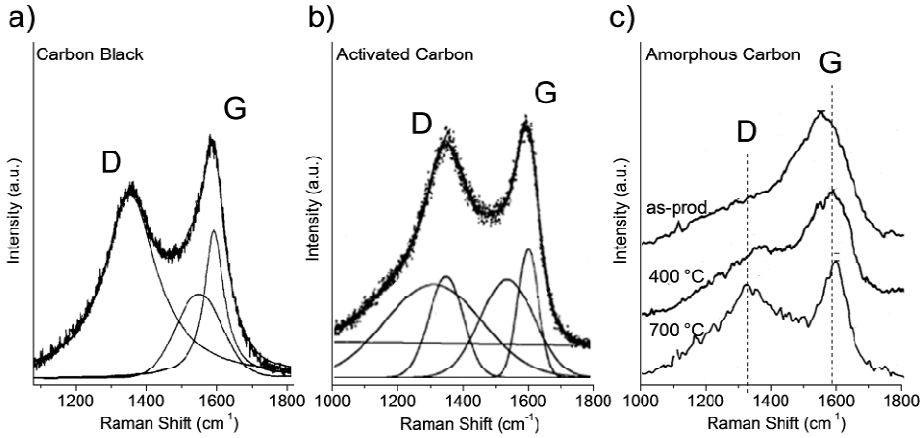

Figure 2.25: Raman spectra of carbon black (a), activated carbon (b) and amorphous carbon grown by ion-beam sputtering (c). The solid lines under the Raman curves in a) and b) are the results of peak fitting. Experimental data was obtained from Ref. 300 (a), Ref. 301 (b) and Ref. 302 (c), recorded using 468 nm (a) and 514 nm (b, c) laser excitation.

section 2.3.3.3. The peak at ~ 1600 cm^{-1} is referred to as G band and is assigned to the in-plane stretching vibrations of sp^2 sites (see section 2.3.3). **Figure 2.25**b shows the Raman spectrum of an activated carbon made from carbonized cokes (KOH-activated).[301] Activated carbons are characterized by high surface to volume ratios (SSA > 1000 m^2/g) and high porosity. Similar to carbon black, activated carbon exhibits two peaks around 1360 and 1600 cm^{-1}, corresponding to the D and G bands of graphitic carbon, respectively, and a broad Gaussian peak around 1560 cm^{-1}.[268,301] Both carbon black and activated carbon show an up-shift of the G band from its original position at 1581 cm^{-1} (bulk graphite) to ~ 1600 cm^{-1}. However, unlike carbon black, activated carbon shows an additional broad Raman feature centered around 1330 cm^{-1}(**Figure 2.25**b).[268,301] Peak positions and FWHM values of both carbon samples are shown in **Table 2.3**. The slightly higher D band position, as in the case of carbon black results from the excitation wavelength-dependence of the D band frequency. The corresponding value calculated for 514 nm laser excitation is ~1350 cm^{-1} and thus similar to that observed for activated carbon.

Table 2.3: Raman peak position and FWHM (in parentheses) of different carbon materials.

Sample	*D band*	*G band*	*Peak 3*	*Peak 4*
Carbon Black[a]	1371 (176)	1602 (65)	1559 (181)	-
Activated Carbon[b]	1351 (145)	1605 (74)	1534 (199)	1273 (323)
Amorphous Carbon[b]	1295 (410)	1536 (220)	-	-
TiC-CDC (600°C)[b]	1350 (186)	1595 (85)	1512 (125)	1171 (201)

[a] *recorded using 468 nm laser excitation*
[b] *recorded using 514 nm laser excitation*

The broad features at 1100-1300 cm^{-1} and 1500-1560 cm^{-1} (**Figure 2.25** and **Table 2.3**) are believed to originate from the D and G bands of highly amorphous sp^2 carbon, respectively.[247,274,301] The vibrational frequencies of sp^3 bonded carbons are well below 1500

cm^{-1} and do not contribute to the Raman intensity at higher frequencies.[247,274,301] Moreover, since Raman scattering cross-section of the sp^2 phase is more than 50 times higher than that of the sp^3 carbon under 514 nm laser excitation[304], contributions of small amounts of sp^3 sites are negligible.

Figure 2.25c shows the Raman spectra of a highly amorphous carbon film (a-C)[302], produced by ion-beam sputtering, which exhibits two broad, overlapping Raman bands centered at ~ 1295 cm^{-1} (D band) and 1536 cm^{-1} (G band). However, treatments in nitrogen at elevated temperatures leads to a decrease in the FWHM and both peaks are shifted towards higher frequencies, reaching 1340 for the D band, and 1587 cm^{-1} for the G band, after annealing at 700 °C. Both D and G band position of highly amorphous sp^2 carbon are in good agreement with the Raman features at 1273 cm^{-1} (Peak 4) and 1534 cm^{-1} (Peak 3), respectively, observed in the Raman spectra of activated carbon and some carbon blacks (**Figure 2.25** and **Table 2.3**).

The disordered-induced changes in the Raman spectra of carbon materials containing mixtures of sp^3 and sp^2 sites, have been described in detail by Ferrari et al.[247,274,305] In a three-stage model (**Figure 2.26**) they describe major structural changes that occur going from graphite to nanographite, to nanocrystalline graphite, to amorphous (a-C) and finally to tetrahedral amorphous carbon (ta-C).[247] In stage 1, graphitic domains decrease in size, then they become topologically disordered (stage 2), and finally the aromatic rings open and transform into chain-like structures, while the sp^3 content increases up to 80 - 90% (stage 3) (**Figure 2.26**). The entire process is referred to as amorphization, while the reverse transition is called crystallization or graphitization.

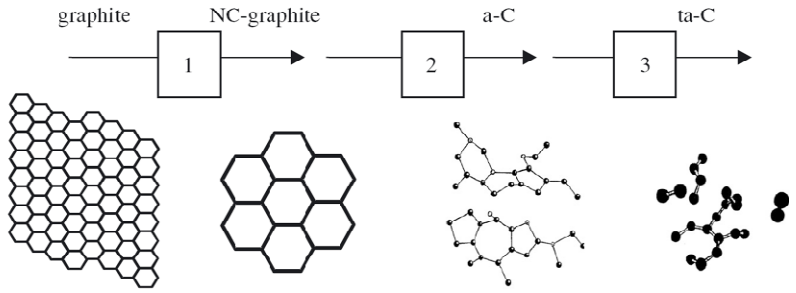

Figure 2.26: Three-stage model describing structural changes with increasing amorphization and disorder, going from bulk to nanocrystalline (NC) graphite (stage 1), to amorphous carbon (stage 2), to tetrahedral amorphous carbon (stage 3). Graph obtained from Ref. 268.

The Raman spectra of carbon materials depend strongly on the clustering of the sp^2 phase, changes in bond order (length and angle), the number of rings and chains, as well as the amount of sp^3 carbon. **Figure 2.27** shows the changes in D and G bands that occur as one moves from stage 1 to stage 3. For a better understanding, it is appropriate to look at the molecular interpretation of both Raman peaks. The G peak results from bond stretching of all pairs of sp^2 atoms in both, rings and chains. The D peak is due to the breathing modes of the aromatic sp^2 rings, but is symmetry forbidden in defect-free bulk graphite and only Raman active in the presents of defects and disorder.[229,247] The intensity (peak height) is proportional to the number of sixfold aromatic sp^2 rings. Ring orders other than six decrease the D band intensity. The width of the D band (FWHM) is related to the ordering and size distribution of sp^2 rings. Presence of five,- seven,- and eightfold rings leads to an increase the FWHM. If no rings exist, consequently no D band is detected.

In stage 1, the size of the graphitic domain, commonly referred to as in-plane correlation length *L*, is reduced (see **Figure 2.26**) and, as a result, the G band shifts from its initial position at ~ 1581 cm^{-1} to ~ 1600 cm^{-1} (**Figure 2.27**). The shift has been ascribed to phonon confinement effects, but can also result from the appearance of a new, defect-

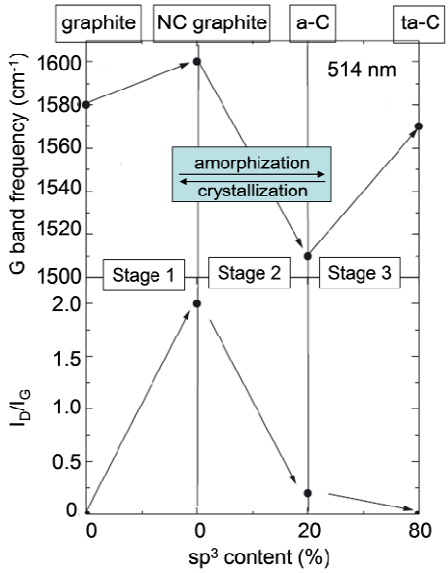

Figure 2.27: Three-stage model showing changes in the D and G band with increasing disorder going from graphite to nanocrystalline (NC) graphite, to amorphous (a-C) and finally tetrahedral amorphous carbon (ta-C). Raman data was measured using 514 nm laser excitation. Graph obtained from Ref 268.

induced Raman feature centered at ~ 1620 cm^{-1}, called D' band (see section 2.3.3.3).[247,305] Moreover, the D band appears and continuously increases in intensity with decreasing *L*, leading to an increase in the intensity ratio between D and G band (I_D/I_G) (**Figure 2.27**).

Stage 2 is characterized by the introduction of topological disorder into the graphitic planes (**Figure 2.26**). Although carbon-carbon bonds are still mainly of sp^2 type, increasing disorder in bond-angle and bond-length softens the phonon modes and leads to a downshift in the G band position to approximately 1500 - 1520 cm^{-1} (**Figure 2.27**). At the end of stage 2, the carbon is completely disordered, consisting mainly of sp^2 carbon (80 - 90%) in the form of distorted five-, six-, seven,- or even eightfold rings and only a few chain-like structures.[247,268]

The G band position of amorphous carbon depends on the excitation wavelength and increases with decreasing laser wavelength, similar to the D band. However, unlike the D

band, the dispersive nature of the G band increases with disorder and is not observed for graphitic materials such as carbon black, activated carbon or nanocrystalline graphite.[305,306]

Figure 2.25c demonstrates that highly amorphous carbon exhibits a much lower D band intensity than more ordered films that were annealed at 400 and 700 °C. As disorder increases, domain sizes are confined to less than 2 - 3 nm and the number of rings becomes smaller, until they finally start to open up. The loss of sp^2 rings leads to a decrease in the D band intensity.

In stage 2, the D band intensity is directly proportional to number of rings. Therefore, an increase in the D band intensity of amorphous carbons indicates higher ordering, the opposite of what is observed for graphitic carbons.[229,247,305] Since the G band originates only from the stretching vibrations of individual sp^2 pairs, its intensity remains constant with increasing disorder.

In stage 3, all ring structures are transformed into chains and the sp^3 content increases up to 85% (**Figure 2.27**). The π states of sp^2 pairs in chain-like structures or within a sp^3 matrix are more localized, leading to shorter bond-lengths and thus higher vibrational frequencies. As a consequence, the G band position is upshifted to ~ 1570 cm^{-1} (for 514nm excitation wavelength). However, due to its dispersive nature, the position of the G band strongly depends on the laser excitation and increases with decreasing wavelength. Moreover, the dispersion is related to the composition of the sample. Amorphous carbons that contain only sp^2 rings show a maximum G band position of ~1600 cm^{-1}, while for samples compromising both rings and chains, the G band shift can reach up to 1690 cm^{-1}, under UV excitation.

The conversion of the remaining rings into chains leads to a further decreases in the I_D/I_G ratio until $I_D/I_G = 0$ (absence of rings). The FWHM of the G band increases with

decreasing correlation length throughout all stages, and is therefore a direct measure of disorder in carbon samples. Some graphitic carbons show an additional disorder-induced Raman feature at ~ 1620 cm^{-1}, called D', which overlaps with the G band. Since in some cases it is impossible to assign individual contributions, analysis of the FWHM of both Raman peaks may be inaccurate and size estimates become erroneous.

While the Raman spectra of amorphous carbon films and disordered materials such as carbon black or activated carbon have been studied extensively, novel nanomaterials synthesized using CDC techniques have received much less attention.

2.3.5.2 Carbide-Derived Carbon

A large variety of carbon structures including amorphous and graphitic carbon, nanotubes, nanodiamond, fullerenes, onions, and ribbons can be produced using the CDC synthesis techniques (see section 2.1.3).[307] In this section we will focus on CDCs that were chlorinated at temperatures below 1200 °C without addition of hydrogen, leading mainly to amorphous carbons with high contents of sp^2 sites.

Figure 2.28 shows the Raman spectra of TiC-CDC[166] and ZrC-CDC[308] chlorinated at different temperatures between 200 and 1200 °C. TiC-CDC[166] (**Figure 2.28**a) and ZrC-CDC[308] (**Figure 2.28**b) show two broad Raman features corresponding to the D and G bands of sp^2 carbon. The Raman spectrum of as-received ZrC and other CDCs shows very weak D and G bands, indicating only small traces of free carbon. Peak width (FWHM) and intensity ratio between D and G band reveal the disordered nature of both CDCs, especially for low chlorination temperatures. Increasing the chlorination temperature from 200 to 1200 °C leads to a decrease in the FWHM of both Raman peaks, suggesting higher ordering

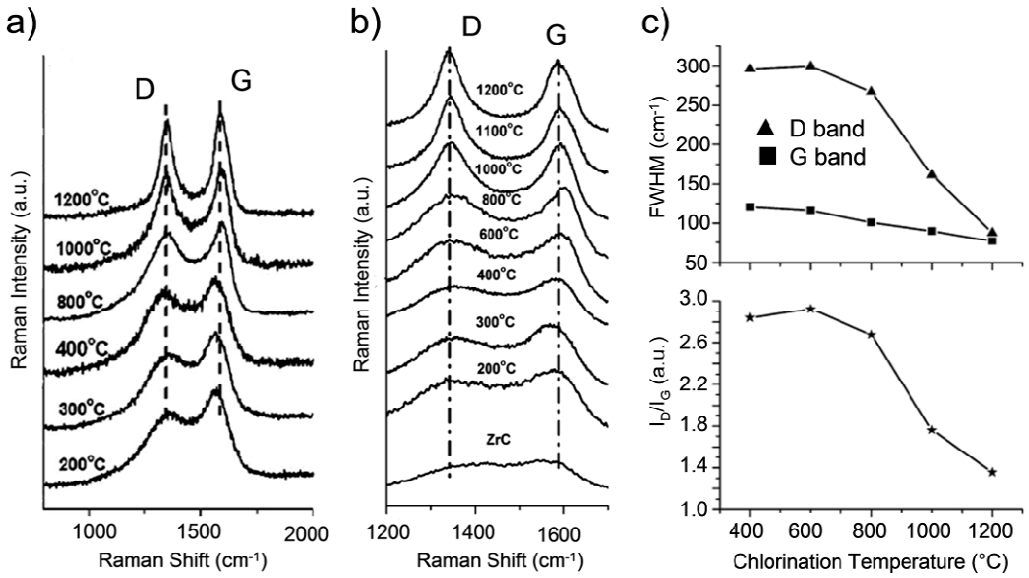

Figure 2.28: Raman spectra of TiC-CDC (a) and ZrC-CDC (b) synthesized at different temperatures. Analysis of Raman spectra of ZrC-CDC (c) shows a significant decrease in I_D/I_G and in peak width (FWHM) of D and G band with increasing temperature. All Raman spectra were recorded using 514 nm laser excitation. Spectra were obtained from Ref. 166 (a) and Ref. 308 (b, c).

at elevated temperatures, in agreement with HRTEM studies.[61,69,166,309] The sharp decrease in the FWHM of the D band of ZrC-CDC (**Figure 2.28**c) between 800 and 1000 °C indicates a large increase in ordering in this temperature range. A similar temperature behavior is observed other CDCs.

As for most CDCs, the intensity ratio between D and G band (I_D/I_G) decreases with synthesis temperature (**Figure 2.28**c). A change in I_D/I_G is usually related to amorphization or graphitization and ascribed to changes in the sp^2/sp^3 ratio.[247,274,305] However, CDCs chlorinated at different temperatures (same carbide precursor) have been shown to exhibit a relative constant sp^2/sp^3 ratio (see section 2.1.3).[70] Therefore, differences in Raman spectra are mainly due to changes in bond ordering, not in hybridization.

CDCs made from different carbides, but under similar synthesis conditions, contain different amounts of sp^2 and sp^3 sites (see **Figure 2.5**).[70] In that case, both ordering and hybridization determine shape and intensity of the Raman spectra. Therefore, changes in the I_D/I_G ratio depend on both the chlorination conditions and the lattice structure of the host carbide. For example, changes in I_D/I_G are more pronounced in the Raman spectra of ZrC-CDCs compared to TiC-CDCs chlorinated at the same temperature (**Figure 2.28**).

In summary, shape and intensity of the Raman spectra of CDCs are similar to that of other carbon nanomaterials, including amorphous carbon, carbon black and activated carbon. Variations in the synthesis conditions (e.g. carbide precursor, chlorination temperature) and the related changes in the D and G bands are therefore well described by the three-stage model of Ferrari et al.[247,305]

2.4 Summary

Different carbon nanostructures exist simultaneously at the nanoscale, all showing unique and novel properties. Unfortunately, current synthesis techniques provide mixtures of various nanostructures, amorphous carbon and catalyst particles, thus limiting the number of potential applications. Even if pure materials were available, the size-dependence of most nanomaterial properties requires a high structural selectivity. Several purification techniques have been developed and are either based on treatments in acids and bases, or involve the processing of other toxic substances.

While these techniques are widely used, they do not provide sufficient purity. Liquid phase purification is not an environmentally friendly process and requires corrosion-resistant equipment, as well as costly waste disposal processes. Alternative dry chemistry approaches,

such as catalyst assisted oxidation or ozone-enriched air oxidation, also require the use of aggressive substances or supplementary catalysts, which result in an additional contamination. Moreover, in many previous studies "trial and error" rather than insight and theory approaches have been applied. As a result, a lack of understanding and limited process control leads to extensive sample losses of up to 90%.

Because oxidation in air would be a controllable and environmentally friendly process, selective purification of carbon nanomaterials such as CNTs and ND in air is very attractive. In contrast to current purification techniques, air oxidation does not require the use of toxic or aggressive chemicals, catalysts or inhibitors and opens avenues for numerous new applications of carbon nanomaterials.

So far, selective oxidation of carbon nanomaterials has not been optimized or was considered not feasible as in the case of ND[119]. However, for the production and application of nanostructures on an industrial scale, it is very important to develop a simple and efficient route to, for example, selectively remove sp^2-bonded carbon from nanodiamond and amorphous carbon from nanotubes with minimal or no loss of diamond or nanotubes.

In situ Raman spectroscopy allows for a detailed and time-resolved investigation of the kinetics of complex physical/chemical processes such as oxidation. Using *in situ* Raman spectroscopy, one is able to monitor the oxidation and related structural changes of carbon nanostructures in real time, in order to identify the optimum purification conditions.

While oxidation is mainly used for purification of carbon nanostructures, it may also be an efficient tool for size control and surface modification. By selectively oxidizing, for example, smaller carbon nanotubes or diamond crystals, it can provide a simple technique for narrowing size distributions in carbon nanomaterials. Finally, modification of the

porosity (activation) of carbon is another example of controlled oxidation and may allow optimization of the pore structure and surface area of CDCs for various applications.

2.5 Objectives

The objective of this study is to investigate the oxidation behavior of nanostructured carbon materials under isothermal or non-isothermal conditions using *in situ* Raman spectroscopy and to develop a simple, highly selective, environmentally friendly and scalable oxidation method that can be used for purification and modification of different carbon nanomaterials. In particular, the following tasks will be performed:

- Exploration of the potential of *in situ* Raman spectroscopy for monitoring oxidation kinetics, changes in sample composition and structure of carbon nanomaterials
- Utilization of *in situ* Raman spectroscopy at high temperatures to investigate differences in the oxidation mechanism of various carbon nanostructures and understand the effects of particle size (or tube diameter), impurities (catalyst) and surface structure (chemical functionality) on the oxidation behavior of nanocarbons.
- Systematic study of the oxidation kinetics and the potential of air oxidation for size control and surface functionalization of SWCNTs, DWCNTs and MWCNTs, and development of a simple and environment-friendly oxidation technique for CNTs in order to optimize conditions for purification.
- Application of the same selective oxidation method to ND to remove non-diamond carbon from nanodiamond powders and improve the fundamental understanding of phonon confinement effects, phase transitions and surface chemistry of nanodiamond on its Raman spectra.

- Development of a procedure for accurate measurement of crystal size using Raman spectroscopy and use it for control and adjustment of the size distribution in nanodiamond powder by oxidation.
- Investigation of the potential of oxidation for physical activation of carbide-derived carbons in order to fine-tune the pore structure and increase surface area and pore volume of pores of the required size while retaining a narrow pore size distribution

3 MATERIALS AND METHODS

3.1 Materials

3.1.1 Carbon Nanotubes

SWCNT samples came from Tubes@Rice and were prepared by the HiPCO process. Detailed information on the synthesis conditions and composition of the sample is given elsewhere.[310]

DWCNTs were obtained from the Université Paul Sabatier, Toulouse (France) and produced by a CCVD method using a $Mg_{1-x}Co_xO$ solid solution catalyst containing Mo oxide. [110]

MWCNTs were provided by Arkema (France) and produced by a chemical vapor deposition (CVD) technique using iron catalyst.[131] In order to produce highly ordered MWCNTs, as-received MWCNTs were annealed for 3 h at 1800 °C in a vacuum furnace with graphite heaters (Solar Atmospheres) at a pressure of 10^{-6} Torr and a heating/cooling rate of ~ 10 °C/min.

3.1.2 Detonation Nanodiamond

ND powders UD50, UD90 and UD98 were supplied by NanoBlox, Inc. (USA). NDAlit powder was supplied by Alit (Ukraine). Black UD50 is the raw detonation soot. NDAlit, UD90 and UD98 samples were prepared by different multistage acid purifications using nitric and sulfuric acid.

3.1.3 Carbide-Derived Carbon

600°C-TiC-CDC was produced by chlorinating TiC (particle size ≤ 2 μm, density ~ 4.93 g/cm^3) in a quartz tube furnace[309], while chlorination at 1000 °C and 1300 °C was done in a graphite furnace[166]. The sample names "600°C-TiC-CDC", "1000°C-TiC-CDC" and "1300°C-TiC-CDC" refer to the chlorination temperature during CDC synthesis. A more detailed description of the CDC synthesis is given elsewhere.[40,166]

3.1.4 Other Materials Used

3.1.4.1 Carbon Onions

Carbon onions were produced by vacuum annealing of as-received ND powder (UD50). The powder was filled in a cylindrical container of a glassy carbon, placed in a vacuum furnace (Solar Atmospheres, USA) and annealed for 2 h under high vacuum conditions (10^{-5} - 10^{-6} Torr) at 1800 °C.[311]

3.1.4.2 Carbon Black

Highly graphitized carbon black (PUREBLACK) with a grain size of ~ 45 nm was provided by Superior Graphite. PUREBLACK is produced by incomplete combustion of petroleum-based oil at temperatures above 1000 °C.

3.2 Methods

3.2.1 Raman Spectroscopy and *In Situ* Analysis

Raman analysis was performed using two Renishaw Raman (1000/2000) Microspectrometers in backscattering geometry, equipped with high sensitivity ultra-low noise RenCam CCD detectors (**Figure 3.1**).

UV Raman spectra were recorded using a Renishaw 2000 Raman spectrometer with a 325 nm HeCd laser (3.81 eV, 2400 l/mm grating, 15x/40x objective, max. 1300 W/cm^2) and a 100 cm^{-1} cut-off notch filter.

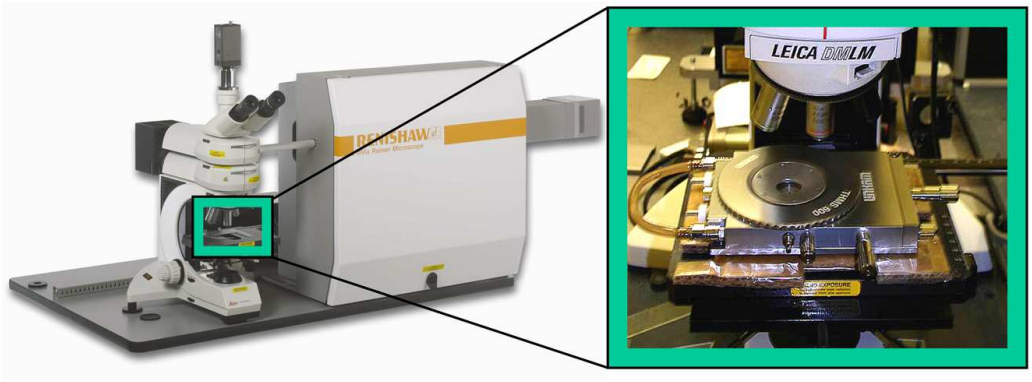

Figure 3.1: *In situ* Raman spectroscopy setup with Renishaw 1000/2000 Raman Micro-spectrometer and Linkam THMS 600 heating/cooling stage.

VIS Raman spectra were acquired with a Renishaw 1000 Raman spectrometer (5x/20x/50x/100x Objective) using a 514 nm Ar+ laser (2.14 eV, 1800 l/mm grating, max. 800 W/cm^2), a 633 nm HeNe laser (1.96 eV, 1800 l/mm grating) and a 785 nm semiconductor diode laser (1.59 eV, 1200 l/mm grating, 7500 W/cm^2) equipped with a 100 cm^{-1} cut-off notch filter and Raman imaging and Raman mapping capabilities.

In situ Raman studies were performed under 325 and 514, 633 and 785 nm excitation using a Linkam THMS600 heating/cooling stage placed under the Raman microscope as shown in **Figure 3.1**. Long focus objectives were used to protect the equipment against the heat produced by the stage. To minimize the influence of sample inhomogeneities, every measurement was done at the same spot during in situ experiments. This appeared difficult with respect to heating-induced sample drift.

All Raman measurements were repeated five times to produce statistically reliable results. Data analysis was performed using GRAMS-32 and WiRE 2.0 software from Renishaw.

3.2.1.1 Oxidation of Carbon Nanotubes

CNT samples were heated in a Linkam THMS600 stage, operated in static air between 20 and 600 °C. The CNT powders were dispersed in ethanol to produce a thin film of nanotubes on a glass slide. The samples were then kept in the heating stage and placed under the microscope of the Raman spectrometer. The stage was calibrated by using the melting points of $AgNO_3$ (209 °C), Sn (232 °C), KNO_3 (334 °C), and $Ca(OH)_2$ (580 °C). In every case, the difference between the measured and expected melting point did not exceed 2 °C.

The oxidation process followed two different heating procedures. The first procedure (nonisothermal) includes heating from room temperature up to 600 °C at a rate of 5 °C/min while holding each measurement temperature for about 4 min. Spectra were taken in steps of 50 °C in the range from 50 to 350 °C, followed by 25 °C steps from 350 to 400 °C and 10 °C steps from 400 to 600 °C. After reaching the desired temperature, the sample was cooled down at 20 °C/min until reaching 80 °C and then cooled at 10 °C/min down to room temperature.

In the second oxidation procedure (isothermal), CNT samples were heated at 50 °C/min and exposed to the desired temperature for 330 min. In that case, Raman spectra were acquired every 15 min after reaching the dwell temperature. After 330 min, samples were cooled down with 50 °C/min rate until reaching 80 °C followed by cooling at ~ 10 °C/min to room temperature. Isothermal oxidation experiments were carried out at 350, 365, 370, 375, 400, 430, 440, 475 and 550 °C for SWCNTs and DWCNTs and at 400, 430, 460, 500 and 530 °C for MWCNTs.

Sample size and conditions in the hot stage also influence the oxidation reaction. A potential problem might be an insufficient air circulation and oxidation in the oxygen-lean O_2-CO-CO_2 atmosphere. However, experiments with the opened stage showed no significant changes in the results, suggesting that the influence of the small sample volume is negligible.

3.2.1.2 Oxidation of Nanodiamond

Oxidative purification was conducted under isothermal conditions using the THM600 Linkam heating stage and a tube furnace. Isothermal experiments included two steps: (i) rapid heating at 50 °C/min to the selected temperature and (ii) isothermal oxidation for 5 h in ambient air at atmospheric pressure.

The ND powders used for crystal size characterization were oxidized for 2, 6, 17, 26 and 42 h at 430 °C, in a closed tube furnace in static air at atmospheric pressure.

3.2.1.3 Activation of Carbide-Derived Carbon

Activation of 1000°C-TiC-CDC and 600°C-TiC-CDC was performed in dry air and CO_2, respectively. Approximately 200 mg of CDC powder was placed in a tube furnace for each activation experiment. The quartz tube was then purged at ambient temperature and pressure for 4 h at a constant gas flow (air or CO_2) of 200 ml/min. Samples were heated at a rate of 25 °C/min under a constant gas flow of ~ 50 ml/min until the desired activation temperature was reached. Samples were weighed before and after the treatment at room temperature in order to determine the weight loss during oxidation.

3.2.2 Laser-Induced Heating of Carbon Nanomaterials

3.2.2.1 Effect of Laser Wavelength and Energy Density

The Raman characterization of different carbon nanomaterials in inert (Ar) atmosphere revealed a strong influence of the laser power (energy density) on the Raman spectra.[312] In general, an increase in the laser power leads to a decrease in the Raman frequency. For example, when using the most common excitation source in Raman spectroscopy - the 514 nm line of an Ar^+ laser - the G Band in the Raman spectrum of carbon onions (**Figure 3.2**a) shifts from ~ 1594 cm^{-1} (0.1 mW) down to ~ 1565 cm^{-1} (0.7 mW). The downshift is related to an increase in the sample temperature and has been measured for other carbon materials including graphite and CNTs (see section 4.1).

There exists several ways to measure temperature using Raman spectroscopy. The most common techniques include monitoring the anti-Stokes to Stokes intensity ratio or determining changes in the Raman shift of the peaks. Since the Renishaw UV Raman

spectrometer (325 nm) is equipped with a longpass edge filter, which does not allow anti-Stokes measurements, we used the latter method.

In order to estimate the laser-induced heating in the carbon onion sample, we determined the relationship between G band position and sample temperature (inset in **Figure 3.2**a) by using the lowest laser power possible and Ar atmosphere to prevent sample oxidation. The experiment revealed a downshift of ~ 0.034 cm^{-1}/°C which is slightly higher than the values reported for graphite and CNTs (see section 4.1.2), due to stronger bending of graphitic layers in carbon onions. Based on these results, G band positions of 1578 and 1565 cm^{-1} indicate temperatures of approximately 500 and 890 °C, respectively. It should be noted that these estimates assume the laser-heating at 0.1 mW to be negligible, which is most likely not the case. Since oxidation of most carbon nanostructures starts well below 500 °C, the presence of oxygen would inevitably lead to material burning and change the sample composition within the excited volume. A laser power of 0.3 mW (400 W/cm^2) is lower than the values commonly used for Raman analysis.

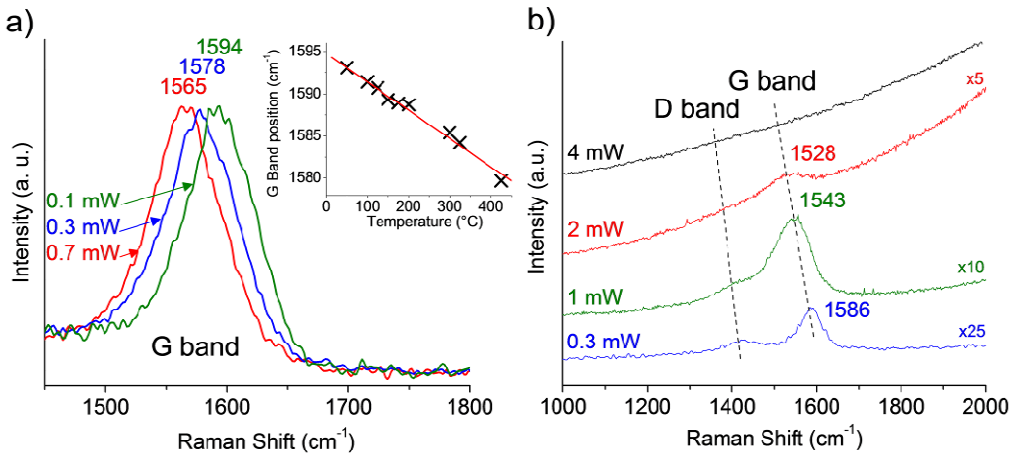

Figure 3.2: Raman spectra of carbon onions (Ref. 312). (a) G band recorded at 0.1, 0.3 and 0.7 mW with a 514 nm Argon laser (50x objective). The inset shows the temperature dependence of the G band position. (b) Raman spectra recorded at 0.3, 1, 2 and 4 mW using a 325 nm UV laser. The intensity of the spectra was adjusted as shown in the figure.

Raman analysis of the same sample upon and 325nm UV laser excitation in Ar atmosphere showed a similar energy-dependence (**Figure 3.2**b). In addition, Raman spectra revealed an increasing background intensity at higher laser power which was occupied by the emission of a bright white light from the excitation spot. As expected, the G band shifts to lower frequencies with increasing laser power. While one could accurately identify the G band position at lower powers (0.3 and 1 mW), light emission was not observed. At a high laser power, the Raman spectra is increasingly overshadowed by a broad background radiation as indicated by the magnification number and determining peak positions becomes difficult (**Figure 3.2**b). The temperatures calculated from the G band positions are 242 °C (1586 cm^{-1}) 1545 °C (1543 cm^{-1}) and 2000 °C (1528 cm^{-1}), respectively. It should be noted, that while there is a linear relationship between the G band position and temperature between 25 and 500 °C (inset in **Figure 3.2**a), this assumption might oversimplify the behavior at higher temperatures (> 1000 °C). Moreover, the recorded Raman spectra represent an average over the excited sample volume. Therefore, local temperatures within the sample may be slightly lower or higher compared to the measured average value.

In order to determine the nature of the emitted light and to confirm the temperature estimates obtained by Raman spectroscopy we changed the excitation wavelength from 325 nm (3.81 eV, max. 1300 W/cm^2) to 785 nm (1.58 eV, max. 7500 W/cm^2) and recorded the emission spectrum using an external UV-VIS-NIR spectrometer. Laser heating (thermal emission) increases with increasing laser power, and is less dependent on the excitation wavelength compared to photoluminescence or other light emitting electronic transitions, which require certain minimum photon energies. While the photon energy (in eV) of red light is much lower, the energy density (in W/cm^2) of the diode laser used in this study is greater compared to the UV source used. **Figure 3.3**a shows the light emission of carbon

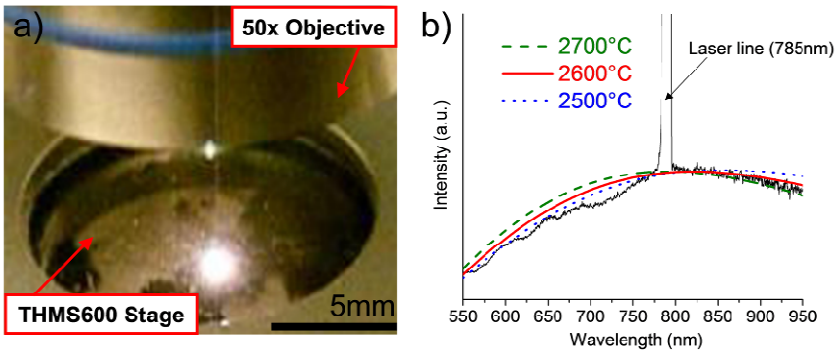

Figure 3.3: a) Photograph showing light emission of carbon black upon 785 nm laser excitation in an argon atmosphere. The corresponding emission spectrum was recorded using external UV-VIS-NIR spectrometer. The lines represent the calculated blackbody emission curves of 50 nm carbon black particles at different temperatures. Data obtained from Ref. 312.

black powder under 785 nm excitation. Indeed, the intensity of the light was found to be stronger compared to 325 nm, revealing a thermal nature of the emitted light (black body radiation). The absence of sharp emission lines also eliminates plasma as a possible emission source. On the other hand, photoluminescence usually shows significantly lower intensities and should not be dependent upon the environment. It should therefore occur even when the sample is immersed in water. This was not observed in our experiments.

Assuming the emitted light to be mainly thermal radiation, one can determine the sample temperature using Planck's radiation law. However, such measurements require a high accuracy, because small changes in the position of the curve maxima used for temperature measurements result in large temperature variations. Conventional Raman spectrometers are not suitable for recording emission spectra over a broad wavelength range due to the dispersive operation mode and slow moving optics, which increases the probability of intensity changes during acquisition and decreases the accuracy of temperature data measurements. Moreover, conventional Raman spectrometers do not have second order filtering and the interpretation of results becomes difficult.

The high intensity of the emitted light upon 785 nm laser excitation allowed for measurements of the spectral composition using an external HR4000CG-UV-NIR spectrometer. The emission spectrum of carbon black is shown in **Figure 3.3**b. Carbon black was preferably used for blackbody-based temperature calculations because its index of refraction is well known.[313] The emission spectrum was corrected for contributions from the optics and the grating following the approach of Keyvan et al.[314] The temperature was determined by comparing the experimental data with the calculated emission spectrum. The size-dependent thermal emission spectrum of carbon black particles can be calculated using Planck's black body distribution function. The intensity of the emitted light is given by:

$$I(\lambda, r) = \frac{64\pi^3 c^2 r^3 h}{\lambda^6 \times \left[e^{\frac{hc}{\lambda k_b T}} - 1 \right]} \times \mathrm{Im}\left[\frac{m^2 - 1}{m^2 + 2} \right] \times \Delta\lambda \qquad (3\text{-}1)$$

where r is the radius of the particle, λ is the wavelength, T is the temperature (in K), and m is the complex index of refraction. The parameters c, k_b and h are the speed of light in vacuum, the Boltzmann and Planck constants, respectively. Equation 4-1 was derived using the approach of Rohlfing et al.[315] The black body spectrum of carbon black (particle size ~ 50 nm) was calculated for three different temperatures. Based on the maxima of the emission curve, the local sample temperature was approximately ~ 2600 °C (**Figure 3.3**b). The sharp peak at 785 nm results from elastic scattering of the laser light (Rayleigh scattering).

Our experiments showed that laser heating and light emission can be different for different sample spots and depend on both the structure of the carbon and bulk density of the sample. For example, while carbon onions, carbon black and ND exhibit strong heating and showed light emission at almost each spot excited by the laser beam, its occurrence was

much lower for MWCNTs. The main difference between MWCNTs and the other nanostructures is the size. While the particle size (gyration radius) of ND, carbon black or carbon onions is under 100 nm in any dimension, MWCNTs have a comparable size in cross-section, but are at least two orders of magnitude longer. In that case, the energy transferred from the laser beam to the nanoparticles is dissipated much faster and over a larger area, thus reducing local heating.

3.2.2.2 Structural Changes upon Laser Excitation

In order to determine possible changes in structure and composition of carbon nanomaterials upon laser excitation, we recorded Raman spectra of carbon black and ND before and after light emission was observed (**Figure 3.4**).

Figure 3.4a (top) shows the Raman spectrum of carbon back before light emission with the corresponding optical image of the measurement spot. The main features in the Raman spectrum of carbon black are two peaks centered at ~ 1340 cm^{-1} (D band) and 1580 cm^{-1} (G band), respectively. After light emission, formation of a black film was observed around the excited sample area, while some carbon black within the excited volume was removed (**Figure 3.4**a, bottom). The Raman spectrum recorded at the initial excitation spot shows almost no changes. Peak shape and intensity ratio between D and G band are similar to the spectrum of the carbon black. However, the Raman spectrum of the film is quite different and shows significant changes. While the D band and G band are well separated in carbon black, they overlap in the spectrum recorded from the film and are noticeably broadened. The G band position is shifted to lower wavenumbers indicating the presence of amorphous

species and an increase in disorder. Shape and position of the peaks are similar to that of amorphous carbon (see section 2.4).

These results suggest the evaporation of carbon upon laser excitation and its subsequent re-deposition around the excitation spot. SEM images (not shown) of the carbon black sample before and after light emission confirmed these assumption. Although our estimates indicate high temperatures within the excited volume, melting of graphitic carbon is not expected at temperatures below 3500 °C. However, sublimation of carbon typically occurs below the melting point at ambient pressure. Evaporation and re-deposition of carbon occur at the very first moment upon laser excitation. During light emission, no further changes are observed. The laser heats and evaporates carbon black, reaching temperatures of > 3000 °C within the focal point of the beam. Carbon black around the focus spot is heated too, but the energy density of the laser is insufficient to reach the evaporation temperature. The emitted light is thermal radiation of the crystals that are slightly out of focus and reach temperatures of up to 2600 °C, but are not evaporated.

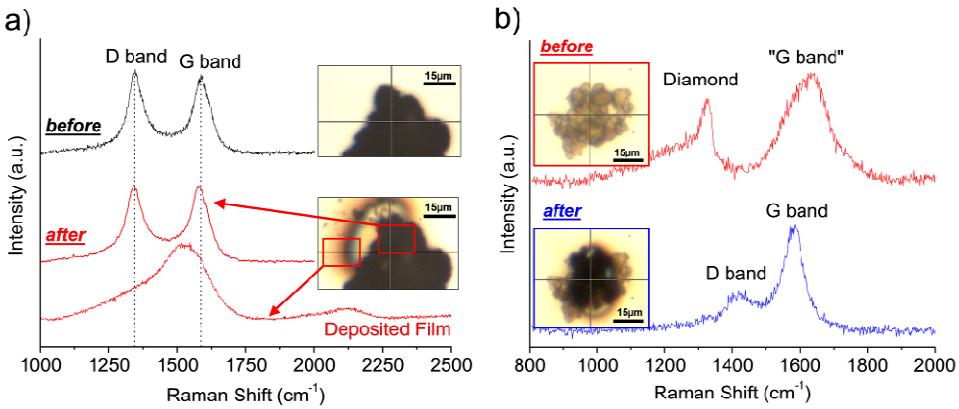

Figure 3.4: Raman spectra and corresponding optical images of a) carbon black (514 nm excitation) and b) nanodiamond (325 nm laser excitation) before and after laser-induced light emission, recorded in Ar atmosphere (Ref. 312). Carbon black is evaporated by the laser and re-deposited as amorphous carbon around the excitation spot. ND is evaporated or transformed into graphitic carbon upon irradiation.

Structural changes during light emission were also observed for ND powder (**Figure 3.4**b). The Raman spectrum (325 nm) of the ND powder before emission shows two characteristic features: a downshifted and broadened diamond peak at ~ 1325 cm^{-1} and a broad band (referred to as "G band") centered at ~ 1620 cm^{-1}(**Figure 3.4**a, top). After light emission, the Raman spectrum shows the characteristic features of graphitic carbon. The G band shows a lower peak width and is downshifted to ~ 1580 cm^{-1}(**Figure 3.4**b, bottom). The intensity of the diamond peak significantly decreases, while the D band appears in the Raman spectrum after light emission, indicating a conversion of ND into graphitic carbon upon laser excitation. Optical images of the sample before and after light emission support this assumption. The color of the ND powder changes from grey-brown to black, suggesting the formation of sp^2-bonded carbon species. It is well known that graphitization of ND and the formation of onion-like carbon and polygonized particles occur upon heating above 1100 - 1200 °C.[311,316] In addition, similar to carbon black, the formation of a thin film was observed around the excited sample spot, indicating significantly higher temperatures in the focused spot of the beam.

3.2.3 Sample Cooling and Effect on Raman Spectra

Strong absorption of light in a broad wavelength range and poor thermal conductance between particles in carbon nanopowders can lead to extensive heating during Raman spectroscopy characterization, even at a very low (< 0.4 mW) power.[312] Depending on the surrounding atmosphere, laser-induced oxidation, structural damage or changes in the composition of carbon nanomaterials are likely to occur. Even if temperatures are not high enough to oxidize or evaporate carbon structures, heat-induced shifts in peak position and

changes in Raman intensity are often the consequence. In most cases, changes in sample composition occur immediately, because the steady state is reached in less than a second under the laser beam, and are hardly noticeable during acquisition of spectra. Researchers thus often underestimate the risk of heat-induced sample damage and may come to erroneous conclusions.

In our experiments, local sample heating induced by the laser during in situ Raman studies was minimised by using a low laser beam power (0.1 - 0.2 mW) and defocusing the laser at the sample surface. Obtaining high quality spectra was generally difficult due to a trade-off between the long acquisition time (or high laser power) required for the high signal-to-noise ratio and the opposite conditions needed to prevent sample damage resulting from heating and oxidation in air. If necessary, measurements were performed on samples dispersed in water (when indicated) or in argon atmosphere to prevent sample heating. Water dissipated the induced heat and thus keeps the local temperature low.

However, as discussed in detail in section 4.5, the use of liquid water as a cooling medium has some serious limitations in the case of carbon nanomaterials.[317] The recommendation to use water is based upon the assumption that it does not interfere with Raman spectra. Indeed, a low sensitivity of Raman spectroscopy towards water is a well-known advantage over IR spectroscopy[318], and is often mentioned as a reason for a wide use of Raman spectroscopy in studying biomolecules in physiological aqueous environments. However, if the Raman signal of a material is weak, as in the case of many carbon nanomaterials, then even a small contribution from water cannot be neglected. In our experiments, we observed that for ND measured under a layer of water in a Petri dish, the intensity of the 1640 cm^{-1} Raman peak noticeably increased, even when the thickness of the water layer was just a fraction of a millimeter (**Figure 3.5**).

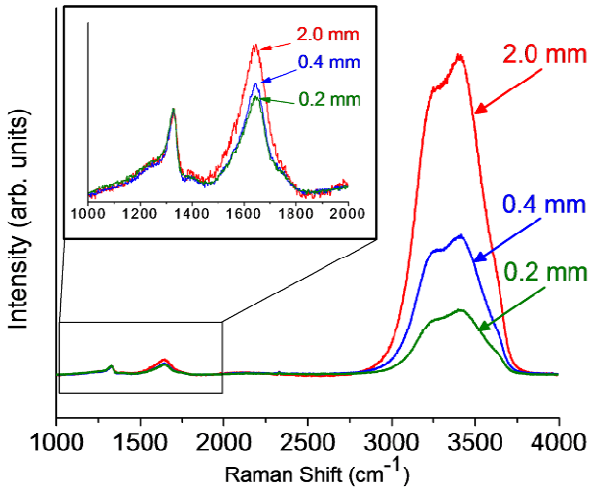

Figure 3.5: Contribution of water coolant to the 1640 cm^{-1} peak in the Raman spectra of ND powder recorded through different thickness (in mm) of the water layer (Ref. 316). Spectra recorded using 325 nm laser wavelength.

If the thickness was a millimeter or more, the intensity of this peak increased dramatically. In previously published studies, when water cooling was used for ND, there were no indications of control over the water layer thickness. As such, the 1640 cm^{-1} peak measured with this technique may turn out to be mainly attributed to O-H bending vibrations in liquid H_2O. In addition, water has a strong stretching O-H Raman mode at 3300 – 3700 cm^{-1}, broadened due to hydrogen bonds. However, in contrast to the 1640 cm^{-1} O-H peak, which requires careful analysis in order to be detected, the water-related O-H stretch band is so intense that it totally overwhelms the C-H range and the second-order Raman spectrum of carbon, and can thus be easily detected even at very low water concentration, when no liquid water is apparently present. Therefore it is extremely important to analyze possible contributions from coolants such as water, especially when deriving any conclusions based on the peaks between 1500 and 1800 cm^{-1}, such as the I_D/I_G intensity ratio commonly used for evaluating ordering in carbon materials, or sp^2/diamond

carbon ratio for ND. In such cases, for the purpose of cooling, other liquids may be considered having no peaks in the range of interest (for instance, high purity CCl_4 or CS_2 which only show peaks below 1000 cm^{-1} in Raman spectra [318], though both should be used with great precautions as they are toxic). In any event, possible coolant interference must be examined and properly accounted for.

3.2.4 Modification of Surface Chemistry

The surface chemistry of carbon nanomaterials has been modified by high temperature treatments in hydrogen and argon using the apparatus show in (**Figure 3.6**). The reactant gases (H_2, Ar) were of "ultra high purity" grade and supplied by Air Gas (USA). Hydrogenation and argon-annealing were performed for 2 h at 800 °C and 1 h at 700, 800 and 900 °C, respectively. Samples were placed in a quartz boat, weighed and inserted into a quartz tube positioned inside a tube furnace. The furnace tube was isolated from the

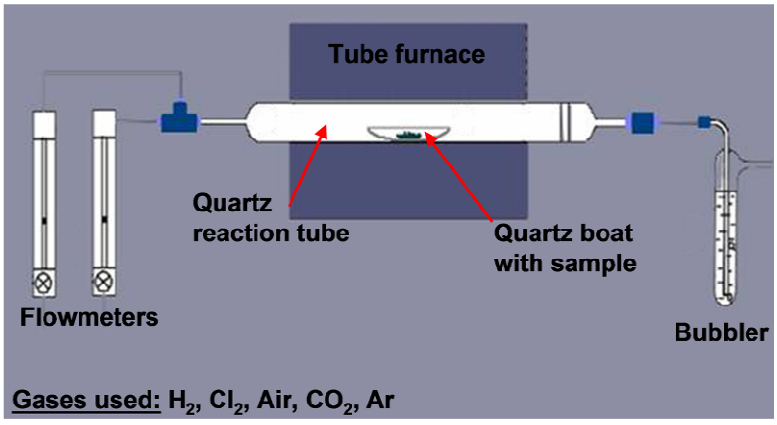

Figure 3.6: Schematic of experimental setup for surface modification of carbon nanomaterials. Flow of gaseous reactants is regulated by two flow meters. The quartz tube is heated by a tube furnace. A bubbler is used to inhibit diffusion of gases from laboratory atmosphere into the tube.

atmosphere and purged with Ar (> 30 ml/min) at room temperature for 1 h to remove gases of the ambient atmosphere. After purging, the flow of a reagent gas was started (30 ml/min), and heating was turned on. Upon achieving the desired temperature, the sample was held at this temperature under the reagent flow for a specified time. The furnace was switched off and the sample was allowed to cool to room temperature under the reagent gas flow. Upon completion of the treatment, the quartz boat with the sample was removed from the tube and weighed again to determine weight change.

3.2.5 Thermogravimetric Analysis

Thermogravimetric analysis (TGA) was performed using a SDT 2960 DTA-TGA from TA instruments and a Perkin Elmer TGA 7.

In all experiments a gas flow of 40 ml/min was applied. Specimen powders (5 - 10 mg) were placed on a platinum pan and loaded into the instrument. Two different heating procedures were used. In non-isothermal experiments samples were heated from 25 to 800 °C at 2 °C/min. Isothermal studies involved rapid heating (50 °C/min) to the desired temperature, followed by and isothermal step for ~ 300 minutes.

3.2.6 Crystal Size Measurements

The ability to control and measure the crystal size is of great importance for many nanomaterial applications. Characterization techniques such as dynamic light scattering or gas sorption, which are widely used for measuring the particle size of powders, cannot provide reliable data due to the strong affinity of nanomaterials to agglomerate. In this case,

the size of agglomerates rather than single crystallites is measured. In this study we conducted a detailed size analysis using Raman spectroscopy, X-ray diffraction (XRD) and high resolution transmission electron microcopy (HRTEM) in order to measure changes in crystal size and determine the limitations of these techniques for particle size analysis.

3.2.6.1 Transmission Electron Microscopy

JEOL 2010F field emission HRTEM operating at accelerating voltage of 100 kV and 200 kV was used for high-resolution imaging of carbon nanomaterials. HRTEM samples were prepared by dispersing the carbon nanomaterials in isopropyl alcohol over a copper grid coated with a lacey carbon film.

Although HRTEM is able to visualize individual nanocrystals, such analysis is cost intensive and lacks in statistical reliability, because a very limited number of particles is counted. This is especially critical in the case of inhomogeneous samples. Other drawbacks are the complex sample preparation and the high temperatures generated by the electron beam, both of which can change structure and composition of carbon nanomaterials. However, analysis of a larger number of HRTEM images obtained from different parts of the sample may allow for a rough estimate of the crystal size distribution. In addition, important information on lattice defects and particle shape can be obtained.

3.2.6.2 X-ray Diffraction

X-ray diffraction (XRD) analysis was performed using a Siemens D500 powder diffractometer in 2Θ-configuration, equipped with a 1500 W copper fine focus tube (CuKα,

λ = 1.54056 Å) and a graphite monochrometer. A step size of 0.02° (2Θ) and a collection time between 1 and 5 seconds per step were chosen for the analysis. Diffraction patterns were analyzed using Jade+ (MDI) analysis software and Jade MDI powder diffraction library.

X-ray diffraction (XRD), which also directly probes the crystal size, provides a more accurate and statistically significant estimate of the average crystal size. Size measurements are typically carried out using the Williamson-Hall analysis (WHA). Similar to the Deby-Scherrer equation, the WHA measures the increase in the FWHM of the diffraction peaks with decreasing size, but also accounts for possible lattice strains. Unfortunately, both the WHA and the Deby-Scherrer equation also have some serious limitations, since they do not take into account the broad size distribution present in most ND powders. XRD is based on constructive interference (Bragg's Law). Therefore, larger crystals give stronger contributions to the intensity of the diffraction peak, while smaller crystals primarily enlarge the base of the peak. As a consequence, both methods typically overestimate the crystal size and lead to inaccurate results for samples that contain both large and small crystals. Lattice defects such as cracks and dislocations, which are also neglected in both models, cause a similar line broadening and lead to a further distortion of the results.

3.2.6.3 Raman Spectroscopy

As suggested by Richter et al. and Nemanich et al., Raman spectroscopy can also be used to measure the crystal size of nanostructured solids following the phonon confinement model, which relates changes in position and line shape of the Raman peaks to the crystal size. So far, in the case of ND, Raman analysis can only provide semi-quantitative results for

size measurements due to little understanding of the Raman spectra of ND and a lack of agreement between theoretical predictions of the model and experimental Raman data. However, as we will show in section 4.6, when taking into account the broad size distribution of ND powders and contributions of lattice defects, a significant improvement can be achieved.

Although the results determined by Raman spectroscopy are in agreement with HRTEM and XRD studies, a correct interpretation of Raman data and quantitative size measurements still require additional information on sample structure and composition. Therefore, a combined use of various characterizations techniques such as XRD, HRTEM and Raman spectroscopy is recommended for a reliable determination of the size of ND crystals.

3.2.7 Other Techniques Used

3.2.7.1 Fourier Transform Infrared Spectroscopy

Fourier transform infrared (FTIR) spectra were collected using a Digilab FTIR spectrometer (Varian Excalibur FTS-3000) equipped with a UMA 600 microscope and a sensitive MCT detector. Carbon samples were mixed with potassium bromide (KBr), pressed into pellets of ~ 1 mm thickness and measured in transmission mode. Spectra were recorded between 1000 and 4000 cm^{-1}.

3.2.7.2 X-ray Adsorption Near Edge Structure

Soft x-ray absorption near-edge structure (XANES) spectroscopy experiments were performed at undulator beamline 8.0 at the Advanced Light Source (ALS) at Lawrence Berkeley National Laboratory (LBNL). Spectra were obtained by measuring the total electron yield by monitoring the total sample photocurrent. The incoming radiation flux was monitored by measuring the total photocurrent produced in a highly transmissive Au mesh inserted into the beam. All XANES spectra were normalized to the Au mesh photocurrent. The monochromator was calibrated by aligning the π^* resonance in the carbon K-edge of highly oriented pyrolytic graphite (HOPG) to 285.4 eV. After a linear background subtraction, all spectra were normalized to the post-edge step heights.

3.2.7.3 Electrical Resistance Measurements

The resistivity/conductivity measurements were performed using a Zahner IM6d impedance analyzer ranging from 0.1 to 10 Hz. The reliability of the AC results was confirmed by I-U measurements (DC) using the same samples. The ND powders were pressed in a Teflon cell and conducted with two copper electrodes.

3.2.7.4 UV-VIS-NIR Spectroscopy

The JASCO V-570 UV-VIS-NIR Spectrophotometer is a double beam spectrometer with two monochromators which cover the wavelength range of 190-2500 nm. The dual detector design incorporates a photomultiplier detector for the UV-Visible and a Peltier-cooled lead sulphide (PbS) detector for the NIR region. The spectrophotometer is equipped

with an ILV-471 Integrating sphere, which collects elastically scattered light and directs it onto the detector.

3.2.7.5 Specific Surface Area and Pore Size Distribution

The pore structure of the TiC-CDCs was characterized by gas sorption measurements using a Quadrasorb apparatus (Quantachrome Instruments) in N_2 at 77 K and CO_2 at 273 K. The specific surface area (SSA) was calculated using Brunauer-Emmett-Teller (BET) analysis from N_2 sorption. The pore size distribution was determined from N_2 and CO_2 isotherms using the non-local density functional theory model (NLDFT), which assumed slit pores.[319] The volume of pores below 1.5 nm (micropores) was calculated from CO_2 sorption, using the same NLDFT model. The porosity of SiC-CDC was measured using Quantachrome Autosorb-1 with Ar adsorbate at −195.8 °C. Sorption isotherms were analyzed by Quantachrome's data reduction software (version 1.27).[319]

4 RESULTS

4.1 *In situ* Raman Spectroscopy Study of Carbon Nanotubes

Oxidation has become a frequently used method for removal of disordered carbon species from carbon nanotubes, but it can also induce damage to the tubes and destroy most of the sample. *In situ* Raman spectroscopy allows a time-resolved investigation of changes in structure and composition of carbon nanomaterials during oxidation. In the following sections results are shown from *in situ* Raman spectroscopy studies of the oxidation of single-, double- and multi-wall carbon nanotubes (SWCNTs, DWCNTs and MWCNTs) under isothermal and nonisothermal conditions. The effects of oxidation, temperature and defect-formation on the structure and properties of CNTs are also discussed.

4.1.1 Elimination of D Band from Raman Spectra of Carbon Nanotubes

Figure 4.1 shows the Raman spectra of as-received DWCNTs recorded using 514 and 785 nm laser excitation.[320] The G band can be well fitted with two Lorentzian peaks at 1593 and 1568 cm^{-1}, a broad Gaussian peak around 1525 cm^{-1} for 514 nm, Lorentzian peaks at 1592 and 1564 cm^{-1}, and broader Gaussian peaks at 1548 and 1519 cm^{-1} for the 785 nm laser wavelength (**Figure 4.1**a). The peaks at 1593 cm^{-1} (514 nm) and 1592 cm^{-1} (785 nm) are referred to as G^+, while all other peaks are assigned to G^-. The narrower Lorentzian peaks are ascribed to semiconducting nanotubes, while the broader peaks are attributed to metallic tubes or result from overlapping of several peaks arising from tubes with similar diameters.[188,197] Measurements at different sample spots revealed small variations in the peak

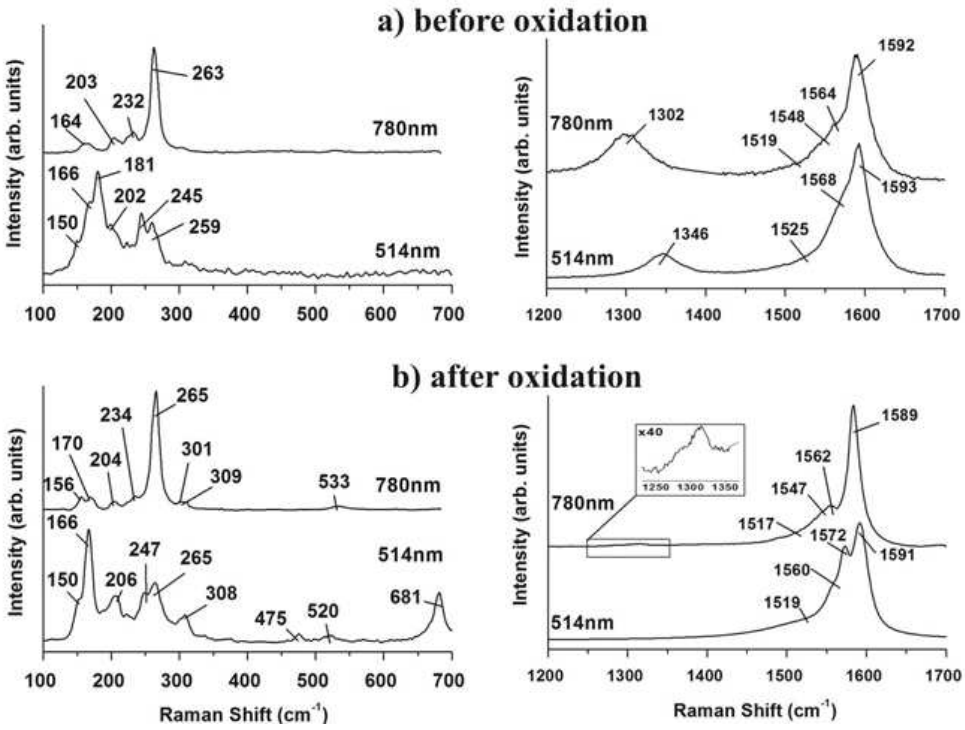

Figure 4.1: Raman spectra of DWCNTs recorded using 785 nm and 514 nm laser excitation obtained (a) before and (b) after oxidation (Ref. 320). Intensities of the spectra have been adjusted to improve presentation.

positions, which may result from heating effects and inhomogeneities in sample composition. The accuracy of the measured Raman frequencies is ± 2 cm^{-1} of the values presented in the graphs.

514 nm excitation wavelength maximizes the Raman intensity of graphitic carbons, due to resonance enhancement, and leads to a strong Raman signal. On the other hand, 785 nm laser excitation maximizes contributions from amorphous species, leading to larger I_D/I_G ratio, thus allowing a more accurate analysis of the disordered phases. The I_D/I_G ratio was determined using the integrated intensity (peak area) of D and G bands. Raman spectra acquired with 514 nm laser wavelength give an I_D/I_G of approximately 0.22. This value increases up to 0.40 for 785 nm excitation due to the wavelength-dependence of the Raman

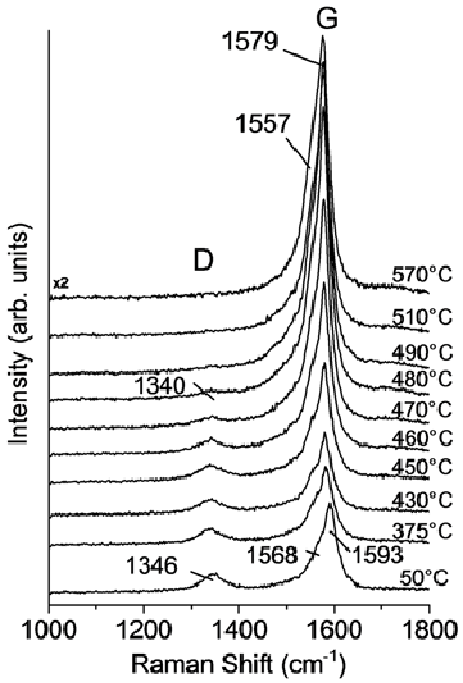

Figure 4.2: *In situ* Raman spectroscopy study of the changes in the D and G band of DWCNTs during heating from 25 to 600 °C in air (514 nm laser excitation wavelength). Graph obtained from Ref. 320.

scattering cross-section of both D and G bands (see section 2.4.2). The D band position shows a dependence on the excitation wavelength as well (**Figure 4.1**), which is a characteristic feature of a double-resonance process.[173] It should be noted that, due to the presence of structural defects, the D band is observed for most CNT samples, even if the amount of amorphous carbon is very low.

Figure 4.2 shows the *in situ* Raman spectra of DWCNTs recorded during heating from 25 to 600 °C in air. The D peak, which results from defects and disordered carbon, starts to decrease at ~ 430 °C until it completely disappears around 510 °C. A linear downshift of all peaks is observed with increasing temperature (**Figure 4.2**). The value of the thermal shift of the G band was reported to be 0.030 cm^{-1}/°C (G^+)for SWCNTs[178] and 0.024 cm^{-1}/°C for

graphite. The present experiment for the DWCNTs, using 514 nm wavelength excitation, showed a downshift of 0.029 cm^{-1}/°C for the 1568 cm^{-1} peak and a value of 0.026 cm^{-1}/°C for the 1593 cm^{-1} peak (**Figure 4.2**). Thus the measured values are between that of SWCNT and graphite, as expected. The thermal shift of the D, G^+ and G^- bands will be discussed in section 4.1.2.2.

Another important observation is that the intensity changes of D and G band at high temperatures follow different trends (**Figure 4.2**). The initial decrease in I_D/I_G appears to be mainly due to the increase of the G band intensity. A quantitative analysis of the Raman data (**Figure 4.3**) shows that the intensity of the G band starts to increase at ~ 440 °C, reaches a maximum around 500 °C, and decreases to its original values when reaching 600 °C. As shown in **Figure 4.3**, the decrease in D band intensity occurs at temperatures 20 - 30 °C higher than the increase in G band intensity. An explanation for the early intensity increase of G band may be the possible removal of hydrocarbons (the tube synthesis was conducted in a hydrogen-containing atmosphere) and disordered carbon, which were shielding the

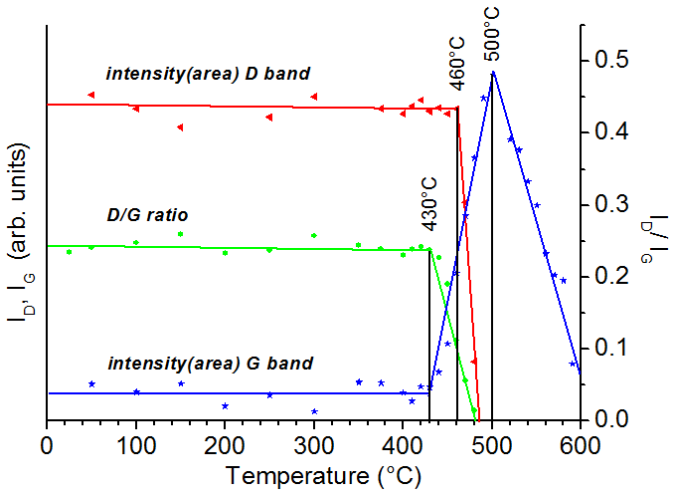

Figure 4.3: Comparison of intensity changes in the D and G bands during oxidation of a DWCNT sample in air (measured with 514 nm laser wavelength). Graph obtained from Ref. 320.

Raman signal from the CNTs. The fact that the G band's absolute intensity starts to increase around the same temperature as the D band decreases seems to support this hypothesis. Further evidence is provided by the fact that a higher intensity (200 - 300 %) of the G band was observed (same sample spot) after cooling to room temperature in every experiment. When an already oxidized sample was used for the *in situ* Raman studies, no increase in G band intensity was observed. In this case, there was no disordered carbon on the tube surface which could influence the Raman signal of the tubes.

Figure 4.1b shows the Raman spectra of the DWCNT sample after heating (measured at room temperature). The graph demonstrates that the splitting of the G band is more pronounced after heating and that the temperature-induced shift of the peaks is not completely reversible. This can be explained by the removal of amorphous carbon and highly defective CNTs. As discussed in section 2.3.3.2, the G^+ peak (~ 1590 cm^{-1}) does not depend on the tube diameter.[321] Thus, its position should not change after oxidation of smaller tubes as a result of their decreasing contribution to the total Raman intensity of G band. The peak is slightly sharpened, but shows only little shift in frequency (**Figure 4.1**b). However, the lower frequency component of the G band, G^- (peaks at or below 1570 cm^{-1}), depends on the tube-diameter and is therefore affected by the oxidation of the smaller CNTs, leading to irreversible changes in peak positions and larger G band splitting.

The RBM range shows no significant changes, indicating that the size distribution of the DWCNT sample has not been changed. New peaks observed between 475 and 690 cm^{-1} (**Figure 4.1**a) can be ascribed to metal oxides, formed by oxidation of remaining catalyst impurities. The RBM modes of as-received DWCNTs and temperature-induced changes during heating will be discussed in section 4.1.2.

The most noticeable effect during the in situ Raman studies was the near complete disappearance of the disorder induced D band after oxidation (**Figure 4.2** and **Figure 4.3**). Using the 514 nm laser, the D band is not observed at all above 510 °C. In the case of 785 nm laser excitation, which produces the largest D band intensity, the I_D/I_G ratio decreases from 0.43 before heating to < 0.015 after oxidation.

These results show that for the DWCNT sample, the D band originates mainly from amorphous carbon present in the sample and not from defects in the wall-structure of the nanotubes. While the concentration of defects probably increases during the oxidation, disordered carbon and the associated D band disappear. However, as discussed in section 2.3.3.2, only metallic CNTs contribute to the D band intensity. Therefore, the absence of any Raman signal between 1300 and 1400 cm^{-1} could also indicate a selective removal of semiconducting CNTs, or the presence of exclusively highly-ordered, defect-free DWCNTs.

4.1.2 Nonisothermal Oxidation: Comparison of SWCNTs and DWCNTs

4.1.2.1 Raman Spectra of As-Received SWCNTs and DWCNTs

Figure 4.4 compares the D and G bands of DWCNTs (a) and SWCNTs (b), recorded using a 633 nm laser excitation.[322] The G band of the as-received DWCNTs can be fitted with Lorentzian peaks at 1588 cm^{-1} (G^+) and 1550 cm^{-1} (G^-) and a broad Gaussian peak around 1526 cm^{-1} (**Figure 4.4**a) As mentioned before, the narrow Lorentzian peaks are ascribed to semiconducting CNTs, while the broader peaks are attributed to metallic tubes or may also result from an overlap of peaks coming from tubes with different diameters.[188,197] DWCNTs show a larger I_D/I_G ratio (~ 0.25) compared to SWCNTs (~ 0.07). A lower I_D/I_G

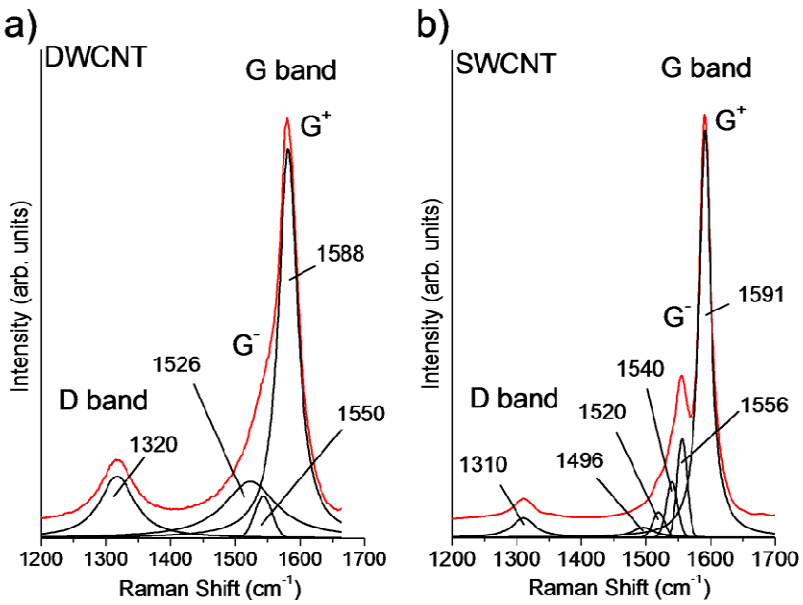

Figure 4.4: Comparison of room temperature Raman spectra of as-received DWCNTs (a) and SWCNTs (b). Graph obtained from Ref. 322. Spectra were recorded using a 633 nm excitation wavelength.

value for the SWCNT sample suggests a smaller concentration of structural defects and/or amorphous material. Moreover, in the case of SWCNTs (**Figure 4.4**b), there is a larger G band splitting with respect to the G^- and G^+ Raman modes, and three different peaks (1556, 1540 and 1520 cm^{-1}) resulting from the transversal radial vibrations contributing to G^- can be observed.

The as-received DWCNTs show several Raman features between 130 and 340 cm^{-1} (**Figure 4.5**a). These peaks originate from collective radial vibrations (RBM) of all carbon atoms and are strongly influenced by the resonant Raman effect.[178] Similarly to SWCNTs, the RBM frequencies ω (cm^{-1}) of DWCNTs are inversely proportional to the tube diameter d (nm). Considering both interactions between outer and inner tubes and tube-tube interactions within bundles, and assuming the influence of van der Waals interactions in

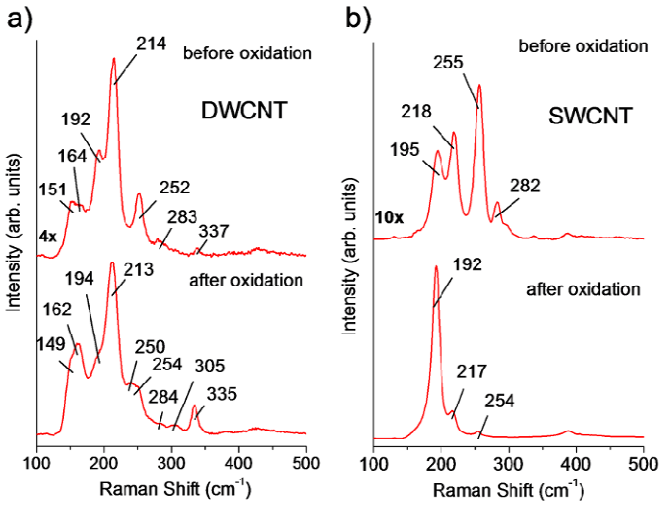

Figure 4.5: RBM frequency range of the Raman spectra of DWCNTs (a) and SWCNTs (b) before and after nonisothermal oxidation (Ref. 322). Spectra were acquired at room temperature using a 633 nm laser excitation.

DWCNTs to be similar to the behavior of SWCNTs within bundles we can calculate ω according to[323,324]

$$\omega = \frac{238}{d^{0.93}}. \qquad (4\text{-}1)$$

The smallest ever observed inner diameter for DWCNTs is 0.40 nm. Considering an interlayer spacing of 0.34 nm between the inner and outer tube, one can conclude that all RBM frequencies higher than 200 cm^{-1} must be ascribed to inner tubes while lower frequencies can be associated with both, inner and outer tubes. Peaks between 130 and 340 cm^{-1} correspond to a diameter range of 0.7 - 1.9 nm (**Figure 4.5**a), which is within the range of diameters determined from HRTEM of the same sample (0.53 to 2.53 nm for inner and from 1.2 to 3.23 nm for outer tubes)[110]. The increase in intensity of the peak at 337 cm^{-1} after oxidation may be explained by oxidation of outer tubes and the resulting increase in the Raman intensity of the smaller inner tubes. However, it may also originate from remaining metal catalysts and the corresponding oxides formed during heating. Because oxidation of

DWCNTs increases the relative amount of catalyst particles in the sample, the contribution of catalyst impurities to the Raman spectrum is expected to increase during heating. We also observed new peaks (475, 520 and 683 cm^{-1}) appearing at temperatures > 500 °C which again can be attributed to cobalt oxide.

The resonance enhancement for laser energies between 1.59 and 2.41 eV mostly favors the vibration modes above 200 cm^{-1}.[323] Therefore, it is important to note that RBM intensities do not reflect the real amount of CNTs of a particular size because of the enhancement effect, which selectively amplifies the Raman signal from nanotubes that are in resonance with the incoming laser radiation. The RBM spectra of SWCNTs (**Figure 4.5**b) show a narrower diameter distribution compared to the DWCNTs, as expected. For the investigated SWCNTs the RBM peaks are between 190 and 290 cm^{-1}, corresponding to a diameter range of approximately 0.8 - 1.3 nm. The RBM spectra of the SWCNT sample exhibit a lower number of peaks, but with a higher relative intensity compared to the RBM intensity of DWCNTs. This can be explained by the smaller diameter distribution of the SWCNT sample and the fact that the RBM spectra of DWCNTs are an overlap of the Raman signals coming from both inner and outer tubes. Thus the RBM spectra of DWCNTs have a wider frequency range, but with a lower intensity.

Similar to DWCNTs, the peak at ~ 388 cm^{-1} in the Raman spectra of SWCNTs (**Figure 4.5**b) is expected to result from catalyst particles or other impurities in the sample. The intensity of this Raman feature does not change after oxidation, while lower frequency peaks, corresponding to larger and more stable SWCNTs, show a noticeable decrease in intensity.

4.1.2.2 *In situ* Raman Study of Nonisothermal Oxidation

Figure 4.6 shows the Raman spectra of SWCNTs and DWCNTs recorded during heating from 25 to 600 °C (in air) using 633 nm laser excitation. In the case of DWCNTs (**Figure 4.6**a), I_D/I_G starts to decrease above 450 °C until the D band nearly disappears upon reaching 550 °C. In the case of SWCNTs (**Figure 4.6**b), no significant changes in I_D/I_G are observed below 400 °C. However, between 400 and 500 °C, a decrease in I_D/I_G together with a decrease in both D and G band intensity serve as a clear sign for the oxidation of both disordered carbon and CNTs.

As expected, we found a linear downshift with temperature for both D and G bands. DWCNTs exhibit different frequency shifts of peaks giving rise to the G band Raman signal (**Figure 4.7**a). Our experiments using a 633 nm wavelength excitation exhibit a downshift of 0.029 cm^{-1}/°C for 1568 cm^{-1} and 1525 cm^{-1} peaks, which were fitted as one peak at 1550 cm^{-1}

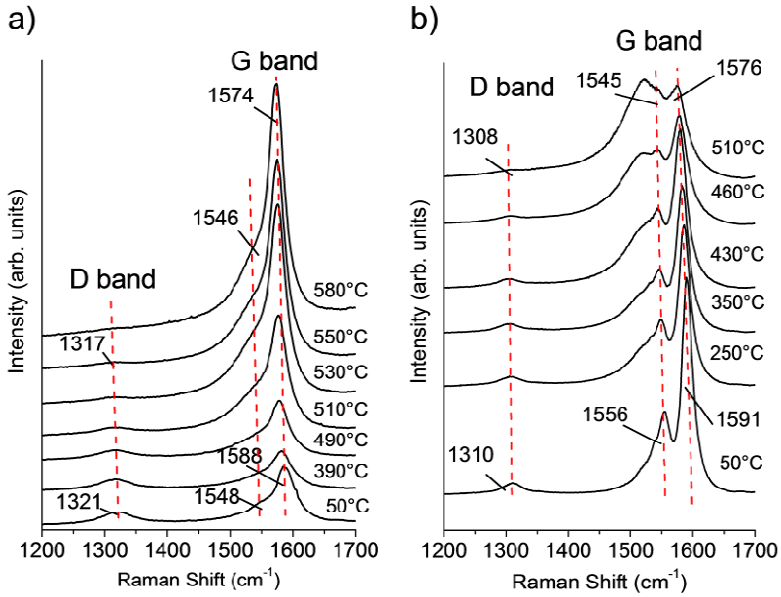

Figure 4.6: In situ Raman spectra of DWCNTs (a) and SWCNTs (b) during nonisothermal oxidation in air (Ref. 322). Spectra were recorded using a 633 nm excitation wavelength.

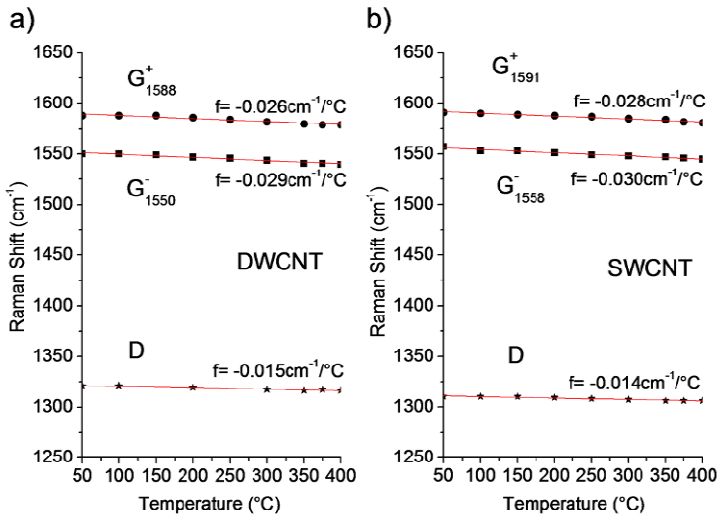

Figure 4.7: Comparison of temperature-induced frequency shifts of the D, G^+ and G^- bands of DWCNTs (a) and SWCNTs (b) recorded using 633 nm laser excitation (Ref. 322).

and a value of 0.026 $cm^{-1}/°C$ for the peak at 1588 cm^{-1}. Oxidation of SWCNTs (**Figure 4.7**b) yields downshifts of 0.030 $cm^{-1}/°C$ for the G^- peak around 1558 cm^{-1} and 0.028 $cm^{-1}/°C$ for the G^+ peak at 1591 cm^{-1}. Thus, the value of temperature-induced shifts of the G band frequencies in the DWCNTs Raman spectra is between the values of SWCNTs and graphite (0.024 $cm^{-1}/°C$), as expected.[325]

The temperature-dependencies of the D band vary slightly for SWCNTs and DWCNTs and are ~ 0.014 $cm^{-1}/°C$ and ~ 0.015 $cm^{-1}/°C$, respectively, which is in agreement with published data.[326]

The origin of the observed behavior of D and G bands in the case of DWCNTs can be explained by the removal of disordered carbon, which shields the Raman signal of the CNTs. The SWCNT sample, showing no increase in G band intensity, contains less amorphous carbon compared to DWCNTs. Since the SWCNTs were purified after synthesis, we attribute the observed D band intensity to defects in the wall structure of the

nanotubes, rather than amorphous carbon. This assumption is supported by the fact that D and G bands behave in a similar manner at temperatures above 400 °C. Changes in the RBM range of the SWCNTs after oxidation also affirm this hypothesis (**Figure 4.5**b). Small diameter tubes showing higher RBM frequencies start to decrease in intensity at elevated temperatures or even disappear after oxidation.

4.1.2.3 Selective Oxidation of Small-Diameter Carbon Nanotubes.

An increase in the Raman intensity of CNTs was generally observed at about 400 °C, the temperature range where disordered carbon is oxidized. A subsequent decrease in intensity of the G band at higher temperatures is due to the oxidation of CNTs, starting with the smallest tubes as discussed in section 4.1.2.1. Even after oxidation at temperatures above 500 °C, the RBMs do not always show significant changes. We therefore assume that changes in the structure and composition of the sample above 500 °C strongly depend on the duration of oxidation, the temperature, as well as the measured sample spot. The oxidation was never completed and usually stopped at different temperatures between 550 and 600 °C when the Raman signal of carbon was still recordable.

Figure 4.8 shows the *in situ* Raman analysis of the low frequency RBM range for DWCNTs, acquired using three different laser excitation wavelengths. The intensity of the peaks between 220 and 280 cm^{-1} decreases constantly during heating from room temperature to 400 °C (**Figure 4.8**a). Since there are no observable changes in the D and G band shape or intensity, the differences cannot be attributed to structural changes or selective oxidation of CNTs. However, RBM frequencies are strongly related to the electronic band structure through the resonance effects. Therefore, temperature-induced changes in electronic density

of states may affect the intensity of the RBM signal at elevated temperatures and lead to the observed temperature-dependence.

In situ measurements during heating of DWCNTs at 5 °C/min up to 400 °C, directly followed by cooling to room temperature, show certain RBM peaks decreasing and increasing in intensity while the sample is heated or cooled. The observed changes are completely reversible and somewhat different for frequencies originating from nanotubes with different diameters or when using different excitation wavelengths. Changes in the intensity distribution of the RBM range can thus be caused not only by changing the laser wavelength, but also by changing temperature. This is an important finding, considering the fact that laser-induced sample heating is most likely to occur during Raman analysis of carbon nanomaterials.

It should be mentioned that there is also a temperature-induced downshift in the RBM frequencies. The shift is only noticeable for some RBM peaks (**Figure 4.8**), and it is less

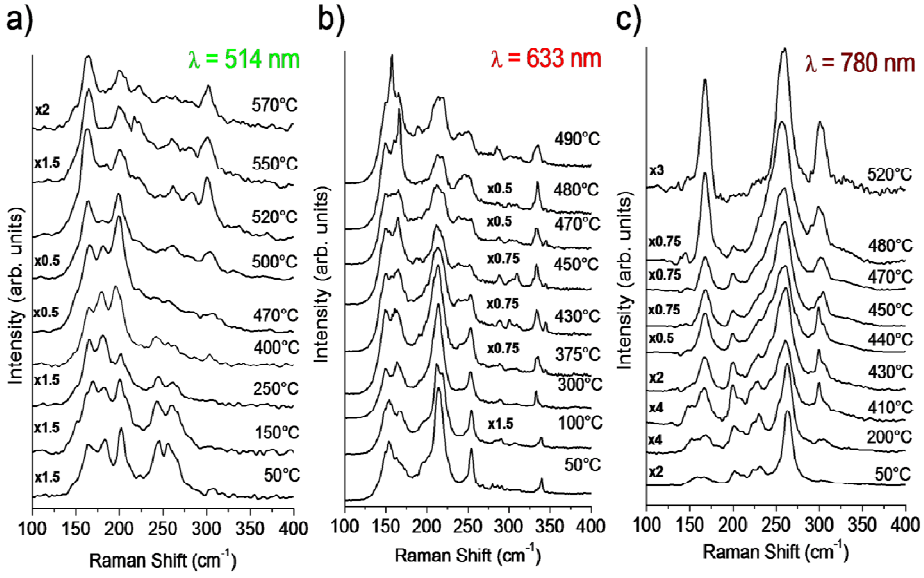

Figure 4.8: Multiwavelength Raman spectra of DWCNTs recorded in situ using a 514 (a), 633 (b) and 785 nm (c) laser excitation (Ref. 322). Different laser wavelengths lead to different RBM spectra due to resonant enhancement effects.

pronounced than that observed for D and G bands. Since the comparison of the RBM spectra of DWCNTs before and after heating shows no significant changes (**Figure 4.5**a), we assign the effect of varying RBM intensities during heating (**Figure 4.8**) to the temperature effect on the C=C bonding. Although the influence of the oxidation of CNTs on the RBM intensity seems to be negligible below 500 °C, it increases and dominates the *in situ* Raman spectra at higher temperatures (550 - 600 °C).

The *in situ* RBM Raman spectra of DWCNTs show the highest intensities in the temperature range between 450 and 500 °C (**Figure 4.8**). In this temperature range, the G band also reaches a maximum intensity while the D band disappears (**Figure 4.6**). The small amount of amorphous carbon within the as-received DWCNT sample shields RBM-Raman scattering similar to the G band Raman signal. Thus, the intensity of the RBMs and the G band exhibit similar behavior and removal of amorphous carbon by oxidation leads to an increase in the Raman scattering intensity of DWCNTs in general. After reaching a maximum around 500 °C, the RBM intensity decreases due to the oxidation of carbon nanotubes. Furthermore, it can be seen that after reaching temperatures above 400 °C, the intensity of several RBM peaks between 300 and 350 cm^{-1} starts to increase (**Figure 4.8**a and c). This effect can be explained by the oxidation of outer tubes and the increase in the detection of the Raman scattering of the smaller inner tubes exhibiting higher RBM frequencies. Inner tubes are not oxidized before the outer ones are damaged or destroyed. The oxygen molecules can not go through the outer walls, and thus they unable to reach the carbon atoms inside the closed tubes.

4.1.3 Purification of Carbon Nanotubes by Isothermal Oxidation

In nonisothermal oxidation experiments, the G band does not decrease at temperatures below 480 °C, suggesting that oxidation of CNTs does not occur, while amorphous carbon can be removed well below this temperature. However, these experiments did not provide information about the kinetics of the process or the minimal temperature requirement for the removal of amorphous carbon. To understand the kinetics of oxidation, a treatment under isothermal conditions was used. **Figure 4.9**a shows changes in I_D/I_G as a function of

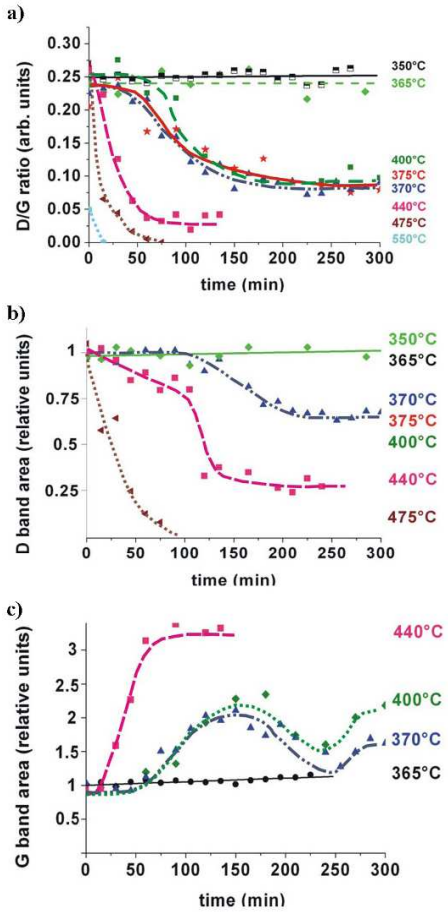

Figure 4.9: Results of isothermal oxidation of the DWCNTs showing the I_D/I_G ratio (a), relative D band intensity (b), and relative G band intensity (c) as a function of the oxidation time at different temperatures (Ref. 322). Spectra were recorded using a 633 nm excitation wavelength. The curves for 350 and 365 °C in (b) are superimposed, and idem for 370, 375 and 400 °C.

the oxidation time. Below 365 °C no changes are observed and neither amorphous carbon nor other carbon species appear to oxidize under these conditions. This is in agreement with **Figure 4.9**b, which shows no changes in the D band area (integrated intensity) below 365 °C. The same behavior can be observed while looking at the G band area. The activation energy needed for breaking the carbon bonds is not provided below that temperature (see section 4.3.1). The first changes in I_D/I_G are observed at 370 °C (**Figure 4.9**a). In these experiments, the ratio decreased from ~ 0.25 to approximately 0.08. The ratio starts to decrease after the 20 - 50 minutes incubation period, which may be required for oxygen chemisorption or the removal of functional groups from the carbon surface, reaches the final value of 0.08 after 220 - 240 minutes and does not show further changes with time. In the range of 370 - 400 °C, similar changes in I_D/I_G are observable, suggesting that only the amorphous carbon is oxidized and the nanotubes are not affected by oxidation. The incubation period disappears and I_D/I_G decreases further to zero after a relatively short time as the processing temperature increases from 440 to 550 °C. Defective and small-diameter CNTs are oxidized in this temperature range leading to the disappearance of the D band. To determine the exact reason for the decrease in I_D/I_G, both the D and G bands must be investigated separately. In the case of 370, 375 and 400 °C, the D band area shows behavior similar to I_D/I_G. The relative value of the D band decreases to about 35% of its original value, while I_D/I_G decreases by ~ 65%. An explanation for the difference can be seen in **Figure 4.9**c. The decrease of the D band intensity is closely related to a large increase in the G band area. Between the 50^{th} and 150^{th} minute, a small decrease in the D band area (10 - 15%) is accompanied by a doubling of the G band area, ending in a large decrease of I_D/I_G. After about 150 minutes, both the G band area and I_D/I_G reach a maximum and minimum,

respectively. The subsequent decrease of the D band changes I_D/I_G significantly since the G band area and intensity are decreasing as well. The isothermal oxidations at 440, 470 and 550 °C exhibit a different behavior (**Figure 4.9**a): I_D/I_G starts to decrease during heating since oxidation of the amorphous carbon starts before reaching the final temperature. However, 440 °C is not high enough to eliminate the D band in the DWCNTs, but the final I_D/I_G value (0.04) is much lower than the values for 370, 375 and 400 °C. Analysis of **Figure 4.9**b and c leads to the conclusion that, along with the amorphous species, smaller and defective tubes are oxidized, resulting in an additional decrease in the D band area at 440 °C (**Figure 4.9**b), compared to isothermal experiments at temperatures between 370 and 400 °C. Please note that the lines for 350 and 365 °C can be superimposed, and the curves obtained at 370, 375 and 400 °C are almost identical. The significant increase of the G band intensity (**Figure 4.9**c) can be explained by the fact that the observed G band Raman signal comes mostly from tubes of a particular diameter range, due to resonant effects. Thus, oxidation of smaller tubes results in a higher percentage of resonantly enhanced nanotubes. Temperatures above 480 °C lead to the total oxidation of DWCNT samples, showing elimination of D band and time-dependent G band decrease.

Figure 4.11 supports these assumptions. For oxidation temperatures between 350 and 370 °C the RBM frequency ranges show similar shapes and intensity ratios between the peaks within the Raman spectrum, indicating that no nanotube structures are damaged or removed by oxidation. Temperatures above 440 °C lead to changes in the peak shape and intensity ratios of both, the G band and RBM modes, induced by the oxidation of tubes with different diameters (**Figure 4.11**). The D band intensity shows no decrease for temperatures below 370 °C, while the decrease is similar for temperatures between 370 and 400 °C where

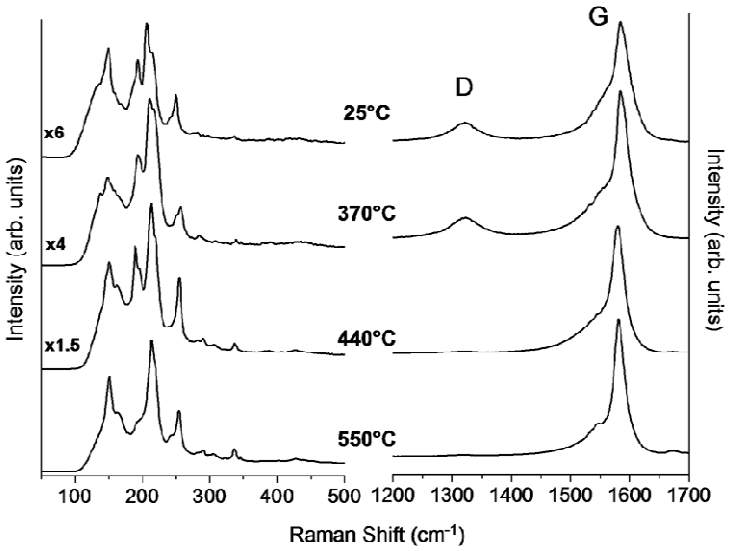

Figure 4.11: The first-order Raman spectra of DWCNTs after isothermal oxidation for 5 h at different temperatures, recorded at room temperature using 633 nm laser excitation (Ref. 322).

it reaches a final value of 65% of its original value (**Figure 4.9**b). Above 440 °C the final D band intensity, at the completion of the oxidation treatment, depends on the process temperature. Thus, the temperature range for the heating-induced purification of DWCNTs, with respect to the amorphous carbon, is between 370 and 400 °C. These results show that it is possible to develop an effective temperature-dependant oxidation method for nanotubes with different diameters and structural perfection.

Oxidation of larger amounts of DWCNTs using a furnace under similar conditions (**Figure 4.12**a) demonstrates the feasibility of scaling up the process. The furnace oxidation at 375 °C for 300 minutes showed a similar decrease in I_D/I_G as after the heating stage experiments. A similar furnace experiment at 360 °C shows no changes in the D band intensity, nor in I_D/I_G. Thus, the temperature range between 370 and 400 °C provides the optimal conditions for purification of the investigated DWCNTs.

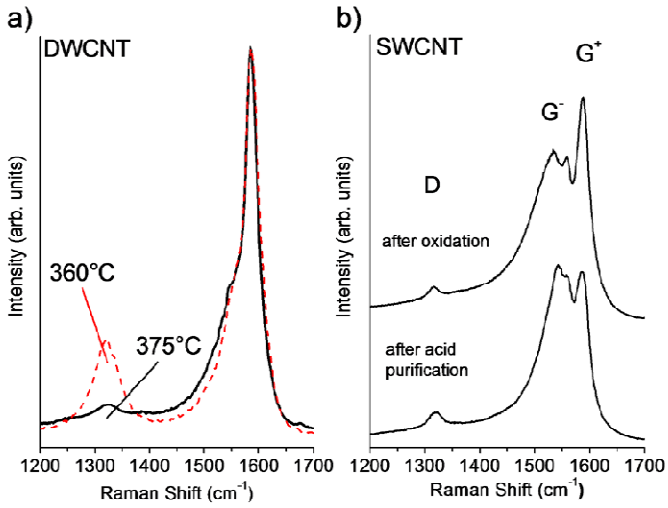

Figure 4.12: Raman spectra of (a) DWCNTs after air-oxidation in a tube furnace for 5 h at 360 °C (dashed line) and 375 °C (solid line), and (b) SWCNTs after nonisothermal oxidation and washing in hydrochloric acid at room temperature for 24 h (Ref. 322).

Figure 4.12b shows the comparison between the air-oxidized and acid-treated[310] SWCNTs. The air-oxidation leads to a lower I_D/I_G ratio, which decreased from its original value of 0.07 to 0.02 after oxidation, compared to the increased value to 0.11 after acid treatment. Thus, isothermal oxidation of CNTs is a promising method of purification with respect to the removal of non-tubular carbon and defective tubes.

Figure 4.13 shows HRTEM images of the DWCNT samples before oxidation (a,b), after oxidation (c,d) and after additional acid treatment (e,f) commonly used to remove catalyst particles from the sample. Two adjacent images are shown for each sample at high and low magnification, respectively. **Figure 4.13**b shows that some amorphous carbon is present in the sample before oxidation, typically at the surface of the nanotubes. However, it should be be noted that **Figure 4.13**b is not representative of the whole sample, which shows a high purity and only traces of amorphous carbon. After the oxidation (**Figure 4.13**c and d), the disordered carbon is completely removed and only catalyst particles are left next

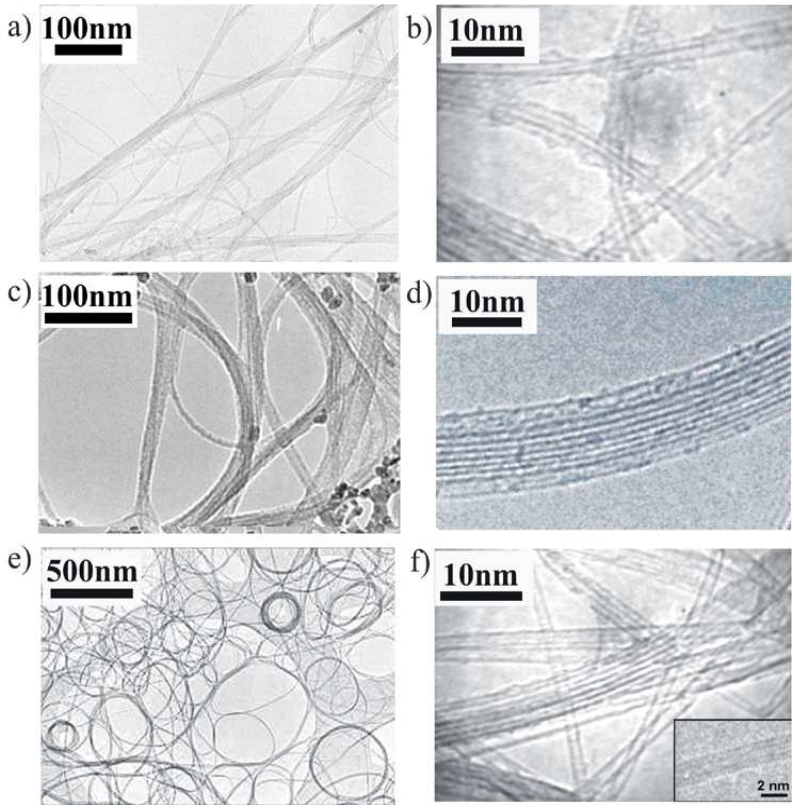

Figure 4.13: Low-resolution (left panel) and high-resolution (right panel) TEM images of the DWCNT sample (a,b) before, (b,c) after oxidation and (e,f) after oxidation followed by acid treatment to remove the catalyst (Ref. 320).

to the nanotubes. These oxide particles are larger than the initial nanometric metal catalytic particles due to coalescence and likely volume increase upon oxidation. Also, the content of particles in the sample (relative to the nanotubes) increases after heating to 600°C, as expected. While HRTEM does not provide statistically reliable data on the content of defects in the tube walls, it clearly shows that the oxidized tubes are not defect-free (**Figure 4.13**d) and do not look more perfect compared to the nonoxidized DWCNTs (**Figure 4.13**b). The wall defects, which are expected to include oxygen-terminated carbons, should provide highly reactive sites on the CNTs. Defect-formation and oxidation-based functionalization of CNTs will be discussed in the following section. However, these defects

did not cause a double-resonance effect and did not produce a D band in Raman spectra, suggesting presence of primarily metallic CNTs (**Figure 4.1**b). An acid treatment for removing the catalyst particles following the oxidation (**Figure 4.13**e and f) leads to a very pure and clean sample containing neither catalyst particles nor amorphous carbon, only DWCNTs ready for use.

While the weight loss after heating to 600 °C was significant, further heating experiments in air have shown that complete removal of disordered carbon leading to disappearance of D band can be achieved by a long-term isothermal treatment at temperatures below 400 °C, at a much smaller weight loss.

4.1.4 Defect Formation and Functionalization of MWCNTs

4.1.4.1 Raman Spectra of As-Received and Graphitized MWCNTs

Figure 4.14 shows the Raman spectra of as-received and vacuum-annealed (at 1800 °C for 3 h) MWCNTs.[327] Both spectra were normalized with respect to the D band intensity for comparison purposes. Thus, only statements about relative intensity changes can be made. The Raman spectrum of the as-received MWCNTs (**Figure 4.14**a) was fitted using two Lorentzian peaks at 1330 cm^{-1} (D band) and 1581 cm^{-1} (G band), and a Gaussian peak at 1615 cm^{-1} (D' band), with a full-with at half maximum (FWHM) of 54.9, 45.6 and 27.9 cm^{-1}, respectively (**Table 4.1**). The G and D' bands show a clear separation. Due to inhomogeneities in the size of the tubes, a varying defect density, tube bundling and a rough sample surface, values between 1581 and 1584 cm^{-1} were observed for the G band

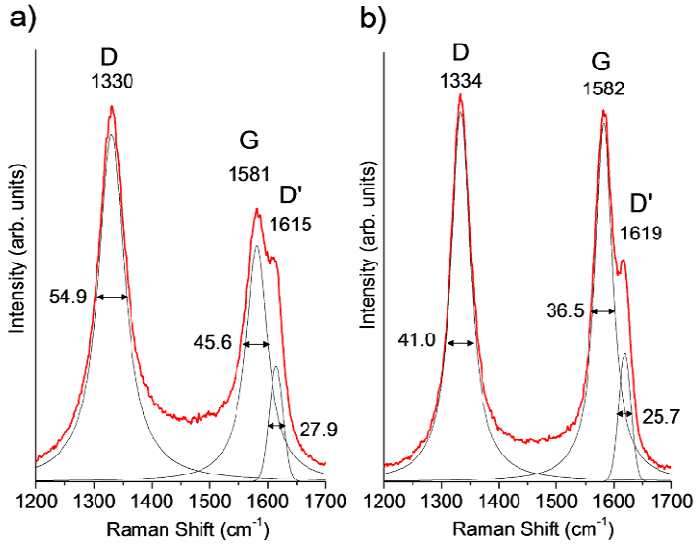

Figure 4.14: Raman spectra of as-received (a) and graphitized (b) MWCNTs (Ref. 327). The peak position and FWHM are indicated.

frequency. The I_D/I_G ratio of the as-received MWCNTs shows a value of ~ 1.8. For the same inhomogeneity reasons, I_D/I_G values ranged from 1.4 to 2.1.

The Raman spectrum of the graphitized MWCNTs (**Figure 4.14**b) shows similar, but more narrow features: the D band at 1334 cm^{-1} (Lorentzian), G band at 1582 cm^{-1} (Lorentzian), and D' band at 1619 cm^{-1} (Gaussian) with FWHM of 41.0, 36.5 and 25.7 cm^{-1}, respectively (**Table 4.1**). The graphitized MWCNTs exhibit a lower I_D/I_G value with an average of ~ 1.1. The D' band is more distinguishable after annealing, due to a peak

Table 4.1: Comparison of the spectral parameters in the Raman spectra of as-received and oxidized MWCNTs treated in different environments.

	D band		G band		D' band		I_D/I_G
	Position [cm^{-1}]	FWHM [cm^{-1}]	Position [cm^{-1}]	FWHM [cm^{-1}]	Position [cm^{-1}]	FWHM [cm^{-1}]	
As-received	1330	54.9	1581-1584	45.6	1615	27.9	1.8
Graphitized	1334	41.0	1582	36.5	1619	25.7	1.1
Air-oxidized (¼ h @ 550°C)	1333	46.7	1583	41.7	1618	25.4	2.1
Acid-oxidized (24 h in HNO_3)	1330	59.8	1584	51.4	1614	26.4	2.5

sharpening and a wavenumber up-shift. Since I_D/I_G can be used as a measure of the graphitic nature of carbon materials, we conclude that vacuum annealing (at 1800 °C for 3 h) improves the structural order and the purity of the MWCNTs sample. A lower FWHM of D and G bands in the spectrum of the graphitized MWCNTs confirms this assumption.

While I_D/I_G changes upon graphitization, the D' intensity remains almost constant. The D' vibrational mode, which does not exist in pure graphite, is observed with a high intensity in intercalated graphite compounds.[237,238] It has been assigned to the in-plane vibrations of the outer parts of graphite domains. We can conclude that the small coherent vibrational domains in the direction perpendicular to the MWCNTs walls enable this mode. Therefore, from a statistical point of view, adding more defects might not change this coherent length or at least not enough to observe it in the Raman spectra. The spectrum from annealed MWCNTs shows a constant value from point to point of the G band's position (at ~ 1582 cm^{-1}), indicating an increased structural uniformity. Indeed, the as-received sample consists of nanotubes with some structural defects and amorphous carbon sitting on the outer walls which are removed by annealing.

Although vacuum annealing at ~ 1800 °C improves the crystallinity and decreases the local defect concentration of the tubes, some defects still remain. Only upon an additional increase in temperature do graphitic layers become straighter and more continuous, but polygonization occurs.[131] Thus, annealing below 2000 °C removes amorphous carbon and catalytic particles from the MWCNTs, without damaging the tubular structure. The method provides many advantages compared to a chemical purification because it allows the complete removal of metal impurities, including particles trapped inside the tubes. Metal-free nanotubes are desired for many applications, especially biomedical ones in which high

purity and defined surfaces are required. HRTEM studies (not shown) on as-received and vacuum-annealed MWCNT confirmed these results.[327]

4.1.4.2 Isothermal and Nonisothermal Oxidation in Air

Due to their larger diameters, MWCNTs experience smaller curvature-induced strain on the C=C bonds. Thus, the resistance to oxidation increases, leading to higher activation energies and oxidation temperatures compared to SWCNTs and DWCNTs. In order to determine the temperature range for the oxidation of the as-received and graphitized MWCNTs in air, we performed TGA for both samples (**Figure 4.15**a). The graphs are normalized by the sample weight measured at 200 °C. At this temperature, only water and adsorbed species are removed from the tube surface, but oxidation of carbon does not occur. **Figure 4.15**a shows that the oxidation of the as-received MWCNTs begins at 440 -

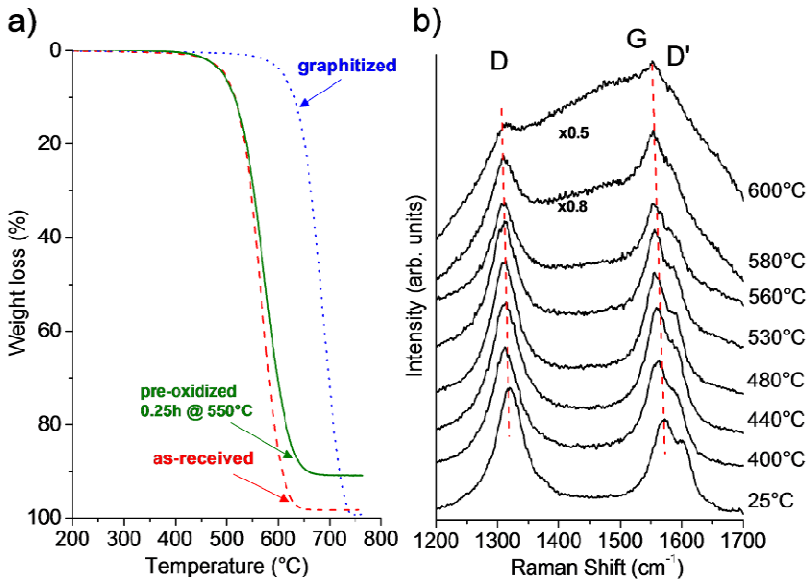

Figure 4.15: Weight loss curves (TGA) of as-received, air-oxidized and graphitized MWCNTs (a) and *in situ* Raman spectra of oxidation (non-isothermal) of as-received MWCNTs (b). Graph obtained from Ref. 327.

450 °C, reaching a maximum sample loss rate around 550 °C. The remaining residue of ~ 2 wt% results from iron inclusions, which form iron oxide and remain after oxidation of MWCNTs.

Graphitized MWCNTs are more resistant against oxidation than as-received MWCNTs, and no oxidation-induced weight loss is observed below ~ 550 °C. The improved thermal stability results from the lower defect density and the removal of iron inclusions. The oxidation takes place between 600 and 750 °C, while the maximum weight loss rate occurs around 685 °C. The entire sample is lost at 750 °C, while no iron oxide can be found, indicating successful purification by vacuum annealing. A more detailed analysis of the oxidation kinetics and activation energies of as-received and graphitized MWCNTs is presented in section 4.3.1.

Due to prior purification steps, the as-received MWCNTs from Arkema do not contain large amounts of amorphous carbon, and we can assume that the D band intensity mainly results from structural defects in the tubes. Note that the inherent fluctuations in the D band intensity overshadow small oxidation-induced intensity changes. Such fluctuations were observed in each experiment and result from heat-induced sample drift and the sample inhomogeneities mentioned above.

The *in situ* studies showed a linear wavenumber downshift with increasing temperature for all bands (**Figure 4.15**b). The measurements exhibit a downshift of ~ 0.017 cm^{-1}/°C for D, ~ 0.025 cm^{-1}/°C for G, and ~ 0.028 cm^{-1}/°C for D'. As expected, the value of the temperature-induced shift of the G band of MWCNTs is between the values of SWCNTs (0.03 cm^{-1}/°C) and DWCNTs (0.026 cm^{-1}/°C) and high purity graphite (0.024 cm^{-1}/°C). It should be mentioned that the downshift may also be influenced by laser-induced heating. The *in situ* measurements showed no significant change in I_D/I_G below ~ 450 °C (**Figure**

4.15b). The intensities of D and G bands started to decrease simultaneously between 450 and 500 °C, while I_D/I_G showed almost no variation indicating a general sample loss without change in ordering (**Figure 4.15**b). A further temperature increase to ~ 600 °C speeds up the oxidation reaction and increases the sample loss. As expected, *in situ* experiments with graphitized MWCNTs showed similar temperature-induced wavenumber shifts, but no considerable change in the intensity of the Raman bands below 600 °C due to the absence of catalyst particles. This is in sound agreement with the TGA results shown in **Figure 4.15**a.

To further improve the control over the creation of defects, isothermal oxidation experiments were performed. **Figure 4.16**a shows the Raman spectra of MWCNTs after isothermal oxidation for 5 h at 400, 430, 460, 500 and 530 °C in static laboratory air. The spectra were recorded at room temperature after the treatment, normalized with respect to

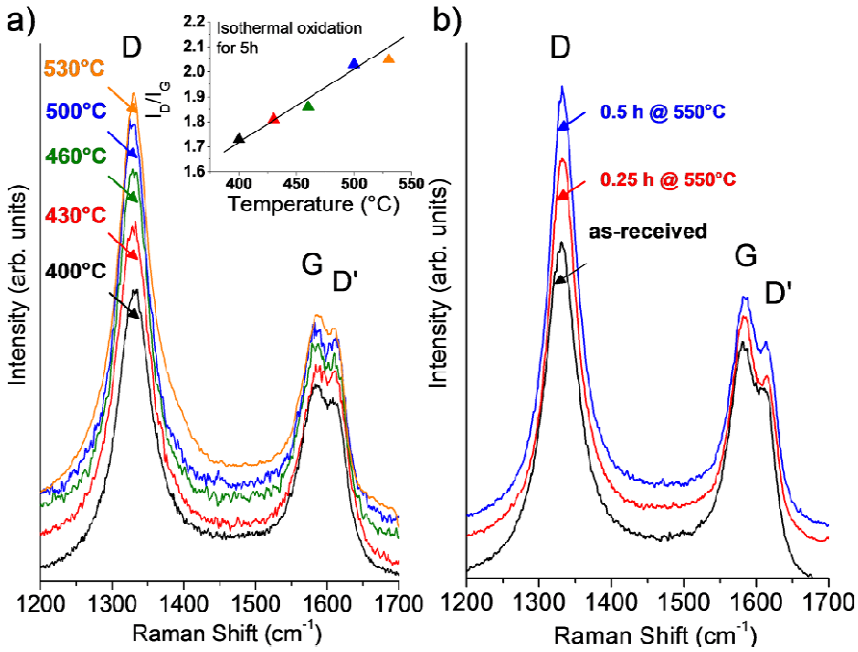

Figure 4.16: a) Raman spectra of MWCNTs after isothermal oxidation at different temperatures in air, recorded at room temperature. The inset shows changes in the I_D/I_G ratio as a function of oxidation temperature. b) A "flash oxidation" allows a similar increase in I_D/I_G, but without a significant loss of the sample. Raman spectra were obtained from Ref. 327, and recorded using 633 nm laser excitation.

the G band intensity, and displayed with a slight offset for clarity. The Raman spectrum of the nanotubes oxidized at 400 °C is similar to that of the as-received tubes, with a slightly lower I_D/I_G of ~ 1.75. This decrease results from the removal of the amorphous carbon layer at the MWCNTs surface, without oxidizing or damaging the MWCNTs. From 430 to 530 °C, the oxidation reactions occur at the most reactive sites, i.e. the tube ends (**Figure 4.16**a). The graphitic order of the nanotubes is reduced, resulting in an increase in I_D/I_G up to 2.05 at 530 °C. The analysis of the spectra showed that I_D/I_G increases almost linearly with temperature between 400 and 530 °C (inset in **Figure 4.16**a). No further increase was observed after 530 °C and the sample loss after 5 h was very large. Although isothermal measurements allowed a controlled change in I_D/I_G, the overall sample loss after 5 h oxidation was too high and unacceptable for industrial applications. Thus, in the following section, we report another approach consisting of a "flash oxidation" using a short treatment at high temperature. This approach allowed the creation of defects uniformly distributed over the tube surface, without a significant weight loss. At high temperatures, structural defects should be created simultaneously everywhere on the nanotubes surface, but the quick cooling inhibits further damage in the nanotubes' structure.

Figure 4.16b shows the Raman spectra of the as-received MWCNTs oxidized for 15 min and 30 min at 550 °C. I_D/I_G increases from 1.8 to 2.1 (15 min) and 2.3 (30 min). Thus, the values of I_D/I_G after a short term oxidation at 550 °C are equal or higher than that after 5 h at 530 °C (I_D/I_G ~ 2.05). This might be related to a higher defect density and a lower sample loss (< 10 wt%).[131] We can conclude that a "flash oxidation" is a promising method to introduce defective sites into MWCNTs.

To determine the thermal stability of the MWCNTs oxidized using the "flash oxidation" method, TGA studies were performed. The pre-oxidized MWCNTs (15 min at 550 °C) behaved similarly to the as-received nanotubes (**Figure 4.15**a). In both cases, the oxidation starts at 440 - 450 °C. Note that the pre-oxidized sample shows a larger remaining weight due to the higher iron content. Indeed, since some carbon is removed during the prior oxidation, the resulting iron concentration is higher. However, the thermal stability is not affected by this higher iron content. This can be explained by the fact that the maximum catalytic effect of iron is reached at approximately 1 - 3 wt%, while a further increase in the iron concentration does not affect the reaction kinetics.[328,329] This iron can be removed by a subsequent HCl treatment.

4.1.4.3 Surface Chemistry of Oxidized MWCNTs

Figure 4.17 shows the FTIR spectra of as-received and air-oxidized MWCNTs, in comparison to an acid-treated MWCNT sample (8 h at 75 °C in HNO_3). The main features in the FTIR spectra of as-received tubes result from O-H vibrations (3280 - 3675 cm^{-1} stretch and 1640 - 1660 cm^{-1} bend) which are assigned to -O-H groups of adsorbed water or covalently bonded functional groups. Since traces of water remaining in the KBr pellets could not completely be removed, even though extensive heating before the measurement (24 h at 100 °C) had been performed, we assume that a majority of the O-H vibrations originate from water in the sample rather than functional groups attached to the surface of the MWCNTs. The FTIR spectra of air-oxidized and acid treated MWCNTs show some additional features. The broad band at ~ 1730 cm^{-1} results from the C=O stretching vibrations of carboxyl and carbonyl groups. The origin of the band at 1566 cm^{-1} is still

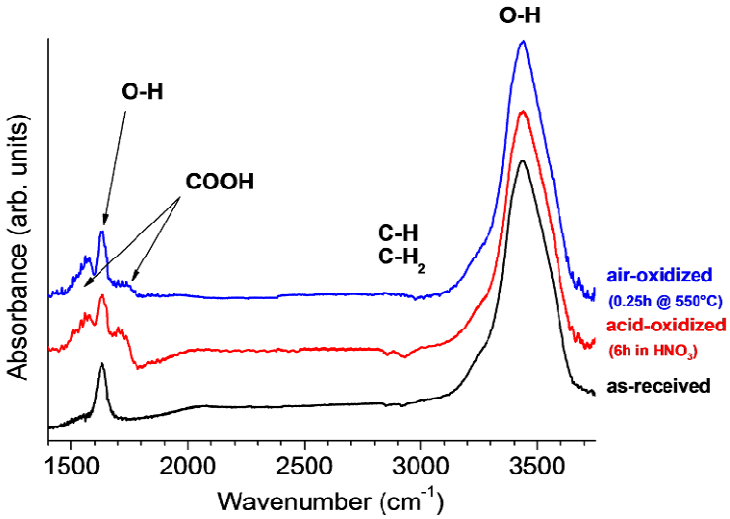

Figure 4.17: FTIR spectra of as-received, air-oxidized and acid-treated MWCNTs (Ref. 326). The assigned functional groups are indicated.

controversial.[330-332] Some authors believe that the band results from the in-plane vibrations of the graphitic walls in carbon nanotubes.[333,334] Others suggest that the spectral features between 1540 and 1590 cm^{-1} are also related to carboxyl[335] and carbonyl groups.[336] Our experiments support the latter assumption. Indeed, the IR band at 1566 cm^{-1} was always accompanied by the 1730 cm^{-1} band, while it did not appear in the FTIR spectrum of the untreated as-received MWCNTs. The FTIR analysis of carbon samples is very complex and strongly depends on the sample itself, the treatments, and the experimental environment. These circumstances lead to spectral variations. However, FTIR studies showed some distinct differences between the as-received and treated MWCNTs. Both, air-oxidized and acid treated samples show the presence of C=O bond vibrations, while they were not observed for as-received MWCNTs. Thus, the FTIR analysis further proves the existence of defects in the walls of the nanotubes and the subsequent formation of functional groups.

4.2 *In situ* Raman Spectroscopy of Oxidation of Nanodiamond

The presence of large amounts of non-diamond carbon in detonation synthesized nanodiamond (ND) severely limits a large number of applications of this exciting nanomaterial. In this section we investigate the potential of air oxidation to selectively remove sp^2 bonded carbon from ND powders and introduce a simple, efficient and environmentally-friendly route to purify ND powders. The oxidized ND powders will then be used to improve the in-depth understanding of Raman spectra of ND and analyze in detail the effects of surface functional groups (sections 4.5) and crystal size (section 4.6).

4.2.1 *In situ* Analysis and UV Raman Characterization

4.2.1.1 Raman Spectra of As-Received Nanodiamond Powders

The most conventional excitation source for Raman spectroscopy, a 514 nm Ar laser (green line), is known to cause a strong fluorescence during the analysis of ND samples. Compared to visible Raman, UV-Raman analysis offers a stronger diamond signal due to the resonance enhancement effect.[281] We therefore decided to focus our efforts on using UV (244 and 325 nm) excitations for the analysis of ND powders.

The UV Raman spectra of three ND powders are shown in **Figure 4.18**.[121] UD50 exhibits the characteristic Raman features of graphitic carbon: the G band at ~ 1590 cm^{-1} and the disorder-induced D-band at ~ 1400 cm^{-1}. The Raman signal of diamond cannot be observed. Because of the high content of graphitic carbon and its larger Raman scattering cross-section compared to diamond, the Raman spectrum of UD50 is dominated by the Raman features of sp^2-bonded carbon (D and G bands), which overshadow the diamond

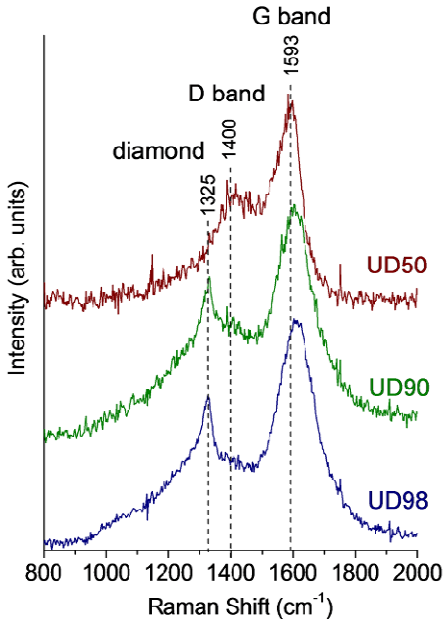

Figure 4.18: UV Raman spectra of three ND powders recorded using 325 nm laser excitation (Ref. 121). UD50 is the detonation soot, UD90 and UD98 were purified using multi-stage acid treatments.

band. In addition, fullerenic shells enclose the diamond crystals and further weaken their Raman signal. The Raman spectra of UD90 and UD98 are similar to each other and are both noticeably different from UD50. They show an asymmetrically broadened diamond peak at ~ 1325 cm^{-1} with a shoulder towards lower wavenumbers, and a broad, asymmetric peak with a maximum at 1640 cm^{-1}. While the peak at 1590 cm^{-1} in the case of UD50 can be identified as G band of graphitic carbon, the assignment of the peak at 1620 cm^{-1} observed in UD90 and UD98 as well as in many other ND samples reported in literature[266,298,337,338] is not straightforward and will be discussed in section 4.4.2. An overview on the sample composition of UD50, UD90 and UD98 is given in **Table 2.2**.

4.2.1.2 *In Situ* Studies and UV Raman Spectroscopy Characterization

In order to determine the appropriate temperature range for the selective oxidation of sp^2 carbon, nonisothermal TGA was performed in air. **Figure 4.19** compares the oxidation behavior of UD50, UD90 and UD98, and shows differences in the oxidation rate and the temperature at which the maximum weight loss occurs. At temperatures below 375 °C, the

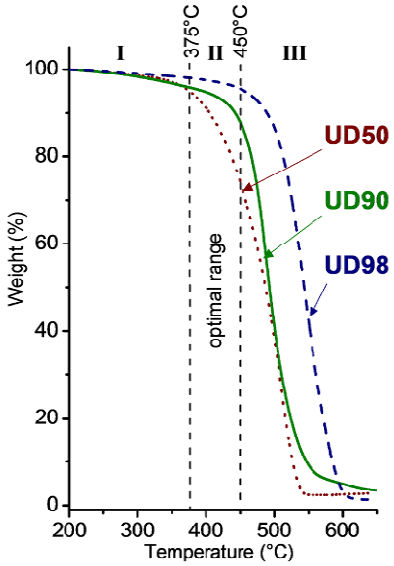

Figure 4.19: Nonisothermal TGA of ND samples in air (Ref. 121).
The graphs are normalized by the sample weight at 200 °C.

oxidation is inhibited or its rate is too low to allow noticeable removal of carbon within a reasonable time frame (range I). At temperatures above 450 °C, all kinds of carbon in the sample, including amorphous, graphitic, and diamond phases are quickly oxidized (range III). In the intermediate temperature zone (range II), the oxidation rate shows substantial differences between the samples: while the mass of relatively pure UD98 does not change noticeably, UD50 with a substantial graphitic content (see **Table 2.2**) shows a significant weight loss.

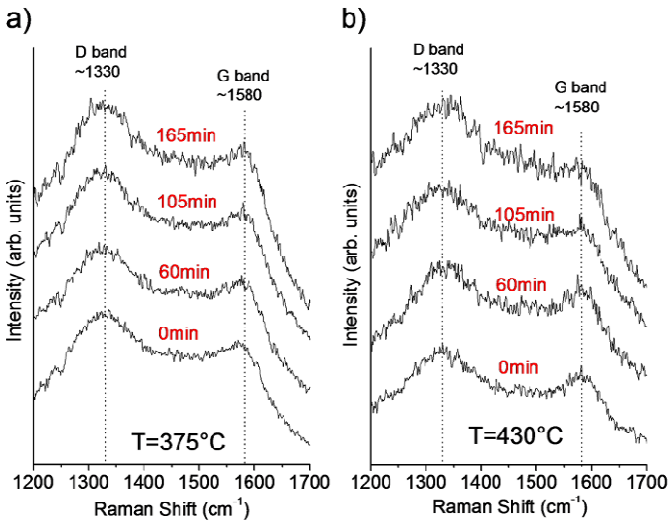

Figure 4.20: *In situ* Raman spectra of oxidation of ND (UD50) under isothermal conditions for 3 h at 375 (a) and 430 °C (b), respectively, recorded using 633 nm laser excitation.

Figure 4.20 shows the results of *in situ* Raman studies during isothermal oxidation of UD50 for 3h at 375 °C (boundary temperature between range I and II) and 430 °C (within range II) in air. The unpurified ND powder (detonation soot) was chosen because UD50 has a large content of non-diamond carbon and temperature-induced spectral changes during heating are more evident compared to UD90 and UD98. In order to accurately monitor changes in the composition of the sample and to maximize the Raman intensity of amorphous and graphitic carbon, we recorded *in situ* spectra using 633 nm laser excitation. At 375 °C, the boundary temperature between range I and II, no significant changes in the Raman spectra were observed, suggesting the weight loss in range I to result mainly from the removal of adsorbed species, rather than oxidation of carbon. However, at temperatures around ~ 430 °C (range II), a decrease in the G band intensity occurs for longer oxidation times (> 1 h), indicating the removal of graphitic carbon during heating. While these results

can be used to determine the appropriate temperature range for oxidation of sp2 carbons in ND powders, they provide no structural information on the diamond phase.

In order to further optimize the oxidation procedure and avoid damage or loss of ND crystals, we recorded UV Rama spectra of four different UD50 powders oxidized for 5 h at 375, 400, 425 and 450 °C, respectively (**Figure 4.21**a).

As expected, lower oxidation temperatures (< 375 °C) are not sufficient to remove amorphous and graphitic carbon. At temperatures above 450 °C, oxidized powders become inhomogeneous with respect to the ratio of diamond and non-diamond carbon phases. The Raman intensities of the diamond peak at ~ 1325 cm^{-1} and G band at ~ 1600 cm^{-1} vary strongly when comparing the UV Raman spectra recorded at different sample spots (data not shown), suggesting that all types of carbon are oxidized simultaneously leading to an inhomogeneous diamond distribution. When using oxidation temperatures between the extremes (375 - 450 °C), non-diamond carbon can be removed selectively and a significant loss of diamond can be avoided. The Raman spectrum of UD50 oxidized at 400 °C

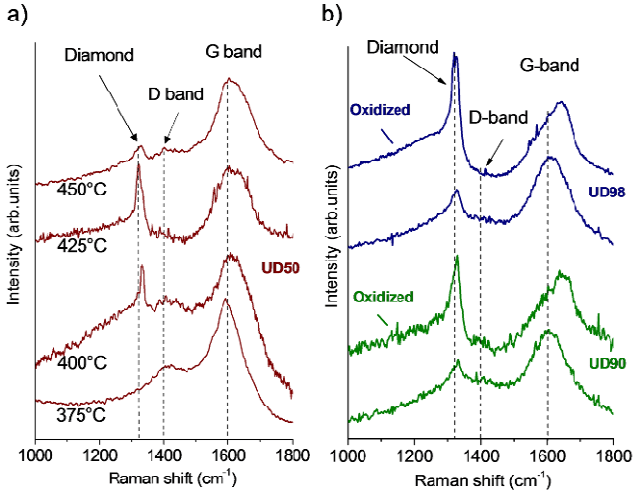

Figure 4.21: UV (325 nm) Raman spectra of UD50 after oxidation at 375, 400, 425 and 450 °C for 5 h in air (a) and comparison of UD90/UD98 before and after oxidation for 5 h at 425 °C (b). Graph obtained from Ref. 121.

demonstrates a substantially enhanced diamond signal. The intensity ratio between the diamond band and the G band in the Raman spectrum of ND reaches a maximum within this temperature range, indicating the best conditions for ND purification, which maximize the diamond content and minimize the amount of both amorphous and graphitic carbon.

While the optimal oxidation temperature could be affected by both the sample composition and the experimental conditions, temperatures within 400 - 430 °C range were found to be most favorable in the present study. Small changes in the oxidation temperature within the given range can be used to find a compromise between the higher purification rate (lower time and costs) and the acceptable weight loss due to minor oxidation of the diamond phase.

Figure 4.21b compares the UV-Raman spectra of UD90 and UD98 before and after oxidation for 5 h at 425 °C in air. The Raman spectra of the as-received UD90 and UD98 show a lower intensity of D-band as compared to UD50 and presence of a diamond peak. The oxidation leads to a significant increase in the relative intensity of the diamond peak in both samples. The determined oxidation conditions were then used to purify larger amounts of ND in a chamber furnace to simulate industrial conditions. The weight loss in these experiments was very close to the amount of sp^2 carbon in the samples (see **Table 4.2**).

While air oxidation evidently removes fullerenic shells and other sp^2-bonded carbon impurities from the samples, it also influences the surface chemistry and may affect shape and position of the Raman peaks. The strong upshift of the G peak to ~ 1640 cm^{-1} in the oxidized samples could be the manifestations of formation of carbonyl oxygen containing functional groups (e.g. ketone) on sp^2 or sp^3-bonded carbon.[339] A similar upshift of the G band was also observed in disordered diamond-like carbon (also called tetrahedral carbon) with a high content of sp^3-bonded carbon, and explained by resonance phenomena.[339]

However we believe that since ND surface atoms account for over 20% of total atoms in ND particles below 5 nm, surface functionalities are responsible for this peak. Both structure and surface terminations of oxidized ND powders are discussed in the following section. The surface chemistry and the effects of functional groups on the Raman spectra of ND will be analyzed separately in section 4.4.

4.2.2 Structure and Surface Terminations of Oxidized Nanodiamond

4.2.2.1 X-ray Absorption Near Edge Structure

XANES allowed us to quantify the sp^3 content in ND samples and learn about their bonding structure. As compared to electron energy loss spectroscopy (EELS), XANES is a more quantitative technique that offers a better spectral resolution, minimizes the sample damage, and allows one to obtain an averaged signal from the macroscopic sample. **Figure 4.22** compares the XANES spectra of graphite, microcrystalline diamond and all ND samples before and after oxidation in air. The spectra of ND exhibit two peaks centered at ~ 285.4 and ~ 286.5 eV, and a broad band absorption with a threshold at ~ 289 eV. The peak at ~ 285.4 eV is assigned to the $1s \rightarrow \pi^*$ transition of sp^2-bonded carbon[340], while the ~ 286.5 eV peak can be related to the chemisorbed oxygen (C=O)[340,341]. Our assignment of this peak is also supported by the correlation of its relative intensity with the intensity of peaks in the second order O K-edge at ~ 272 eV (not shown). The broad peak with an absorption edge at ~ 289 eV is related to the $1s \rightarrow \sigma^*$ transitions. Diamond lacks π^* states and shows an absorption edge at 289 eV ($1s \rightarrow \sigma^*$ of sp^3-bonded C), while graphite shows two absorption edges at 284 eV ($1s \rightarrow \pi^*$) and 291 eV ($1s \rightarrow \sigma^*$ of sp^2-bonded C). The

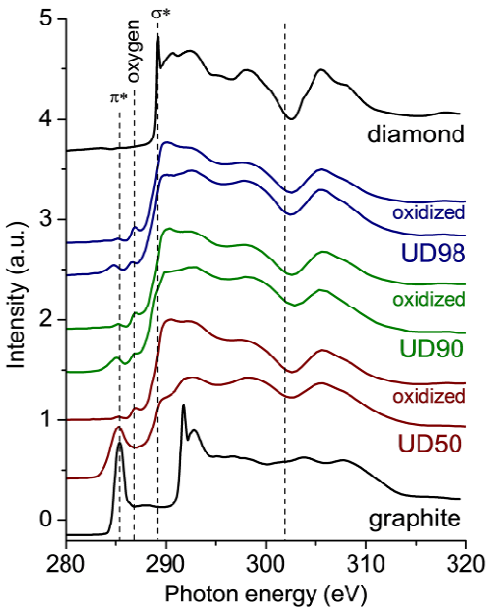

Figure 4.22: C *K-edge* XANES spectra of UD50, UD90, and UD98 before and after oxidation for 5 h at 425 °C in air. Reference XANES spectra of microcrystalline diamond and highly ordered pyrolitic graphite (HOPG) are shown for comparison. Graph obtained from Ref. 121.

oxidation treatment of ND samples resulted in the substantial decrease of $1s \rightarrow \pi^*$ related transitions and a more pronounced second band gap dip of diamond at ~ 302.5 eV, confirming Raman studies previously discussed. Some increase in the oxygen-related peak intensities was also observed.

The relative content of sp^2 and sp^3 sites was calculated by comparing the relative intensity ratios of π^*/σ^* states in ND samples and in HOPG (pure sp^2 carbon) according to:

$$sp^2 content\ (in\%) = \frac{(\pi^*/\sigma^*)_{ND}}{(\pi^*/\sigma^*)_{HOPG}}, \tag{4-2}$$

and

$$sp^3 content\ (in\ \%) = 100\% - sp^2 content\,. \tag{4-3}$$

Table 4.2: Results of the sp^3 content analysis (XANES) of ND samples before and after five hour oxidation at 425 °C in air (Ref. 121).

	UD50	UD50 oxidized	UD90	UD90 oxidized	UD98	UD98 oxidized
sp^3 content, %	23	95	70	94	81	96
sp^2 content, %	77	5	30	6	19	4
sp^3/sp^2	0.3	19	2.3	16	4.3	24

sp^3 diamond (>5μm): 97-97.5%
sp^2 graphite (HOPG): 100%

For the numerical integration, the energy ranges of 282 - 287 eV and 293 - 302 eV were used to represent the π* and σ* states' contributions to the XANES spectra.

The results of the semi-quantitative analysis of sp^3-bonded carbon content in ND samples are presented in **Table 4.2**. Not only did oxidation in air decrease sp^2-bonded carbon impurities in the ND (UD90 and UD98) samples pre-purified by acidic treatment by about five times, but it was also capable of selectively removing graphitic carbon in the soot sample (UD50), thus increasing the sp^3/sp^2 ratio in this sample by nearly two orders of magnitude from 0.3 to 19 (**Table 4.2**). The purity of the oxidized UD98 is comparable to that of microcrystalline diamond. While some authors claimed a high content (> 92%) of diamond in the ND powders, those conclusions were based on X-ray photoelectron spectroscopy (XPS) and X-ray diffraction (XRD) measurements of the diamond/graphite ratio [342] and can not be considerable reliable, because XRD overestimates the diamond content and surface analysis techniques cannot provide good quantitative data for powdered materials. To the best of our knowledge, > 95% sp^3 carbon has never been found in ND samples by XANES or nuclear magnetic resonance (NMR) spectroscopy.

4.2.2.2 High-Resolution Transmission Electron Microscopy

HRTEM studies fully support results of Raman and XANES analyses, showing elimination of graphitic ribbons, carbon onions and graphitic shells in UD50 and a substantial decrease in amorphous carbon content in UD90 and UD98 after oxidation.

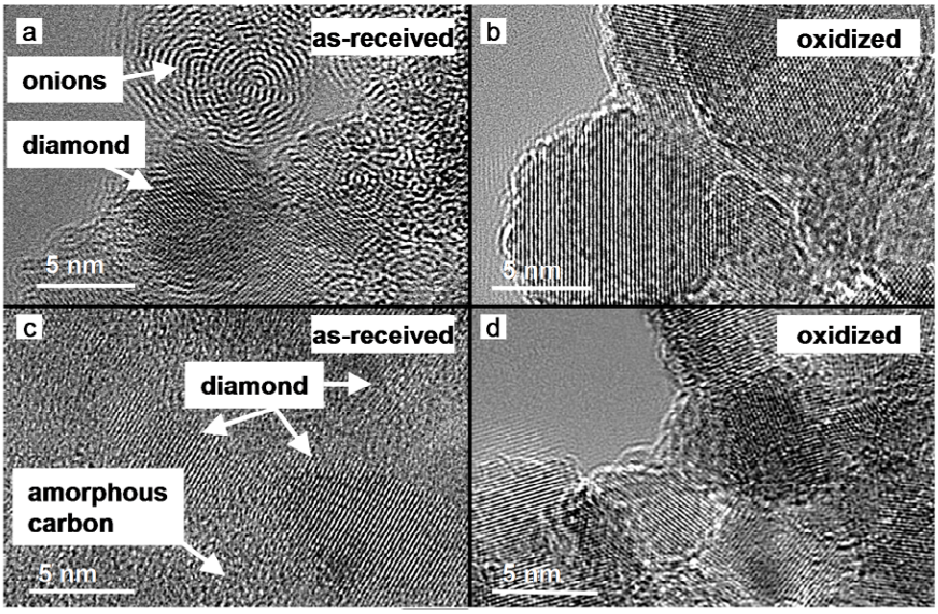

Figure 4.23: HRTEM images of (a, b) UD50 and (c, d) UD90 before and after oxidation for 5 h at 425 °C in air. Graph obtained from Ref. 121.

Figure 4.23 shows representative high resolution micrographs of UD50 and UD90 before and after annealing in air. The microstructure of UD98 was very similar to that of UD90 and thus is not presented separately. This is in agreement with XANES measurements showing a similar sp^2/sp^3 carbon ratio for these grades, both before and after oxidation.

4.2.3 Properties of Oxidized Nanodiamond

4.2.3.1 Optical Properties

Visual analysis of dry ND suggests substantial improvement in its technological properties after oxidation. The oxidized powder in the vials shows a liquid-like behavior when shaken, and flows easily, probably due to particle separation and breaking of agglomerates. **Figure 4.24** shows optical images of as-received and oxidized ND. In general, the darkness of powders correlates quite well with the content of sp^2-bonded carbon and other impurities in the samples (compare **Figure 4.24** with **Table 2.2** and **Table 4.2**). Untreated UD50 appears velvet black. UD90 and UD98 look grey (UD90) or grey-brown (UD98). The purified ND samples appear much lighter in color compared to prior oxidation. While all oxidized samples contain only small amounts of sp^2 carbon (< 5%), the high content of metal impurities in oxidized UD50 leads to a grey-brown color, probably due to presence of iron oxide. Purified UD90 and UD98 are light-grey, with oxidized UD98

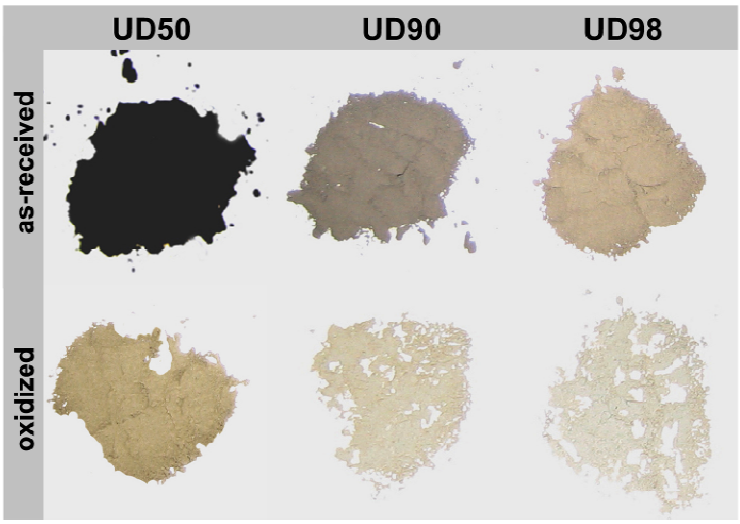

Figure 4.24: Optical images of UD50, UD90, and UD98 before and after oxidation for 5 h at 425 °C in air. Graph obtained from Ref. 121.

being the purest material, showing a color similar to that of microcrystalline diamond powder.

The color of powders is determined by their absorption characteristics. In the case of nanomaterials such as ND, where the particle size is comparable to or smaller than the wavelength of light (λ), elastic Rayleigh scattering also affects the appearance of a material. For example, Edelman et al. found that the absorbance of a black solution of 4 nm diamond crystals is proportional to λ^{-2} and their results were in agreement with theoretical calculations that assumed light is absorbed by sp^2 carbon at the surface of ND.[343] In similar studies on water suspensions made of ND with a particle size (agglomerated ND crystals) between 35 and 60 nm, the measured absorbance was found to be proportional to λ^{-4}, which is characteristic of Rayleigh scattering.[344] Suspensions of 190 nm and 360 nm particle size were opaque and colored light grey and dark grey, respectively.[344] With a decrease in particle size, the color of the suspensions changed from grey to brown to yellow and became more transparent. While these experiments clearly demonstrate the effects of agglomeration on optical properties of materials, they do not allow for distinguishing between Rayleigh scattering and absorption.

In this work, we recorded the absorption spectra of ND powders using an integrating sphere (Ulbricht sphere), which detects elastically scattered light and therefore measures the real absorption. **Figure 4.25** shows the UV-VIS-NIR absorption spectra of the as-received ND powders in comparison with oxidized UD90 (5 h at 425 °C). Due to its black color and the high content of sp^2 carbon (> 70%), UD50 strongly absorbs light throughout then entire wavelength range studied (200 - 2000 nm). Acid-treated UD90 and UD98 with diamond contents of 70 and 81%, respectively, exhibit a significant decrease in absorbance, especially

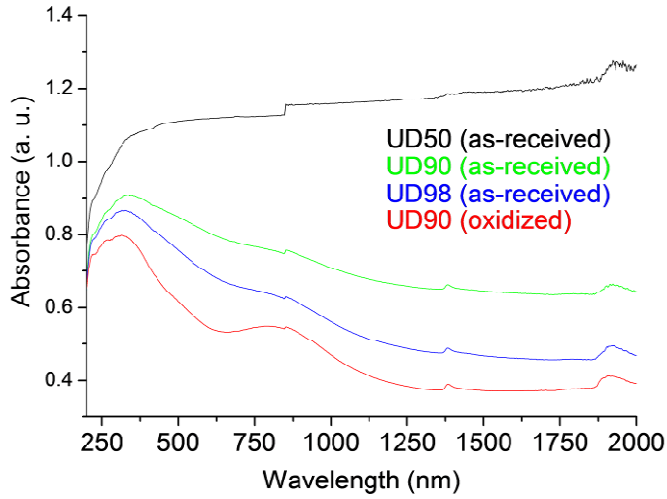

Figure 4.25: UV-VIS-NIR absorption spectra of UD50, UD98 and UD90 before and after oxidation.

in the spectral range between 600 - 2000 nm. Air oxidation further reduces absorption in the VIS-NIR range. Oxidized UD90 shows an almost 50% decrease in absorbance compared to as-received (acid-treated) UD90. Acid-treated and oxidized ND powders show broad absorption peaks at 200 - 500 nm and 700 - 1000 nm. The small features at 850 and 1385 nm, as well as the peak at ~ 1930 nm are spectrometer artifacts and not related to ND. The broad feature between 200 and 500 nm has been assigned to absorption by sp^2-bonded carbon atoms at the surface of ND.[337,344] Depending on the type of treatments used upon synthesis and the level of purity, ND powders contain different amounts of residual sp^2 carbon and various surface functionalities. Even well-purified (acid-treated) ND powders contain graphitic regions and fullerene-like structures formed at the diamond surface. This so-called buckydiamond is a stable morphology of carbon at the nanoscale.

While the absorption features of UD90 and UD98 may be ascribed to light absorption by sp^2 sites, this explanation does not hold for oxidized UD90 with a sp^2 content below 5%. A possible explanation for the observed absorption characteristics could be the rich surface

chemistry of ND. Several functional groups were found to strongly absorb in lower wavelength range.[1] In addition, ND crystals contain lattice defects and impurities (e.g. nitrogen, sulfur), which also absorb light in the UV-VIS spectral range.[258] Therefore, the interpretation of absorption features of highly complex ND particles compromising sp^2 and sp^3 carbon, a rich surface chemistry and catalyst impurities, is difficult. However, purification and oxidation of ND clearly reduce absorbance by lowering the sp^2 content, leading to a higher transparency in the VIS-NIR range. Even small amounts of sp^2 carbon in acid-purified ND, such as in UD90 and UD98, significantly alter the optical properties of ND, revealing the importance of air oxidation for ND purification.

The transparency of ND is important for many potential applications in scratch resistant optics, windows, and displays. The absorption properties of oxidized ND may also be of great benefit for sunscreen formulations, since it is highly transparent in the visible spectral range, and, at the same time, exhibit remarkable UV shielding.

4.2.3.2 Electronic Properties

Removal of graphitic carbon by oxidation is also expected to decrease the electrical conductivity of ND powders. The samples were pressed in a Teflon cell and connected to the circuit using two copper electrodes. It should be noted that the powder density and thus the conduction between nanoparticles in the cell depends on the pressure applied during sample preparation. However, since the same filling procedure was used for all samples, the obtained results can be used as qualitative measures to indicate changes upon ND purification and can predict potential trends. **Figure 4.26** shows the resistivity of different ND powders measured using an impedance analyzer (alternating current). I-U measurements

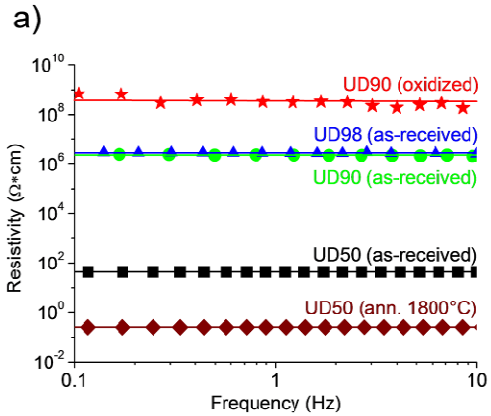

Figure 4.26: Resistivity of different ND powders in comparison with air oxidized and vacuum annealed ND. The resistivity decreases logarithmically with the sp^2 content.

(direct current) confirmed these results (not shown). As-received UD50 is a conductor and exhibits the lowest resistivity due to the high content of graphitic carbon. Acid-purified UD90 and UD98 with diamond contents of ~ 70 and ~ 81%, respectively, are insulators with resistivities several orders of magnitude higher than UD50. A further decrease in the sp^2 content (< 5 %) upon oxidation of UD90 leads to a resistivity as high as > 10^8 Ω·cm.

The resistivities ρ of all ND samples are shown in **Table 4.3**. The corresponding conductivities, σ, were calculated according to:

$$\sigma = \frac{1}{\rho}. \tag{4-4}$$

Table 4.3: Resistivity and conductivity of different ND powders in comparison with MWCNTs and carbon black (nanocrystalline graphite).

Sample	Resistivity ρ (Ω*cm)	Conductivity σ (S/m)
UD50 (as-received)	(4.2 ± 0.2) x10^{1}	(2.4 ± 0.1)
UD90 (as-received)	(2.3 ± 0.6) x10^{6}	(4.4 ± 1.1) x10^{-5}
UD98 (as-received)	(2.8 ± 0.7) x10^{6}	(3.6 ± 0.9) x10^{-5}
UD90 (oxidized)	(1.5 ± 0.5) x10^{8}	(6.7 ± 2.2) x10^{-7}
UD50 (annealed 1800°C)	(2.5 ± 0.4) x10^{-1}	(4.0 ± 0.6) x10^{2}
Carbon Black	(1.06 ± 0.01)	(0.94 ± 0.01) x10^{2}
MWCNT	(2.9 ± 0.1) x10^{-1}	(3.5 ± 0.1) x10^{2}

Vacuum annealing at high temperatures (> 1500 °C) transforms sp^3 sites into graphitic carbon (sp^2).[38] Therefore, vacuum annealed UD50 contains only sp^2 bonded carbon, leading to a further decrease in resistivity, as expected. For comparison, two graphitic, nanostructured carbon powders (Carbon black and MWCNTs) were analyzed using the same experimental setup. Vacuum annealed UD50 (0.25 Ω·cm) and MWCNTs (0.29 Ω·cm) show similar resistivities, whereas carbon black (1.06 Ω·cm) exhibits a slightly higher resistivity. While all three samples contain ~ 100% sp^2 carbon, particle size and shape are different, leading to different powder densities and variations in electrical contact between nanoparticles.

In summary, the resistivity of ND powders is determined by the sp^2 carbon content. Oxidation in air allows for almost complete removal of sp^2 sites, leading to resistivities as high as > 10^8 Ω·cm.

4.3 Activation of Carbide-Derived Carbon in Air and CO_2

Although large pore volumes (up to 85%) can be achieved by using precursors with large metal/carbon ratios for carbide-derived carbon synthesis (CDC), large pore formation and structure collapse occur when precursors with low carbon contents are used.[163,307] From a practical standpoint, it is therefore more suitable to use low cost precursors such as TiC or SiC with smaller metal/carbon ratios (pore volume ~ 55%), and adjust the porosity after CDC synthesis using activation techniques. While activation of carbons derived from various organic precursors has been widely studied, this process may similarly be able to increase the pore volume and specific surface area of CDC. In the following section, we present the results of air and CO_2 activation of TiC-CDC at different activation temperatures and times.

4.3.1 Raman Characterization of Nonactivated TiC-CDC

Figure 4.27 shows the Raman spectra of TiC-CDC chlorinated at 600, 1000 and 1300 °C, respectively.[345] 600°C-TiC-CDC (**Figure 4.27**a) exhibits broad D and G bands at 1351 and 1595 cm^{-1} of similar intensity, with a full-width at half maximum (FWHM) of 186 and 85 cm^{-1}, respectively, indicating the presence of mainly amorphous sp^2 carbon. At low chlorination temperatures, TiC-CDC is constituted mainly of amorphous carbon and little or no graphite.[166] While for 1000°C-TiC-CDC (**Figure 4.27**b) both Raman peaks are noticeably sharpened, shape and intensity distribution somewhat vary for different sample spots. Chlorination at high temperatures leads to increasing graphitization and a less homogeneous sample composition. Raman spectra recorded from regions of high graphitization show a sharp (FWHM ~ 31 cm^{-1}) and intense G band at ~ 1581 cm^{-1}. Amorphous parts of the sample exhibit intensity ratios comparable to that of 600°C-TiC-CDC, while the FWHM of the D band is reduced to about ~ 88 cm^{-1}, suggesting a general increase in bond ordering.

Previous HRTEM studies showed that TiC-CDC becomes more organized at higher chlorination temperatures, and carbon atoms reassemble into curved graphene sheets and

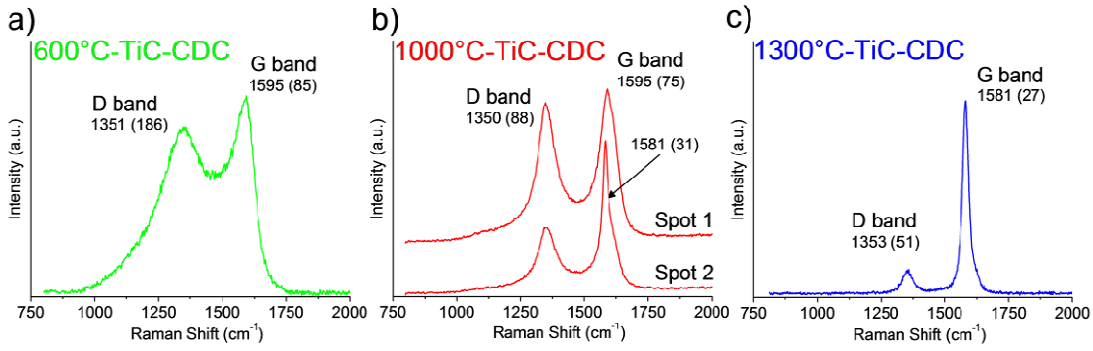

Figure 4.27: Raman spectra of TiC-CDC chlorinated at 600 °C (a), 1000 °C (b) and 1300 °C (c). With increasing chlorination temperature D and G bands are sharpened. Full width at half maximum (FWHM) values are shown in parentheses. Spectra were obtained from Ref. 345 and were recorded using 514 nm laser excitation.

graphitic ribbons, with interplanar spacing close to that of graphite (0.34 nm).[166] 1300°C-TiC-CDC (**Figure 4.27**c) exhibits a higher homogeneity compared to 1000°C-TiC-CDC. Both D (1353 cm^{-1}) and G band (1581 cm^{-1}) are significantly sharpened, showing FWHM values of 51 and 27 cm^{-1}, respectively. The low D band intensity, a G band position of 1581 cm^{-1} and the reduced peak width of both Raman bands suggest a high level of graphitization.

4.3.2 Oxidation in Air

4.3.2.1 Thermogravimetric Analysis

In order to study the oxidation kinetics of nanoporous carbon materials we performed TGA (in air) on three TiC-CDC samples, chlorinated at 600, 1000 and 1300 °C, respectively (**Figure 4.28**). The weight loss between 350 and 525 °C results mainly from the oxidation of amorphous carbon and 600°C-TiC-CDC and 1000°C-TiC-CDC show similar oxidation behavior. At temperatures above 525 °C, 600°C-TiC-CDC and 1000°C-TiC-CDC differ in

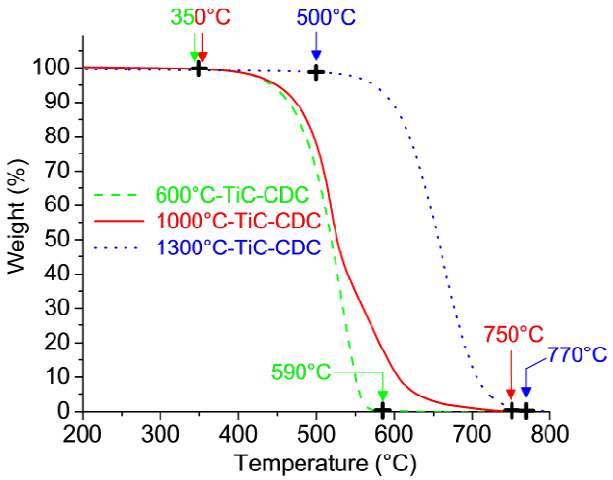

Figure 4.28 Nonisothermal TGA of TiC-CDC chlorinated at 600, 1000 and 1300 °C (Ref. 345). Weight-loss curves were recorded in air at a constant heating rate of 2 °C/min.

burn-off rates. The composition of 600°C-TiC-CDC does not change during oxidation due to the high homogeneity of the sample. However, in case of 1000°C-TiC-CDC, the remaining ~ 40 wt% mainly consist of graphitized carbon showing a higher resistance to oxidation compared to amorphous material, as indicated by the lower burn-off rate (**Figure 4.28**). TGA analysis shows that oxidation of TiC-CDC (in air) does not start below 350 °C, but occurs at a reasonable rate between 400 and 450 °C for both 600°C-TiC-CDC and 1000°C-TiC-CDC. The graphitized 1300°C-TiC-CDC requires significant higher oxidation temperatures > 500 °C and is therefore less favorable for activation. Moreover, a higher synthesis temperature leads an increase in the average pore size and a broadened pore size distribution.[166] We therefore focused our efforts on activation of 600°C-TiC-CDC and 1000°C-TiC-CDC, and set the initial activation temperature to 430 °C in order to achieve sufficient control over the porosity development.

4.3.2.2 Specific Surface Area and Pore Volume

Changes in porosity of 1000°C-TiC-CDC after activation (in air) for 3, 6.5 and 10 h at 430 °C are shown in **Figure 4.29**. The SSA increases with activation time (**Figure 4.29**a), reaching a maximum value of ~ 1800 m^2/g after 6.5 h with no further increase at higher burn-off. A similar saturation of the SSA has been observed during activation of other carbon materials.[346] Related changes in the pore volume are shown in **Figure 4.29**b. The total pore volume increases from 0.7 to 0.78 (+ 11.4%), 0.84 (+ 20%) and 0.87 (+ 24%) after activation for 3, 6.5 and 10 h, respectively, while the micropore volume corresponding to the volume of pores smaller than 1.5 nm increases from 0.34 to 0.36 cm^3/g (+ 6%) during activation for 3 h, but stabilizes around 0.36 cm^3/g for longer activation times. The observed

porosity development may be explained by a two-step process starting with 1) the formation of new micropores at moderate conditions, and 2) widening into larger pores for longer times, leading to an increase of the total pore volume.[72,75] **Figure 4.29**c shows changes in SSA and burn-off during activation for 3 and 6.5 h at different temperatures between 400 and 550 °C. The SSA increases with burn-off (weight loss) at lower activation temperatures, reaches a maximum value of ~ 1800 m^2/g after 6.5 h at 425 °C and 3 h at 475 °C, respectively, but shows no further increase with burn-off at higher temperatures.

The corresponding changes in pore volume are shown in **Figure 4.29**d. While the total pore volume significantly increases with activation temperature (up to 55%), the micropore

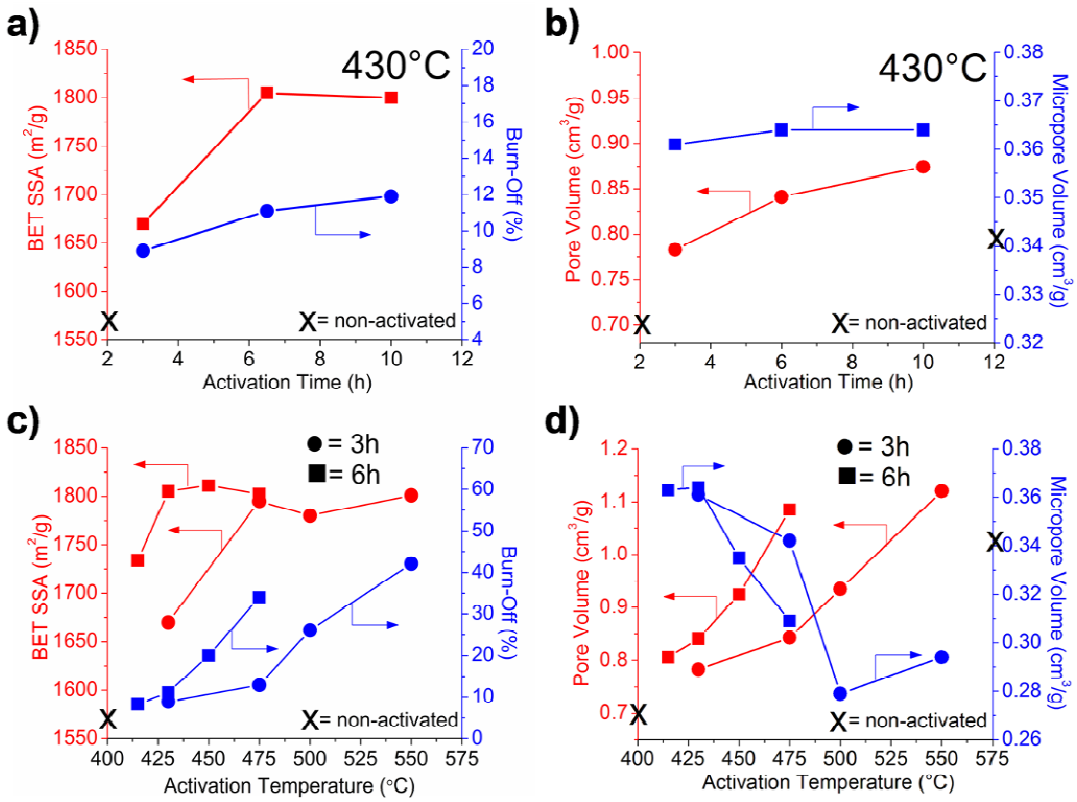

Figure 4.29: Changes in SSA (a) and pore volume (b) after activation of 1000°C-TiC-CDC in air at 430 °C for different times (Ref. 345). Similar trends were found for SSA (c) and pore volume (d) after activation at different temperatures between 400 and 500 °C.

volume shows a small increase (+ 6%) at low temperature, but decreases at higher activation temperatures, suggesting the enlargement of micropores into mesopores.

Our results demonstrate that activation in air at lower temperatures (~ 430 °C) and for long activation times (> 6.5 h) leads to the highest micropore volume (+ 6%) and SSA (+ 14%) values at a weight loss of just ~ 10%, which is much lower than 40%, typical for manufacturing of activated carbons.[160,347,348] The total pore volume increases (up to 60%) with burn-off, and reaches a maximum for high activation temperatures and long activation times. The optimum activation conditions with respect to a high SSA at a low weight loss are 6.5 h at 430 °C and 3 h at 475 °C.

4.3.2.3 Pore Size Characterization

The resulting changes in the pore-size distribution of 1000°C-TiC-CDC after activation in air are shown in **Figure 4.30**. It should be noted that jaggedness in the PSDs are a result of the numerical model rather than an actual feature of the pore structure. Oxidation of 1000°C-TiC-CDC for 3 h at 430 °C (**Figure 4.30**a) leads to a slight increase in the volume of pores smaller than 0.8 nm. Increasing oxidation time reduces the contribution of small pores to the total pore volume, shifting the average pore-size from 1.10 (non-activated) to 1.20 and 1.25 nm after 3 and 6 h activation at 430 °C, respectively. An increase in activation temperature at constant activation time leads to a decrease of the pore volume for pore sizes below 0.8 nm (**Figure 4.30**b) and to formation of larger pores (> 2 nm). The average pore size changes from 1.10 (non-activated) to 1.22, 1.50 and 1.90 nm after 6.5 h activation at 415, 450 and 475 °C, respectively.

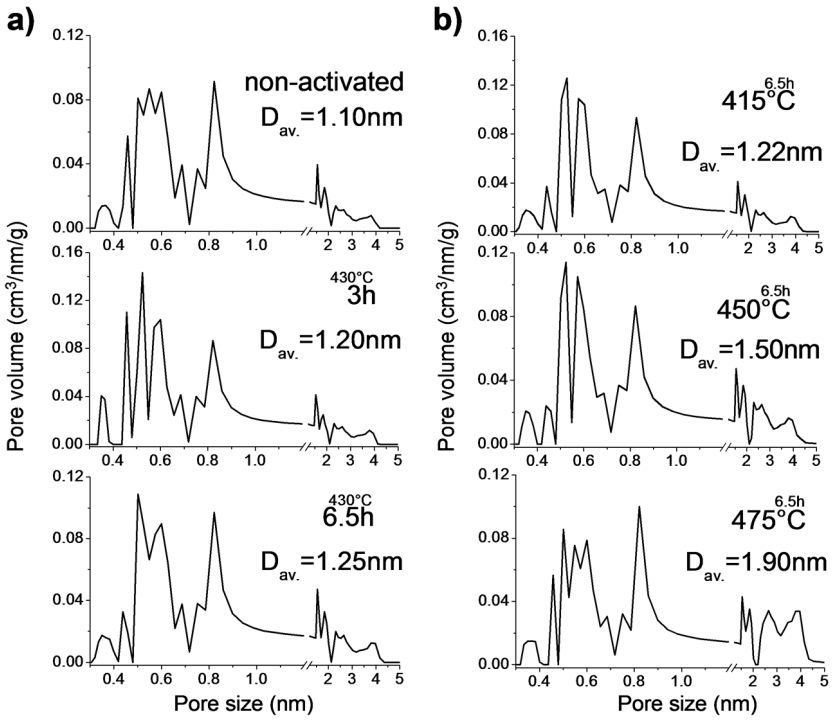

Figure 4.30: Pore-size distribution and average pore diameter ($D_{av.}$) of 1000°C-TiC-CDC after activation in air for 3 and 6.5 h at 430 °C (a) and 6.5 h at 415, 450 and 475 °C (b). Data obtained from Ref. 345.

The results of activation in air demonstrate the possibility of increasing the porosity of TiC-CDC; however, SSA and pore volume showed only a moderate increase and were accompanied by a large weight loss. The micropore volume, which is crucial for many CDC applications[66,349], remained almost unchanged, and mesopores appear at high activation temperatures and long activation times, leading to an increase in the total pore volume and SSA saturation.

4.3.3 Oxidation in CO_2

4.3.3.1 Specific Surface Area and Pore Volume

In an attempt to achieve an increase in the micropore volume, 600°C-TiC-CDC was activated using CO_2. Graphitization and ribbon formation in high-temperature CDCs, such as 1000°C-TiC-CDC and 1300°C-TiC-CDC, lead to relatively large pore sizes and are therefore unfavorable for most CDC applications. The lower chlorination temperature of 600°C-TiC-CDC minimizes the formation of graphitic carbon (see **Figure 4.27**). **Figure 4.31** shows changes in SSA and porosity of 600°C-TiC-CDC after activation at various conditions. At constant activation time (2 h), the BET SSA is proportional to the burn-off and increases with temperature from about 1300 m^2/g (non-activated) to > 3000 m^2/g at 950 °C (**Figure 4.31**a). At 875 °C, both total pore volume (+ 28%) and micropore volume (+ 18%) increase compared to non-activated 600°C-TiC-CDC (**Figure 4.31**b). While the total pore volume follows the trend of the BET SSA and increases with increasing activation temperature (+ 150% at 950 °C), the micropore volume decreases (- 8% at 950 °C), falling below that of non-activated 600°C-TiC-CDC (**Figure 4.31**b).

Figure 4.31c compares burn-off and BET SSA of 600°C-TiC-CDC for different activation times at 875 and 950 °C, respectively. BET SSA and burn-off follow similar trends for both activation temperatures and increase with activation time. While at lower activation temperatures, SSA and burn-off after ~ 8 h approach a maximum value of ~ 2700 m^2/g and ~ 55 wt%, respectively, values up to 3100 m^2/g at a weight loss of 75 wt% are obtained at high activation temperatures (950 °C). The corresponding changes in the pore volume are shown in **Figure 4.31**d. The total pore volume follows the trend of the BET SSA and increases with activation time, reaching maximum values of 1.14 cm^3/g (12 h at 875 °C) and

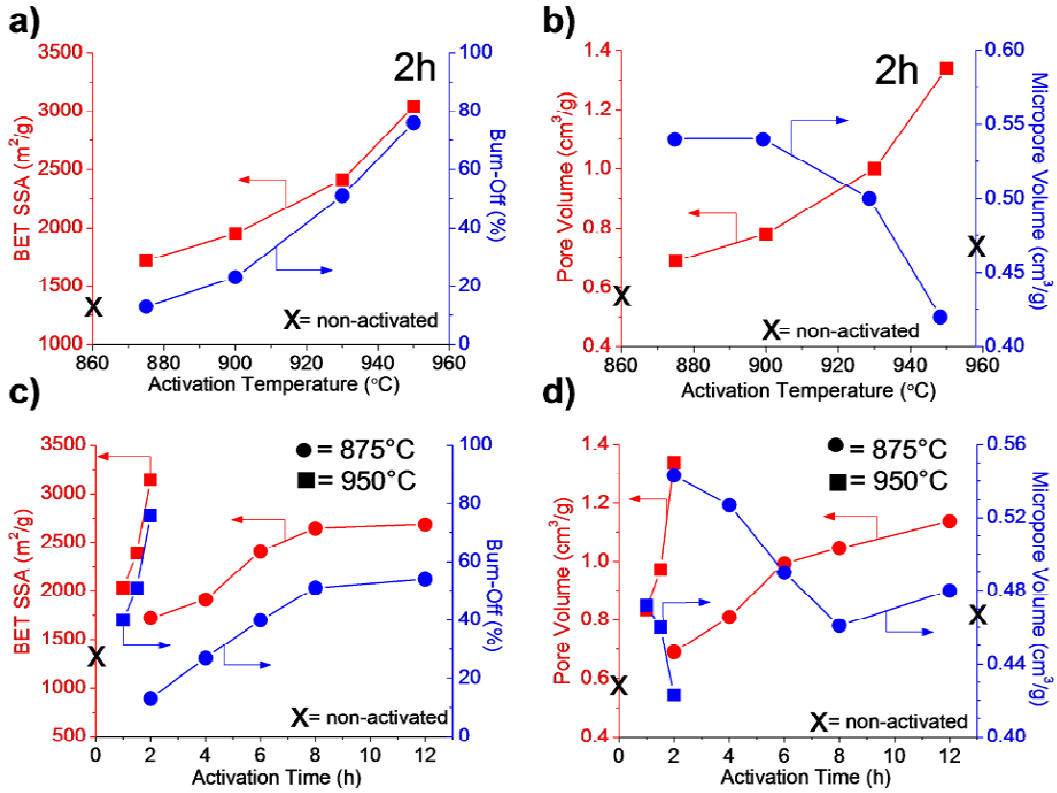

Figure 4.31: BET SSA and pore volume of 600°C-TiC-CDC after oxidation in CO_2 as a function of activation temperature (a, b) and activation time (c, d). Graph obtained from Ref. 345.

1.34 cm^3/g (2 h at 950 °C). The micropore volume is the highest for short activation times but decreases with time, similar to air activation, following the two-step process with initial formation of new micropores followed by the enlargement of those micropores into mesopores as described above. While activation at lower temperatures leads to an initial micropore volume increase of about 17%, higher temperatures always lead to a micropore volume lower than in non-activated 600°C-TiC-CDC.

The optimum conditions for activation of 600°C-TiC-CDC in CO_2 with respect to a high SSA, development of micropores and low weight loss are therefore low activation temperatures (~ 875 °C) and long activation times (> 8 h). High temperatures and longer

activation times lead to a larger total pore volume, but are unfavorable for the formation of micropores.

4.3.3.2 Pore Size Characterization

The pore size distributions of CO_2-activated 600°C-TiC-CDC are plotted in **Figure 4.32**. The average pore size shifts towards higher values with increasing activation time (**Figure 4.32**a) and activation temperature (**Figure 4.32**b). Oxidation for 4 and 12 h at 875 °C leads to an increase in the average pore size from 0.73 to 0.96 and 1.51 nm, respectively (**Figure 4.32**a).

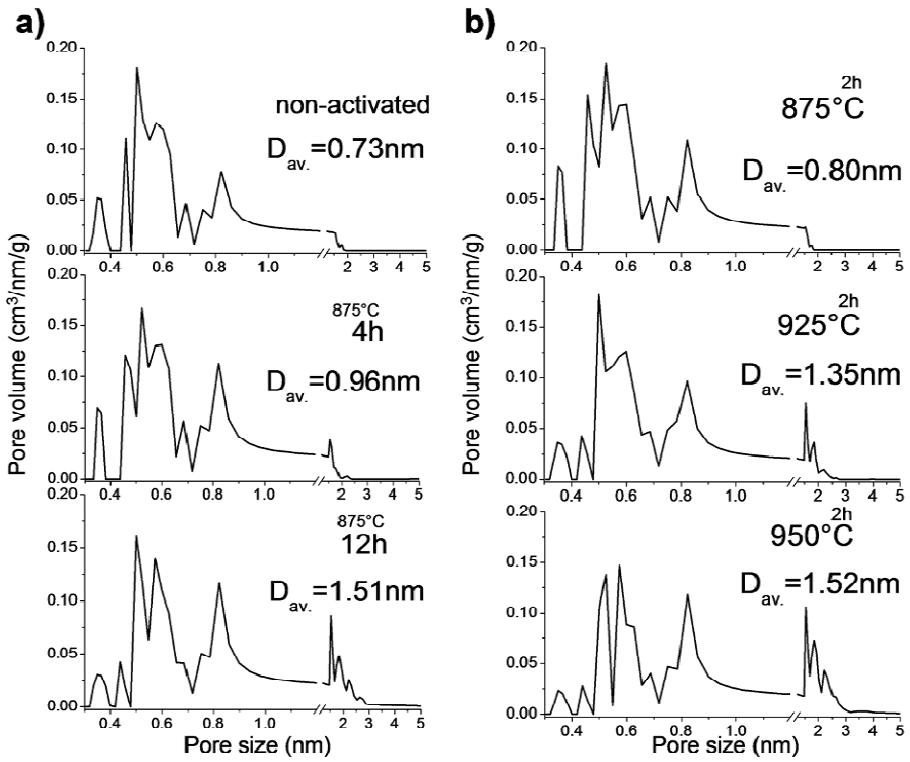

Figure 4.32: Changes in pore size distribution and average pore size of 600°C-TiC-CDC after activation in CO2 for 4 and 12 h at 875 °C (a) and 2 h at 875, 925 and 950 °C (b). Graph obtained from Ref. 345.

The observed shift results mainly from a decrease in the pore volume of pores smaller than 0.8 nm, due to the formation of larger pores in the size range of 1 - 2 nm and above. At constant activation temperature, oxidation in CO_2 enlarges small pores with time, thus decreasing micropore and increasing mesopore volume. Similar trends were found for activation at different temperatures (constant time). Activation for 2 h at 875, 925 and 950 °C (**Figure 4.32**b) increases the average pore size from the initial 0.73 to 0.80, 1.35 and 1.52 nm, respectively.

4.3.3.3 Raman Spectrum of CO_2-Activated TiC-CDC

Figure 4.33a compares the Raman spectra of 600°C-TiC-CDC before and after CO_2-activation at 875 and 950 °C for 8 and 2 h, respectively. In order to accurately measure changes in Raman intensity, spectra were fitted using 4 Lorentzian/Gaussian peaks centered at 1170, 1350, 1510, and 1595 cm^{-1}. The Raman bands at 1350 and 1595 cm^{-1} have been assigned to graphitic sp^2 carbon, and are referred to as D and G band. Both D and G bands are noticeably sharpened. The FWHM decreases from 186 and 85 cm^{-1} (as-received) to 185 and 83 cm^{-1} (875 °C/8 h) and 178 and 78 cm^{-1} (950 °C/2 h), respectively. The peaks at 1170 and 1510 cm^{-1} are believed to originate from sp^3 carbon phases and C-H contribution or semicircle ring stretch vibrations of benzene, respectively.[350] However, EXAFS[166], EELS[70] and pair distribution function studies[351] show ~ 10 at.% or less of sp^3 carbon in TiC-CDC. The interpretation of changes in the Raman spectrum of CDCs is further complicated by the presence of amorphous carbon and graphite, and functional groups contributing to the Raman signal. Although the intensity ratio between D and G band has successfully been

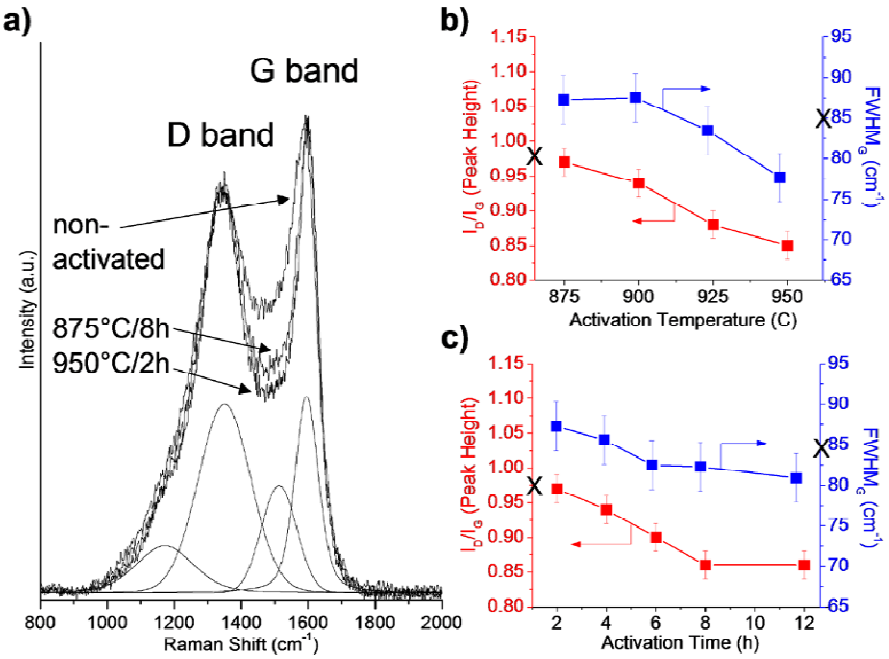

Figure 4.33: a) Changes in the Raman spectrum of 600°C-TiC-CDC after activation in CO_2 for 2 and 8 h at 950 and 875 °C, respectively. I_D/I_G ratio and FWHM decrease with activation temperature (b) and activation time (c), suggesting higher ordering and removal of amorphous carbon during activation. Raman spectra were obtained from Ref. 345 and were measured using 514 nm laser excitation.

used to determine the coherence length (crystal size) in graphitic materials such as carbon blacks, great care must be taken with a highly disordered material such as 600°C-TiC-CDC.

A reduction in the width of the G band (FWHM) and a decrease in the I_D/I_G ratio indicate increasing graphitization and/or removal of amorphous carbon.[274] The relative percentage of graphitic carbon increases during activation, and the I_D/I_G ratio decreases with activation time (**Figure 4.33**b) and activation temperature (**Figure 4.33**c), as expected.

4.3.4 Activation of Other Carbide-Derived Carbons

To confirm that the developed procedure is applicable to other CDCs, we performed several experiments on SiC-CDC and demonstrated a similar trend. SiC-CDC has an average pore size of about 0.8 nm, which weakly depends on the synthesis temperature [352]. It maintains a disordered carbon network structure to higher synthesis temperatures compared to other CDCs [353]. Unfortunately, the pore volume is only about ~ 0.5 g/cm^3, limiting

Table 4.4: Changes in pore volume and SSA of SiC-CDC after activation in CO2 for 15 h at 750 °C and 1 h at 950 °C.

	BET SSA [m^2/g]	Pore Vol. [cm^3/g]	Micropore Vol. [cm^3/g]
1100°C-SiC-CDC	1424	0.52	0.48
750°C/15h	1749	0.75	0.70
950°C/1h	1833	0.87	0.77

applications SiC-CDC for gas sorption. However, almost all pores are micropores, smaller than 1.5 nm. Therefore, activation may potentially increase the volume of micropores, producing a very useful sorbent. **Table 4.4** shows the results from activation of 1100°C-SiC-CDC at different temperatures in CO_2.

An increase in the micropore volume associated to a ~ 20% increase in SSA is observed. While the oxidation conditions have not been optimized in case of 1100°C-SiC-CDC, the results clearly indicate that physical activation under CO_2 is applicable to CDC derived from other metal carbides.

4.4 Reaction Kinetics and Catalytic Effects

Size, shape and bonding configuration of carbon nanostructures strongly affect their resistance to oxidation. A major challenge during the study of reaction kinetics of nanomaterials is the fact that current synthesis methods do not provide well defined samples, but mixtures of different nanostructures that also contain amorphous species and other impurities. In the following section, we analyze the reaction kinetics of different carbon nanostructures during oxidation and study the effects of bond-ordering, defect concentrations and impurities on the thermal stability of nanomaterials. The activation energies of the oxidation reactions are determined using isothermal and nonisothermal thermogravimetric analysis.

4.4.1 Carbon Nanotubes

4.4.1.1 Nonisothermal Thermogravimetric Analysis

Figure 4.34 shows the results of the thermogravimetric analysis of different CNTs during oxidation between 25 and 750 °C in air. The graphs are normalized by the sample weight measured at 200 °C (100%) and after the oxidation (0%), in order to eliminate contributions from adsorbed species and metal impurities. Below 200 °C, only water and adsorbed organic impurities are removed from the tube surface, but the oxidation of carbon does not occur. The effect of metal catalyst on oxidation kinetics will be discussed separately in section 4.3.4.

The weight-loss curves of DWCNTs and MWCNTs (as-received and vacuum annealed) are presented in **Figure 4.34**a. The oxidation of the DWCNT sample starts around 375 °C and is completed ~ 550 °C, while the oxidation of as-received MWCNTs does not occur below 430 °C, or the reaction rate is too low to allow a noticeable sample loss. The weight loss below ~ 420 °C during oxidation of DWCNTs may be mainly due to removal of amorphous carbon (**Figure 4.34**a). As-received MWCNTs have a higher defect concentration, but contain less amorphous carbon. Between 430 and 550 °C, all carbon

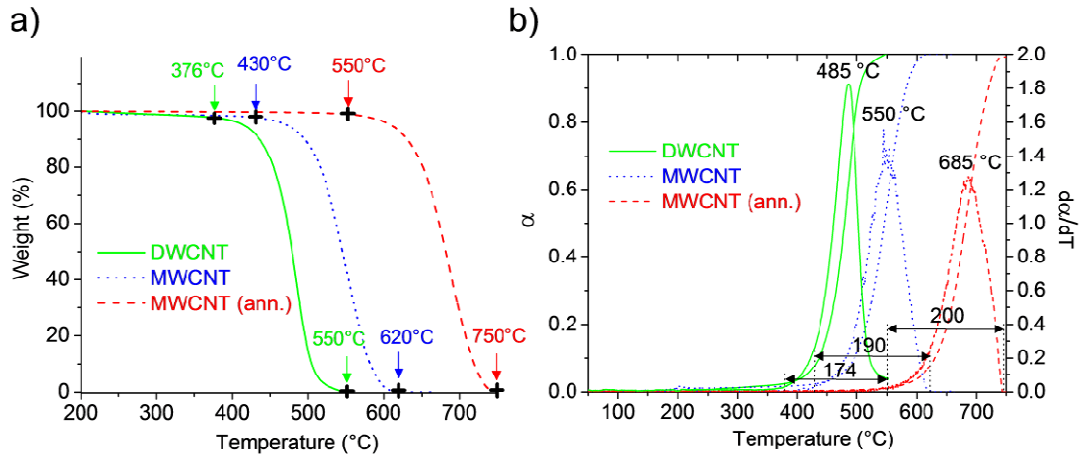

Figure 4.34: Thermogravimetric analysis of oxidation of DWCNTs (as-received) and MWCNTs (as-received and vacuum-annealed). a) Weight-loss of CNTs and temperatures indicating the start and end of the oxidation process. b) The weight fraction α and its derivative $d\alpha/dT$ are used to determine the temperature at which the maximum weight-loss occurs.

species including amorphous carbon, DWCNTs and MWCNTs are oxidized simultaneously (**Figure 4.34**a and b). By the time the temperature reaches ~ 620 °C, the entire MWCNT sample has been oxidized. Graphitized MWCNTs are more resistant against oxidation than DWCNTs and as-received MWCNTs. No oxidation-induced weight loss is observed below ~ 550 °C, a temperature at which all DWCNTs and most as-received MWCNTs have been

oxidized. The improved thermal stability results from the lower defect density and the removal of iron inclusions during vacuum annealing.

Several important kinetic parameters for the individual oxidation reactions can be obtained from thermal analysis curves. The temperature at which the maximum weight loss occurs (maximum weight loss rate) was determined using the weight faction α:

$$\alpha = \frac{m_0 - m}{m_0}, \tag{4-5}$$

and its derivative, the oxidation reaction rate dα/dT:

$$\frac{d\alpha}{dT} = \frac{d\left(\frac{m_0 - m}{m_0}\right)}{dT}, \tag{4-6}$$

where m_0 and m are the initial sample weight and sample weight at time temperature T, respectively. The maximum weight loss rate of DWCNTs, as-received and vacuum annealed MWCNTs is characterized by a maximum $d\alpha/dT$ and occurs at 485, 550 and 685 °C, respectively (**Figure 4.34**b). The temperature range in which the oxidation of the carbon powders takes place is represented by the peak width of the $d\alpha/dT$ curve. The DWCNT sample, which contains both amorphous carbon and nanotubes, exhibits the smallest peak width and the entire sample is oxidized in a temperature window of roughly ~ 175 °C. Although MWCNT samples typically contain less amorphous carbon, the oxidation window is broadened compared to DWCNTs, showing values of 190 and 200 °C for as-received and vacuum annealed MWCNTs, respectively. The differences can be explained the broader size-distribution of MWCNTs. The oxidation resistance of CNTs depends on the curvature and thus the diameter of the nanotubes. A broader diameter distribution leads to a wider range of activation energies and oxidation temperatures. Moreover, the inner walls cannot be

reached by oxygen molecules and are therefore not oxidized before the outer walls are removed. Even if temperatures are high enough to oxidize the inner tubes, blocking of oxygen by larger outer-tubes inhibit oxidation at lower temperatures. Oxidation of CNTs starts with outer tubes and proceeds layer by layer until reaching the inner walls of the nanotubes.

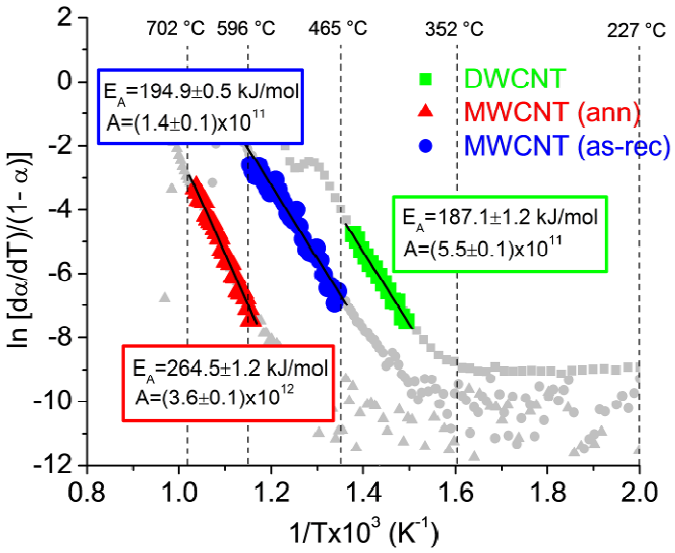

Figure 4.35: Achar-Brindley-Sharp-Wendeworth plot determining the activation energies (E_A) and frequency factors (A) for oxidation of DWCNTs and MWCNTs (as-received and vacuum annealed).

As a consequence, oxidation of MWCNTs with three, four or more walls requires more time than oxidation of small-diameter DWCNTs. Since the temperature increases continuously with time, the oxidation rate curve ($d\alpha/dT$) is broadened (**Figure 4.34**b). The large peak width of vacuum annealed MWCNTs may be explained by healing of defects and formation of highly graphitic structures due to rearrangement of carbon atoms during high-temperature annealing (**Figure 4.34**b). While less-ordered tubes are oxidized at lower temperatures, defect-free and highly graphitized carbon structures require higher oxidation temperatures.

The activation energies E_A for the oxidation reactions were determined using the Achar-Brindley-Sharp-Wendeworth (ABSW) equation:[354,355]

$$\ln\left[\frac{1}{F(\alpha)}\cdot\frac{d\alpha}{dT}\right]=\ln\left(\frac{A}{\beta}\right)-\frac{E_A}{R}\cdot\frac{1}{T}, \qquad (4\text{-}7)$$

where R is the universal gas constant (8.314 J/(K·mol), T is the temperature (in K), β is the heating rate, $d\alpha/dT$ is the oxidation reaction rate, A is frequency factor or probability constant (in min^{-1}), and $F(\alpha)$[356,357] is the differential function describing the reaction mechanism. The oxidation of carbon materials can be divided into several steps, as discussed in detail in section 2.2.1. At lower oxidation temperatures (350 - 600 °C), the chemical reaction is the rate controlling step, whereas at higher temperatures (600 - 800 °C) diffusion of oxygen and carbon dioxide in the pores becomes the limiting process. Several studies on carbon fibers and other carbon materials revealed that, at temperatures below 500 °C, the oxidation process is well described by a first order reaction using the "random nucleation and growth mechanism" (Mampel unimolecular law[358]) where $F(\alpha) = 1-\alpha$.[95,359]

Equation 4-7 shows that there is a linear relationship between the logarithm of $[d\alpha/dT/F(\alpha)]$ and the reciprocal of the oxidation temperature T. By setting $F(\alpha) = 1-\alpha$ and plotting $\ln[d\alpha/dT/F(\alpha)]$ over $1/T$ we can determine the kinetic parameters E_A and A using a linear regression (**Figure 4.35**). As discussed in section 2.2.1, the activation energy E_A is a measure of the energy required for the oxygen-carbon reaction to occur. The frequency factor A represents the probability of a molecule to become activated, and is also a measure of the total number of molecules that possess the activation energy. The temperature ranges used for the linear regression are indicated in **Figure 4.35**. The calculated activation energies (frequency factors) for DWCNTs, as-received and vacuum-annealed MWCNTs are

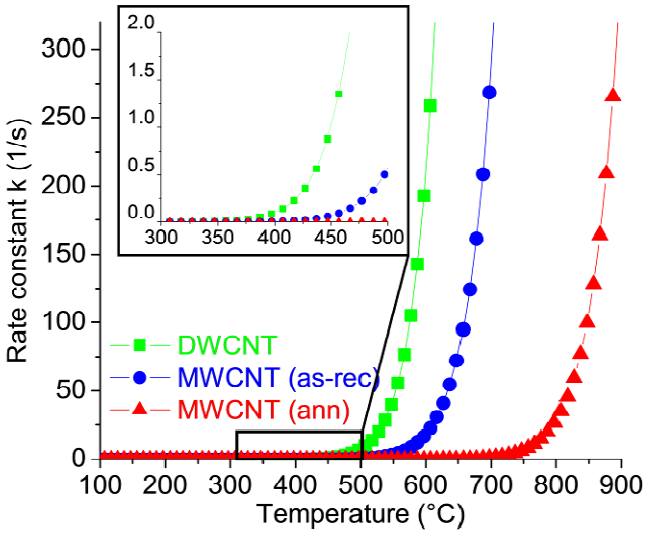

Figure 4.36: Reaction rate constant of DWCNTs and MWCNTs (as-received and vacuum-annealed) determined using the calculated activation energies and frequency factors.

187.1 kJ/mol ($5.52 \cdot 10^{11}$ min^{-1}), 194.9 kJ/mol ($1.36 \cdot 10^{11}$ min^{-1}) and 264.5 kJ/mol ($3.6 \cdot 10^{12}$ min^{-1}), respectively. The corresponding regression errors (standard deviation) are given in **Figure 4.35** and below 1%.

As expected, vacuum annealed MWCNTs showing defect-free, highly graphitized nanotube structures exhibit the highest apparent activation energy (E_A = 264. 5 kJ/mol). The activation energies of DWCNTs (E_A = 187.1 kJ/mol) and as-received MWCNTs (E_A = 194.9 kJ/mol) are similar, which may not be expected considering the differences size and tube curvature. However, MWCNTs contain a larger number of defects and iron catalyst, which in turn lower the activation energy of the nanotubes.

The measured activation energies (and frequency factors) are in agreement with data reported in literature. In case of MWCNTs, E_A values ranging from 225 up to 292 kJ/mol have been found.[86,103] Studies on SWCNTs showed activation energies between 119 and

183 kJ/mol.[80,86] The calculated activation energies E_A and frequency factors A (in s^{-1}) can be used to determine the reaction rate constant k (in s^{-1}) according to

$$k = A \cdot e^{-\frac{E_A}{RT}}, \tag{4-8}$$

where T is the temperature (in K) and R is the universal gas constant (8.3145 J/mol). The resulting reaction rate constants of DWCNTs and MWCNTs (as-received and vacuum-annealed) are shown in **Figure 4.36**. DWCNTs exhibit the highest reaction rate constant, even at low temperatures (inset in **Figure 4.36**). The rate constant is small below 450 °C, but increases rapidly between 500 and 600 °C. As-received and vacuum-annealed MWCNTs exhibits significant lower rate constants in this temperature range. While in case of the as-received MWCNTs the rate constant increases above 600 °C, it remains negligible for the vacuum-annealed tubes upon reaching 750 - 775 °C.

4.4.1.2 Isothermal Oxidation Kinetic Study

In order to confirm the results obtained from nonisothermal TGA studies, we investigated the oxidation behavior of CNTs under isothermal conditions. The weight loss of DWCNTs and MWCNTs during isothermal oxidation at different temperatures between 375 and 590 °C is shown in **Figure 4.37**. The time-dependence of the weight loss can be used to determine the activation energies of the oxidation reaction. Under isothermal conditions, the weight fraction α can be expressed as:

$$\alpha = \frac{m_0 - m}{m_0} = k \cdot t, \tag{4-9}$$

where k is the reaction rate (constant at fixed temperature) and m_0 and m are the initial sample weight and sample weight at time t, respectively. The correlation between the

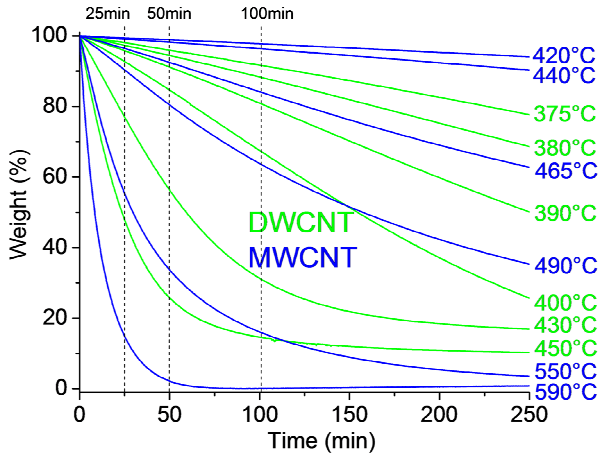

Figure 4.37: Isothermal TGA curves of DWCNTs and MWCNTs measured for 280 minutes at different temperatures in air. The weight loss data at 25, 50 and 100 minutes was used to determine the activation energies.

oxidation temperature T and the corresponding reaction rate k is given be the Arrhenius equation:

$$\ln k = \ln A - \frac{E_A}{R} \cdot \frac{1}{T}, \tag{4-10}$$

where E_A is the apparent activation energy of the oxidation (in kJ/mol), T is the temperature (in K), R is the gas constant, and A is the frequency factor. Combining equations 4-9 and 4-10 gives:

$$\ln \alpha = \ln A + \ln t - \frac{E_A}{R} \cdot \frac{1}{T}. \tag{4-11}$$

Since [ln A + ln t] is constant for a fixed temperature, plotting ln α versus $1/T$ lead to a linear relationship, known as Arrhenius plot. The activation energy E_A can be calculated from the slope of the curve, while the interception with the y-axis determines the frequency factor A. The weight fraction α of DWCNTs and MWCNTs was determined using the weight loss at different temperatures between 375 and 590 °C after oxidation for 25, 50 and 100 minutes (**Figure 4.37**). The resulting Arrhenius curves are shown in **Figure 4.38**. Each

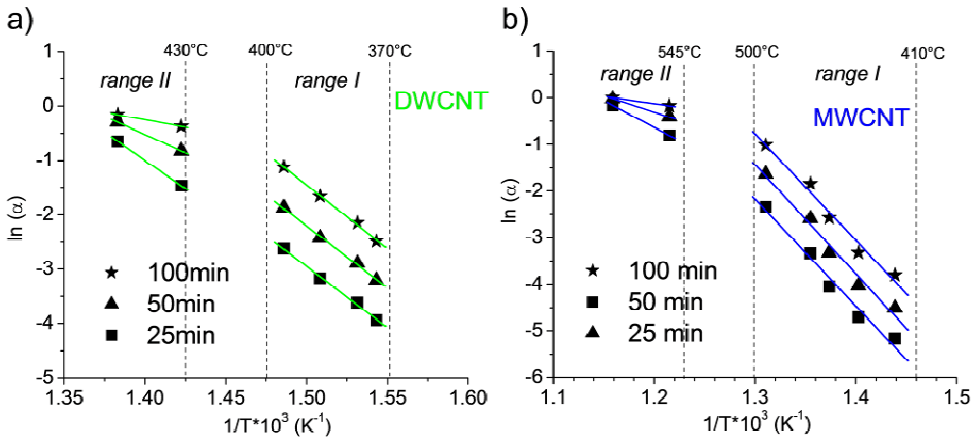

Figure 4.38: Arrhenius plot of DWCNTs (a) and MWCNTs (b). The weight fraction α was determined at different temperature between 370 and 590 °C after oxidation for 25, 50 and 100 minutes. Linear regression has been used to fit the experimental data.

data set corresponds to a fixed oxidation time (t = 25, 50 and 100 minutes). The Arrhenius plots of both DWCNTs and MWCNTs can be divided into two regions: a time-independent (range I) and a time-dependent (range II) temperature regime. At low oxidation temperatures (370 - 400 °C for DWCNTs and 410 - 500 °C for MWCNTs), the slope of the Arrhenius curve is similar for 25, 50 and 100 minutes oxidation periods, suggesting a reaction-controlled oxidation mechanism (see section 2.2.1.2).

However, at higher oxidation temperatures (> 400 °C for DWCNTs and > 500 °C for MWCNTs), the slope of the Arrhenius curves decreases with increasing oxidation time, indicating that is the rate controlling process. The temperature at which diffusion limitation becomes the dominate process is different for DWCNTs and MWCNTs. Moreover, the critical transition temperatures of DWCNTs (400 - 430 °C) and MWCNTs (500 - 545 °C) appear to be much lower compared to other carbon materials, such as graphite or carbon fibers (~ 600 °C).

Table 4.5: Activation energies E_A and frequency factors A of DWCNTs and MWCNTs measured during isothermal oxidation.

Time	DWCNT		MWCNT	
	range I	*range II*	*range I*	*range II*
	E_A *in kJ/mol* *A in* min^{-1}	E_A *in kJ/mol* *A in* min^{-1}	E_A *in kJ/mol* *A in* min^{-1}	E_A *in kJ/mol* *A in* min^{-1}
25 min	187.0±7.7 (9.1±0.4)x10^{11}	172.7 (6.3x10^{10})	190.5±17.2 (3.9±0.4)x10^{10}	95.1 (1.9x10^{4})
50 min	189.2±6.0 (1.5±0.05)x10^{12}	112.0 (1.8x10^{6})	194.6±16.8 (7.9±0.8)x10^{10}	57.4 (5.8x10^{1})
100 min	194.2±6.1 (3.8±0.1)x10^{12}	45.9 (1.8x10^{1})	189.9±16.5 (3.6±0.3)x10^{10}	25.8 (3.6x10^{-1})

The calculated activation energies and corresponding frequency factors for the individual Arrhenius curves are shown in **Table 4.5**. At low oxidation temperatures (range I) the average activation energies (frequency factors) of DWCNTs and MWCNTs are 190.1 ± 10.8 kJ/mol ((2.1 ± 3.9)·10^{12} min^{-1}) and 191.7 ± 19.7 kJ/mol ((5.1 ± 6.3)·10^{10} min^{-1}), respectively. The averaged values are in good agreement with results obtained from nonisothermal TGA studies, revealing that both MWCNTs and DWCNTs exhibit similar activation energies. The time-dependency of the kinetic parameters in the temperature range II requires diffusion-based models for quantitative analysis, which is outside of the scope of this work.

4.4.2 Nanodiamond

The kinetic parameters for the oxidation reactions of different ND powders were determined using the nonisothermal Achar-Brindley-Sharp-Wendeworth approach described in section 4.3.1.1. The temperature-dependent weight loss of UD50, UD90 and UD98 is

obtained from the isothermal TGA data in **Figure 4.19**. The corresponding weight fractions (α) and oxidation rates ($d\alpha/dT$) are shown in **Figure 4.39**.

The oxidation of UD50 starts around 350 °C and reaches the highest weight-loss rate at ~ 510 °C. The entire sample has been oxidized upon reaching 550 °C, suggesting a temperature window of about 200 °C in which UD50 is oxidized. Although oxidation of UD90 does not occur below 400 °C, the maximum weight loss takes place at lower temperatures (490 °C) compared to UD50. This discrepancy can be explained by differences in sample composition. As discussed in section 2.2.2.2 and 4.2.1.1, UD50 contains up to 70% of amorphous and graphitic sp^2 carbon surrounding the diamond crystals. In some cases, crystals are encapsulated in fullerenic shells which shield the diamond core against any interaction with their environment. While oxidation of amorphous and disordered sp^2 species in carbon nanomaterials starts around 350 °C, the more stable fullerene shells surrounding the diamond cores inhibit diamond oxidation, thus shifting the maximum in the oxidation rate to higher values. Similarly, metal impurities such as iron, which are known to catalyze the carbon-oxygen reaction, are also encapsulated by graphitic carbons, preventing catalytic reactions at lower temperatures. The temperature window for the oxidation of

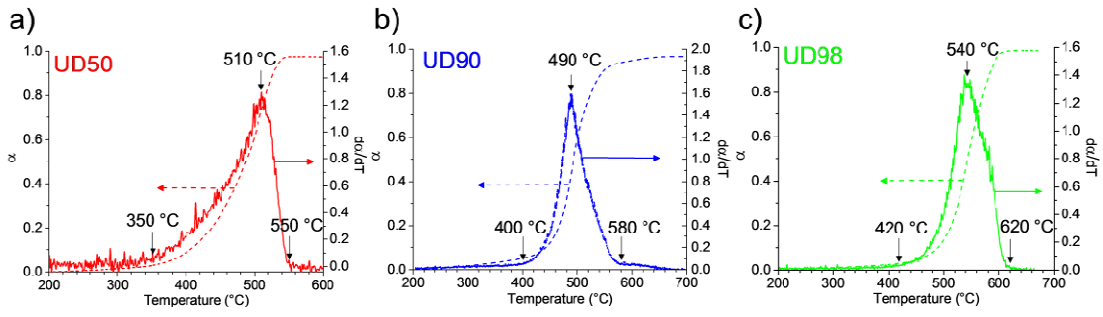

Figure 4.39: Weight fraction α and oxidation rate $d\alpha/dT$ of three different ND powders (UD50, UD90 and UD98). The highest oxidation rate is determined by a maximum in $d\alpha/dT$. The weight loss data was obtained from figure 4.19.

UD90 is ~ 180 °C and thus slightly smaller than that of UD50, as expected. Although acid-purified UD90 has a remaining sp^2 content of ~ 30%, the larger structural variety in UD50 results in broader distribution of oxidation temperatures. In case of UD98, both the start (420 °C) and the maximum weight loss (540 °C) of the oxidation reaction are shifted to higher temperatures. This may be explained by the higher purity of UD98. While the sp^2 carbon content remains rather high (~ 20%), the extensive acid-purification following the production cycle significantly decreased the amount of iron in the sample.

Weight fraction (α) and oxidation rate ($d\alpha/dT$) were used to determine the kinetic parameters of the ND powders according to equation 4-7. The relationship between $\ln[d\alpha/dT/(1-\alpha)]$ and $1/T$ (ABSW plot) is shown in **Figure 4.40**. Activation energies and frequency factors of UD50, UD90 and UD98 were calculated using a linear regression as indicated in **Figure 4.40**.

UD50 exhibits two different oxidation regimes. The low temperature range (370-480 °C) is dominated by the oxidation of amorphous and graphitic sp^2 carbon, which accounts for roughly 70% of the sample weight. The corresponding activation energy and frequency factor are E_A = 88.6 ± 0.3 kJ/mol and A = (1.9 ± 0.1)·10^4 min^{-1}, respectively. In the high-temperature range, the slope steepens and becomes comparable to that of UD90 and UD98 due to oxidation of the remaining diamond crystals. The values of E_A and A change to 190.3 ± 0.3 kJ/mol and (1.9 ± 0.1)·10^{11} min^{-1}, respectively.

In the case of UD90, the slope is constant between 420 and ~490 °C and leads to an activation energy of E_A = 223.2 ± 0.4 kJ/mol and a frequency factor of A = (5.6 ± 0.1)·10^{13} min^{-1}. The activation energy is higher compared to that of UD50 in the high-temperature regime, probably due to the lower Fe content in UD90. The encapsulated Fe particles are

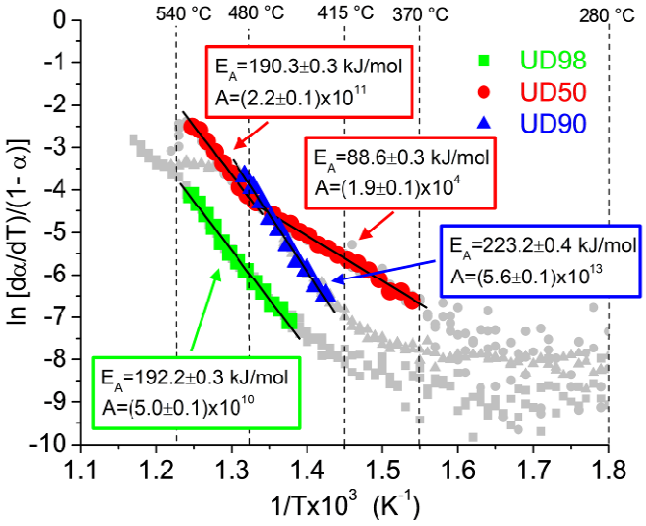

Figure 4.40: Achar-Brindley-Sharp-Wendeworth plot of UD50, UD90 and UD98. The corresponding activation energies and frequency factors were calculated using a linear regression. The fitted data points are indicated in red, blue, and green for UD50, UD90 and UD98, respectively.

catalytically inactive in the low-temperature range. However, upon exposure to high temperatures, the surrounding fullerene shells are removed and Fe catalyzes the carbon-oxygen reaction. The slope of UD90 increases between 370 and 420 °C due to the oxidation of sp^2 carbon, but the amount is too small to allow a separate analysis of the kinetic parameters. At temperatures above ~ 490 °C, oxidation continues but the slope decreases, because of the transition to a diffusion controlled reaction mechanism which lowers the activation energy.

The curve of UD98 shows a similar behavior. However, the calculated activation energy is comparable to that of UD50 at high temperatures, and thus is slightly lower than the values measured for UD90. Since purified UD98 contains a smaller amount of Fe and other metal impurities, the lower activation energy cannot be attributed to catalytic effects. A possible explanation might be a larger contribution of diffusion processes since the

oxidation occurs at higher temperatures compared to UD90. Another reason for the observed differences could be changes in the surface chemistry of UD98 during extensive acid-purification. Treatments in oxidizing acids such HNO_3 or H_2SO_4 increase the concentration of oxygen-containing functional groups on the surface of the diamond crystals and lower their activation energy.

The obtained results are in good agreement with data reported in literature. Pichot et al. measured E_A = 142 ± 5 kJ/mol and E_A = 189 ± 26 kJ/mol for the graphitic and the diamond phase, respectively.[360] The ND samples analyzed by Chiganov et al. exhibited activation energies of E_A = 160 kJ/mol (sp^2 carbon) and E_A = 180 kJ/mol (diamond).[119] The differences in the activation energies of the sp^2 carbon are most likely due to differences in structure and composition of the sp^2 phase. UD50 is the unpurified detonations soot, whereas samples analyzed by Pichot et al. and Chiganov et al. have been partially purified. However, it should be noted that neither of these studies showed a complete removal of Fe and other metal catalysts, making an interpretation of the reported data more difficult.

The reaction rate constants of UD50, UD90 and UD98 were calculated using equation 4-8 and are shown in **Figure 4.41**. In the case of UD50, two different reaction rate constants were determined. UD50(1) is attributed to the oxidation of amorphous and graphitic sp^2 carbon in the low temperature range. The corresponding rate constant is higher than that of UD90 and UD98 at temperatures below 450 °C (inset in **Figure 4.41**). At temperatures above 460 - 470 °C (inset in **Figure 4.41**), the rate constants of UD90 and UD50(2) increase considerably and exceed that of the sp^2 carbon (UD50(1)). UD98 exhibits a lower oxidation rate constant than UD90, probably due to the lower Fe content. The lower rate constant of UD50(1) at higher temperatures can be explained by the fact that activation energy and

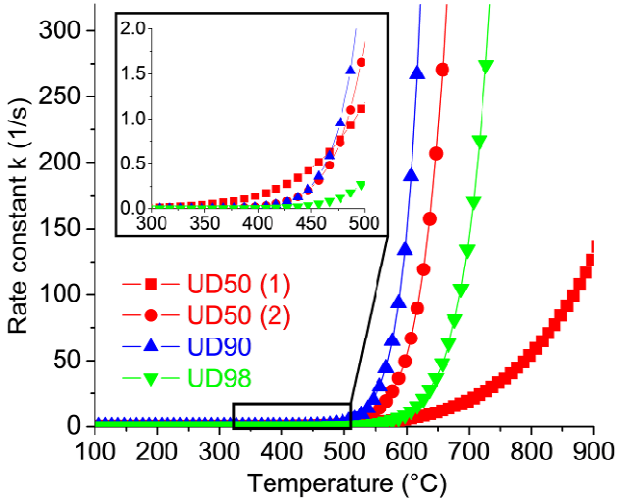

Figure 4.41: Reaction rate constants of UD50, UD90 and UD98 determined using calculated activation energies and frequency factors. UD50(1) corresponds to the rate of the sp^2 phase, while UD50(2) is related to sp^3 carbon.

frequency factor were determined at lower temperatures. Fe particles are encapsulated in graphitic shells and the reaction remains noncatalytic. In contrast, the oxidation of the diamond phase at higher temperatures in UD50, UD90, and UD98 is catalyzed by Fe after removal of the fullerene shells, surrounding the metal particles.

4.4.3 Carbide-Derived Carbon

4.4.3.1 Nonisothermal Thermogravimetric Analysis

In order to study the oxidation mechanism and the reaction kinetics of CDC, we determined weight fraction α and oxidation rate $d\alpha/dT$ of three TiC-CDC samples (**Figure 4.42**) from the TGA data shown in **Figure 4.28**. 600°C-TiC-CDC containing mainly amorphous carbon is oxidized between 350 and 590 °C, reaching the maximal weight-loss rate at approximately 530 °C (**Figure 4.42**a). Oxidation of 1000°C-TiC-CDC (**Figure 4.42**b)

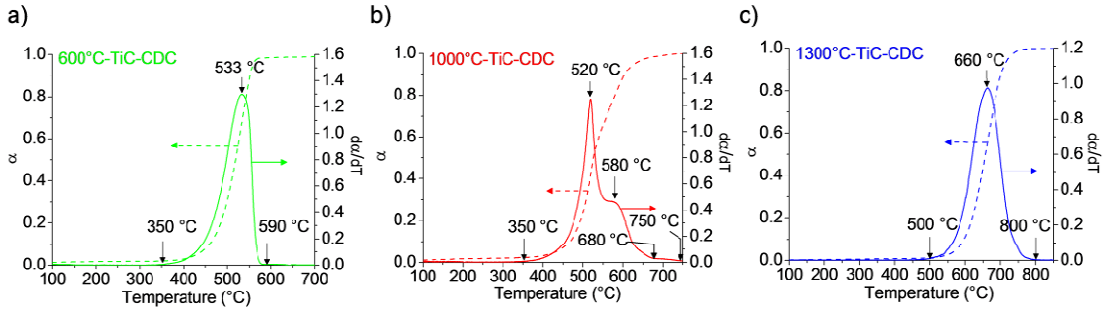

Figure 4.42: Weight fraction α and oxidation rate dα/dT of three TiC-CDC samples chlorinated at 600 °C (a), 1000 °C (b) and 1300 °C (c), respectively. Weight-loss data was obtained from figure 4.28.

consisting of both amorphous and graphitic carbon, starts at similar temperatures (~ 350 °C), but the maximum weight loss occurs at lower temperatures (~ 520 °C). This can be explained by the smaller amount of amorphous carbon in 1000°C-TiC-CDC, and/or slight differences in ordering. 600°C-TiC-CDC and 1000°C-TiC-CDC were synthesized under different conditions and the amorphous phase of both samples may exhibit different structural properties. At temperatures above 550 °C, 600°C-TiC-CDC and 1000°C-TiC-CDC show very different behavior (**Figure 4.42**a and b). The oxidation of the remaining graphitic carbon in 1000°C-TiC-CDC starts around ~ 550 °C, leading to an increase in the weight-loss rate at higher temperatures and a second maximum at approximately 580 °C. The composition of 600°C-TiC-CDC does not change during oxidation and the weight loss decreases continuously after reaching the maximum oxidation rate at ~ 530 °C. The higher resistance to oxidation of graphitic carbons also leads to a broadening of the temperature window (> 330 °C) in which oxidation occurs. The majority of the 1000°C-TiC-CDC sample is oxidized between 350 and 680 °C, but weight loss continues up to 750 °C (**Figure 4.42**b), indicating differences in bond-ordering and level of graphitization.

Oxidation of 1300°C-TiC-CDC takes place between 500 and 800 °C (**Figure 4.42**c). The temperature at which the maximum weight loss occurs is upshifted to 660 °C, suggesting a significant increase in ordering and graphitization. The absence of amorphous carbon narrows the temperature window (~ 300 °C) of the oxidation, compared to the less homogeneous 1000°C-TiC-CDC sample (> 330 °C). However, the temperature range remains larger than that of 600°C-TiC-CDC and most graphitic nanomaterials, suggesting a larger structural variety and a broader distribution of oxidation temperatures.

The oxidation mechanism of the TiC-CDC samples was analyzed using the Achar-Brindley-Sharp-Wendworth method described in section 4.3.1.1. The kinetic parameters were determined by plotting $\ln[d\alpha/dT/(1-\alpha)]$ over $1/T$ (**Figure 4.43**). Activation energy and frequency factor were calculated from the linear regression curves shown in **Figure 4.43**.

The weight loss of 600°C-TiC-CDC starts around 350 °C and the slope of the curve remains almost constant throughout the entire temperature range (350 - 560 °C). The slight

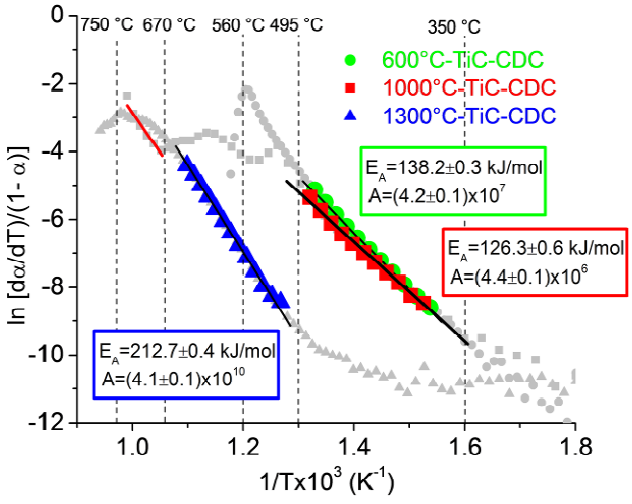

Figure 4.43: Achar-Brindley-Sharp-Wendworth plot of three TiC-CDC samples chlorinated at 600, 1000 and 1300 °C, respectively. Activation energies E_A and frequency factors A were calculated using a linear regression of the experimental data show in color (red, blue and green).

increase between 500 and 560 °C most likely results from the oxidation of more ordered carbons in the sample. Although their content in 600°C-TiC-CDC is very low, they dominate the oxidation at high temperatures after less ordered carbon has been oxidized. The activation energy and the frequency factor are E_A = 138.2 ± 0.3 kJ/mol and A = (4.2 ± 0.1)·10^7 min^{-1}, respectively (**Figure 4.43**).

The slope of the 1000°C-TiC-CDC curve is similar to that of 600°C-TiC-CDC in the low temperature regime (350 - 500 °C) and dominated by the oxidation of amorphous carbon (**Figure 4.43**). The corresponding kinetic parameters are E_A = 126.3 ± 0.6 kJ/mol and A = (4.4 ± 0.1)·10^6 min^{-1}. Unlike 600°C-TiC-CDC, the weight loss of 1000°C-TiC-CDC continues at higher temperatures (550 - 750 °C) due to the oxidation of more ordered and graphitic carbon present in the sample (see **Figure 4.42**). Although one would expect a steeper slope in the high-temperature range because of the higher thermal resistance (larger activation energies) of graphitic carbons, the slope decreases above ~ 520 °C, suggesting a transition in the reaction mechanism to diffusion controlled oxidation.

However, diffusion-limited oxidation processes require the presence of large amounts of reactants and/or reaction products. If the amount of TiC-CDC available for oxidation decreases, diffusion becomes less significant. This may explain the increasing slope at the end of the oxidation reactions between 520 and 560 °C for 600°C-TiC-CDC and between 670 and 750 °C for 1000°C-TiC-CDC (**Figure 4.43**). The slope, and thus the activation energy (E_A = 199.0 ± 7.2 kJ/mol), of the corresponding curve section are similar to that of other graphitic carbons. The linear regression used for the calculation is indicated by the red line in **Figure 4.43**.

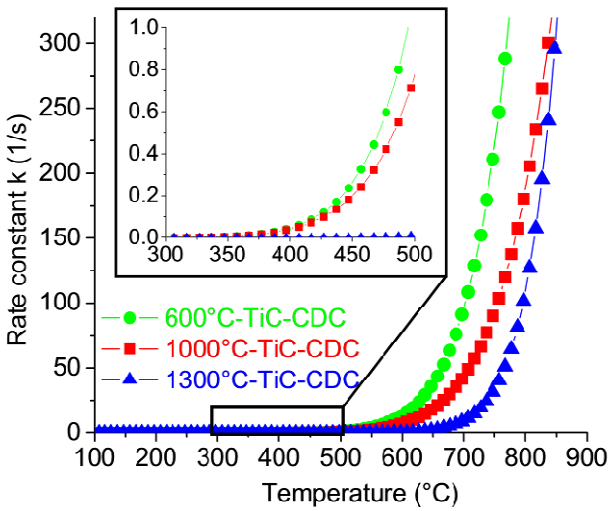

Figure 4.44: Reaction rate constants of TiC-CDC chlorinated at 600, 1000 and 1300 °C. The rate constants were calculated using the activation energies and frequency factors determined by nonisothermal TGA.

Graphitized 1300°C-TiC-CDC did not oxidize below 500 °C and showed a linear behavior between 550 and 670 °C. The slope of the curve is steeper compared to 600°C-TiC-CDC and 1000°C-TiC-CDC at low temperatures, but appears similar to the curve segment of 1000°C-TiC-CDC between 670 and 750 °C (**Figure 4.43**). The values of the corresponding activation energy and frequency factor are 212.7 ± 0.4 kJ/mol and $(4.1 \pm 0.1) \cdot 10^{10}$ min^{-1}.

The reaction rate constants of 600°C-TiC-CDC, 1000°C-TiC-CDC and 1300°C-TiC-CDC are show in **Figure 4.44**. 600°C-TiC-CDC and 1000°C-TiC-CDC show higher reaction rate constants at lower temperature (300 - 500 °C) compared too 1300°C-TiC-CDC. Both samples contain amorphous species, showing significant lower oxidation resistance than the highly graphitized carbon in 1300°C-TiC-CDC.

4.4.3.2 Isothermal Thermogravimetric Analysis

In order to confirm the results obtained from nonisothermal TGA, we analyzed the weight loss of the TiC-CDC samples under isothermal conditions. The weight loss curves of 600°C-TiC-CDC, 1000°C-TiC-CDC and 1300°C-TiC-CDC are shown in **Figure 4.45**. Activation energies and frequency factors were determined by measuring the weight loss of each sample after 25, 50 and 100 min, following the approach described in section 4.4.1.2. Using equation 4-9, we calculated the weight fraction α and plotted ln α over $1/T$ (Arrhenius plot) for each data set (25, 50 and 100 minutes).

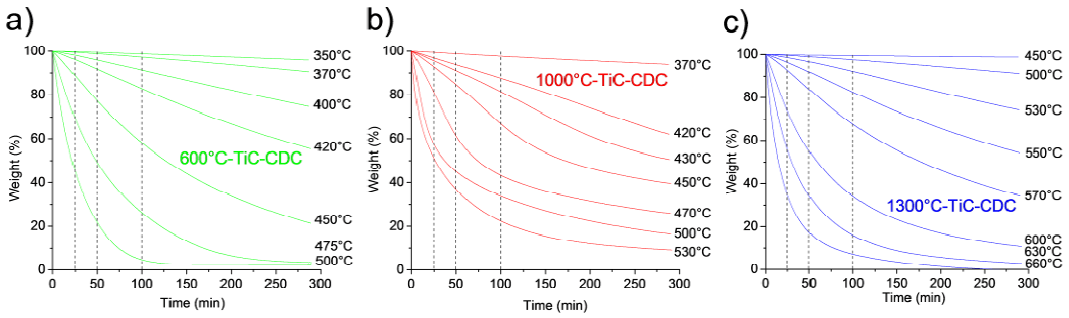

Figure 4.45: Weight loss curves of TiC-CDC chlorinated at 600 (a), 1000(b) and 1300 °C under isothermal conditions. The weight loss was measured for 300 minutes at different temperatures in air. The weight loss data at 25, 50 and 100 minutes was used to determine the activation energies

The resulting curves were fitted using a linear regression (**Figure 4.46**) and both activation energy and frequency factor were extracted from the fit according to equation 4-10, and are listed in **Table 4.6**.

The Arrhenius plots of the TiC-CDC samples can be split into different temperature regimes. In the cases of 600°C-TiC-CDC (**Figure 4.46**a) and 1000°C-TiC-CDC (**Figure 4.46**b), we distinguish between a low temperature (range I) and a high temperature regime (range II). Although the transition temperature may vary slightly for 600°C-TiC-CDC and

Table 4.6: Activation energies (E_A) and frequency factors (A) of TiC-CDC chlorinated at different temperatures. The values were calculated from the linear regression curves shown in figure 4.46.

Time	600°C-TiC-CDC		1000°C-TiC-CDC		1300°C-TiC-CDC		
	range I	*range II*	*range I*	*range II*	*range I*	*range II*	*range III*
	E_A in kJ/mol A in min^{-1}	E_A in kJ/mol A in min^{-1}	E_A in kJ/mol A in min^{-1}	E_A in kJ/mol A in min^{-1}	E_A in kJ/mol A in min^{-1}	E_A in kJ/mol A in min^{-1}	E_A in kJ/mol A in min^{-1}
25 min	140.1±1.9 (5.7±0.1)x10^7	111.5 (7.5x10^5)	131.3±8.3 (1.1±0.1)x10^7	23.4 (6.5x10^{-1})	88.0 (1.7x10^2)	222.9±7.7 (2.1±0.1)x10^{11}	93.0 (4.2x10^3)
50 min	137.4±1.4 (3.8±0.1)x10^7	83.3 (6.7x103^3)	132.6±8.2 (1.3±0.1)x10^7	24.0 (4.6x10^{-1})	134.6 (3.7x10^5)	194.5±9.7 (3.6±0.2)x10^9	53.8 (1.7x10^1)
100 min	131.1±1.3 (1.3±0.1)x10^7	49.5 (2.1x10^1)	126.5±2.1 (4.5±0.1)x10^6	27.7 (4.9x10^{-1})	133.4 (2.6x10^5)	186.6±8.6 (1.1±0.1)x10^9	23.7 (2.0x10^{-1})

1000°C-TiC-CDC, the reaction mechanism in the same range is similar. The oxidation mechanism in range I is controlled by the chemical reaction between carbon and oxygen, and the slope of the Arrhenius curve is independent of the oxidation time. Range II is increasingly dominated by diffusion processes, and kinetic parameters such as activation energy and frequency factor become time-dependent. The average activation energies for 600°C-TiC-CDC and 1000°C-TiC-CDC in range I are 136.2 ± 6.4kJ/mol and 130.1 ± 10.7 kJ/mol, respectively. The corresponding frequency factors were found as (3.6 ± 2.2)·10^7 min^{-1} and (9.5 ± 4.4)·10^6 min^{-1}, respectively. The activation energies in range II decrease with

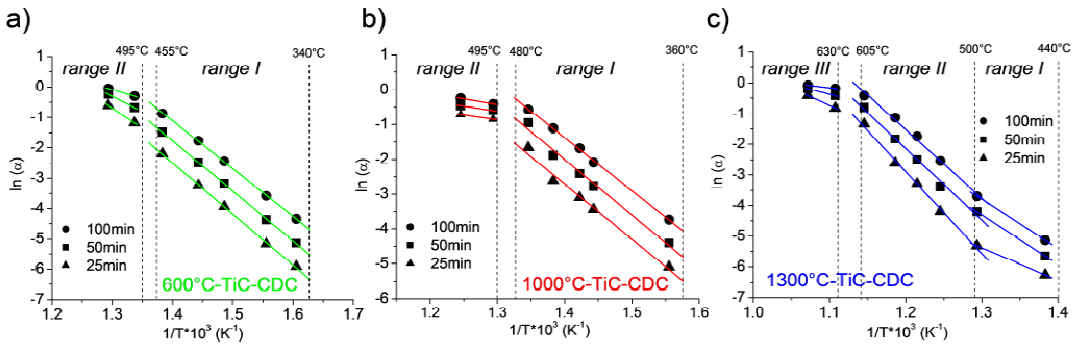

Figure 4.46: Arrhenius plot of TiC-CDC chlorinated at 600 (a), 1000 (b) and 1300 °C(c). The weight fraction α was determined at different temperature between 350 and 630 °C after oxidation for 25, 50 and 100 minutes. Linear regression has been used to fit the experimental data.

increasing time (see **Table 4.6**) and approach values between 20 and 50 kJ/mol, as expected for diffusion-controlled oxidation reactions.

The Arrhenius plot of 1100°C-TiC-CDC can be divided into three oxidation regimes. Range I is characterized by the oxidation of amorphous and disordered carbon at temperatures below ~ 500 °C. The calculated activation energies (~ 135 kJ/mol) are time-independent and similar to that of 600°C-TiC-CDC and 1000°C-TiC-CDC. Although the amount of amorphous carbon in 1300°C-TiC-CDC is very small, it accounts for the weight loss at temperatures below 550 °C and thus determines the oxidation rate. The majority of the 1300°C-TiC-CDC sample is oxidized in range II, followed by a diffusion-based decline in the slope of the Arrhenius curve (range III). While in the cases of 600°C-TiC-CDC and 1000°C-TiC-CDC, the transition to a diffusion-controlled reaction mechanism takes place between 480 and 500 °C, it does not occur below 600 °C for 1300°C-TiC-CDC. The discrepancies are explained by the fact that the total weight loss of 1300°C-TiC-CDC at 500 °C is much smaller compared to 600°C-TiC-CDC and 1000°C-TiC-CDC, and oxidation rates are too low for diffusion to become the reaction controlling process. The average activation energy and frequency factor of 1300°C-TiC-CDC in range II are 201.3 ± 23.3 kJ/mol and $1.0 \cdot 10^{9}$-$2.2 \cdot 10^{11}$ min^{-1}, respectively. The larger scattering of the results originates in a weak time-dependency of the Arrhenius curve, indicating contributions from diffusion processes. Therefore, the kinetic parameters for shorter oxidation times (25 and 50 minutes) are likely to be more accurate and less affected by the time-dependency.
The activation energies and frequency factors are in good agreement with values obtained from nonisothermal TGA, as expected.

4.4.4 Catalytic Effect of Metal Impurities

The synthesis of most carbon nanomaterials requires the use of metal catalysts in order to achieve sufficient control over their structure and properties. Although several catalyst-free synthesis techniques have been developed during the last decades, and yield and efficiency of existing synthesis methods have been improved, large-scale production of carbon nanomaterials still requires addition of metals such Fe, Ni, Co and Mo to induce and promote growth of nanostructures. Unfortunately, most common purification methods are not able to remove all metal impurities and up to 1 - 2 wt% of metal catalyst remain in the sample. As discussed in section 2.2.1.5, metals such as Fe and Ni are known to catalyze the carbon-oxygen reaction and lower oxidation temperatures and activation energies of carbon materials.

Figure 4.47 shows a photograph taken during (**Figure 4.47**a and b) and after (**Figure 4.47**c) oxidation of UD90 at 450 °C in an open tube furnace. A large number of glowing particles were observed at the sample surface during oxidation, indicating a catalytic reaction. The sparking particles were highly mobile and covered distances of up to 1 cm until they extinguished after a few seconds. After oxidation, the sample showed two region of different composition (**Figure 4.47**c). The powder in the center of the quartz boat consisted mainly of iron oxide, as indicated by the red-brown color. At the edge of the quartz boat, the sample remained grey or turned slightly lighter in color, suggesting the presents of ND powder. The differences in the sample composition may be explained a temperature and/or concentration gradient which lead to stronger catalytic oxidation of ND in the center of the quartz boat. However, the catalytic effect of the metal impurities in ND powders is evident.

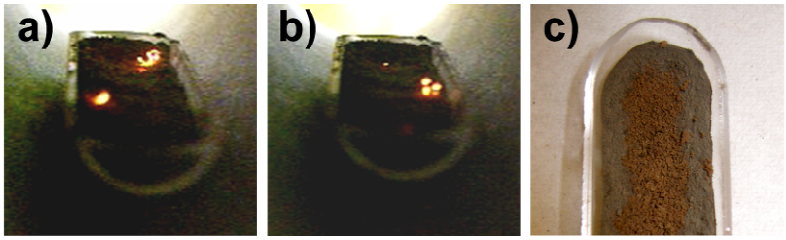

Figure 4.47: Photograph of UD90 during (a, b) and after (c) oxidation at 450 °C in an open tube furnace.

The Fe content (in wt.%) of as-received, oxidized and acid-purified ND powders is shown in **Table 4.7**. Values in the upper row were determined by measuring the weight loss of the ND samples after removal of all carbon phases upon oxidation for 4 h at 800 °C, and analyzing the residual using energy-dispersive X-ray spectroscopy (EDS). The values presented in the lower row were provided by the manufacturer and measured using inductively coupled plasma (ICP). The errors indicated in the table result mainly from inhomogeneities in sample composition.

Table 4.7 Fe content in different ND powders measured using energy-dispersive X-ray spectroscopy (EDS) and inductively coupled plasma (ICP).

Analysis Method	UD90 as-received	UD90 oxidized	UD90 oxid+HCl	UD50 as-received	UD98 as-received
EDS	0.5±0.2	0.7±0.2	0.40±0.05	-	-
ICP[a]	0.68	0.9±0.3	0.20±0.07	1.3	0.24

[a] *as reported by the supplier (measured by Inductively Coupled Plasma)*

In order to demonstrate the effect of Fe on the oxidation behavior of carbon nanomaterials, we performed TGA analysis (**Figure 4.48**a) of metal-free carbon black with and without an addition of UD50 (mixture 1:1). Carbon black alone demonstrated resistance to oxidation at temperatures below ~ 600 °C. However, the mixed powder (Fe content ~ 0.65 wt %) was fully oxidized before even reaching 600 °C.

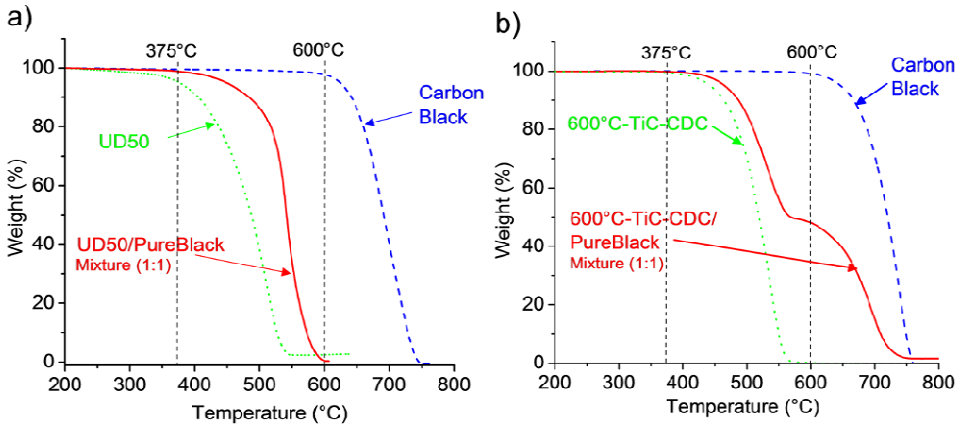

Figure 4.48: TGA curves of metal-free carbon black with and without an addition (mixture 1:1) of UD50 (a) and 600°C-TiC-CDC (b). As-received UD50 and 600°C-TiC-CDC are shown for comparison.

In order to prove that the observed decrease in oxidation temperature of approximately 150 °C results from a catalytic process, and not from heat created by the exothermic oxidation of amorphous carbon, we performed TGA under similar conditions using a mixture of carbon black and highly amorphous Fe-free 600°C-TiC-CDC. **Figure 4.48**b shows that oxidation of the carbon mixture occurs in two distinct temperature ranges. Below 600 °C only TiC-CDC (~ 50 wt%) is oxidized, suggesting that the reaction heat created by oxidation of amorphous carbon between 375 and 600 °C does not significantly affect the activation energy of carbon black. This clearly demonstrates that in the case of ND powders containing Fe impurities, catalytic processes dominate the oxidation reactions.

Catalytic reactions also affect the oxidation mechanism of MWCNTs. TGA experiments and several furnace oxidations were used to measure the weight-loss of MWCNT samples after complete carbon burn-off. The remaining sample weight after oxidation was 2.8 ± 0.4 wt%. Using Raman spectroscopy we analyzed the residual material and identified α-Fe_2O_3 (hematite) to be the predominant phase. Therefore, assuming a Fe/O mass ratio of roughly 7/3, we estimate an initial Fe content of 1.9 ± 0.3 wt%.

According to literature data on catalytic oxidation of carbon materials (see section 2.2.1), a carbon content of > 0.2 wt% is sufficient to catalyze the carbon oxygen reaction. None of the carbon-containing nanomaterials showed sufficient purity to exclude contribution from catalytic reactions.

4.5 Effect of Functional Groups on Raman Spectra of Nanodiamond

The UV Raman spectrum of ND consists of several characteristic features: a first-order Raman mode of diamond lattice which is broadened and red shifted in ND (a peak at ~ 1325 cm^{-1}) compared to bulk diamond (~ 1332 cm^{-1}); a double-resonant D-band around 1400 cm^{-1} (at 325 nm excitation), resulting from disordered and amorphous sp^2 carbon; and a broad asymmetric peak between 1500 and 1800 cm^{-1} (see section 2.3.4). The latter peak has at least four different explanations proposed for its origin. In most cases, it is labeled as the "G band" and directly assigned to the in-plane vibrations of graphitic carbon. However, because the peak significantly differs from the G band of graphitic materials both in shape and position,[296,297] it is sometimes assigned to a mixed sp^2/sp^3 carbon structure [298], or is referred to as a peak of "sp^2 carbon" [299] or "sp^2 clusters" [265], but without any explanation regarding the structure (amorphous, graphitic etc.). There have also been attempts to relate this peak to localized interstitial C=C pairs within the diamond lattice also known as "dumb-bell defects".[260,266]

However, with plenty of various functional groups exposed on the ND surface, the broad band(s) between 1500 and 1800 cm^{-1} may result from overlapping Raman signals of sp^2 carbon species, surface groups such as OH, COOH, and C=C pairs embedded inside the diamond core. In this case, the peak position, intensity, width and shape may all be

influenced by the interplay of these contributions, i.e. may be different for different types of ND.

In the following section, we show how surface structure and surface chemistry affect the Raman spectrum of ND. The ND powders studied in this section were produced by modifying as-received UD90 using various procedures. The resulting samples have been named accordingly: UD90Ox (air oxidized), UD90OxHCl (air oxidized, HCl treated) and UD90H (hydrogenated). UD90Ox was produced from UD90 by air oxidation at 425ºC for 5 h (see section 4.2.1). UD90OxHCl is a product of UD90Ox treatment with boiling aqueous HCl to remove metallic impurities. UD90H was produced by heating UD90 in a H_2 atmosphere at 800ºC for 2 h.

4.5.1 Surface Chemistry of As-Received and Oxidized Nanodiamond

Oxidation in air is one of the simplest ways to purify ND from non-diamond carbon species (see section 4.2.1). However, in addition to purification, air oxidation dramatically changes the surface chemistry of ND.

While Raman spectroscopy is useful to analyze structural features and distinguish between the different carbon species, FTIR spectroscopy was used to determine functional groups and adsorbed molecules on the surface of the carbon. Black and strongly absorbing as-received UD50 shows no detectable FTIR vibrations due to the high content of graphitic and amorphous carbon structures (**Figure 4.49**). The main features in the FTIR spectra of as-received UD90 and UD98 powders are related to C=O (1740 - 1757 cm^{-1}), C-H (2853 - 2962 cm^{-1}) and O-H vibrations (3280 - 3675 cm^{-1} stretch and 1640 - 1660 cm^{-1} bend) which can be assigned to -COOH, -CH_2-, -CH_3 and -OH groups of chemically bonded and

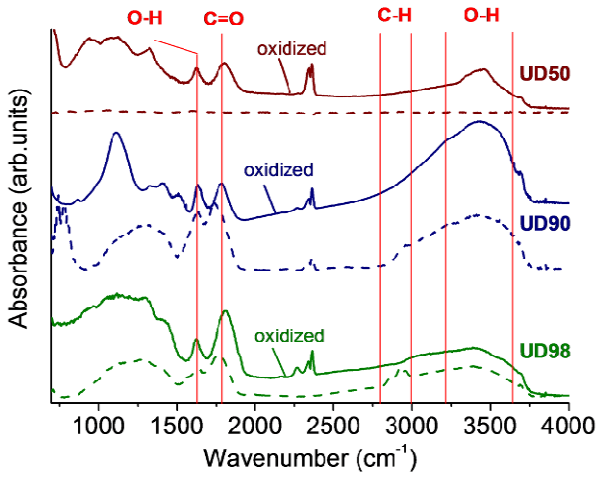

Figure 4.49: FTIR spectra of as-received (dashed line) and air oxidized (solid line) ND samples.

adsorbed surface species, mainly resulting from acid purification[361-363]. The comparison of FTIR spectra of purified (solid lines) and as-received (dashed lines) powders (**Figure 4.49**) reflects the conversion of a variety of surface functional groups into their oxidized derivatives. After oxidation, -CH_2- and -CH_3 groups are completely removed from UD90 and UD98, the amount of –OH groups is increased and C=O vibrations are upshifted by 20-40 cm^{-1} indicating a conversion of ketones, aldehides and esters on the surface into carboxylic acids, anhydrides, or cyclic ketones. The most prominent changes in the surface termination after oxidation were found for UD50 (**Figure 4.49**). Upon the removal of graphitic layers by oxidation, the surface of UD50 became accessible for chemical reactions and is immediately saturated with oxygen or oxygen-containing functional groups.

4.5.2 *In Situ* Raman Studies during Heating in Argon Atmosphere

To further investigate the origin of the 1640 cm^{-1} peak, we monitored temperature-induced changes in the Raman spectrum of ND. *In situ* Raman spectra were recorded in Ar flow to avoid sample oxidation, changes of the surface chemistry, and adsorption from air. As expected for the G band in graphitic materials, the 1640 cm^{-1} peak showed a red shift with an increase in temperature (**Figure 4.50**a). However, the slope of the curve was much steeper than for graphite or nanotubes[327,364], the temperature dependence was nonlinear, and the shape of the 1640 cm^{-1} ND peak changed upon heating. Subsequent cooling of the

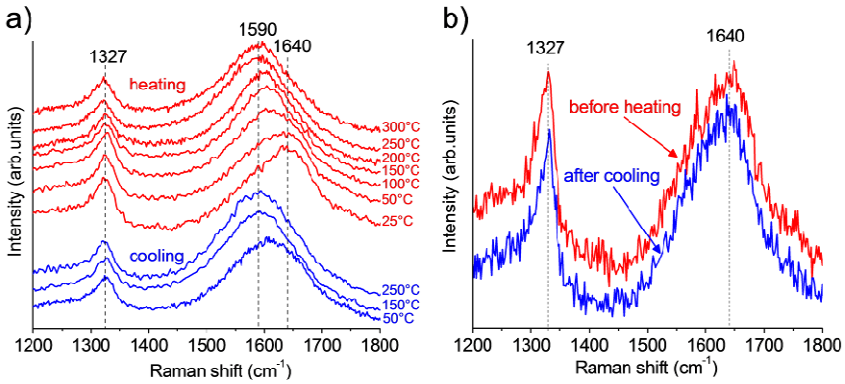

Figure 4.50: *In situ* UV Raman spectra of ND (Alit) in Argon atmosphere at different temperatures (a) and UV Raman spectra of ND (Alit) recorded in air at room temperature before heating and after cooling (b). Spectra recorded using 325 nm laser wavelength. Graph was obtained from Ref. 317.

sample to room temperature in Ar flow did not restore the original shape (**Figure 4.50**a) or position (**Figure 4.51**) of the peak. While the intensity of the peak is nearly constant during the heating-cooling cycle, the peak asymmetry decreases at higher temperatures and disappears around 200 ºC. The peak asymmetry does not re-appear upon cooling to room temperature in Ar flow (**Figure 4.50**a), but is restored after 30 minutes of exposing the cooled sample to ambient air (**Figure 4.50**b) by opening the heating stage. These changes

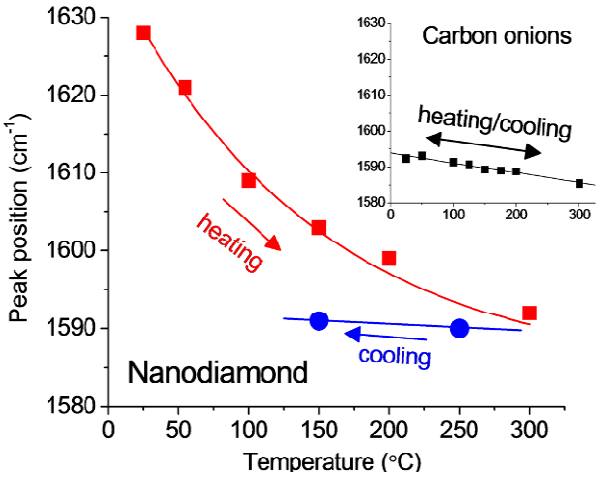

Figure 4.51: Temperature dependence of the 1640 cm^{-1} Raman peak position of ND (Alit) in comparison to G band of carbon onions of similar size. Graph obtained from Ref. 317. Arrows indicate temperature changes.

are not what one would expect for a temperature-induced shift of the G band. The thermal shift of the G band in graphitic materials is known to be completely reversible and a linear function of temperature.[327,364]

Using the same experimental conditions, we measured the temperature changes of the G band of vacuum-annealed UD50 composed of onion-like graphitic particles with sizes of 5-50 nm [365] (inset in **Figure 4.51**). As expected, the position of the G band for this material was found to be fully reversible and a linear function of temperature, with a derivative of 0.029 $cm^{-1}/°C$, which is close to that of carbon nanotubes (0.023 – 0.030 $cm^{-1}/°C$).[327,364] It is interesting, that while very different from the temperature shift of the G band of carbon onions during heating, the 1640 cm^{-1} peak shift of UD90 upon cooling was close to the temperature behavior of the G band of the onions (**Figure 4.51**). This unusual temperature behavior contradicts several assignments of the 1640 cm^{-1} peak in the Raman spectrum of ND proposed in literature, which suggests that it cannot originate from: surface sp^2

carbon[265,337], surface amorphous carbon[338], mixed sp^2/sp^3 carbon[298], or split interstitial defects inside the diamond core of ND[266], as they should all result in small, linear and reversible changes within the temperature range 25 - 300 ºC. While it was shown before that split interstitial defects in bulk diamond can be "healed" by annealing in an inert atmosphere [366], it happens at temperature much higher than 300 ºC. Moreover, once the defects have been annealed, they could not be restored simply by exposing the cooled sample to air, as observed in the case of the 1640 cm^{-1} peak in the Raman spectrum of ND (**Figure 4.50**).

4.5.3 Surface Functionalization and Graphitization of Nanodiamond

Taking into account the observed heating-cooling behavior, we put forth a different explanation regarding the origin of the 1640 cm^{-1} peak in ND. The irreversible loss of asymmetry during heating-cooling in an inert gas flow could be accounted for by the removal of some surface species, which contribute to the Raman spectrum of ND and to the observed peak asymmetry. The subsequent restoration of the asymmetric peak shape upon

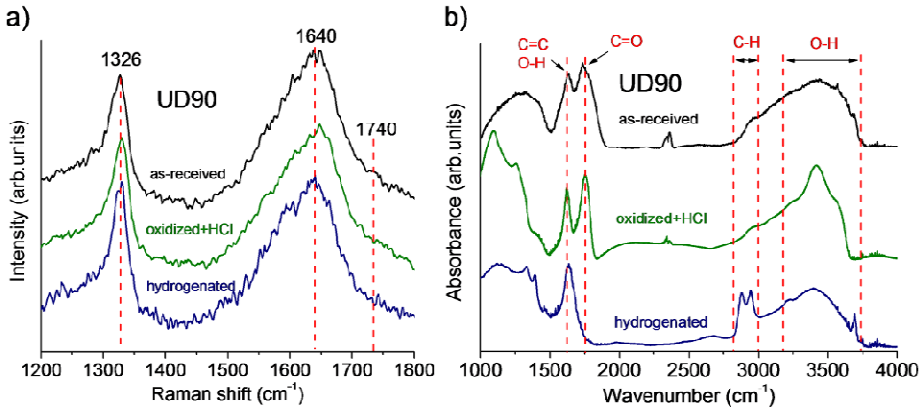

Figure 4.52: UV Raman (a) and FTIR spectra (b) of ND (UD90) with different surface chemistry. Raman spectra were recorded using 325 nm laser wavelength. Graph obtained from Ref. 317.

exposure to ambient air implies that those species are re-created on the surface of ND, which can be explained by adsorption of, or reaction with, components of air. The two most likely bond vibrations that give rise to Raman peaks in this range are O-H bending and C=O stretching.[367]

To distinguish between these two contributions, we eliminated C=O containing groups from the surface of ND by annealing the UD90 powder for 2 h in a hydrogen gas flow of 20 ml/min at 800 °C.[365] The contribution of carbonyl groups is ruled out by observation of the Raman peak at 1640 cm^{-1} for the hydrogenated sample (**Figure 4.52**a), which shows no traces of C=O in FTIR (**Figure 4.52**b). At the same time, O-H peaks in FTIR are not influenced by the hydrogen annealing, supporting the hypothesis that O-H bending vibrations can contribute to the 1640 cm^{-1} peak. Selective removal of O-H containing groups from the surface of ND would provide a direct test of this hypothesis. Unfortunately, it is difficult to realize without simultaneously changing the sp^2/sp^3 carbon ratio. Hydrogen treatment does not remove hydroxyl groups. Moreover, depending on conditions of the treatment, it can increase the O-H content as a result of C=O to C-O-H conversion.[365] High-temperature inert gas annealing, which removes all functional groups[365], cannot be used because it leads to the graphitization of ND, which will naturally affect the shape and position of the 1640 cm^{-1} Raman peak.

Based on presented analysis, we thus assume that the 1640 cm^{-1} peak in the Raman spectrum of ND results from overlapping of contributions from sp^2 carbon and O-H bending vibrations. The source of O-H vibrations is either covalently attached surface functional groups and/or adsorbed water. ND powders readily adsorb moisture from air, surpassing many other carbon nanomaterials in this respect, as illustrated by the TGA curves recorded in air (**Figure 4.53**). The initial weight loss of ~ 10% on a UD90 curve at

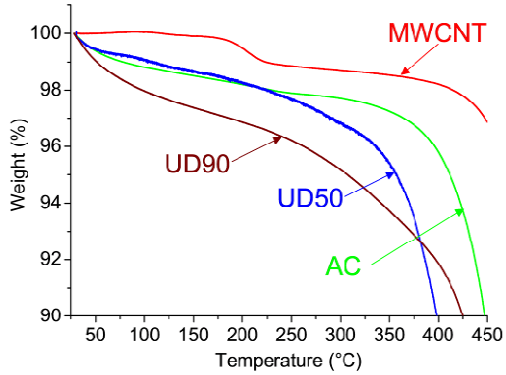

Figure 4.53: TGA curves of MWCNTs, UD50, UD90 and activated carbon (AC) recorded in air using a heating rate of 1 ºC/min. Graph obtained from Ref. 317.

temperature below the onset of amorphous carbon oxidation at ~ 400 ºC [368] corresponds mainly to water desorption.

Several other experiments were carried out in order to test the O-H contribution hypothesis. UV Raman spectra of UD90Ox recorded at room temperature and normalized with respect to the intensity of the 1640 cm^{-1} peak are shown in **Figure 4.54**. Oxidation in air results in the removal of sp^2 carbon and formation of oxygen containing surface functional groups such as O-H, COOH, C=O, and $(CO)_2O$ (anhydro-).[368] If the entire 1640 cm^{-1} peak were a peak of sp^2 carbon, then a longer oxidation time would simply result in a decrease of the intensity of this peak. It turns out that not only the intensity, but the shape of this peak is changed with oxidation time (**Figure 4.54**).

Both changes are natural under the assumption that the 1640 cm^{-1} peak is a superposition of the G band of graphitic carbon and O-H bending vibrations from adsorbed or covalently linked species on the ND surface. With longer oxidation time, the relative intensity of the G band (at 1590 cm^{-1}) decreases compared to the O-H bending (at 1640 cm^{-1}) (**Figure 4.54**a). Peak fitting using three Lorentzian functions fixed at 1590 cm^{-1},

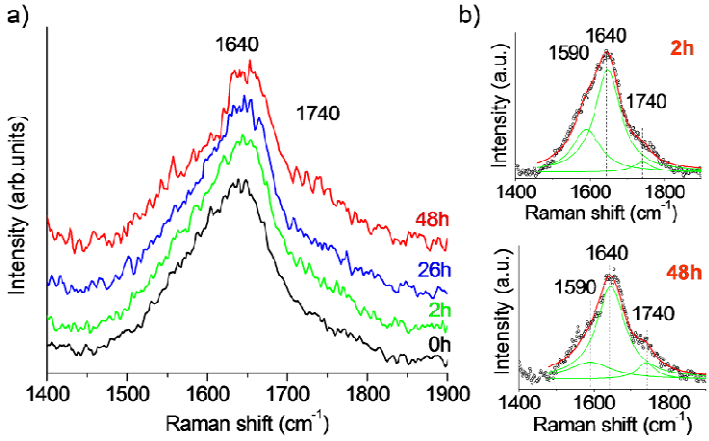

Figure 4.54: UV Raman spectra of as-received and air oxidized UD90 (a) and results of peak fitting for ND oxidized for 2 and 48 h using three Lorentz functions fixed at 1590, 1640 and 1740 cm^{-1} (b). Spectra were obtained from Ref. 317 and were recorded using 325 nm laser wavelength.

1640 cm^{-1} and 1740 cm^{-1} reproduces the overall shape of the composite peak and the trend of the sp^2/O-H ratio with increasing oxidation time (**Figure 4.54**b). The peak fitting also gives an idea of the overestimation that is potentially introduced when evaluating the amount of non-diamond carbon content based on the Raman spectra, assuming the whole 1640 cm^{-1} peak to be a peak of sp^2 carbon.

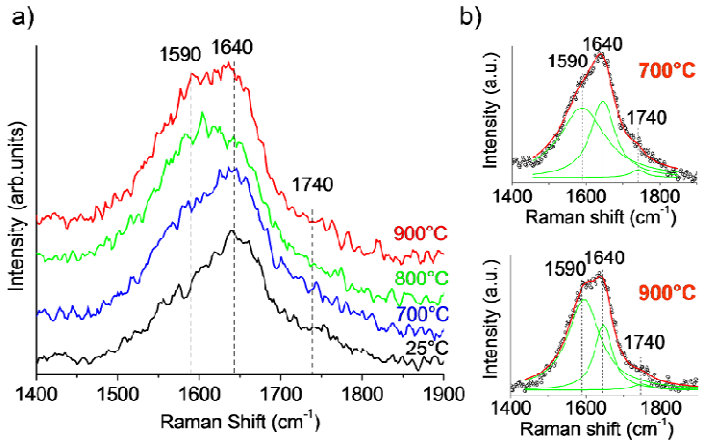

Figure 4.55: UV Raman spectra of air oxidized UD90 before and after Argon annealing for 1 h at 700, 800 and 900 °C(a) and results of peak fitting using three Lorentz functions fixed at 1590, 1640 and 1740 cm^{-1} (b). Spectra were obtained from Ref. 317 and were recorded using 325 nm laser wavelength.

Oxidation, which increases the content of carbonyl groups, also results in a pronounced shoulder at ~ 1740 cm^{-1} (**Figure 4.54**a), which is the correct position for the C=O stretching Raman peak.[367] Thus, the spectra in **Figure 4.54** show that the 1640 cm^{-1} peak is a superposition of the G band of graphitic carbon, the O-H bending and C=O stretching vibrations. Annealing of UD90Ox in Ar at 700 – 900 ºC leads to the opposite trend in the O-H/sp^2 peak ratio (**Figure 4.55**), which corresponds to the progressive removal of O-H groups and an increase of sp^2 carbon content with annealing temperature.

At higher temperatures, the Ar annealing would completely remove surface functionalities and convert ND particles into carbon onions[365] with the 1640 cm^{-1} Raman peak being transformed into the G band of graphitic carbon positioned at 1590 cm^{-1}.

4.5.3.1 *In Situ* FTIR Studies during Heating of Nanodiamond

In order to monitor the removal of O-H-containing species and related changes in the 1640 cm^{-1} peak, we recorded FTIR spectra of UD90 at elevated temperatures (**Figure 4.56**). As the quartz window of the heating stage absorbs in IR it was impossible to record the FTIR spectra in Ar atmosphere, therefore the spectra in **Figure 4.56** were recorded in air. Upon heating, the IR peak at 1640 cm^{-1} underwent a slight red shift between 100 and 300 ºC. The shift may be induced by the weakening of O-H bonds with temperature or by the gradual removal of O-H groups (both of chemically linked and adsorbed species), revealing a peak of conjugated C=C stretch vibrations located at 1600 - 1620 cm^{-1}. [367] The O-H stretch band (a broad peak at 3200 - 3600 cm^{-1} in **Figure 4.56**) is significantly decreased at $T \geq 200$ ºC, suggesting that at $T \geq 200$ ºC, the stretching of conjugated C=C bonds is the main reason for the ~ 1620 cm^{-1} IR absorption. At 425 ºC, the oxidation of sp^2 carbon in

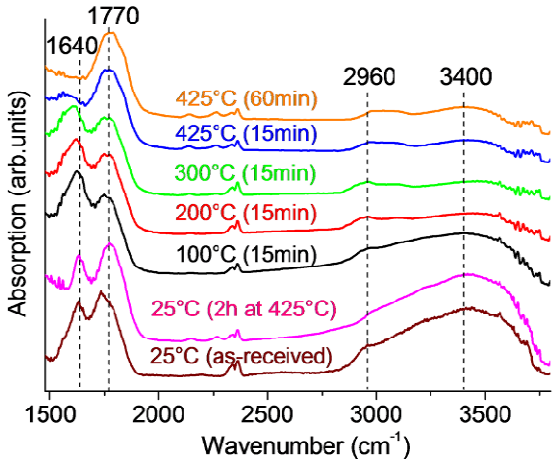

Figure 4.56: *In situ* FTIR spectra of UD90 held at specified temperatures and cooled down to room temperature after being held constant for 2 h at 425 ºC (Ref. 317). All spectra were recorded from ND being in contact with air all time.

ND powders[368] leads to the disappearance of the small broad C=C peak at ~ 1600 cm^{-1} within 60 minutes (**Figure 4.56**). When the sample is cooled down to room temperature after being held for 2 h at 425 ºC in air, the peak at 1640 cm^{-1} is restored (**Figure 4.56**), suggesting a significant contribution from O-H bending vibrations at room temperature. The observed temperature trend of the 1640 cm^{-1} IR peak of UD90 is in good agreement with previous results.[361] However, it should be noted that the temperature at which this IR peak begins to change or completely disappears depends on the surface chemistry of ND and can vary for different powders. For example, for NDAlit powder (not shown), we have found that the IR peak at 1620 - 1640 cm^{-1} totally disappears within 5 minutes at 300 ºC in air.

Assuming the hypothesis of strong O-H bending contribution to the Raman spectrum of ND is true, an unusually low intensity of Raman signal in the range 3000 - 3700 cm^{-1} as compared to the peak at 1640 cm^{-1} for a dry UD90Ox sample (**Figure 4.57**) should be mentioned. The 3000 - 3700 cm^{-1} range corresponds to O-H stretching vibrations, which are typically more intense than O-H bending vibrations. Indeed, the difference can clearly be

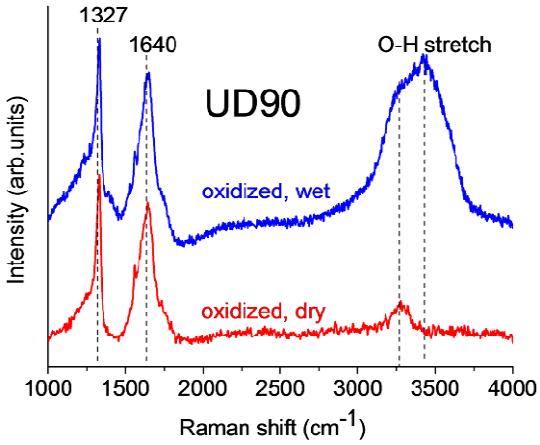

Figure 4.57: Contribution of water coolant to first- and second-order UV Raman spectrum of ND powder. Spectra were obtained from Ref. 317 and were recorded using 325 nm laser wavelength.

seen by comparing the intensities of 1640 cm^{-1} and 3000–3700 cm^{-1} peaks in a spectrum of bulk water (see **Figure 3.5**). However, for water molecules confined in a small volume on the surface or between the aggregated ND particles, the ratio of the intensities can be significantly different from that observed in bulk water. It has been theoretically shown before for water inside single-walled carbon nanotubes that the confinement reduces the number of hydrogen bonds from 2-4 per H_2O molecule in bulk water to just 1 molecule.[369]

Reduction in hydrogen bond number results in splitting the broad O-H stretch peak into two peaks. The first peak, centered at ~ 3250 cm^{-1} and with an intensity lower than the of O-H, can be ascribed to O-H groups that are involved in hydrogen bonding between H_2O molecules. The second peak is located at a higher frequency (~ 3250 cm^{-1}) and shows a higher intensity compared to the 1640 feature. This peak corresponds to non-hydrogen bonded O-H groups. Because the non-hydrogen bonded O-H groups of water in a nanotube are subjected to steric hindrance regarding the stretching vibrations, the position of the second O-H stretch peak is predicted to be unusually high (> 4000 cm^{-1}).[369]

For a dry UD90Ox sample (**Figure 4.57**) we observed a small broad peak at 3270 cm^{-1} and no other peaks up to 4000 cm^{-1} (the upper limit for our spectrometer). Thus, the unusual intensity ratio of O-H bending and stretching vibrations, observed for a dry UD90Ox powder in **Figure 4.57**, can be attributed to the effect of confinement of O-H stretching vibrations, which have been studied theoretically for carbon nanotubes[369,370] and other porous materials, and may take place in confined space between the particles in dry nanodiamond powder. The nanophase of water around ND particles has been recently found in ND gels by DSC[371]. The unusual thermodynamic properties were well explained by the confinement.

4.6 Change of Nanodiamond Crystal Size by Oxidation in Air

As the dimensions of a crystal are reduced, the increasing surface/volume ratio results in significant changes of properties, especially when entering the lower nanometer range. For example, ND particles with diameters about 4 nm have ~ 20% of the total number of atoms on the surface. Because the physical properties of nanocrystals are strongly size-dependent, it is crucial to control and accurately measure the crystal size. To some extent, ND crystal size can be controlled by the synthesis conditions, e. g., the volume of the detonation chamber.[372] However, it is not something that can be easily changed. Therefore, ND suppliers provide powders of a size that they can produce. However, there were only few attempts to control the average crystal size in ND powders, including sintering and other compaction techniques.[373,374]

In this section, we focus our efforts on determining the potential of air oxidation for adjusting the crystal size in ND powders. Earlier studies on oxidation of nanodiamond

resulted in an increase of the average crystal size, suggesting the removal of smaller diamond crystals.[375,376] However, a reduction in average crystal size has yet not been achieved.

The oxidized ND samples were analyzed by high-resolution transmission electron microscopy (HRTEM), X-ray diffraction (XRD) and Raman spectroscopy in order to monitor changes in structure and size of the diamond crystals upon oxidation.

4.6.1 Transmission Electron Microscopy Studies

As-received UD90 was oxidized for 2, 6, 17, 26 and 42 h at 430 °C, which is the temperature for slow ND oxidation as discussed in section 4.2.1.[377] **Figure 4.58**a and b show the HRTEM images of two ND powders oxidized at 430 °C for 2 and 42 h, respectively. While oxidation for 2 h (**Figure 4.58**a) removes mainly amorphous carbon and other non-diamond species[368], longer oxidation times result in selective oxidation of smaller crystals

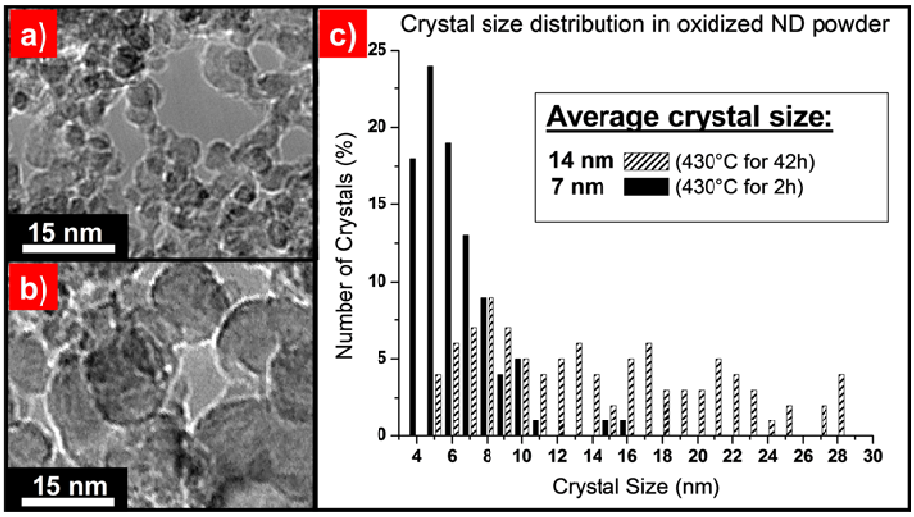

Figure 4.58: TEM analysis of nanodiamond powders (Ref. 377). HRTEM images of ND powders oxidized at 430 °C for a) 2 h and b) 42 h. Oxidation in air selectively removes small diamond crystals, shifting c) the crystal site distribution towards larger values. HRTEM images were slightly defocused to reveal crystal contours.

(**Figure 4.58**b), thus shifting the size distribution towards larger values. The weight loss due to oxidation was 13% and 74% after 2 and 42 h, respectively.

We determined the size of ~ 200 crystals in each sample in order to estimate the average crystal size (**Figure 4.58**c). While 2h oxidation in air results in an average crystal size of ~ 7 nm, the value is upshifted to ~ 14 nm after 42 h oxidation. Since crystal growth is not expected under such conditions, large crystals (15 - 30 nm) observed after oxidation must be present in the pristine powder. However, because they are usually covered by smaller crystals and remain within agglomerates, it is difficult to observe them in HRTEM, indicating the limitations of this characterization technique and the low statistical reliability.

4.6.2 Size Characterization Using X-ray Diffraction

We conducted XRD analysis (**Figure 4.59**) for a more accurate and statistically significant estimate of changes in the average crystal size. The XRD patterns of ND powder oxidized at 430 °C for 2 h and 42 h show peaks at 43.9°, 75.5° and 91.5° corresponding to the [111], [220] and [311] planes of the cubic diamond lattice (a_C = 3.571 Å), respectively (**Figure 4.59**a). Small peaks appearing in the XRD pattern after 42 h oxidation are due to iron oxide and other impurities in the sample, the content of which increases with increasing loss of diamond due to oxidation. Increasing background at low angles originates from the sample holder. The Scherrer equation, often used for size characterization in crystalline materials, neglects potential lattice strains and can lead to values smaller than the actual crystal size.[378]

By measuring the broadening of the diffraction peaks using the Williamson-Hall analysis[379] (**Figure 4.59**b) one can estimate the crystal size (L) as well as potential lattice strains (ε). Both contribute to an increase in the linewidth β given by:

$$\beta = \beta_L + \beta_\varepsilon , \tag{4-12}$$

with

$$\beta_\varepsilon = \frac{K \cdot \lambda}{\cos\Theta \cdot L} , \tag{4-13}$$

and

$$\beta_\varepsilon = 4\varepsilon \cdot tan\Theta , \tag{4-14}$$

where K is a constant reflecting the particle shape (K = 1 for spherical particles), Θ is the scattering angle and λ is the wavelength of the X-ray radiation (λ = 0.154 nm). Combining equations 4-12, 4-13 and 4-14 we obtain:

$$\frac{\beta \cdot \cos\Theta}{\lambda} = \frac{1}{L} + \frac{4\varepsilon \cdot tan\Theta}{\lambda} \tag{4-15}$$

Plotting ($\beta \cdot \cos\Theta/\lambda$) versus ($2 \cdot \sin\Theta/\lambda$) gives a straight line with the slope 2ε and an intercept of $1/L$, known as Williamson-Hall plot (**Figure 4.59**b)[379]. While the [111] and [311]

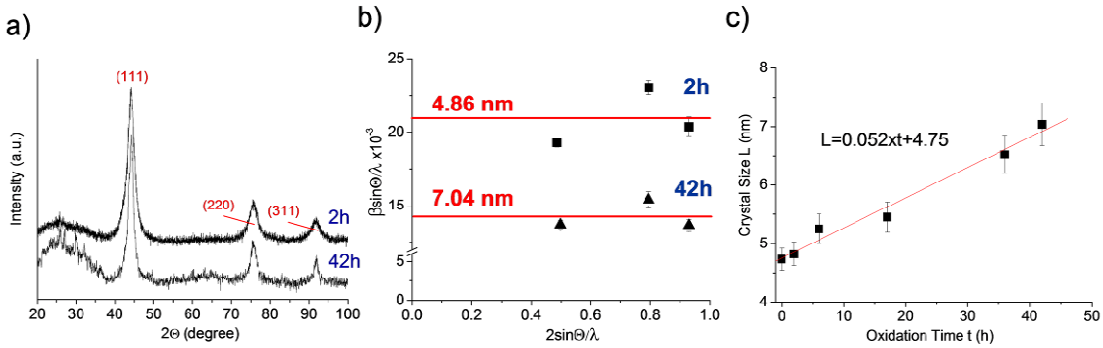

Figure 4.59: (a) XRD pattern of ND powder oxidized at 430 °C for 2 h and 42 h, showing the characteristic [111], [220] and [311] diffraction peaks of diamond (Ref. 377). (b) The line broadening can be used to estimate the crystal size using the Williamson-Hall analysis. (c) ND crystal size as a function of oxidation time.

peaks show similar broadening, the value of the [220] line was found to be slightly higher. This effect, which was observed before[380], is believed to result from a hexagonal distortion of the cubic diamond lattice, but cannot be ascribed to strain anisotropy.[381] The particle size can be estimated by averaging the broadening of the [111], [220] and [311] peaks using a straight line (**Figure 4.59**b) giving a value of 4.8 nm and 7.0 nm after 2 and 42 h oxidation, respectively. Using this approach we calculated the average crystal size of the oxidized powders (**Figure 4.59**c). However, it is necessary to keep in mind that averaging the contributions from different scattering peaks might further increase the discrepancies between calculated values and the actual crystal size. Moreover, Palosz et al. demonstrated that diamond nanocrystals typically exhibit lattice strains due to the extensive surface reconstruction in the core-shell nanoparticles, suggesting that size-calculations based on the Deby-Scherrer equation such as the Williamson-Hall analysis may oversimplify the diffraction of nanocrystals and should only be considered semi-quantitative.[382]

4.6.3 Crystal Size Measurements Using Raman Spectroscopy

As discussed in section 2.3.4.2, Raman spectroscopy can also be used to measure the crystal size of nanostructured solids. In most cases size characterization using Raman spectroscopy is based on the phonon confinement model (PCM), which uses changes in Raman frequency and Raman peak shape to estimate the crystal size.

Although several attempts have been made to relate confinement-induced changes in the Raman spectrum of ND to the crystal size, the agreement between calculated and experimental data and the accuracy of the fitting procedure are still unsatisfactory. Therefore, Raman spectroscopy is currently not able to quantitatively measure the average crystal size in

ND powders. However, with a better understanding of phonon confinement effects in the Raman spectrum of ND, Raman spectroscopy may be used to accurately measure the average crystal size and determine changes in the size distribution.

In the following section we investigate the effects of crystal size, defect concentration and size distributions on the Raman spectra of ND and modify the PCM in order to account for their contributions and to improve the agreement between the theoretical predictions and experimental Raman data.

4.6.3.1 Raman Spectra of Oxidized Nanodiamond

Figure 4.60a shows the changes of the diamond Raman peak after oxidation in air at 430 °C for 2, 6, 17, 26 and 42 h. The corresponding average crystal sizes have been determined by X-ray diffraction using the Williamson-Hall analysis (see section 4.6.1.2) and are 4.8, 5.2, 5.5, 6.5 and 7.0 nm, respectively. In order to minimize laser-heating and avoid laser-induced oxidation, ND powders were dispersed in water during Raman analysis. Although O-H groups were found to contribute to the Raman spectrum of ND, as discussed in section 3.2.2, they do not affect the Raman intensity in the frequency range between 1100 and 1400 cm^{-1} (**Figure 4.60**b).

The confinement-induced asymmetry of the Raman peak decreases with increasing oxidation time, leading to a narrower diamond line (**Figure 4.60**a). It is important to note that the intensity of the shoulder around ~ 1250 cm^{-1} also decreases with oxidation time, suggesting a possible correlation with the crystal size. Although a similar peak is observed in the Raman spectra of highly amorphous sp^2 carbons[247,301], we do not expect significant contributions of sp^2 species because of the high diamond content > 96% in oxidized ND

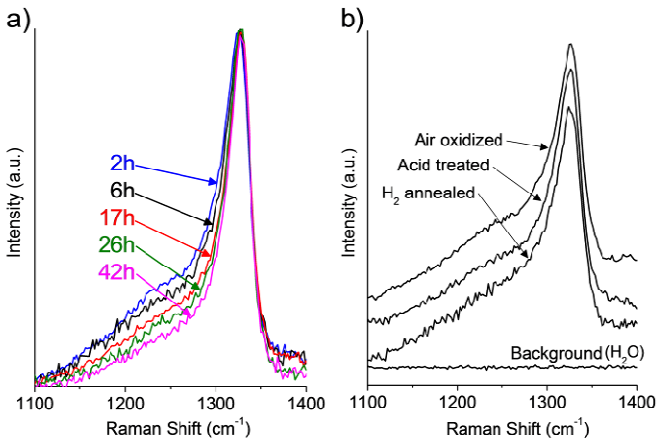

Figure 4.60: a) Diamond Raman peak recorded after oxidation at 430 °C for 2, 6, 17, 26 and 42 h in air. b) Comparison of air-oxidized, acid-treated and H_2-annealed ND showing no significant changes in Raman spectra between 1100 and 1400 cm^{-1}. All spectra were recorded using 325 nm laser excitation and water cooling to avoid laser-induced heating. Graph obtained from Ref. 377.

powders. While the shoulder at ~ 1250 cm^{-1} has been observed before[276,383], it received much less attention compared to other Raman features and remains largely unknown. Some authors have assigned the shoulder to confinement effects in general, but the peak has never been described in detail or considered in the PCM.

To exclude possible contributions from functional groups or surface plasmons, we modified the surface chemistry of the ND crystals using air oxidation (oxidized UD90), acid treatments (as-received UD90 was acid-purified) and hydrogen annealing (**Figure 4.60**b). The corresponding FTIR spectra are shown in **Figure 4.49** and **Figure 4.52**b. It can be seen that changing the surface chemistry does not significantly affect the Raman spectrum in the frequency range 1100 - 1400 cm^{-1}, and both asymmetric peak-broadening as well as the shoulder at 1250 cm^{-1} remain nearly unchanged. Therefore, we assume that the shoulder results directly from the ND crystals as a consequence of their confined size.

4.6.3.2 Limitations of Current Phonon Confinement Models

In most of the former studies only a single ND sample was analyzed and compared to microcrystalline or bulk diamond. However, for a precise study of confinement related changes in the Raman spectra of nanocrystals and to improve the reliability of the PCM, it is necessary to provide different samples in the size range of 3 - 20 nm, where confinement effects are dominant and easy to observe.

Another crucial factor is the laser excitation wavelength used during Raman analysis. The intensity ratio between diamond and non-diamond Raman features is low in the visible range, but increases as the wavelength enters the UV range. Thus Raman spectra recorded from ND samples using visible laser excitation are often dominated by Raman features of non-diamond species, which hinder a line-shape analysis of the diamond peak. In other cases, strong fluorescence overlaps with the Raman spectra, requiring background subtraction and extensive base-line corrections (see **Figure 2.24**). In both cases, an exact determination of the diamond peak line-shape, position and width is difficult, if not impossible.

UV laser excitation minimizes contributions from non-diamond species to the Raman spectra and allows an unadulterated characterization of the diamond line. However, since photon energies are higher compared to visible light and strongly absorbed by ND samples, laser-induced heating is more likely and can lead to excessive sample damage during Raman analysis (see section 3.2.2). Even at low temperatures, where sample burning or other structural changes are inhibited, temperature-induced shifts in the Raman peak position[272,384] overlap with confinement effects and lead to inaccurate results during size-characterization.

Finally, while qualitative size analysis using Raman spectroscopy is commonly based on visual judgement with respect to evaluating the agreement between calculated and measured Raman spectra, quantitative size measurements with high accuracy require a computational approach to determine the best fit of experimental data.

We first measured the ND crystal size of the oxidized powders using the models of Ager et al.[275] and Yoshikawa et al.[276] (**Figure 4.61**). The theoretical Raman spectra were calculated following equation 2-33:

$$I(w) \cong \int_0^1 \frac{\exp(-\vec{q}^2 L^2/4)\cdot 4\pi\vec{q}^2}{\left[\omega-\varpi(\vec{q})\right]^2-(\Gamma/2)^2}dq\,,$$

where q is the phonon wave vector, ω is the Raman frequency, L is the crystal size, and $\omega(q)$ and Γ are the phonon dispersion relation and the natural line width of the zone-center Raman line, respectively. A detailed derivation of equation 2-33 is given in section 2.3.4.2.

The approach of Yoshikawa et al. accounts for size-related changes in the phonon lifetime, leading to larger downshift and higher peak asymmetry compared to Ager et al. (**Figure 4.61**a). Although differences are considerably small for larger crystals, they become

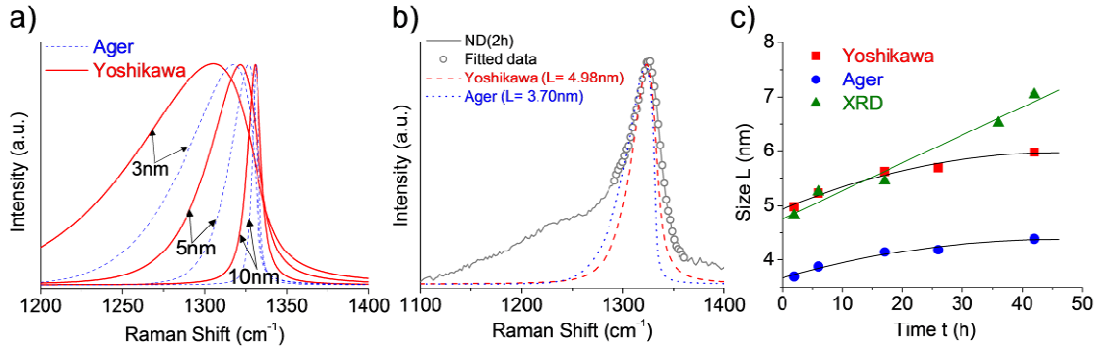

Figure 4.61: (a) Calculated Raman spectra for 3, 5 and 10 nm diamond crystals using the approach of Ager et. al and Yoshikawa et al. (b) Raman spectrum of ND powder oxidized for 2 h at 430 °C in air and corresponding peak fit. Data used for peak fitting is indicated by the circles. (c) Calculated crystal size for ND powders oxidized for 2, 6, 17, 26 and 42 h at 430 °C. X-ray diffraction data is shown for comparison.

significant for crystal sizes below 10 nm and are therefore important for size-characterization of ND powders.

Since both models do not account for the shoulder at ~ 1250 cm^{-1}, we only fit experimental data in the range 1290 - 1360 cm^{-1}. The obtained fits and the corresponding crystal sizes for the ND powder oxidized for 2 h at 425 °C, referred to as ND(2h), are shown in **Figure 4.61**b. Although both models lead to crystal sizes comparable to that obtained from XRD in the range 3 - 5 nm, the agreement between calculated and recorded Raman spectra is fairly low. The calculated crystal sizes of all oxidized powders are presented in **Figure 4.61**b, in comparison to XRD results. While Ager's model leads to slightly lower size values, both approaches show an increase in crystal size with increasing oxidation time, in agreement with XRD data. Crystal sizes calculated using Yoshikawa's model closely match the values obtained from XRD analysis for 2, 6, and 17 h, but are lower for longer oxidation times (> 20 nm). Changes in crystal size L (in nm) with increasing oxidation time t (in h), as measured by Raman spectroscopy, can be described using a second order polynomial:

$$L = C_1 \cdot t^2 + C_2 \cdot t + C_3 \qquad (4\text{-}16)$$

where C_1 = $-5.0 \cdot 10^{-4}$, C_2 = 0.04, C_3 = 4.94 for Yoshikawa's, and C_1 = $-3.4 \cdot 10^{-4}$, C_2 = 0.03, C_3 = 3.68 for Ager's model.

It should be noted that the measured sizes represent average values. HRTEM characterization of the oxidized ND powders revealed a broad size distribution, showing ND crystals sizes of 3 to 20 nm or larger (see **Figure 4.58**). Faster oxidation of small-diameter ND crystals leads to an up-shift in the average crystal size. The discrepancies between XRD and Raman-based size calculations observed for longer oxidation times (> 20 h) may result from the difference in the effective cross-section of both techniques with

respect to the increasing contribution of larger ND crystals. The sensitivity towards defects and changes in lattice spacing is also expected to be different for both techniques.

4.6.3.3 Changes in Phonon Lifetime

In their model Yoshikawa et al. assumed the line width Γ (FWHM) of the diamond peak representing the phonon lifetime, to be dependent on the crystal size L. Their experiments on microcrystalline diamond revealed a broadening of the diamond peak with decreasing crystal size, which was approximated by the relation:

$$\Gamma = A + \frac{B}{L}, \tag{4-17}$$

where Γ and L are the FWHM (in cm^{-1}) and ND crystal size (in nm), respectively. The parameter B is material-specific and characterizes the size-dependency of the FWHM. A represents the FWHM of bulk diamond, but includes the spectrometer-related line broadening. The parameters determined by Yoshikawa et al. are A = 2.990 cm^{-1} and B = 145.74. Sun et al[385] used a similar approach and found A = 9.45 cm^{-1} and B = 275.73. However, these results were determined using microcrystalline diamond and might not hold at the nanoscale. In order to test the reliability of the reported size-dependency, we set Γ as fitting parameter, in addition to the crystal size L. The obtained results are presented in **Figure 4.62**. It can be seen that optimizing both L and Γ leads to a better agreement between calculated and measured Raman spectra, in particular at higher frequencies (compare **Figure 4.62**a and **Figure 4.61**a). The values of L and Γ of all oxidized ND powders are shown in **Figure 4.62**b.

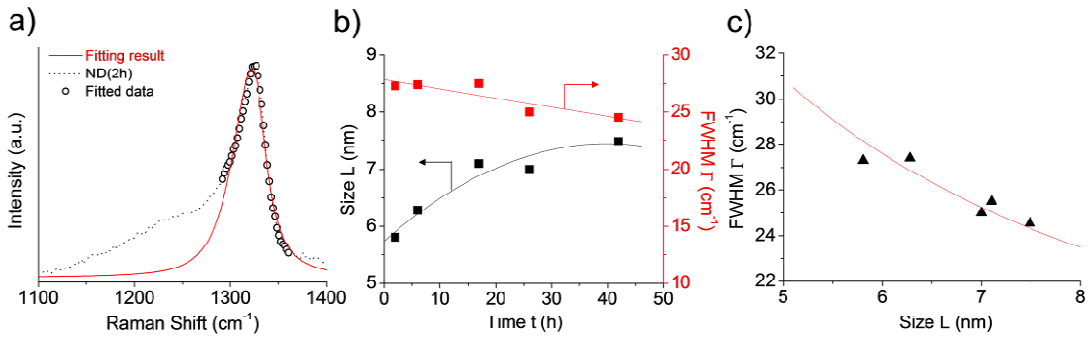

Figure 4.62: (a) Raman spectrum of oxidized ND (2 h at 430 °C) fitted using peak width Γ (FWHM) and crystal size L as fitting parameter. Similar fits were used for all oxidized ND powders to determine (b) changes in Γ and L as function of oxidation time and (c) the relationship between both parameters.

As expected, the L increases with increasing oxidation time. The time-dependency of L (in nm) can be described by equation 4-16. The corresponding parameters are $C_1 = -1.1 \cdot 10^{-3}$, $C_2 = 0.08$, and $C_3 = 5.74$. The FWHM (in cm^{-1}) decreases linearly with oxidation time following:

$$\Gamma = D_1 \cdot t + D_2 , \qquad (4\text{-}18)$$

where D_1 and D_2 are -0.08 and 27.8, respectively. The resulting relationship between L and Γ is shown in **Figure 4.62**b. The data was fitted by equation 4-17 according to the approach suggested by Yoshikawa et al. and Sun et al. The parameter A was set to 11.0 cm^{-1}. This value corresponds to the FWHM measured for bulk diamond and includes the spectrometer-related line broadening. B was obtained from the fit and found to be 99.66, which is smaller than the values reported by Yoshikawa et al. (145.74) and Sun et al. (275.73). The large differences may be explained by the fact that their results were obtained from microcrystalline diamond rather than samples showing different crystal sizes in the nanometer range. Although consideration of changes in the phonon lifetime of nanocrystals

leads to a better agreement between theoretical and experimental Raman data, the discrepancies remain fairly large.

4.6.3.4 Size Distribution in Nanodiamond Powders

ND powders contain diamond crystals with sizes ranging from 3 to 30 nm as shown in section 4.6.1. While the majority of the nanocrystals show diameters between 4 and 5 nm, the Raman scattering cross section is proportional to the crystal volume and thus much larger for larger crystals. On the other hand, confinement effects such as the asymmetric peak broadening are more distinct for small crystals (< 10 nm). Therefore, experimentally obtained Raman spectra are expected to contain Raman features from both small and large ND crystals. However, a simultaneous contribution to the total Raman intensity leads to a complex line-shape that cannot be fitted using a single peak in the PCM.

Figure 4.63 shows the calculated diamond Raman peaks of 3, 5 and 7 nm ND crystals, in comparison to a sample that contains different amounts of 3 and 7 nm crystals, each contributing equally to the overall intensity. The Raman signal of a 3 nm crystal is more than 12 times weaker than that of a 7 nm ND crystal. Thus, although the relative amount of large

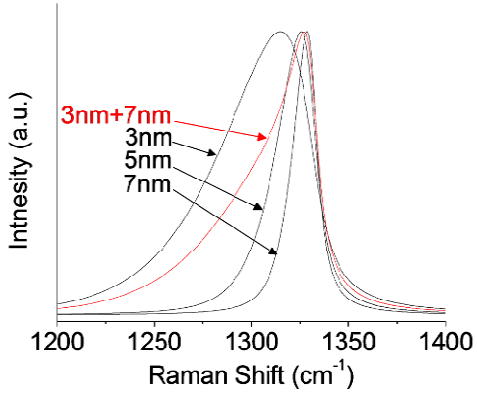

Figure 4.63: Calculated Raman spectra for different ND crystal sizes in comparison to that of a sample containing a binary size-distribution.

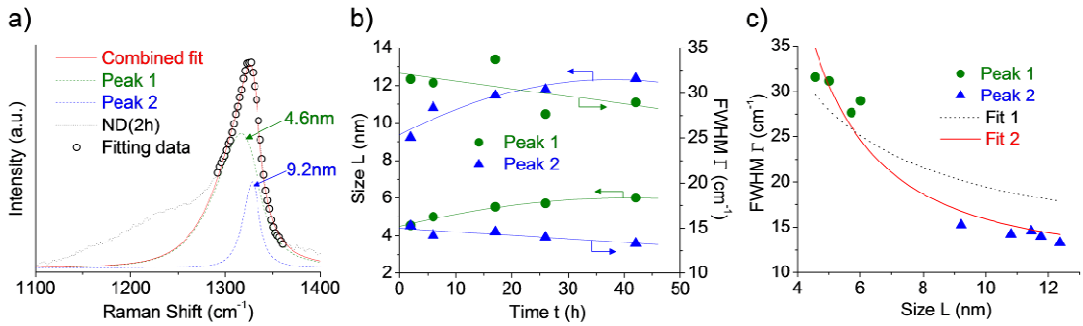

Figure 4.64: (a) Raman spectrum of oxidized ND (2 h at 430 °C) fitted using two peaks in order to account for small and large ND crystals. A similar fitting procedure was used for all oxidized ND powders in order to determine (b) changes in Γ and L as function of oxidation time and (c) the relationship between both fitting parameters.

ND crystals in the sample is small, their contributions to the overall Raman intensity cannot be neglected. However, the calculated Raman intensity of a sample containing only 5 nm ND crystals is very different compared to the spectra resulting from a mixture of 3 and 7 nm crystals (**Figure 4.63**), even though both samples exhibit the same average crystal size (5 nm).

In order to account for the complex line shape resulting from simultaneous contributions of different crystals sizes, we fitted the Raman spectra of all oxidized powders using two separate peaks, with Peak 1 and Peak 2 representing smaller and larger ND crystals, respectively (**Figure 4.64**a). Changes in L and Γ upon oxidation are shown in **Figure 4.64**b. Both Raman peaks indicate a nonlinear increase in L with increasing oxidation time following relation 4-16. The corresponding parameters are C_1 = -2.1·10^{-3}, C_2 = 0.16, C_3 = 9.4 for Peak 1, and C_1 = -9.0·10^{-4}, C_2 = 0.07, C_3 = 4.5 for Peak 2.

Γ decreases linearly and can be approximated by equation 4-18, where D_1 and D_2 were found as -0.04 and 15.0 for Peak 1, and -0.085 and 32.2 for Peak 2. The relationship between L and Γ is plotted in **Figure 4.64**c. It can be seen that equation 4-17 (Fit 1), used for the fit

in **Figure 4.62**, results in a rather poor fit to the computed data. A better agreement (Fit 2) is achieved using the relation:

$$\Gamma = A + \frac{B}{L^2}. \tag{4-19}$$

The parameter A was set to 11.0 and represents the measured FWHM of bulk diamond. The value of B was found as 491.25.

Therefore, accounting for the broad size distribution of ND powders leads to a better agreement between calculated and experimental Raman data (compare **Figure 4.64**a and **Figure 4.61**b). Considering the volume-dependence of the Raman intensity, one can potentially estimate the contribution of various crystal sizes to the total Raman intensity and determine the size distribution in the ND powders. **Figure 4.65**a and b show the Raman spectra of ND oxidized for 2 and 42 h, respectively. Both spectra were fitted using 3

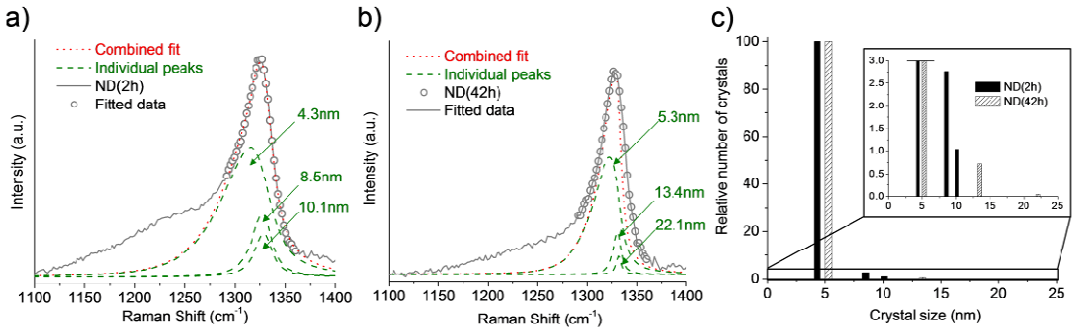

Figure 4.65: Raman spectra of ND oxidized for 2 h (a) and 42 h (b) fitted using 3 individual peaks. The size distribution was determined by correcting the Raman intensity if the individual crystal sizes for differences in crystal volume.

individual peaks. The corresponding crystal sizes are 4.3, 8.5 and 10.1 nm for ND(2h) and 5.3, 13.4 and 22.1 nm for ND(42h). The relative number of ND crystals was determined by correcting the Raman intensity of each peak for the crystal volume. The resulting size distribution is shown in **Figure 4.65**c. It can be seen that the size distribution broadens with

increasing oxidation time and the average crystal size is shifted towards higher vales, in good agreement with results obtained from HRTEM (**Figure 4.58**) and XRD (**Figure 4.59**) studies.

However, the described approach remains unable to account for the broad shoulder centered at ~ 1250 cm^{-1}. Therefore, two additional factors will be taken into consideration, lattice defects and the fine structure of the phonon branches in the vibrational density of states, both of which will be discussed in the following section.

4.6.3.5 Phonon Dispersion and Lattice Defects

Previous studies on phonon confinement in nanocrystals did not account for possible contributions from lattice defects. However, *L* represents the coherence length and is therefore a measure of the distance between dislocation, vacancies, interstitials, impurities and other defects within the crystal lattice. The assumption that *L* represents the crystal size is only valid for defect-free crystals, where the surface is considered to limit the propagation of the phonons. This assumption does not hold for imperfect crystals produced by detonation methods which contain cracks and dislocations as shown in **Figure 4.66**. Other

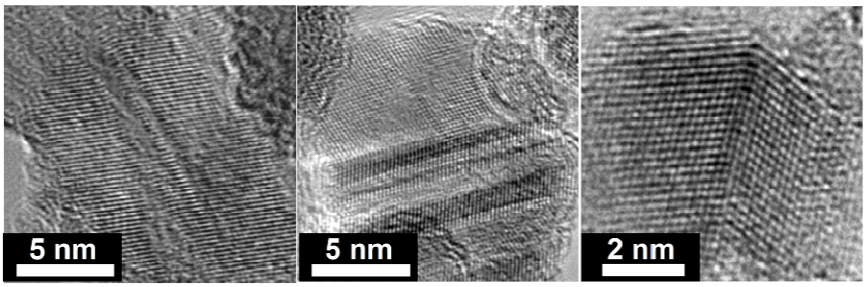

Figure 4.66: HRTEM images of ND crystals. Detonation synthesized ND crystals exhibit lattice defects such as cracks and dislocations which affect phonon propagation.

lattice defects such as impurity interstitials, dumbbell-defects, and vacancies have also been observed before. As a consequence, the coherence length L becomes significantly smaller than the actual ND crystal size.

Therefore, while the results above were produced assuming the ND crystals to be larger than 3 nm (L > 3 nm), we now allow vibrational domains (coherence lengths) with L < 3 nm to contribute to the Raman spectrum. In addition, the frequency range used for fitting is extended to 1100 - 1400 cm^{-1}.

The fitting results for ND(2h) are shown in **Figure 4.67**a. Two peaks have been used for the analysis. It can be seen that the agreement between calculated and measured Raman spectra is significantly improved and the broad shoulder (< 1300 cm^{-1}) can be well fitted

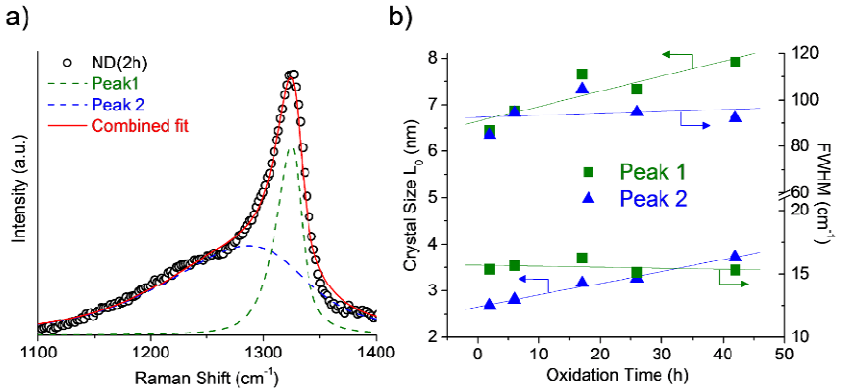

Figure 4.67: (a) Raman spectrum of oxidized ND (2 h at 430 °C) fitted using two peaks. (b) Changes in L and FWHM with increasing oxidation time.

using this approach (**Figure 4.67**a). The corresponding L (and Γ) for Peak 1 and Peak 2 are 6.45 nm (15.6 cm^{-1}) and 2.67 nm (84.8 cm^{-1}), respectively. Changes in L and Γ upon oxidation are shown in **Figure 4.67**b. Peak 1 corresponds to L values in the range 6 - 8 nm and may be assigned to defect-free 6 - 8 nm ND crystals or to less defective, larger ND

crystals (> 8 nm). The L values obtained from Peak 2 are significant smaller and range between 2.6 and 3.7 nm. Assuming the majority of the ND crystals to be 4 - 8 nm in size, a coherence length of 2 - 4 nm may suggest 1-2 defects per ND crystals. While this is in good agreement with HRTEM studies, the reported numbers merely represent the average values. Defect-free ND crystals of similar size and crystals with 3 or more defects have also been observed.

Ager et al. and Yoshikawa et al. estimated the crystal size by reducing the three-dimensional integration in equation 2-37 to a one-dimensional integration over a spherical Brillouin zone (BZ) using an averaged one-dimensional dispersion curve of the form $\omega(\vec{q}) = A + B \cdot \cos(\vec{q} \cdot \pi)$. However, this approximation is only valid for small phonon wave vectors $|\vec{q}| < 0.1$, but oversimplifies the energy dispersion of the phonon modes for larger wave vectors. A coherence length of 2.6 nm would allow phonons with wave vectors $|\vec{q}| > 0.1$ to contribute to the Raman signal. According to equations 2-25 and 2-26, an average crystal size of 4 nm leads to a phonon wave vector uncertainty of $\Delta|\vec{q}| \sim 0.09$. Therefore, while the dispersion relation of Yoshikawa et al. can be used for L = 4 nm, coherence lengths below 3 nm require a more accurate description of the energy dispersion of the individual phonon branches, in particular for $|\vec{q}| > 0.1$. Moreover, it should be noted that equation 2-25 underestimates the uncertainty for strongly confined phonons and phonons with larger $\vec{q}$ values may contribute to the Raman spectra, requiring a more accurate consideration of the phonon energy dispersion relations.

In this study we used the calculated dispersion relations from Pavone et al. (**Figure 4.68**), which are in good agreement with experimental data obtained so far. The optical

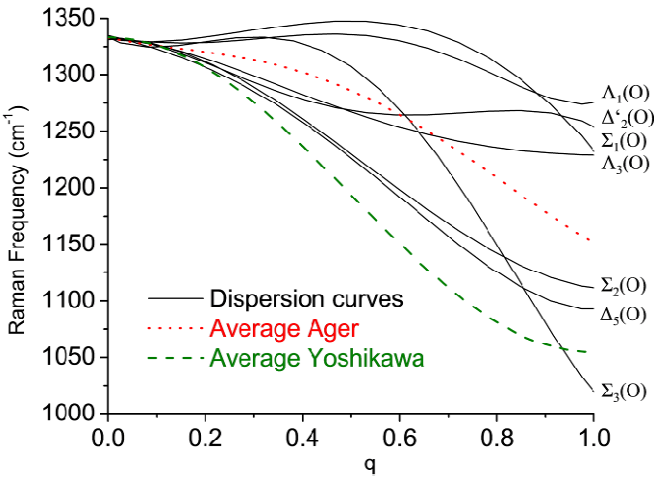

Figure 4.68: Energy dispersion of phonon modes in diamond after Pavone et al. (solid black lines).

phonon branches of the [110], [100] and [111] direction are referred to as Σ, Δ, and Λ, respectively, following the notation of Warren et al.[386,387] and plotted in **Figure 4.68**. The individual phonon branches were fitted using polynomial functions of the type:

$$w(q) = A + B \cdot q + C \cdot q^2 + D \cdot q^3 + E \cdot q^4 + F \cdot q^5 \qquad (4\text{-}20)$$

The corresponding coefficients *A*-*F* are shown in **Table 4.8**. It is important to mention that the absolute values for q vary for the Σ, Δ, and Λ directions. The size of the BZ depends on the lattice spacing (see equation 2-31) and is therefore different for the [110], [100] and [111] directions.

Table 4.8: Coefficients of the polynomial fitting functions used to describe the energy dispersion of the individual phonon branches

	A	B	C	D	E	F
Λ_1	1332.41	-48.68	52.92	820.93	-1940.67	1057.13
Λ_3	1332.69	15.89	-774.82	1478.03	-1238.23	415.97
Δ_2	1332.48	-113.54	873.49	-1700.98	1290.34	-449.49
Δ_5	1332.81	51.63	-1381.23	3135.02	-3670.5	1626.12
Σ_3	1332.13	-184.58	1382.08	-2935.51	1424.39	0
Σ_1	1332.02	13.66	-892.48	1639.97	-838.27	0
Σ_2	1332.19	-35.25	-393.37	33.21	175.23	0

Figure 4.68 suggests that only Δ_5(O) and Σ_2(O) branches with $|\vec{q}|$ ~ 0.4, and Σ_3(O) and Λ_3(O) branches with $|\vec{q}|$ ~ 0.6 exhibit phonon frequencies that can contribute to the broad shoulder around 1200-1300 cm^{-1}. The crystal sizes needed to provide the required uncertainty in the phonon wave vector are smaller than the actual ND crystals (L > 4 nm, $|\vec{q}|$ < 0.1).

However, as discussed above, L may be significantly smaller than the actual crystal size. In order to account for defect contributions and the energy dispersion of the phonon branches we fitted the Raman spectrum of ND(2h) using seven peaks, each attributed to one of the individual phonon branches in **Figure 4.68**. The results are shown in **Figure 4.69**. In general, there is a good agreement between calculated and measured Raman data, suggesting that phonon wave vectors from small vibrational domains can indeed be responsible for the broad shoulder at 1250 cm^{-1} typically observed in the Raman spectra of ND powders. The corresponding L values are shown in **Table 4.9**. It should be noted that since the size of the

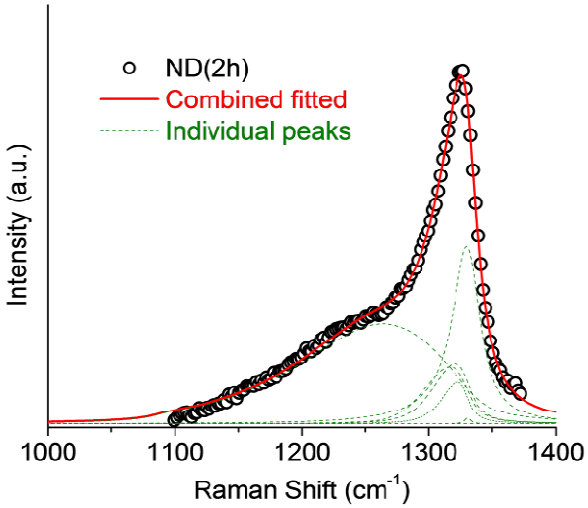

Figure 4.69: Raman spectrum of oxidized ND (2 h at 430 °C) fitted using seven peaks, each representing the contribution of a different dispersion relation.

Table 4.9: Calculated coherence lengths for the phonon branches shown in Figure 4.68.

	L (in units of a)	***L*** (in nm)
Λ_1	54.7	11.3
Λ_3	12.3	2.5
Δ_2	48.9	17.4
Δ_5	5.2	1.9
Σ_3	7.3	1.8
Σ_1	11.5	2.9
Σ_2	15.5	3.9

BZ depends on the crystalline direction, the lattice constant a for the Δ, Σ, and Λ directions used in equation 2-33 is given by 0.357, 0.252, and 0.206 nm, respectively.

While in the computations shown above, each crystal size is only represented by one phonon branch for simplicity reasons, adding the contributions of the remaining six phonon branches for each *L* value would evidently lead to an improvement in the fitting procedure. However, computations using 49 peaks are much more time-consuming.

Although the described approach is more complex, it provides a possible explanation for the broad shoulder at ~ 1250 cm^{-1} and may allow an estimate on the number of defects in the ND crystals.

5 DISCUSSION

5.1 Oxidation of Carbon Nanomaterials

5.1.1 Carbon Nanotubes

The oxidation behavior of CNT samples depends on various factors. While the thermal stability of an individual CNT is defined by its structure (e.g. diameter, number of walls, defect density), the oxidation behavior of bulk samples containing millions of different nanostructures is mainly determined by the size-distribution of the CNTs, as well as contents of amorphous carbon and other impurities such as metal catalyst and surface functionalities.

Due to the complex composition of most CNT samples, an accurate interpretation of thermal analysis data is unfeasible without sufficient information on synthesis conditions and potential post-treatments such as acid-purification. Even if the composition of the sample is known, determining the reaction kinetics is difficult and remains a major challenge due to the simultaneous contributions of the various factors. Therefore, *in situ* Raman spectroscopy and HRTEM studies were used as complementary techniques to allow for a correct interpretation of TGA data and a better understanding of the reaction kinetics that take place.

Figure 5.1 compares the oxidation behavior of DWCNTs and MWCNTs during *in situ* Raman spectroscopy studies (**Figure 5.1**a) and TGA analysis (**Figure 5.1**b). The high oxidation temperatures of vacuum-annealed MWCNTs were beyond the temperature range of the heating stage and did not allow for any *in situ* Raman studies. The oxidation behavior of SWCNTs and related changes in the Raman spectra are comparable to that of DWCNTs

due to similarities in size and structure (see section 4.1.2). Therefore, in the following section we will distinguish between large-diameter MWCNTs and highly crystalline, small-diameter CNTs. DWCNTs were chosen as the representative for small-diameter CNTs.

The oxidation of CNT samples can be divided into three temperature regions (**Figure 5.1**a). At temperatures below ~ 350 °C (region I), only water and other adsorbed species are removed form CNT surface, but oxidation of carbon does not occur. Region II is characterized by the removal of amorphous and disordered carbon from the sample. However, the temperatures remain insufficient for CNT oxidation to occur. Above ~ 400 °C (region III), both amorphous carbon and CNTs are oxidized simultaneously. The individual reaction rates depend on both the temperature and the composition of the sample.

The transition between region I and II typically occurs around 350 - 370 °C. The transition temperature between region II and III varies from sample to sample, and depends on the relative amount of amorphous carbon and the structural properties of the CNTs.

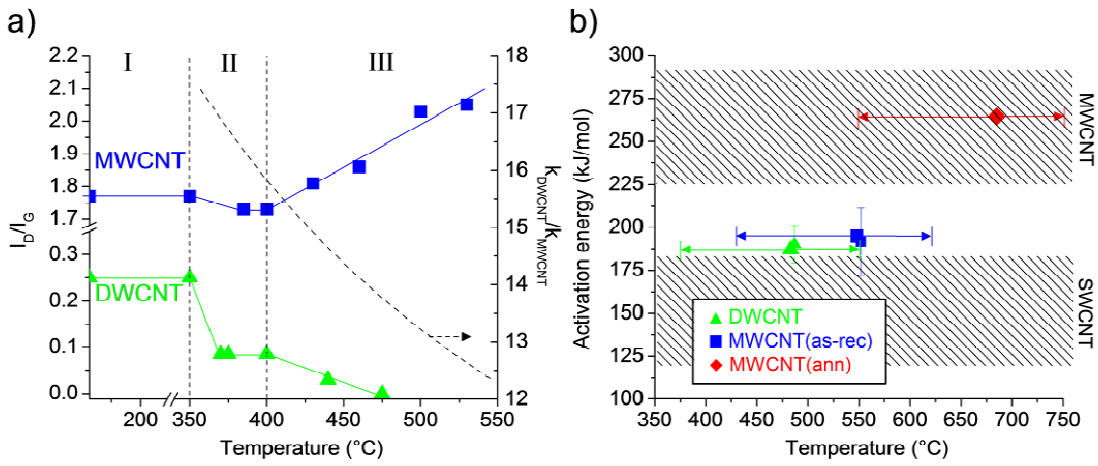

Figure 5.1: Oxidation of DWCNTs and MWCNTs (as-received and vacuum-annealed) analyzed using a) in situ Raman spectroscopy and b) TGA. The shaded area in b) indicated the range of values reported in literature.

As-received DWCNTs exhibit a lower I_D/I_G ratio than as-received MWCNTs, suggesting a higher structural perfection and/or a lower content of amorphous carbon (region I). *In situ* Raman studies under isothermal and nonisothermal conditions demonstrated the possibility of selectively removing amorphous carbon from CNT samples between 350 and 400 °C without damaging the tubes. The removal of amorphous carbon from the DWCNT sample upon oxidation revealed a ~ 65% decrease in I_D/I_G (from 0.25 to 0.09), while in case of MWCNTs the values decreased only by ~ 2 - 3% (from 1.77 to 1.73). These results suggest that the majority of the D band intensity in the Raman spectrum of as-received DWCNTs can be ascribed to amorphous carbon, while the D band of MWCNTs originates mainly from structural defects. Thus, only I_D/I_G values measured at ~ 400 °C can be used to evaluate the structural perfection of the CNTs, while the difference in I_D/I_G before and after oxidation at 400 °C can be understood as a measure of purity (content of amorphous carbon). While the contributions of small amounts of amorphous carbon may be insignificant for the weight loss in TGA studies, they strongly affect the Raman spectra of the samples (shielding effect).

This is an important finding because it demonstrates that in some cases, the I_D/I_G is not an accurate measure of the structural perfection or the purity of CNT samples, and that additional structural characterization during oxidation is required for a correct interpretation of the I_D/I_G ratio and a differentiation between contributions from amorphous carbon and lattice defects. A detailed description of temperature- and oxidation-induced changes in the Raman spectra of SWCNTs, DWCNTs and MWCNTs is given in section 4.1.

Figure 5.1b summarizes the most important kinetic parameters of the oxidation of DWCNTs and MWCNTs. The x-axis represents the temperature at which the maximum

weight loss occurs, while the y-axis characterizes the activation energy determined using the ABSW (large symbols) and Arrhenius (small symbols) plots. The horizontal arrows indicate the temperature range in which the samples are completely oxidized. Activation energies of SWCNTs and MWCNTs reported in literature are shown for comparison and represented by the shaded area. A detailed analysis of the reaction kinetics is given in section 4.1.1.

As-received DWCNTs (~ 187 kJ/mol) and MWCNTs (~ 195 kJ/mol) were found to exhibit similar activation energies which may not be expected, considering the large differences in size and tube curvature (**Figure 5.1**b). However, the presence of metal catalysts (Fe) and the large number of structural defects in MWCNTs lower the activation energy and decrease the significance of size and curvature on the thermal stability. The importance of defects and catalyst particles on the oxidation resistance of CNTs is evident when comparing as-received and vacuum-annealed MWCNTs. Evaporation of Fe and healing of defects during annealing at high temperatures leads to an increase (35%) in the activation energy from 195 to 265 kJ/mol. While one can argue whether the defects are considered as material specific and thus as a characteristic of MWCNTs, these results demonstrate the importance of detailed information on structure and composition of CNT samples for the analysis of reaction kinetics, and may also explain the large variations reported in literature.

For the DWCNT sample, catalytic reactions are less likely. The measured activation energy is therefore expected to be closer to the actual value of the CNTs. However, in the case of DWCNTs, the reaction heat created by the exothermic oxidation of amorphous carbon may distort the results. Activation energies of DWCNTs are slightly higher than values reported for SWCNTs, as expected (**Figure 5.1**b). The activation energy of vacuum-

annealed MWCNTs is in sound agreement with literature data, while as-received MWCNTs exhibit smaller activation energies due to the catalytic effect of iron inclusions.

Although the activation energies of DWCNTs and as-received MWCNTs were found to be similar, the reaction rate constant of DWCNTs (k_{DWCNT}) is significantly higher than that of MWCNTs (k_{MWCNT}) at any given temperature (see section 4.4.1). While the ratio of the reaction rates, k_{DWCNT}/k_{MWCNT}, decreases with increasing temperatures (**Figure 5.1**a), DWCNTs are oxidized at least 12 times faster than MWCNTs at temperatures between 400 and 500 °C. As a consequence, the maximum weight loss (highest oxidation rate) of DWCNTs (~ 485 °C) occurs at much lower temperatures compared to as-received MWCNTs (~ 550 °C). Also, the oxidation of the DWCNT sample starts at lower temperatures (~ 350 °C) due to the higher content of amorphous carbon.

Comparison of Raman spectra of DWCNTs before and after oxidation at different temperatures and *in situ* studies monitoring changes in Raman intensities in real time showed a selective oxidation of highly defective and/or small-diameter CNTs at temperatures above 400 °C, leading to a decrease in I_D/I_G. In contrast, similar studies on MWCNTs revealed a continuous increase in I_D/I_G. The observed behavior can be explained by the large differences in the reaction rate constant and the selective oxidation of defective and small-diameter DWCNTs. Oxidation of MWCNTs occurs at defective sites, but is not size-selective. Carbon atoms are removed from all MWCNTs simultaneously, leading to higher defect density, while the number of MWCNTs remains almost unchanged.

Figure 5.2a shows the I_D/I_G ratio of SWCNTs, DWCNTs and MWCNTs after oxidation at 400 °C in comparison with the temperature-induced down-shift of the G band Raman peak. It can be seen that the I_D/I_G ratio, which characterizes the defect density of the CNTs,

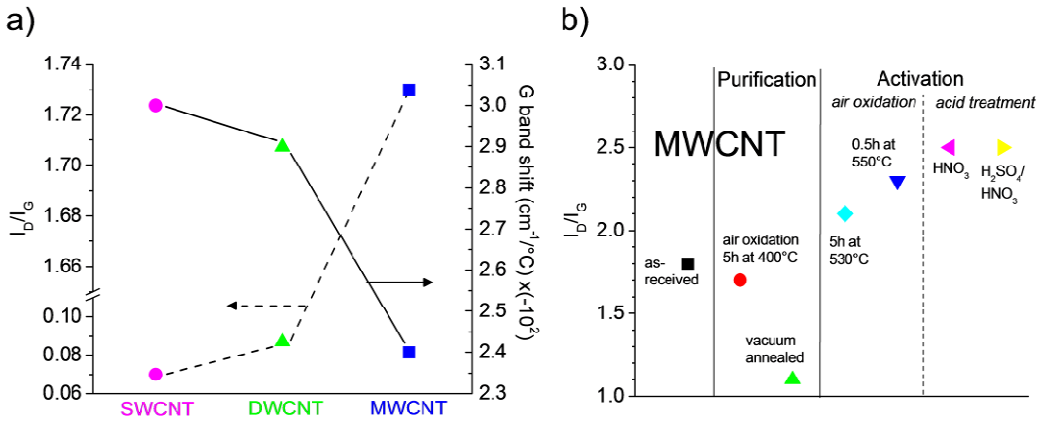

Figure 5.2: Comparison of intensity ratio of D and G Raman bands (I_D/I_G) of SWCNTs, DWCNTs and MWCNTs (a), and changes in I_D/I_G of MWCNTs after various treatments (b).

increases with size (number of walls), while the temperature-dependence of the G band decreases. The larger temperature-dependence of the G band of small CNTs results from the curvature-induced strain on the carbon-carbon bonds, which increases the sensitivity to changes in the environment (e.g. temperature, pressure). For the same reason, activation energies are lower for small-diameter CNTs and increase with tube size. Thus, temperature-induced changes in the Raman spectra of CNTs can also be used to evaluate the thermal stability and oxidation resistivity. However, a determination of the exact relationship requires samples with a narrow size-distribution and a high purity (no amorphous carbon, no metal catalyst).

Figure 5.2b shows changes in I_D/I_G of MWCNTs after various treatments, which can be classified into purification (air oxidation at 350 - 400 °C, vacuum-annealing at 1800 °C) and activation (acid treatments, air oxidation at > 400 °C, flash oxidation at > 500 °C). Purification techniques lower the content of amorphous carbon without damaging the CNTs, while activation treatments increase the number of defects, leading to lower and

higher I_D/I_G values, respectively. If treatment conditions and sample composition are known, I_D/I_G can be used to estimate the defect concentration, which in turn is a measure of the density of surface functionalities, such as carboxylic groups after H_2SO_4/HNO_3 treatments.

It should be noted that the absence of the D band in the Raman spectra may also indicate the selective removal of metallic CNTs, leaving behind only zigzag and semiconducting chiral CNTs, which do not contribute to the D band Raman signal. Therefore, a disappearance of the D band suggests either the removal of defective CNTs or selective oxidation of armchair and metallic chiral CNTs. While our HRTEM studies support the latter hypothesis, more detailed experiments will be required to analyze the relationship between reaction kinetics and electrical properties of the CNTs. However, this is outside the scope of this work.

These results demonstrate the great potential of air oxidation for selective purification of CNT samples, and/or a controlled formation of defects accompanied by a surface functionalization with oxygen-containing functional groups. In addition, vacuum-annealing at 1800 °C was found to induce graphitization of amorphous carbon and healing of structural defects. Catalyst particles were evaporated upon the treatment and completely removed from the sample. Both methods show many advantages compared to a chemical purification (e.g. acid treatments) while providing similar results with respect to purity and control of surface chemistry. Although the I_D/I_G ratio can be used to evaluate purity and defect-concentration of CNT samples, great care must be taken during interpretation of the results, and detailed information on sample composition and synthesis conditions is essential.

5.1.2 Nanodiamond

As discussed in detail in chapter 2, the composition of commercially available ND powders varies largely, depending on the purity of the sample and diamond (sp^3) contents range from roughly 25% (detonation soot) to 80% (acid-purified). The oxidation behavior of ND powders changes for different amounts of sp^2 and sp^3 carbon. Moreover, acid purification, typically following the synthesis step, leads to large differences in content of metal catalyst and surface chemistry, both of which are known to strongly affect the oxidation behavior of carboneous materials.

While in case of CNTs, the intensity ratio between D and G band (I_D/I_G) is often used to evaluate the purity of the sample great care must be taken when using a similar approach for ND powders. The Raman spectrum of ND is more complex and depends strongly on the composition of the sample. Position, intensity and number of Raman peaks change with increasing sp^3/decreasing sp^2 content (**Figure 5.3**a). The Raman spectra of ND powders

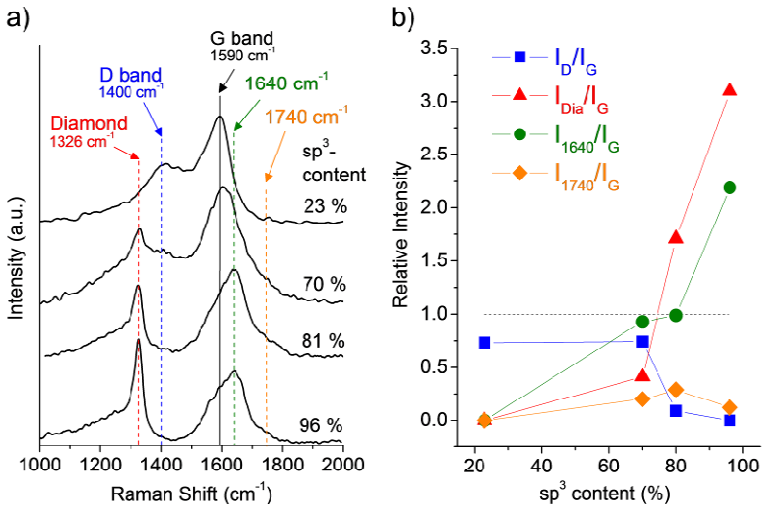

Figure 5.3: (a) Raman spectra of different ND powders with sp^3 content ranging from 23 to 96%. (b) Changes in the intensity of D band, diamond peak and Raman features at 1640 and 1740 cm^{-1}. Intensities are normalized with respect to the G band intensity at 1590 cm^{-1}.

with low sp^3 and high sp^2 carbon content such as UD50 are dominated by the D (1400 cm^{-1}) and G bands (1590 cm^{-1}) of graphitic carbon and exhibit only a weak or no diamond Raman signal. With increasing sp^3 content, the intensity of the diamond peak (1326 cm^{-1}) increases, while the D band Raman signal weakens. Spectral changes between 1500 and 1800 cm^{-1} are more complex and are often wrongly referred to as upshift of the G band. However, as shown in section 4.5, the contribution of sp^2 carbon to the Raman spectra of well purified ND powders (sp^3 > 80%) is rather small and often overestimated. The broad asymmetric Raman feature is composed of at least three peaks of different origin centered at 1590, 1640 and 1740 cm^{-1} which have been assigned to sp^2 carbon, O-H and C=O groups, respectively. It is important to point out, that in the case of ND powders, the accuracy of peak fitting procedures is limited. The diamond peak is characterized by an asymmetric broadening and a broad shoulder towards lower frequencies. While the diamond peak cannot be fitted using an individual Lorentzian or Gaussian peak, the origin of the shoulder is yet not fully understood. Raman peaks between 1500 and 1800 cm^{-1} overlap and in some cases, the individual contributions are not distinguishable. In particular, the position of the G band depends on both ordering and shape of the nanostructure and is different for graphite ribbons, carbon onions or disordered carbon. Therefore, different levels of purity and varying compositions (e.g. metal catalyst, surface chemistry) further complicate peak fitting and lower the reliability of the results. Moreover, the strong luminescence typically observed for ND powders upon VIS or NIR laser excitation requires extensive background corrections, which lead to additional errors in fitting results.

In this work, Raman spectra were recorded using 325 nm laser excitation and fitted using six Lorentzian/Gaussian peaks centered at 1235, 1300, 1326 (diamond), 1400 (D band), 1590 (G band), 1640, and 1740 cm^{-1}. **Figure 5.3**b shows the relative intensity changes (peak

height) for the different Raman features, with respect to the G band intensity at 1590 cm^{-1}, as a function of the sp^3 content. The plotted intensities are normalized with respect to the G band intensity at 1590 cm^{-1}. In general, the intensity ratio between diamond peak and G band (I_{Dia}/I_G) increases with increasing sp^3 content. The sharp increase at ~ 70% sp^3 may result from the removal of graphitic shells surrounding the diamond core. A similar effect was observed during oxidation of DWCNTs, where amorphous carbon on the outer walls of the nanotubes weakened their Raman signal. Removal of the graphitic shells can only be achieved by extensive acid treatment (UD98) or selective oxidation in air (oxidized UD90).

The intensity ratio between D and G band (I_D/I_G) decreases with increasing sp^3 content, as expected. Although both Raman bands originate from sp^2 carbon, the D band intensity decreases at a larger rate as it is proportional to the number of rings, while the G band intensity reflects the number of sp^2 pairs. The intensity of the peaks at 1640 (O-H) and 1740 cm^{-1} (C=O) is related to the surface chemistry of the ND crystals and may vary for ND powders purified by different oxidation techniques (e.g. acid treatment vs. air oxidation).

Similar to the Raman spectrum, the oxidation behavior of ND powders changes with increasing sp^3 content. **Figure 5.4** shows the weight loss rate of UD50 and UD98 between 300 and 700 °C. While both samples are considered ND powders, appearance and oxidation behavior are noticeably different. Black UD50 contains mainly amorphous and graphitic sp^2 carbon (> 70%), while the grey-brown UD98 exhibits a diamond (sp^3) content of > 80%. Similar to CNTs, the oxidation process of ND powders can be divided into three temperature ranges. Below 350 °C (range I), oxidation of carbon does not occur. Between 350 and 425 °C (range II), only amorphous and disordered sp^2 carbon are oxidized. At temperatures above ~ 425 °C (range III), both sp^2- and sp^3-bonded carbons are oxidized

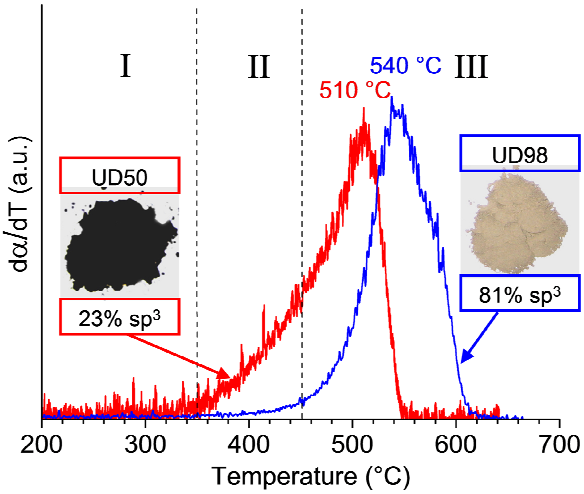

Figure 5.4: Oxidation rate dα/dT of UD50 and UD98 as a function of temperature.

simultaneously. While oxidation of UD50 starts at 350 °C, UD98 shows no weight loss in this temperature range due to the higher purity and absence of amorphous material. The maximum in the weight loss rate of UD50 (~ 510 °C) occurs at lower temperature compared to UD98 (~ 540 °C) because of the higher sp^2 content.

Although the oxidation behavior of UD50 is dominated by sp^2 carbon, oxidation of graphitic carbon and diamond occur in the same temperature range (range III) and do not allow a clear separation of both processes. On the other hand, oxidation of UD98 is dominated by the diamond phase, but contribution of sp^2 carbons to the total weight loss cannot be distinguished by TGA. The presence of different amounts of metal catalyst and large variations in surface chemistry further complicate the oxidation kinetics. UD50 exhibits two different oxidation regimes attributed to removal of amorphous/graphitic sp^2 carbon at low temperatures and oxidation of diamond at temperatures above ~ 425 °C, respectively. However, at elevated temperatures, the rate constant of diamond oxidation exceeds that of the amorphous/graphitic phases, which is not expected considering the higher oxidation

resistance of diamond. This discrepancy can be explained by the catalytic effect of Fe particles. The rate constant of the sp^2 phase was determined in the low temperature range, where Fe particles are encapsulated in graphitic shells and cannot catalyze the carbon-oxygen reactions. At higher temperatures, shells are removed and Fe particles become active.

As a consequence, the measured activation energies (190 - 225 kJ/mol) are distorted by various factors and may therefore not accurately represent the diamond phase. However, the activation energies do represent the composition and thermal properties of the individual ND samples.

These results show that oxidation in air can be used to purify ND powders. Amorphous carbon is selectively removed from the sample between 350 and 420 °C, while oxidation of diamond does not occur. Graphitic carbon can be oxidized between 425 and 435 °C, without a significant loss of the diamond phase.

The changes in the Raman spectra of UD50 (detonation soot) upon oxidation in air have been discussed in detail in section. The corresponding intensity ratios are shown in **Figure 5.5**a. While previous intensity ratios were determined by peak fitting procedures, we used a faster and simplified process which directly measures the Raman intensity at the corresponding peak position. This simplification is well justified given the discussed inaccuracy of the fitting procedure. Although the absolute values are different, comparison of intensity ratios determined using the simplified approach (**Figure 5.5**b) and by peak fitting (**Figure 5.2**b) shows similar trends and reveals the reliability of the obtained data.

As discussed above, temperatures below 350 °C (range I) are not sufficient for carbon oxidation and the I_{Dia}/I_G ratio is similar to that of the detonation soot (UD50). Between 350 and 430 °C (range II) amorphous and graphitic carbons are oxidized, without significant loss of the diamond phase, leading to a maximum in I_{Dia}/I_G. At oxidation temperatures above

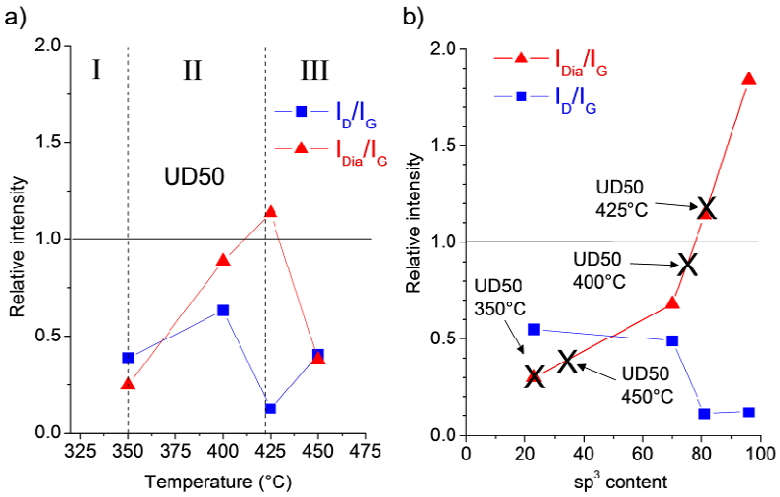

Figure 5.5: (a) Relative intensity of diamond peak (I_{Dia}/I_G) and D band (I_D/I_G) in the Raman spectra of UD50 after oxidation for 5 h at different temperatures normalized with respect to the G band intensity at 1590 cm^{-1}. (b) Diamond content of oxidized UD50 (black cross) estimated using the relationship between I_{Dia}/I_G and the sp^3 content as determined by XANES (see section 4.2.2.1).

430 °C (range III), both sp^2 and sp^3 species oxidize simultaneously, resulting in large inhomogeneities in the sample composition and thus variations in I_{Dia}/I_G.

The diamond content of the oxidized UD50 samples was estimated using the determined relationship between I_{Dia}/I_G and the sp^3 content (see **Figure 5.5**b). The corresponding values are approximately 23, 74, 82, and 34% after oxidation for 5 h at 350, 400, 425, and 450 °C, respectively. Thus, the optimal oxidation temperature for purification of UD50 (in Linkham THMS heating stage) is ~ 425 °C

Oxidation of larger amounts of ND powder in a furnace showed the feasibility of scaling up the process. In that case, the optimal oxidation temperature was found as 430 °C and sp^3 contents up to 96 % were achieved (see **Table 4.2**), the highest ever reported values for ND powders.

These results also show that oxidation in air can be used to adjust the sp^2/sp^3 ratio and thus optimize the optical and electronic properties of ND powders for specific applications. **Figure 5.7**a shows the resistivity of ND powders as a function of the sp^3 content. There exists a clear relationship between the amount of sp^2-bonded sites and the resistivity of the powders. The π-electrons of sp^2 bonded sites are the charge carriers responsible for the high conductivity of graphitic carbons. Therefore, the amount of sp^2 sites determines the electronic properties in ND powders. The resistivity ρ (in Ω·cm) increases with increasing sp^3 and decreasing sp^2 content (in %), and can be roughly approximated by

$$\log \rho = 0.091 \cdot sp^3 - 0.5 . \qquad (5\text{-}1)$$

The electric properties of ND range from highly conductive (graphitized ND, detonation soot) to highly insulating (oxidized UD98).

In contrast, the absorbance of ND powders decreases with increasing sp3 content and depends on the wavelength range (**Figure 5.7**b). Removal of sp^2 sites significantly reduces absorption in VIS-NIR region, while the absorbance in the UV range remains high, making

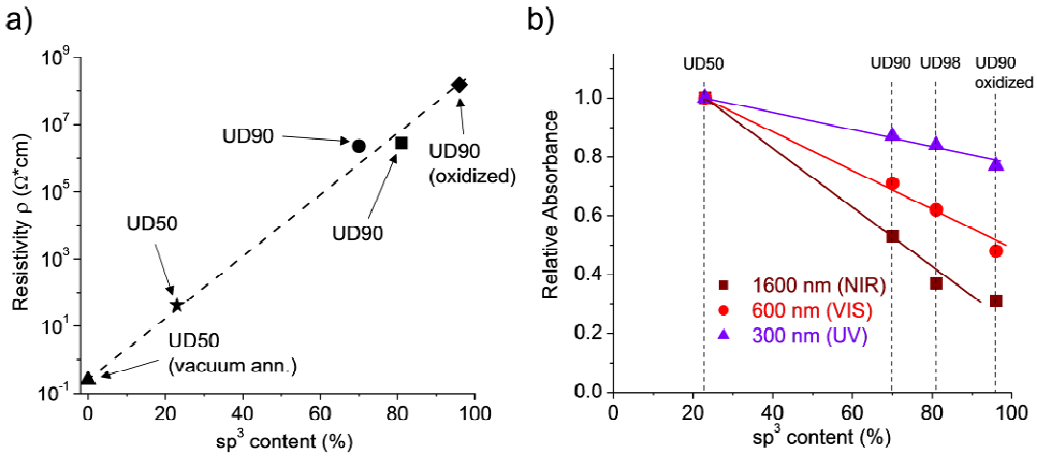

Figure 5.7: Electrical resistivity (a) and absorbance (b) of ND powders as a function of the sp3 content. The absorbance was normalized to the absorbance of detonation soot (UD50) and is therefore referred to as relative absorbance.

oxidized ND powder a potential additive for sun blockers and other sunscreen applications where transparency in the visible (VIS) or near-infrared (NIR) is required.

5.1.3 Carbide-Derived Carbon

Although CDCs can exhibit a great structural variety, depending on the synthesis conditions, most CDCs consist primarily of networks of amorphous and graphitic sp2 carbon. While in case of CNTs and ND powders, oxidation was used to selectively remove carbon impurities, oxidation of TiC-CDC aims to adjust the porosity and the surface area of the carbon network.

Figure 5.8 compares the weight loss rate of 600°C-TiC-CDC, 1000°C-TiC-CDC and 1300°C-TiC-CDC. TiC-CDC synthesized at 600, 1000 and 1300 °C contain different amounts of amorphous and/or graphitic carbon and therefore exhibit a different oxidation behavior. Similar to CNTs and ND, the oxidation process of TiC-CDC can be divided into three temperature ranges. At low temperatures (< 350 °C), oxidation of carbon does not occur (range I). Between 350 and 480 °C (range II) mainly amorphous and disordered carbons are removed from the sample, while above 480 °C (range III) all types of carbon are oxidized simultaneously. Oxidation of highly amorphous 600°C-TiC-CDC starts at 350 °C. The activation energy was determined using isothermal and nonisothermal TGA studies (see section 4.4.3) and found as ~ 130 - 140 kJ/mol. 1300°C-TiC-CDC consists mainly of graphitic carbon and is not oxidized below 500 °C. The resulting activation energy ranges between 200 and 220 kJ/mol. While 600°C-TiC-CDC (amorphous) and 1300°C-TiC-CDC (graphitic) exhibit a relative homogeneous sample composition, 1000°C-TiC-CDC compromises both amorphous and graphitic regions. Therefore, at low temperatures

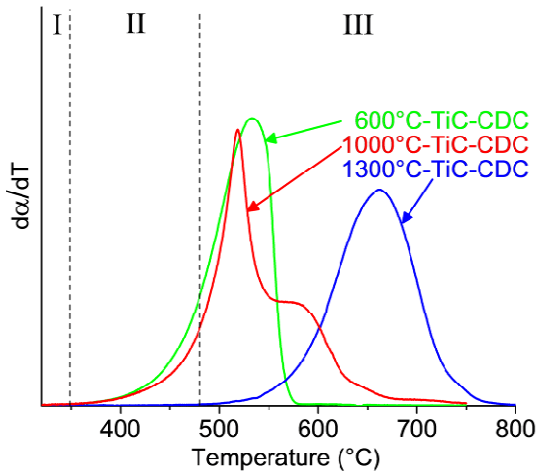

Figure 5.8: Weight loss rate of different TiC-CDC synthesized at 600, 1000 and 1300 °C. The activation energies were determined using isothermal and nonisothermal TGA.

(< 500 °C), the oxidation behavior of 1000°C-TiC-CDC is determined by amorphous phases while at higher temperatures (> 550 °C) oxidation of graphitic carbons is dominant.

1300°C-TiC-CDC requires significantly higher oxidation temperatures compared to 600°C-TiC-CDC and 1000°C-TiC-CDC and is therefore less favorable for activation. Activation of 1000°C-TiC-CDC (in air) and 600°C-TiC-CDC (in CO_2) revealed that both oxidants can be used to control the average pore size in CDCs (**Figure 5.9**a). While air oxidation is suitable for partially graphitized samples such as 1000°C-TiC-CDC, activation in CO_2 allows sufficient control over the porosity of highly amorphous and less oxidation resistant 600°C-TiC-CDC. The higher reactivity of O_2 would lead to a rapid oxidation of amorphous species and thus limit the control over porosity development. CO_2 is a milder oxidizer, but requires higher oxidation temperature.

The observed shifts in pore size result mainly from a decrease in the pore volume of smaller pores. Activation enlarges small pores, thus decreasing micropore (< 1.5 nm) and increasing mesopore (> 1.5 nm) volume. Similar results were obtained for activation of

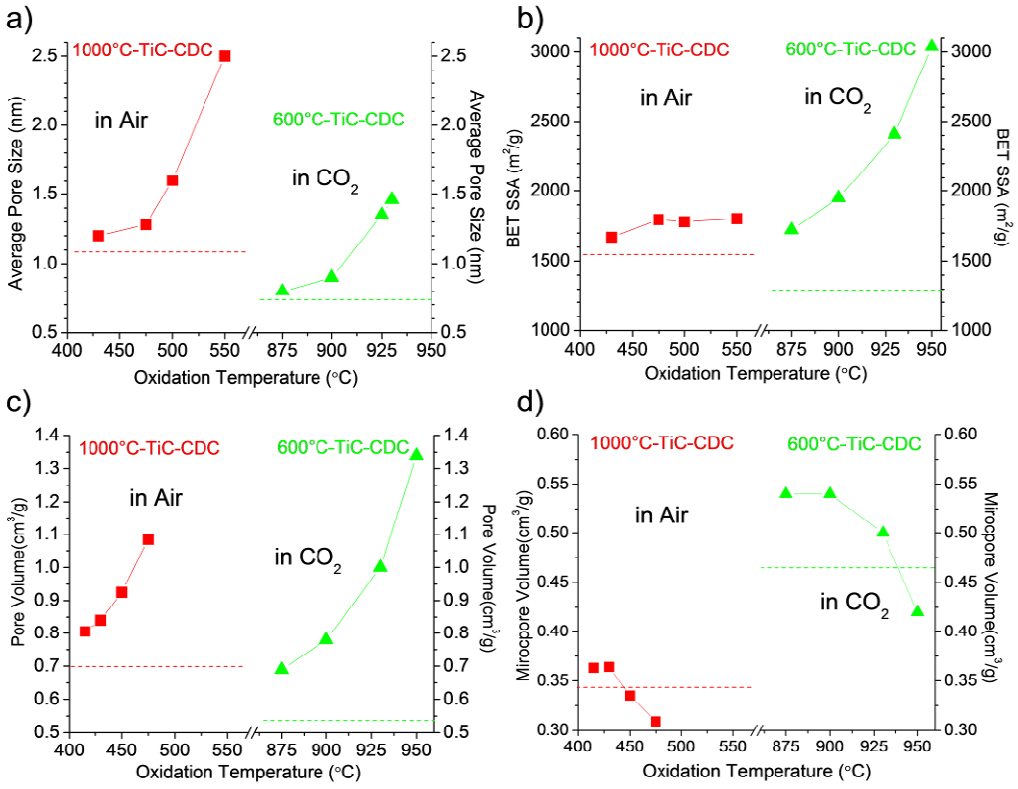

Figure 5.9: Changes in average pore size (a), specific surface area (b), total pore volume (c) and micropore volume (d) upon oxidation of 1000°C-TiC-CDC and 600°C-TiC-CDC in air (6 h) and CO_2 (2 h), respectively. The dotted lines represent the values of non-activated samples.

600°C-TiC-CDC (see **Figure 4.31**a and b) and 1300°C-TiC-CDC (see **Figure 4.29**a and b) under isothermal conditions. Oxidation of 1000°C-TiC-CDC in air was found to provide only moderate control over the SSA, reaching a maximum value of ~ 1800 m^2/g, while CO_2 activation of 600°C-TiC-CDC significantly increases the SSA, reaching values up to 3000 m^2/g or higher.

Both oxidants (air and CO_2) lead to an increase in pore volume compared to the nonactivated samples. Although the relative increase of total pore volume and micropore volume is larger for 600°C-TiC-CDC (**Figure 5.9**c and d), both air and CO_2 activation exhibit similar trends. While the total pore volume significantly increases with activation temperature (**Figure 5.9**c), the micropore volume shows only a small increase at low

temperature (6% for 1000°C-TiC-CDC and 17% for 600°C-TiC-CDC), but decreases at higher activation temperatures following a two-step process with initial formation of new micropores followed by the enlargement of those micropores into mesopores (**Figure 5.9**d). Thus, high temperatures and longer activation times lead to a larger total pore volume, but are unfavorable for the formation of micropores. The optimum conditions for activation of TiC-CDC with respect to a high SSA, development of micropores, and low weight loss are therefore low activation temperatures and long activation times.

Isothermal and nonisothermal activation lead to changes in structure and composition of the TiC-CDC, which affect the Raman spectra of the samples as discussed in section 4.3.3.3. Unfortunately, the inhomogeneous sample composition of 1000°C-TiC-CDC and the resulting variations in I_D/I_G overlap with oxidation induced changes in the Raman spectra and do not allow a clear separation of both effects.

However, in the case of 600°C-TiC-CDC, I_D/I_G may potentially be used to analyze the porosity of sample. A decrease in the I_D/I_G ratio generally indicates a higher level of graphitization and/or removal of amorphous phases. The relative percentage of graphitic carbon increases during activation and I_D/I_G decreases with activation temperature (or activation time). **Figure 5.10**a shows SSA and burn-off after isothermal (squares) and nonisothermal (triangles) activation as a function of I_D/I_G. Both SSA and burn-off decrease linearly with increasing I_D/I_G. A similar behavior is observed for the average pore size and the pore volume.

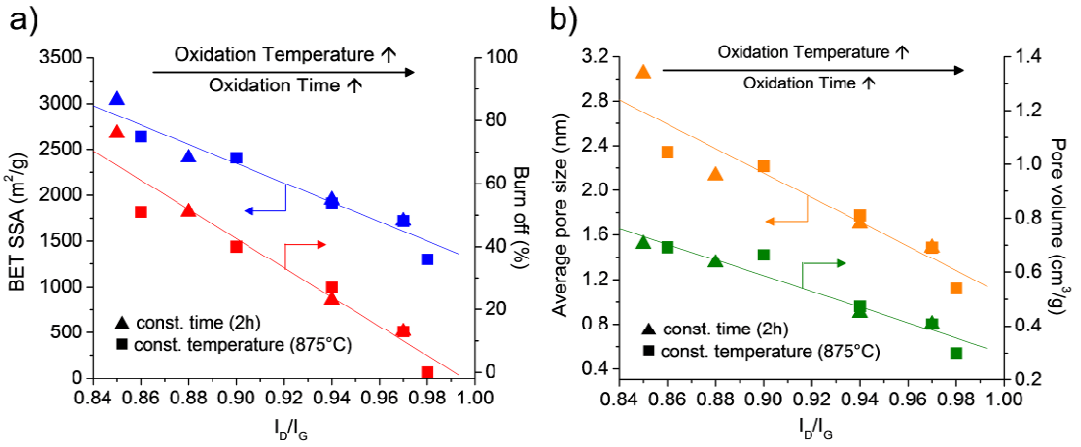

Figure 5.10: Relationship between pore structure and Raman spectra of activated 600°C-TiC-CDC. SSA, average pore size, pore volume, burn-off and I_D/I_G were determined for increasing oxidation time (at 875 °C) and temperature (for 2 h).

The relationship between I_D/I_G and the porosity parameters (SSA, pore volume, average pore size) can be approximated by a linear regression of the type:

$$I_D / I_G = A + B \cdot x, \qquad (5\text{-}2)$$

where x represents the porosity parameter. The corresponding regression coefficients *A* and *B* are shown in **Table 5.1**.

These results demonstrate the possibility of adjusting the porosity of CDCs by physical activation in air and CO_2. Both oxidants can be used to control the average pore size of CDCs derived from low cost carbides with high carbon content, such as TiC and SiC, with a subnanometer accuracy. Air-activation of 1000°C-TiC-CDC leads to an increase in SSA and

Table 5.1: Regression coefficients of the linear relationship between pore structure and I_D/I_G ratio.

	A	*B*
BET SSA	-11833 ± 911	-10543 ± 988
Burn-off	461 ± 41	465 ± 44
Average pore size	7.54 ± 0.64	-7.01 ± 0.69
Pore volume	5.04 ± 0.55	-4.52 ± 0.59

total pore volume, but the microporosity development remains insufficient. The high reactivity of O_2 leads to a rapid enlargement of micropores into mesopores and thus limits the control over porosity development. Activation of 600°C-TiC-CDC in CO_2, which is a milder oxidizer, leads to a 17% increase in the micropore volume and further improvement in SSA and total pore volume compared to air activation. Furthermore, SSA of above 3000 m^2/g and pore volume of 1.3 - 1.4 g/cm^3 can be achieved by activation in CO_2. The developed activation method can be applied to other CDCs, such as SiC-CDC, leading to a similar increase in pore volume and SSA as shown in section 4.3.4.

The ability to control the pore structure of CDCs is of great importance for a large number of applications, especially for adsorption and storage of gases such as hydrogen and methane. Studies on gravimetric H_2 uptake of activated 1000°C-TiC-CDC (3 h at 475 °C) and 600°C-TiC-CDC (8 h at 875 °C) revealed a 14% and 40% increase in H_2 uptake, respectively, compared to nonactivated samples.[345] The increase is larger for CO_2-activated 600°C-TiC-CDC due to a better porosity development, i.e. 40 - 50% increase in SSA and micropore volume improvement. Similar improvements were achieved for methane uptake in activated TiC-CDC. While micropores (< 1.5 nm) are of great importance for hydrogen/methane storage and supercapacitor applications, larger average pore sizes (1.5 - 5 nm) are very attractive for sorption of biological molecules and toxins, which are usually larger in size compared to the electrolyte ions or hydrogen molecules used in most energy-related applications.

5.1.4 Comparison

Although CNTs, ND, CDC, fullerenes, carbon onions, and amorphous carbon are all considered carbon nanomaterials, the shape, stability and structure vary largely. While small differences in size and shape can be neglected for bulk materials, they become significant at the nanoscale and change the properties of a material. Various types of lattice defects, surface chemistries and impurities resulting from the synthesis process typically further differentiate carbon nanomaterials.

The structural and compositional complexity of carbon nanomaterials strongly affects their oxidation behavior. The resistance to oxidation, in the first instance, depends on the stability of the carbon-carbon bonds. However, most carbon nanomaterials consist of mixtures of sp^2- and sp^3-bonded carbon species. Their stability varies from structure to structure and depends on shape and size of the nanoparticle. Differences in surface chemistry and number of lattice defects also affect the oxidation mechanism. While both may be considered as structural properties, an accurate interpretation of oxidation kinetics requires sufficient information on surface chemistry as well as type and number of defects.

Arguably the most significant factor for the oxidation behavior of carbon nanostructures is the presence of metal particles, which catalyze the oxygen-carbon reaction and significantly lower oxidation temperature and activation energies. Unfortunately, industrial production techniques require addition of metal catalysts to promote formation and growth of carbon nanomaterials. Current purification methods do not allow a complete removal of the metal impurities without modifying the nanostructures or changing the composition of the sample. Variations in the amount and nature of these catalyst impurities often inhibit an exact determination of the reaction kinetics.

Lattice defects, surface chemistry and metal impurities therefore simultaneously affect the oxidation reactions, making a differentiation between the individual contributions impossible. The measured activation energies, reaction rate constants and frequency factors thus reflect the oxidation behavior of the sample as a whole, but not that of a particular nanostructure. A direct comparison between different carbon nanostructures, or similar nanostructures produced by different synthesis techniques, is therefore difficult.

Although the oxidation of CNTs, ND and CDC is initially controlled by the chemical reaction between carbon and oxygen, the transition to a diffusion controlled process occurs at different temperatures, depending on the thermal stability and the oxidation rate constant of the material (**Table 5.2**). A higher rate constant leads to a higher mass transfer, making diffusion limitations in a given temperature range more likely. This is important to consider when comparing activation energies and oxidation behavior of different carbon nanomaterials.

In general, there exists a clear difference in oxidation temperature between amorphous carbon (~ 350 °C) and other graphitic or diamond-like phases (> 400 °C) for all nanomaterials studied, allowing a selective oxidation of amorphous species from the

Table 5.2: Starting temperature for diffusion controlled oxidation reactions determined using isothermal and nonisothermal TGA.

Sample	*Temperature*
DWCNT(as-received)	400-430°C
MWCNT(as-received)	500-540°C
MWCNT(vacuum-annealed)	>700°C
ND(detonation soot)	>480°C
ND(purified)	480-540°C
TiC-CDC(amorphous)	450-490°C
TiC-CDC(graphitic)	600-630°C

samples. A separation of graphitic carbon from diamond is more complex, but can be achieved around 425 - 430 °C without significant loss in the diamond phase due to distinct differences in the rate constants of graphitic and diamond-like carbon. While oxidation in air was found suitable for selective removal of amorphous and/or graphitic carbon, the high reactivity of O_2 molecules inhibits a slow and controlled activation of amorphous carbon networks such as 600°-TiC-CDC. However, milder oxidizers such as CO_2 can be applied in a similar fashion using slightly higher oxidation temperatures.

In any case, structural characterization techniques such as Raman spectroscopy are required in order to maximize the efficiency of the oxidation treatment and prevent damage to the remaining nanostructures. The Raman spectra of carbon nanostructures can be very different and depend strongly on the composition of the sample. A correct interpretation of oxidation-induced changes in the Raman spectra of carbon nanomaterials containing mixtures of amorphous, graphitic and diamond-like carbon is therefore difficult. The presence of lattice defects and contributions of surface functional groups further complicate Raman analysis and peak assignment. In the case of graphitic nanomaterials such as CNT, the intensity ratio between D and G band (I_D/I_G) is often used to evaluate the purity of the samples. However, great care must be taken when differentiating between contributions from amorphous species and lattice defects. For other nanomaterials including ND, I_D/I_G is not an appropriate measure of the purity. Although other intensity ratios such as I_{Dia}/I_G may be used, the complexity of the Raman spectra and related uncertainties in the fitting procedures make a comparison between different nanostructures difficult.

5.2 Control and Measurement of Nanodiamond Crystal Size

Oxidation has successfully been used to remove carboneous impurities from CNTs and ND powders and to control the pore structure of CDCs. In the case of CNTs, oxidation also allowed for selective removal of defective and small-diameter CNTs. In this section we discuss the potential of air oxidation for size control in ND powders.

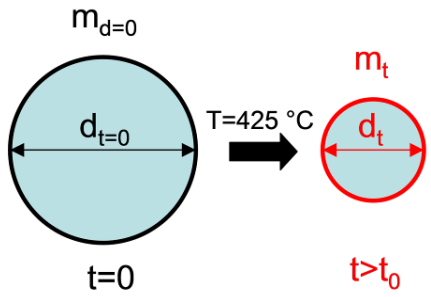

Figure 5.11: Decrease in the size of an individual ND crystal size during oxidation in air (shrinking core model).

The sample weight (m_{total}) of a ND powder is generated by the mass (m) of N individual, diamond crystals. The total mass of the sample can thus be approximated by:

$$m_{total} = N \cdot m = \frac{\pi}{6} N \cdot \rho \cdot d^3, \tag{5-3}$$

where ρ and d are the density and the average diameter of a spherical ND crystals. Assuming N and ρ to be constant, we can express the relative changes in the sample weight through changes in the diameter of the crystal (**Figure 5.11**) according to:

$$\frac{m_t}{m_{t=0}} = \left(\frac{d_t}{d_{t=0}} \right)^3. \tag{5-4}$$

The indices "t=0" and "t" represent the initial values and the values at time t, respectively.

If the oxidation rate k is size-independent, the diameter of the ND crystals decreases linearly with oxidation time following:

$$d_t = d_0 - k \cdot t \,. \tag{5-5}$$

Combining equations 5-4 and 5-5 then leads to:

$$\frac{m_t}{m_{t=0}} = \left(\frac{d_{t=0} - k \cdot t}{d_{t=0}} \right)^3 . \tag{5-6}$$

Figure 5.12a shows the sample weight (m_t) of a ND powder (UD90) measured using isothermal TGA at 430 °C and normalized to the initial sample weight ($m_{t=0}$). The weight loss measurement was started after ~ 300 minutes of oxidation in order exclude contributions from amorphous and graphitic sp^2 carbons. The relative sp^3 content increases from approximately 71% to 96% in this early phase of the oxidation. The weight loss curve was fitted using equation 5-6, assuming the initial average diameter to be $d_{t=0}$ = 5 nm. The obtained fit and the corresponding oxidation rate are shown in **Figure 5.12**b. It can be seen that there is only little agreement between the obtained fit and the experimental TGA data.

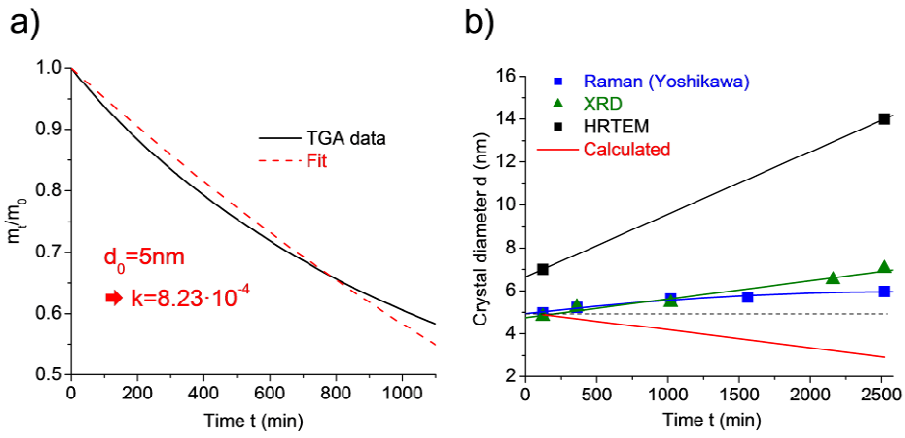

Figure 5.12: (a) Weight loss of ND powder measured using isothermal TGA at 430 °C, normalized to the initial weight. The oxidation rate k was obtained by fitting the weight loss curve using equation 5-6. (b) The crystal diameter was then calculated by equation 5-5 and compared to experimental data determined using Raman spectroscopy, HRTEM and XRD.

According to equation 5-5, the oxidation rate can be used to determine the time-dependent changes in the diameter of the ND crystals. However, while equation 5-5 and 5-6 predict a decrease in diameter with increasing oxidation time, size measurements using Raman spectroscopy, HRTEM and XRD revealed an increase in the average crystal size, suggesting that weight loss of ND powders during isothermal oxidation cannot be described by equations 5-6.

However, considering the broad size distribution of detonation synthesized ND powders, one may expect differences in the behavior for different crystal sizes. Thus, equation 5-4 was modified in order to separately account for the weight contributions of small (m') and large (m'') diamond crystals:

$$\frac{m_t}{m_{t=0}} = \frac{m_t^{'} + m_t^{''}}{m_{t=0}^{'} + m_{t=0}^{''}}. \qquad (5\text{-}7)$$

Combining equations 5-5 and 5-7 then leads to:

$$\frac{m_t}{m_{t=0}} = \frac{\left(d_{t=0}^{'} - k^{'} \cdot t\right)^3 + \left(d_{t=0}^{''} - k^{''} \cdot t\right)^3}{d_{t=0}^{'\,3} + d_{t=0}^{''\,3}} \ . \qquad (5\text{-}8)$$

The initial diameter of the small crystals, which represents the majority of the ND crystals, was set to $d'_{t=0}$= 5nm. The parameters $d''_{t=0}$, k' and k'' were determined by fitting the weight loss data using equation 5-7. The fitting results are presented in **Figure 5.13**a and are in good agreement with TGA data. **Figure 5.13**b shows the corresponding changes in diameter for small (d') and large (d'') ND crystals. While both exhibit a decrease in size, the diameter decrease occurs much faster for smaller crystals due to their higher oxidation rate ($k' \approx 4 \cdot k''$). As a consequence, the average crystals size is shifted towards higher values as indicated in **Figure 5.13**b. This is in good agreement with experimental data obtained from Raman spectroscopy, XRD and HRTEM studies.

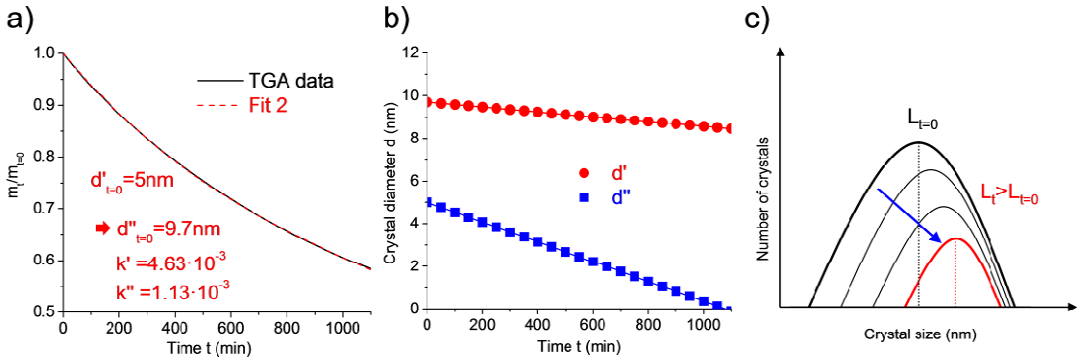

Figure 5.13: (a) Weight loss of ND powder measured using isothermal TGA at 430 °C, normalized to the initial weight. The parameters d"$_{t=0}$, k' and k" were obtained by fitting the weight loss curve using equation 5-7. (b) The corresponding changes in the crystal diameter were calculated by equation 5-5.

These results suggest that oxidation in air cannot be used to decrease the average crystal size of ND powders, due to the higher oxidation rate of small ND crystals. However, the method allows for a controlled increase in the average crystal size with subnanometer accuracy. While the described approach is able to explain the observed increase in the average crystal, it can only be considered as rough approximation and may oversimplify the oxidation behavior of ND samples. In particular, metal catalysts present in the ND samples strongly affect kinetic parameters such as activation energies and oxidation rate constants.[388]

6 SUMMARY AND CONCLUSIONS

- In situ Raman spectroscopy analysis of isothermal and non-isothermal oxidation of DWCNTs in air showed a decrease in the intensity of the D band starting around 370 °C, followed by complete D band elimination at 440 °C. The oxidation process produced the purest CNTs ever reported, which were free of amorphous carbon and highly defective tubes, while the removal of amorphous material was not accompanied by tube damage. In situ Raman measurements allowed us to determine the different contributions to the D band feature and show the relationship between D band, G band and RBM Raman modes in the Raman spectra of DWCNTs upon heating. The described approach thus provides an efficient purification method for DWCNTs and SWCNTs, which is also selective to tube diameter and chirality.
- While oxidation of MWCNTs did not significantly decrease the D band intensity below 450 °C, oxidation in air can be an effective route to control the number of defects on outer walls of the MWCNTs. The intensity ratio between the D and G bands can be used to monitor relative changes in the concentration of defective sites, and to create a high density of carboxyl groups with a moderate sample loss.
- Raman-assisted oxidation studies on detonation-synthesized ND demonstrated the possibility of selectively removing amorphous and graphitic sp2-bonded carbon from ND powders by heating in air. The optimal temperature range for oxidation of the ND powders studied is 400 - 430 °C. Oxidation at 425 °C increased the content of sp^3-bonded carbon up to 96%, as determined by XANES. The weight loss was roughly equal to the initial content of sp^2 carbon in the sample, suggesting little or no loss of the

diamond phase. The purity of ND thus became comparable to that of microcrystalline diamond, and was the highest ever reported for ND powders. Metal impurities, which were initially protected by carbon shells in the as-received samples, become accessible after oxidation and can be completely removed by further treatment in diluted acids. The presented technique is also capable of significantly improving the quality of diamond samples which underwent prior acid purification treatments without appreciable loss of the diamond phase.

- Furthermore, we have shown that oxidation in air can also be used to control the average crystal size in ND powders with subnanometer accuracy. Three different characterization techniques were used for measuring the crystal size because such analysis is very complex for nanocrystals. While HRTEM is able to visualize ND crystals, the calculated size distributions are statistically not reliable and the average size is often overestimated. Agglomeration and difficulties in sample preparation do not allow accurate estimates on average crystals size values. XRD, which directly probes the crystalline structure of a material, is more reliable in terms of statistics and average values, but lattice distortion and strain can interfere with size effects in XRD pattern and lead to an incorrect interpretation of the results.
- Raman spectroscopy, which is also used to measure the crystal size of nanostructured solids through the phonon confinement model (PCM), provides only semi-quantitative results for size measurements in ND powders due to insufficient understanding of the Raman spectra of ND and a lack of agreement between theoretical predictions of the model and experimental Raman data. However, taking into account the broad size distribution of ND powders and the contributions of lattice defects, a significant

improvement in the predictions of the model was achieved. However, a correct interpretation of Raman data and quantitative size measurements still requires additional information on sample structure and composition. Therefore, a combined use of various characterizations techniques such as XRD, HRTEM and Raman spectroscopy can be recommended for a reliable determination of the average size of ND crystals and their distribution.

- The high purity of oxidized ND and our ability to control size and surface chemistry of the nanocrystals allowed for a better understanding of the Raman spectra of ND. A critical analysis of the 1640 cm^{-1} peak observed in UV Raman spectra of ND powders revealed that this peak cannot be assigned solely to amorphous or graphitic carbon at the surface of the ND crystals or split interstitial (dumb-bell) defects inside the diamond core, as suggested in literature. The Raman intensity between 1500 and 1800 cm^{-1} is shown to originate mainly from O-H bending vibrations either of the surface functional groups or adsorbed water, with small contributions (shoulders) coming from sp^2 carbon (1590 cm^{-1}) and C=O stretching vibrations (1740 cm^{-1}). The assignment of the 1640 cm^{-1} Raman peak emphasizes the importance of correctly accounting for the O-H contribution in Raman spectra of ND and other carbon nanomaterials, especially when water cooling of the sample is used.
- Finally, we have demonstrated the possibility of adjusting the porosity of carbide-derived carbons by physical activation (oxidation) in air and CO_2. While air-activation of TiC-CDC leads to an increase in SSA and total pore volume, the microporosity development remains insufficient. The high reactivity of O_2 leads to a rapid enlargement of micropores into mesopores, limiting the control over porosity development. Activation

of TiC-CDC in CO_2, which is a milder oxidizer allowing a better control on the porosity development, leads to larger increase in the micropore volume and further improvement in SSA and total pore volume compared to air activation. Furthermore, SSA of above 3000 m^2/g and pore volume of 1.3 - 1.4 g/cm^3 can be achieved by activation in CO_2. The developed activation method can be applied to other CDCs, with a relatively small SSA and pore volume such as SiC-CDC, leading to a similar increase in pore volume and SSA.

- In summary, we have shown that oxidation in air provides a powerful route to purify carbon nanostructures, but can also be used as an efficient tool for size control and surface modification. ***In situ*** Raman spectroscopy studies under isothermal and nonisothermal conditions allow a detailed and time-resolved investigation of changes in structure and composition during the oxidation process. Using in situ Raman spectroscopy, we were able to monitor the oxidation of different carbon nanostructures and identify their optimum purification conditions, with little or no sample loss.
- For an industrial scale production of carbon nanomaterials, it is important to use a simple and environmentally-friendly purification methods to, for example, selectively remove sp^2-bonded carbon from nanodiamond and amorphous carbon from nanotubes with minimal or no loss of diamond or nanotubes. In contrast to current purification techniques, which usually use mixtures of oxidizing acids, controlled air oxidation does not require the use of toxic or aggressive chemicals, catalysts or inhibitors, thus opening avenues for numerous new applications of carbon nanomaterials.

REFERENCES

(1) Lide, D. R. *CRC handbook of chemistry and physics: a ready-reference book of chemical and physical data*; CRC, Taylor & Francis, 2006.

(2) Pierson, H. O. *Handbook of carbon, graphite, diamond, and fullerenes: properties, processing, and applications*; Noyes Publications: Park Ridge, N.J., USA, 1993.

(3) Mantell, C. L. *Carbon and graphite handbook*; Interscience Publishers: New York, 1968.

(4) Kroto, H. W.; Heath, J. R.; Obrien, S. C.; Curl, R. F.; Smalley, R. E. *Nature* **1985**, *318*, 162.

(5) *Nanomaterials Handbook*; Gogotsi, Y., Ed.; CRC Press, 2006.

(6) Iijima, S. *Nature* **1991**, *354*, 56.

(7) Kroto, H. W. *Nature* **1992**, *359*, 670.

(8) Dolmatov, V. Y. *Russian Chemical Reviews* **2001**, *70*, 607.

(9) Gruen, D. M. *Annual Review of Materials Science* **1999**, *29*, 211.

(10) Dahl, J. E.; Liu, S. G.; Carlson, R. M. K. *Science* **2003**, *299*, 96.

(11) Gouadec, G.; Colomban, P. *Journal of Raman Spectroscopy* **2007**, *38*, 598.

(12) Thostenson, E. T.; Ren, Z. F.; Chou, T. W. *Composites Science and Technology* **2001**, *61*, 1899.

(13) Dai, L. M.; Mau, A. W. H. *Advanced Materials* **2001**, *13*, 899.

(14) Avouris, P. *Chem. Phys.* **2002**, *281*, 429.

(15) Ciraci, S.; Dag, S.; Yildirim, T.; Gulseren, O.; Senger, R. T. *Journal of Physics-Condensed Matter* **2004**, *16*, R901.

(16) Ravindran, S.; Chaudhary, S.; Colburn, B.; Ozkan, M.; Ozkan, C. S. *Nano Letters* **2003**, *3*, 447.

(17) Baughman, R. H.; Zakhidov, A. A.; de Heer, W. A. *Science* **2002**, *297*, 787.

(18) *Synthesis, Properties and Applications of Ultrananocrystalline Diamond*; Gruen, D. M.; Shenderova, O. A.; Vul, A. Y., Eds.; Springer: Dordrecht, Berlin, Heidelberg, New York, 2005; Vol. 192, pp 401.

(19) Dai, L. M. *Polymers for Advanced Technologies* **1999**, *10*, 357.

(20) Dai, L. M.; Soundarrajan, P.; Kim, T. *Pure and Applied Chemistry* **2002**, *74*, 1753.

(21) Dragoman, M.; Grenier, K.; Dubuc, D.; Bary, L.; Plana, R.; Fourn, E.; Flahaut, E. *Journal of Applied Physics* **2007**, *101*, 106103.

(22) Sherigara, B. S.; Kutner, W.; D'Souza, F. *Electroanalysis* **2003**, *15*, 753.

(23) Buhro, W. E.; Colvin, V. L. *Nature Materials* **2003**, *2*, 138.

(24) Sato, H.; Hata, K. *New Diamond and Frontier Carbon Technology* **2006**, *16*, 163.

(25) Ando, Y.; Zhao, X. L. *New Diamond and Frontier Carbon Technology* **2006**, *16*, 123.

(26) Kusaba, M.; Tsunawaki, Y. *Thin Solid Films* **2006**, *506*, 255.

(27) Danilenko, V. V. *Synthesizing and Sintering of Diamond by Explosion*; Energoatomizdat: Moscow, 2003.

(28) Viecelli, J. A.; Ree, F. H. *Journal of Applied Physics* **2000**, *88*, 683.

(29) Shenderova, O. A.; McGuire, G. Nanocrystalline Diamond. In *Nanomaterials handbook*; Gogotsi, Y., Ed.; CRC Taylor and Francis Group: Boca Raton London New York, 2006; pp 203.

(30) Viecelli, J. A.; Bastea, S.; Glosli, J. N.; Ree, F. H. *The Journal of Chemical Physics* **2001**, *115*, 2730.

(31) Tomanek, D.; Schluter, M. A. *Physical Review Letters* **1991**, *67*, 2331.

(32) Barnard, A. S.; Russo, S. P.; Snook, I. K. *Physical Review B* **2003**, *68*.

(33) Zwanger, M. S.; Banhart, F. *Philosophical Magazine B-Physics of Condensed Matter Statistical Mechanics Electronic Optical and Magnetic Properties* **1995**, *72*, 149.

(34) Raty, J. Y.; Galli, G.; Bostedt, C.; van Buuren, T. W.; Terminello, L. J. *Physical Review Letters* **2003**, *90*.

(35) Barnard, A. S.; Russo, S. P.; Snook, I. K. *Diamond and Related Materials* **2003**, *12*, 1867.

(36) Barnard, A. S. *Diamond and Related Materials* **2006**, *15*, 285.

(37) Barnard, A. S.; Zapol, P. *The Journal of Chemical Physics* **2004**, *121*, 4276.

(38) Kuznetsov, V. L.; Chuvilin, A. L.; Butenko, Y. V.; Mal'kov, I. Y.; Titov, V. M. *Chemical Physics Letters* **1994**, *222*, 343.

(39) Park, N.; Lee, K.; Han, S. W.; Yu, J. J.; Ihm, J. *Physical Review B* **2002**, *65*.

(40) Yushin, G.; Nikitin, A.; Gogotsi, Y. Carbide-Derived Carbon. In *Nanomaterials handbook*; Gogotsi, Y., Ed.; CRC Taylor and Francis Group: Boca Raton London New York, 2006; pp 239.

(41) Jorio, A.; Saito, R.; Dresselhaus, G.; Dresselhaus, M. S. *Philos. Trans. R. Soc. London, Ser. A* **2004**, *362*, 2311.

(42) Hamada, N.; Sawada, S.-i.; Oshiyama, A. *Physical Review Letters* **1992**, *68*, 1579.

(43) Rakov, E. G. Chemistry of carbon nanotubes. In *Nanomaterials Handbook*; Gogotsi, Y., Ed.; CRC Press, 2006, 105-176; pp 105.

(44) Flahaut, E.; Peigney, A.; Laurent, C.; Rousset, A. *Journal of Materials Chemistry* **2000**, *10*, 249.

(45) Radosavljevic, M.; Lefebvre, J.; Johnson, A. T. *Physical Review B* **2001**, *64*.

(46) Berber, S.; Kwon, Y. K.; Tomanek, D. *Physical Review Letters* **2000**, *84*, 4613.

(47) Bonard, J.-M.; Kind, H.; Stockli, T.; Nilsson, L.-O. *Solid-State Electron.* **2001**, *45*, 893.

(48) Daenen, M.; de Fouw, R. D.; Hamers, B.; Janssen, P. G. A.; Schouteden, K.; Veld, M. A. J. *The Wondrous World of Carbon Nanotubes. A Review of Current Carbon Nanotube Technologies.* Eindhoven University of Technology, 2003.

(49) Danilenko, V. V. *Physics Of The Solid State* **2004**, *46*, 595.

(50) Davidson, J. L.; Bradshaw, D. T. Compositions with nano-particle size diamond powder and methods of using same for trasferring heat between a heat source and a heat sink; C09K 5/00 ed.; Vanderbilt University: USA, 2005; pp 18.

(51) Red'kin, V. E. *Chemistry and Technology of Fuels and Oils* **2004**, *40*, 164.

(52) Marsh, H.; Rodriguez-Reinoso, F. *Activated Carbon*; Elsevier: Oxford, 2006.

(53) Setton, R.; Bernier, P.; Lefrant, S. *Carbon Molecules and Materials*; Taylor and Francis: London, 2002.

(54) Lim, C. K. *Advances in Chromatography* **1992**, *32*, 1.

(55) Lee, J.; Kim, J.; Hyeon, T. *Advanced Materials* **2006**, *18*, 2073.

(56) Villar-Rodil, S.; Suarez-Garcia, F.; Paredes, J. I.; Martinez-Alonso, A.; Tascon, J. M. D. *Chemistry of Materials* **2005**, *17*, 5893.

(57) Mowla, D.; Do, D. D.; Kaneko, K. Adsorption of water vapor on activated carbon: A brief overview. In *Chemistry and Physics of Carbon,* 2003; Vol. 28; pp 229.

(58) Ioannidou, O.; Zabaniotou, A. *Renewable & Sustainable Energy Reviews* **2007**, *11*, 1966.

(59) Kusunoki, M.; Rokkaku, M.; Suzuki, T. *Applied Physics Letters* **1997**, *71*, 2620.

(60) Zheng, J.; Ekstrom, T. C.; Gordeev, S. K.; Jacob, M. *Journal of Materials Chemistry* **2000**, *10*, 1039.

(61) Danishevskii, A. M.; Mosina, G. N.; Smorgonskaya, E. A.; Gordeev, S. K.; Grechinskaya, A. V.; Jardin, C.; Meaudre, R.; Marty, O. "Effect of preparation conditions on diamond cluster formation in bulk nanoporous carbon", 2003.

(62) Dimovski, S.; Nikitin, A.; Ye, H. H.; Gogotsi, Y. *Journal of Materials Chemistry* **2004**, *14*, 238.

(63) Gogotsi, Y.; Welz, S.; Ersoy, D. A.; McNallan, M. J. *Nature* **2001**, *411*, 283.

(64) Ersoy, D. A.; McNallan, M. J.; Gogotsi, Y. *Materials Research Innovations* **2001**, *5*, 55.

(65) Yushin, G.; Dash, R.; Jagiello, J.; Fischer, J. E.; Gogotsi, Y. *Advanced Functional Materials* **2006**, *16*, 2288.

(66) Largeot, C.; Portet, C.; Chmiola, J.; Taberna, P. L.; Gogotsi, Y.; Simon, P. *Journal of the American Chemical Society* **2008**, *130*, 2730.

(67) Gogotsi, Y.; Dash, R. K.; Yushin, G.; Yildirim, T.; Laudisio, G.; Fischer, J. E. *Journal of the American Chemical Society* **2005**, *127*, 16006.

(68) Gogotsi, Y.; Nikitin, A.; Ye, H. H.; Zhou, W.; Fischer, J. E.; Bo, Y.; Foley, H. C.; Barsoum, M. W. *Nature Materials* **2003**, *2*, 591.

(69) Chmiola, J.; Yushin, G.; Dash, R.; Gogotsi, Y. *Journal of Power Sources* **2006**, *158*, 765.

(70) Urbonaite, S.; Wachtmeister, S.; Mirguet, C.; Coronel, E.; Zou, W. Y.; Csillag, S.; Svensson, G. *Carbon* **2007**, *45*, 2047.

(71) Williams, P. T.; Reed, A. R. *Biomass & Bioenergy* **2006**, *30*, 144.

(72) Rodríguez-Reinoso, F.; Molina-Sabio, M.; González, M. T. *Carbon* **1995**, *33*, 15.

(73) Rodriguez-Reinoso, F.; Molina-Sabio, M. *Carbon* **1992**, *30*, 1111.

(74) Pastor-Villegas, J.; Duran-Valle, C. J. *Carbon* **2002**, *40*, 397.

(75) Navarro, M. V.; Seaton, N. A.; Mastral, A. M.; Murillo, R. *Carbon* **2006**, *44*, 2281.

(76) Munoz-Guillena, M. J.; Illan-Gomez, M. J.; Martin-Martinez, J. M.; Linares-Solano, A.; Salinas-Martinez de Lecea, C. *Energy Fuels* **1992**, *6*, 9.

(77) Huang, Z. H.; Kang, F. Y.; Yang, J. B.; Liang, K. M.; Fu, R. W.; Huang, A. P. *Journal of Materials Science Letters* **2002**, *22*, 293.

(78) Li, J.; Zhang, Y. *Physica E: Low-dimensional Systems and Nanostructures* **2005**, *28*, 309.

(79) Saxby, J. D.; Chatfield, S. P.; Palmisano, A. J.; Vassallo, A. M.; Wilson, M. A.; Pang, L. S. K. *Journal of Physical Chemistry* **1992**, *96*, 17.

(80) Illekova, E.; Csomorova, K. *Journal of Thermal Analysis and Calorimetry* **2005**, *80*, 103.

(81) Gajewski, S.; Maneck, H. E.; Knoll, U.; Neubert, D.; Dorfel, I.; Mach, R.; Strau, B.; Friedrich, J. F. *Diamond Relat. Mater.* **2003**, *12*, 816.

(82) Moon, J. M.; An, K. H.; Lee, Y. H.; Park, Y. S.; Bae, D. J.; Park, G. S. *J. Phys. Chem. B* **2001**, *105*, 5677.

(83) Yang, C. M.; Kaneko, K.; Yudasaka, M.; Iijima, S. *Nano Lett.* **2002**, *2*, 385.

(84) Demidov, A. I.; Markelov, I. A. *Russian Journal of Applied Chemistry* **2005**, *78*, 707.

(85) Goto, K. S.; Han, K. H.; Saintpierre, G. R. *Materials Science and Engineering* **1987**, *88*, 347.

(86) Brukh, R.; Mitra, S. *Journal of Materials Chemistry* **2007**, *17*, 619.

(87) Ulbricht, H.; Moos, G.; Hertel, T. *Surface Science* **2003**, *532*, 852.

(88) Giannozzi, P.; Car, R.; Scoles, G. *The Journal of Chemical Physics* **2003**, *118*, 1003.

(89) Klusek, Z.; Waqar, Z.; Datta, P. K.; Kozlowski, W. *Corrosion Science* **2004**, *46*, 1831.

(90) Yang, R. T.; Wong, C. *Journal of Chemical Physics* **1981**, *75*, 4471.

(91) Lee, S. M.; Lee, Y. H.; Hwang, Y. G.; Hahn, J. R.; Kang, H. *Physical Review Letters* **1999**, *82*, 217.

(92) Chang, H. P.; Bard, A. J. *Journal of the American Chemical Society* **1991**, *113*, 5588.

(93) Yin, Y.; Binner, J. G. P.; Cross, T. E.; Marshall, S. J. *Journal of Materials Science* **1994**, *29*, 2250.

(94) Chang, H. W.; Rhee, S. K. *Carbon* **1978**, *16*, 17.

(95) Gao, P. Z.; Wang, H. J.; Jin, Z. H. *Thermochimica Acta* **2004**, *414*, 59.

(96) Hennig, G. R. *Science* **1965**, *147*, 733.

(97) Evans, E. L.; Griffiths, R. J. M.; Thomas, J. M. *Science* **1971**, *171*, 174.

(98) Yang, R. T.; Wong, C. *Science* **1981**, *214*, 437.

(99) Schlogl, R.; Loose, G.; Wesemann, M. *Solid State Ionics* **1990**, *43*, 183.

(100) Ajayan, P. M.; Ebbesen, T. W.; Ichihashi, T.; Iijima, S.; Tanigaki, K.; Hiura, H. *Nature* **1993**, *362*, 522.

(101) Mazzoni, M. S. C.; Chacham, H.; Ordejón, P.; Sánchez-Portal, D.; Soler, J. M.; Artacho, E. *Physical Review B* **1999**, *60*, R2208.

(102) Shimada, T.; Yanase, H.; Morishita, K.; Hayashi, J.-i.; Chiba, T. *Carbon* **2004**, *42*, 1635.

(103) Ajayan, P. M.; lijima, S. *Nature* **1993**, *361*, 333.

(104) Park, Y. S.; Choi, Y. C.; Kim, K. S.; Chung, D.-C.; Bae, D. J.; An, K. H.; Lim, S. C.; Zhu, X. Y.; Lee, Y. H. *Carbon* **2001**, *39*, 655.

(105) McKee, D. W. Catalyzed Gasification of Carbon. In *Chemistry*; Walker, P. L., Thrower, P., Eds. New York, 1981; Vol. 16.

(106) Vannice, M. A. *Kinetics of catalytic reactions* Springer: New York, 2005.

(107) McKee, D. W. *Carbon* **1970**, *8*, 623.

(108) Ci, L. J.; Rao, Z. L.; Zhou, Z. P.; Tang, D. S.; Yan, Y. Q.; Liang, Y. X.; Liu, D. F.; Yuan, H. J.; Zhou, W. Y.; Wang, G.; Liu, W.; Xie, S. S. *Chemical Physics Letters* **2002**, *359*, 63.

(109) Couteau, E.; Hernadi, K.; Seo, J. W.; Thien-Nga, L.; Miko, C.; Gaal, R.; Forro, L. *Chem. Phys. Lett.* **2003**, *378*, 9.

(110) Flahaut, E.; Bacsa, R.; Peigney, A.; Laurent, C. *Chemical Communications* **2003**, *12*, 1442.

(111) Kosaka, M.; Ebbesen, T. W.; Hiura, H.; Tanigaki, K. *Chem. Phys. Lett.* **1995**, *233*, 47.

(112) Zhou, W.; Ooi, Y. H.; Russo, R.; Papanek, P.; Luzzi, D. E.; Fischer, J. E.; Bronikowski, M. J.; Willis, P. A.; Smalley, R. E. *Chemical Physics Letters* **2001**, *350*, 6.

(113) Bandow, S.; Takizawa, M.; Hirahara, K.; Yudasaka, M.; Iijima, S. *Chemical Physics Letters* **2001**, *337*, 48.

(114) Borowiak-Palen, E.; Pichler, T.; Liu, X.; Knupfer, M.; Graff, A.; Jost, O.; Pompe, W.; Kalenczuk, R. J.; Fink, J. *Chemical Physics Letters* **2002**, *363*, 567.

(115) Gajewski, S.; Maneck, H. E.; Knoll, U.; Neubert, D.; Dorfel, I.; Mach, R.; Strauss, B.; Friedrich, J. F. *Diamond and Related Materials* **2003**, *12*, 816.

(116) Li, W. Z.; Wen, J. G.; Sennett, M.; Ren, Z. F. *Chemical Physics Letters* **2003**, *368*, 299.

(117) Dolmatov, V. Y. *Ultradisperse diamonds of detonation synthesis: production, properties and applications* State Polytechnical University: St. Petersburg, 2003.

(118) Gubarevich, T. M.; Sataev, R. R.; Dolmatov, V. Y. "Chemical purification of ultradisperse diamonds"; 5th All-Union Meeting on Detonation, 1991, Krasnoyarsk USSR.

(119) Chiganov, A. S. *Physics of the Solid State* **2004**, *46*, 595.

(120) Pavlov, E. V.; Skryabin, Y. A. Method For Removal Of Impurity Of Non-Diamond Carbon And Device For Its Realization Russia, 1994.

(121) Osswald, S.; Yushin, G.; Mochalin, V.; Kucheyev, S.; Gogotsi, Y. *J. Am. Chem. Soc.* **2006**, *128*, 11635.

(122) Cataldo, F.; Koscheev, A. P. *Fullerenes Nanotubes and Carbon Nanostructures* **2003**, *11*, 201.

(123) Baskaran, D.; Mays, J. W.; Bratcher, M. S. *Chemistry of Materials* **2005**, *17*, 3389.

(124) Sandler, J.; Shaffer, M. S. P.; Prasse, T.; Bauhofer, W.; Schulte, K.; Windle, A. H. *Polymer* **1999**, *40*, 5967.

(125) Zhang, M.; Su, L.; Mao, L. *Carbon* **2006**, *44*, 276.

(126) Garg, A.; Sinnott, S. B. *Chem. Phys. Lett.* **1998**, *295*, 273.

(127) Kuzmany, H.; Kukovecz, A.; Simon, F.; Holzweber, M.; Kramberger, C.; Pichler, T. *Synth. Met.* **2004**, *141*, 113.

(128) Unger, E.; Graham, A.; Kreupl, F.; Liebau, M.; Hoenlein, W. *Current Applied Physics* **2002**, *2*, 107.

(129) Zhao, W.; Song, C. H.; Pehrsson, P. E. *J. Am. Chem. Soc.* **2002**, *124*, 12418.

(130) Esumi, K.; Ishigami, M.; Nakajima, A.; Sawada, K.; Honda, H. *Carbon* **1996**, *34*, 279.

(131) Behler, K.; Osswald, S.; Ye, H.; Dimovski, S.; Gogotsi, Y. *J. Nanopart. Res.* **2006**, *8*, 615.

(132) Cataldo, F.; Koscheev, A. P. *Fullerenes, Nanotubes and Carbon Nanostructures* **2003**, *11*, 201.

(133) Rosca, I. D.; Watari, F.; Uo, M.; Akasaka, T. *Carbon* **2005**, *43*, 3124.

(134) Wiltshire, J. G.; Khlobystov, A. N.; Li, L. J.; Lyapin, S. G.; Briggs, G. A. D.; Nicholas, R. J. *Chem. Phys. Lett.* **2004**, *386*, 239.

(135) Chen, J.; Hamon, M. A.; Hu, H.; Chen, Y.; Rao, A. M.; Eklund, P. C.; Haddon, R. C. *Science* **1998**, *282*, 95.

(136) Hamon, M. A.; Chen, J.; Hu, H.; Chen, Y. S.; Itkis, M. E.; Rao, A. M.; Eklund, P. C.; Haddon, R. C. *Adv. Mater.* **1999**, *11*, 834.

(137) Pompeo, F.; Resasco, D. E. *Nano Letters* **2002**, *2*, 369.

(138) Xu, M.; Huang, Q. H.; Chen, Q.; Guo, P. S.; Sun, Z. *Chemical Physics Letters* **2003**, *375*, 598.

(139) Mickelson, E. T.; Huffman, C. B.; Rinzler, A. G.; Smalley, R. E.; Hauge, R. H.; Margrave, J. L. *Chemical Physics Letters* **1998**, *296*, 188.

(140) Nakajima, T.; Kasamatsu, S.; Matsuo, Y. *European Journal of Solid State and Inorganic Chemistry* **1996**, *33*, 831.

(141) Toyoda, S.; Yamaguchi, Y.; Hiwatashi, M.; Tomonari, Y.; Murakami, H.; Nakashima, N. *Chemistry-an Asian Journal* **2007**, *2*, 145.

(142) Kim, Y.; Lee, D.; Oh, Y.; Choi, J.; Baik, S. *Synthetic Metals* **2006**, *156*, 999.

(143) Li, L.; Davidson, J. L.; Lukehart, C. M. *Carbon* **2006**, *44*, 2308.

(144) Larionova, I.; Kuznetsov, V.; Frolov, A.; Shenderova, O.; Moseenkov, S.; Mazov, I. *Diamond and Related Materials* **2006**, *15*, 1804.

(145) Ray, M. A.; Shenderova, O.; Hook, W.; Martin, A.; Grishko, V.; Tyler, T.; Cunningham, G. B.; McGuire, G. *Diamond and Related Materials* **2006**, *15*, 1809.

(146) Chen, J.; Deng, S. Z.; Chen, J.; Yu, Z. X.; Xu, N. S. *Applied Physics Letters* **1999**, *74*, 3651.

(147) Eremenko, A. N.; Besedina, O. A.; Obraztsova, II. *Russian Journal of Applied Chemistry* **2004**, *77*, 1935.

(148) Xu, K.; Xue, Q. J. *Physics of the Solid State* **2004**, *46*, 649.

(149) Spitsyn, B. V.; Davidson, J. L.; Gradoboev, M. N.; Galushko, T. B.; Serebryakova, N. V.; Karpukhina, T. A.; Kulakova, II; Melnik, N. N. *Diamond and Related Materials* **2006**, *15*, 296.

(150) Papirer, E.; Lacroix, R.; Donnet, J. B.; Nanse, G.; Fioux, P. *Carbon* **1995**, *33*, 63.

(151) Spitsyn, B. V.; Gradoboev, M. N.; Galushko, T. B.; Karpukhina, T. A.; Serebryakova, N. V.; Kulakova, I. I.; Melnik, N. N. In *Synthesis, Properties and Applications of Ultrananocrystalline diamond, NATO Science Series, II. Mathematics, Physics and Chemistry*; Gruen, D. M., Shenderova, O. A., Vul', A. Y., Eds., 2005; Vol. 192; pp 241 252

(152) Liu, Y.; Gu, Z. N.; Margrave, J. L.; Khabashesku, V. N. *Chemistry Of Materials* **2004**, *16*, 3924.

(153) Liu, Y.; Gu, Z.; Margrave, J. L.; Khabashesku, V. N. *Chem. Mater.* **2004**, *16*, 3924.

(154) Kulakova, I. *Physics of the Solid State* **2004**, *46*, 636.

(155) Zhu, Y.; Shen, X.; Wang, B.; Xu, X.; Feng, Z. *Physics of the Solid State* **2004**, *46*, 681.

(156) Linares-Solano, A.; Lozano-Castelló, D.; Lillo-Ródenas, M. A.; Cazorla-Amorós, D. *Chemistry and Physics of Carbon* **2007**, *30*.

(157) Illan-Gomez, M. J.; Garcia-Garcia, A.; Salinas-Martinez de Lecea, C.; Linares-Solano, A. *Energy Fuels* **1996**, *10*, 1108.

(158) Lillo-Rodenas, M. A.; Marco-Lozar, J. P.; Cazorla-Amoros, D.; Linares-Solano, A. *J. Anal. Appl. Pyr.* **2007**, *80*, 166.

(159) Nian, Y.-R.; Teng, H. *J. Electrochem. Soc.* **2002**, *149*, A1008.

(160) Pastor-Villegas, J.; Durán-Valle, C. J. *Carbon* **2002**, *40*, 397.

(161) Ahmadpour, A.; Do, D. D. *Carbon* **1996**, *34*, 471.

(162) Maciá-Agulló, J. A.; Moore, B. C.; Cazorla-Amorós, D.; Linares-Solano, A. *Carbon* **2004**, *42*, 1367.

(163) Hoffman, E. N.; Yushin, G.; El-Raghy, T.; Gogotsi, Y.; Barsoum, M. W. *Microporous and Mesoporous Materials* **2008**, *112*, 526.

(164) Lu, G. Q.; Do, D. D. *Carbon* **1992**, *30*, 21.

(165) Dawson, E. A.; Parkes, G. M. B.; Barnes, P. A.; Chinn, M. J. *Carbon* **2003**, *41*, 571.

(166) Dash, R.; Chmiola, J.; Yushin, G.; Gogotsi, Y.; Laudisio, G.; Singer, J.; Fischer, J.; Kucheyev, S. *Carbon* **2006**, *44*, 2489.

(167) Ersoy, D.; McNallan, M. J.; Gogotsi, Y. G. *Mater. Res. Innovations* **2001**, *5*, 55.

(168) Mohun, W. A. Mineral Active Carbon and Process for Producing Same US, 1962.

(169) Kittel, C. *Introduction to solid state physics / Charles Kittel*, 13th ed. ed.; Oldenbourg Verlag Muenchen, Wien, 2002.

(170) Rayleigh. *Philosophical Magazine* **1871**, *41*, 274.

(171) Raman, C. V.; Krishnan, K. S. *Nature* **1928**, *121*, 501.

(172) Kneipp, K.; Kneipp, H.; Dresselhaus, M. S.; Lefrant, S. *Philosophical Transactions of the Royal Society of London Series A* **2004**, *362*, 2361.

(173) Thomsen, C.; Reich, S.; Maultzsch, J. *Philosophical Transactions of the Royal Society of London Series a-Mathematical Physical and Engineering Sciences* **2004**, *362*, 2337.

(174) Martin, R. M.; Falicov, L. M. Resonant Raman scattering. In *Light scattering in solids. 1. Introdcutory concepts*; 2 ed.; Cardona, M., Ed.; Springer, 1983; Vol. 8; pp 79.

(175) Jorio, A.; Souza Filho, A. G.; Dresselhaus, G.; Dresselhaus, M. S.; Swan, A. K.; Ünlü, M. S.; Goldberg, B. B.; Pimenta, M. A.; Hafner, J. H.; Lieber, C. M.; Saito, R. *Physical Review B* **2002**, *65*, 155412.

(176) Gubarev, S. I.; Ruf, T.; Cardona, M. *Physical Review B* **1991**, *43*, 1551.

(177) Sapega, V. F.; Cardona, M.; Ploog, K.; Ivchenko, E. L.; Mirlin, D. N. *Physical Review B* **1992**, *45*, 4320.

(178) Rao, A. M.; Richter, E.; Bandow, S.; Chase, B.; Eklund, P. C.; Williams, K. A.; Fang, S.; Subbaswamy, K. R.; Menon, M.; Thess, A.; Smalley, R. E.; Dresselhaus, G.; Dresselhaus, M. S. *Science* **1997**, *275*, 187.

(179) Pimenta, M. A.; Hanlon, E. B.; Marucci, A.; Corio, P.; Brown, S. D. M.; Empedocles, S. A.; Bawendi, M. G.; Dresselhaus, G.; Dresselhaus, M. S. *Brazilian Journal of Physics* **2000**, *30*, 423.

(180) Jorio, A.; Saito, R.; Hafner, J. H.; Lieber, C. M.; Hunter, M.; McClure, T.; Dresselhaus, G.; Dresselhaus, M. S. *Physical Review Letters* **2001**, *86*, 1118.

(181) Wada, N.; Solin, S. A. *Physica B+C* **1981**, *105*, 353.

(182) Sails, S. R.; Gardiner, D. J.; Bowden, M.; Savage, J.; Rodway, D. *Diamond and Related Materials* **1996**, *5*, 589.

(183) Li, X. Y.; Czernuszewicz, R. S.; Kincaid, J. R.; Su, Y. O.; Spiro, T. G. *Journal of Physical Chemistry* **1990**, *94*, 31.

(184) Maruyama, S. Kataura plot and 1D electronic DOS of carbon nanotubes, 2002.

(185) Dresselhaus, M. S.; Dresselhaus, G.; Saito, R. *Carbon* **1995**, *33*, 883.

(186) Mintmire, J. W.; White, C. T. *Physical Review Letters* **1998**, *81*, 2506.

(187) White, C. T.; Mintmire, J. W. *Nature* **1998**, *394*, 29.

(188) Kataura, H.; Kumazawa, Y.; Maniwa, Y.; Umezu, I.; Suzuki, S.; Ohtsuka, Y.; Achiba, Y. *Synthetic Metals* **1999**, *103*, 2555.

(189) Yin, Y.; Walsh, A. G.; Vamivakas, A. N.; Cronin, S. B.; Stolyarov, A. M.; Tinkham, M.; Bacsa, W.; Unlu, M. S.; Goldberg, B. B.; Swan, A. K. *Ieee Journal of Selected Topics in Quantum Electronics* **2006**, *12*, 1083.

(190) Li, X. Y.; Czernuszewicz, R. S.; Kincaid, J. R.; Spiro, T. G. *Journal of the American Chemical Society* **1989**, *111*, 7012.

(191) Hata, T. R.; Scholz, T. A.; Ermakov, I. V.; McClane, R. W.; Khachik, F.; Gellermann, W.; Pershing, L. K. *Journal of Investigative Dermatology* **2000**, *115*, 441.

(192) Wen, Z. Q.; Thomas, G. J. *Biopolymers* **1998**, *45*, 247.

(193) LaPlant, F.; Laurence, G.; BenAmotz, D. *Applied Spectroscopy* **1996**, *50*, 1034.

(194) Jorio, A.; Saito, R.; Dresselhaus, G.; Dresselhaus, M. S. *Philosophical Transactions of the Royal Society a-Mathematical Physical and Engineering Sciences* **2004**, *362*, 2311.

(195) Saito, R.; Dresselhaus, G.; Dresselhaus, M. S. *Physical properties of carbon nanotubes*; Imperial College Press: London, 1998.

(196) Dresselhaus, M. S.; Dresselhaus, G.; Saito, R.; Jorio, A. *Physics Reports* **2005**, *409*, 47.

(197) Brown, S. D. M.; Jorio, A.; Corio, P.; Dresselhaus, M. S.; Dresselhaus, G.; Saito, R.; Kneipp, K. *Physical Review B* **2001**, *6315*.

(198) Jiang, C. Y.; Kempa, K.; Zhao, J. L.; Schlecht, U.; Kolb, U.; Basche, T.; Burghard, M.; Mews, A. *Physical Review B* **2002**, *66*.

(199) Lazzeri, M.; Piscanec, S.; Mauri, F.; Ferrari, A. C.; Robertson, J. *Physical Review B* **2006**, *73*.

(200) Oron-Carl, M.; Hennrich, F.; Kappes, M. M.; Lohneysen, H. v.; Krupke, R. *Nano Lett.* **2005**, *5*, 1761.

(201) Jorio, A.; Pimenta, M. A.; Souza, A. G.; Samsonidze, G. G.; Swan, A. K.; Unlu, M. S.; Goldberg, B. B.; Saito, R.; Dresselhaus, G.; Dresselhaus, M. S. *Physical Review Letters* **2003**, *90*.

(202) Jorio, A.; Fantini, C.; Dantas, M. S. S.; Pimenta, M. A.; Souza, A. G.; Samsonidze, G. G.; Brar, V. W.; Dresselhaus, G.; Dresselhaus, M. S.; Swan, A. K.; Unlu, M. S.; Goldberg, B. B.; Saito, R. *Physical Review B* **2002**, *66*.

(203) Corio, P.; Santos, P. S.; Brar, V. W.; Samsonidze, G. G.; Chou, S. G.; Dresselhaus, M. S. *Chemical Physics Letters* **2003**, *370*, 675.

(204) Arvanitidis, J.; Christofilos, D.; Papagelis, K.; Takenobu, T.; Iwasa, Y.; Kataura, H.; Ves, S.; Kourouklis, G. A. *Physical Review B* **2005**, *72*.

(205) Cronin, S. B.; Swan, A. K.; Unlu, M. S.; Goldberg, B. B.; Dresselhaus, M. S.; Tinkham, M. *Physical Review B* **2005**, *72*.

(206) Graupner, R. *Journal of Raman Spectroscopy* **2007**, *38*, 673.

(207) Maultzsch, J.; Reich, S.; Schlecht, U.; Thomsen, C. *Physical Review Letters* **2003**, *91*.

(208) Puech, P.; Flahaut, E.; Bassil, A.; Juffmann, T.; Beuneu, F.; Bacsa, W. S. *Journal of Raman Spectroscopy* **2007**, *38*, 714.

(209) Zhao, X.; Ando, Y.; Qin, L. C.; Kataura, H.; Maniwa, Y.; Saito, R. *Physica B-Condensed Matter* **2002**, *323*, 265.

(210) Rao, A. M.; Jorio, A.; Pimenta, M. A.; Dantas, M. S. S.; Saito, R.; Dresselhaus, G.; Dresselhaus, M. S. *Physical Review Letters* **2000**, *84*, 1820.

(211) Zhao, X. L.; Ando, Y.; Qin, L. C.; Kataura, H.; Maniwa, Y.; Saito, R. *Applied Physics Letters* **2002**, *81*, 2550.

(212) Fantini, C.; Jorio, A.; Souza, M.; Strano, M. S.; Dresselhaus, M. S.; Pimenta, M. A. *Physical Review Letters* **2004**, *93*, 147406.

(213) Izard, N.; Riehl, D.; Anglaret, E. *Physical Review B* **2005**, *71*.

(214) Bachilo, S. M.; Strano, M. S.; Kittrell, C.; Hauge, R. H.; Smalley, R. E.; Weisman, R. B. *Science* **2002**, *298*, 2361.

(215) Kurti, J.; Kresse, G.; Kuzmany, H. *Physical Review B* **1998**, *58*, R8869.

(216) Rahmani, A.; Sauvajol, J. L.; Rols, S.; Benoit, C. *Physical Review B* **2002**, *66*.

(217) Sanchez-Portal, D.; Artacho, E.; Soler, J. M.; Rubio, A.; Ordejon, P. *Physical Review B* **1999**, *59*, 12678.

(218) Jorio, A.; Fantini, C.; Pimenta, M. A.; Capaz, R. B.; Samsonidze, G. G.; Dresselhaus, G.; Dresselhaus, M. S.; Jiang, J.; Kobayashi, N.; Gruneis, A.; Saito, R. *Physical Review B* **2005**, *71*.

(219) Kurti, J.; Zolyomi, V.; Kertesz, M.; Sun, G.; Baughman, R. H.; Kuzmany, H. *Carbon* **2004**, *42*, 971.

(220) Benoit, J. M.; Buisson, J. P.; Chauvet, O.; Godon, C.; Lefrant, S. *Physical Review B* **2002**, *66*.

(221) Zhao, X. L.; Ando, Y.; Qin, L. C.; Kataura, H.; Maniwa, Y.; Saito, R. *Chemical Physics Letters* **2002**, *361*, 169.

(222) Milnera, M.; Kurti, J.; Hulman, M.; Kuzmany, H. *Physical Review Letters* **2000**, *84*, 1324.

(223) Duesberg, G. S.; Loa, I.; Burghard, M.; Syassen, K.; Roth, S. *Physical Review Letters* **2000**, *85*, 5436.

(224) Duesberg, G. S.; Loa, I.; Burghard, M.; Syassen, K.; Roth, S. *Physical Review Letters* **2000**, *85*, 5436.

(225) Jorio, A.; Souza, A. G.; Brar, V. W.; Swan, A. K.; Unlu, M. S.; Goldberg, B. B.; Righi, A.; Hafner, J. H.; Lieber, C. M.; Saito, R.; Dresselhaus, G.; Dresselhaus, M. S. *Physical Review B* **2002**, *65*.

(226) Jorio, A.; Dresselhaus, G.; Dresselhaus, M. S.; Souza, M.; Dantas, M. S. S.; Pimenta, M. A.; Rao, A. M.; Saito, R.; Liu, C.; Cheng, H. M. *Physical Review Letters* **2000**, *85*, 2617.

(227) Wang, Y.; Kempa, K.; Kimball, B.; Carlson, J. B.; Benham, G.; Li, W. Z.; Kempa, T.; Rybczynski, J.; Herczynski, A.; Ren, Z. F. *Applied Physics Letters* **2004**, *85*, 2607.

(228) Pocsik, I.; Hundhausen, M.; Koos, M.; Ley, L. *Journal of Non-Crystalline Solids* **1998**, *230*, 1083.

(229) Tuinstra, F.; Koenig, J. L. *The Journal of Chemical Physics* **1970**, *53*, 1126.

(230) Vidano, R. P.; Fischbach, D. B.; Willis, L. J.; Loehr, T. M. *Solid State Communications* **1981**, *39*, 341.

(231) Wang, Y.; Alsmeyer, D. C.; McCreery, R. L. *Chemistry of Materials* **1990**, *2*, 557.

(232) Matthews, M. J.; Pimenta, M. A.; Dresselhaus, G.; Dresselhaus, M. S.; Endo, M. *Physical Review B* **1999**, *59*, R6585.

(233) Kawashima, Y.; Katagiri, G. *Physical Review B* **1995**, *52*, 10053.

(234) Thomsen, C.; Reich, S. *Physical Review Letters* **2000**, *85*, 5215.

(235) Saito, R.; Jorio, A.; Souza, A. G.; Dresselhaus, G.; Dresselhaus, M. S.; Pimenta, M. A. *Physical Review Letters* **2002**, *88*.

(236) Ferrari, A. C. *Solid State Communications* **2007**, *143*, 47.

(237) Dresselhaus, M. S.; Dresselhaus, G. *Light Scattering in Solids III*; Springer-Verlag Berlin Heidelberg, 1982.

(238) Solin, S. A.; Caswell, N. *J. Raman Spectrosc.* **1981**, *10*, 129.

(239) Souza, A. G.; Jorio, A.; Swan, A. K.; Unlu, M. S.; Goldberg, B. B.; Saito, R.; Hafner, J. H.; Lieber, C. M.; Pimenta, M. A.; Dresselhaus, G.; Dresselhaus, M. S. *Physical Review B* **2002**, *65*.

(240) Souza, A. G.; Jorio, A.; Samsonidze, G. G.; Dresselhaus, G.; Pimenta, M. A.; Dresselhaus, M. S.; Swan, A. K.; Unlu, M. S.; Goldberg, B. B.; Saito, R. *Physical Review B* **2003**, *67*.

(241) Souza, A. G.; Jorio, A.; Samsonidze, G. G.; Dresselhaus, G.; Dresselhaus, M. S.; Swan, A. K.; Unlu, M. S.; Goldberg, B. B.; Saito, R.; Hafner, J. H.; Lieber, C. M.; Pimenta, M. A. *Chemical Physics Letters* **2002**, *354*, 62.

(242) Maultzsch, J.; Reich, S.; Thomsen, C. *Physical Review B* **2001**, *6412*.

(243) Pimenta, M. A.; Jorio, A.; Brown, S. D. M.; Souza, A. G.; Dresselhaus, G.; Hafner, J. H.; Lieber, C. M.; Saito, R.; Dresselhaus, M. S. *Physical Review B* **2001**, *6404*.

(244) Brown, S. D. M.; Jorio, A.; Dresselhaus, M. S.; Dresselhaus, G. *Physical Review B* **2001**, *64*, 073403.

(245) Maultzsch, J.; Reich, S.; Thomsen, C.; Webster, S.; Czerw, R.; Carroll, D. L.; Vieira, S. M. C.; Birkett, P. R.; Rego, C. A. *Applied Physics Letters* **2002**, *81*, 2647.

(246) Knight, D. S.; White, W. B. *Journal of Materials Research* **1989**, *4*, 385.

(247) Ferrari, A. C.; Robertson, J. *Physical Review B* **2000**, *61*, 14095.

(248) Sato, K.; Saito, R.; Oyama, Y.; Jiang, J.; Cancado, L. G.; Pimenta, M. A.; Jorio, A.; Samsonidze, G. G.; Dresselhaus, G.; Dresselhaus, M. S. *Chemical Physics Letters* **2006**, *427*, 117.

(249) Sinha, K.; Menendez, J. *Physical Review B* **1990**, *41*, 10845.

(250) Wilhelm, H.; Lelaurain, M.; McRae, E.; Humbert, B. *Journal of Applied Physics* **1998**, *84*, 6552.

(251) Souza, A. G.; Jorio, A.; Samsonidze, G. G.; Dresselhaus, G.; Saito, R.; Dresselhaus, M. S. *Nanotechnology* **2003**, *14*, 1130.

(252) Nemanich, R. J.; Glass, J. T.; Lucovsky, G.; Shroder, R. E. *J. Vac. Sci. Technol. A* **1988**, *6*, 1783.

(253) Prawer, S.; Nemanich, R. J. *Phil. Trans. R. Soc. Lond. A* **2004**, *362*, 2477.

(254) Morell, G.; Quinones, O.; Diaz, Y.; Vargas, I. M.; Weiner, B. R.; Katiyar, R. S. *Diamond and Related Materials* **1998**, *7*, 1029.

(255) Liu, M. S.; Bursill, L. A.; Prawer, S.; Beserman, R. *Physical Review B* **2000**, *61*, 3391.

(256) Solin, S. A.; Ramdas, A. K. *Physical Review B* **1970**, *1*, 1687.

(257) Zouboulis, E. S.; Grimsditch, M. *Physical Review B* **1991**, *43*, 12490.

(258) Zaitsev, A. M. *Optical Properties of Diamond*; Springer: Heidelberg, 2001.

(259) Prawer, S.; Nemanich, R. J. *Philos Trans R Soc Lond Ser A* **2004**, *362*, 2537.

(260) Prawer, S.; Nemanich, R. J. *Philosophical Transactions of the Royal Society of London Series A* **2004**, *362*, 2537.

(261) Occelli, F.; Loubeyre, P.; Letoullec, R. *Nature Materials* **2003**, *2*, 151.

(262) Grimsditch, M. H.; Anastassakis, E.; Cardona, M. *Physical Review B* **1978**, *18*, 901.

(263) Wang, Y. G.; Li, H. D.; Xiong, Y. Y.; Zhang, S. L.; Lin, Z. D.; Feng, K. *Diamond and Related Materials* **2000**, *9*, 1708.

(264) Hass, K. C.; Tamor, M. A.; Anthony, T. R.; Banholzer, W. F. *Physical Review B* **1992**, *45*, 7171.

(265) Yoshikawa, M.; Mori, Y.; Obata, H.; Maegawa, M.; Katagiri, G.; Ishida, H.; Ishitani, A. *Applied Physics Letters* **1995**, *67*, 694.

(266) Prawer, S.; Nugent, K. W.; Jamieson, D. N.; Orwa, J. O.; Bursill, L. A.; Peng, J. L. *Chemical Physics Letters* **2000**, *332*, 93.

(267) Nistor, L. C.; VanLanduyt, J.; Ralchenko, V. G.; Obraztsova, E. D.; Smolin, A. A. *Diamond and Related Materials* **1997**, *6*, 159.

(268) Ferrari, A. C.; Robertson, J. *Philosophical Transactions of the Royal Society of London Series A* **2004**, *362*, 2477.

(269) Birrell, J.; Gerbi, J. E.; Auciello, O.; Gibson, J. M.; Johnson, J.; Carlisle, J. A. *Diamond and Related Materials* **2005**, *14*, 86.

(270) Filik, J.; Harvey, J. N.; Allan, N. L.; May, P. W.; Dahl, J. E. P.; Liu, S.; Carlson, R. M. K. *Physical Review B* **2006**, *74*.

(271) Ferrari, A. C.; Robertson, J. *Physical Review B* **2001**, *63*.

(272) Lipp, M. J.; Baonza, V. G.; Evans, W. J.; Lorenzana, H. E. *Physical Review B* **1997**, *56*, 5978.

(273) Perevedentseva, E.; Karmenyan, A.; Chung, P. H.; Cheng, C. L. *Journal of Vacuum Science and Technology B* **2005**, *23*, 1980.

(274) Ferrari, A. C.; Robertson, J. *Philosophical Transactions of the Royal Society of London Series A* **2004**, *362*, 2477.

(275) Ager, J. W.; Veirs, D. K.; Rosenblatt, G. M. *Physical Review B* **1991**, *43*, 6491.

(276) Yoshikawa, M.; Mori, Y.; Obata, H.; Maegawa, M.; Katagiri, G.; Ishida, H.; Ishitani, A. *Applied Physics Letters* **1995**, *67*, 694.

(277) Prawer, S.; Nugent, K. W.; Jamieson, D. N.; Orwa, J. O.; Bursill, L. A.; Peng, J. L. *Chem. Phys. Lett.* **2000**, *332*, 93.

(278) Wang, C. Z.; Ho, K. M. *Phys. Rev. Lett.* **1993**, *71*, 1184.

(279) Nemanich, R. J.; Solin, S. A.; Martin, R. M. *Physical Review B* **1981**, *23*, 6348.

(280) Richter, H.; Wang, Z. P.; Ley, L. *Solid State Communications* **1981**, *39*, 625.

(281) Ferrari, A. C.; Robertson, J. *Phil. Trans. R. Soc. Lond. A* **2004**, *362*, 2267.

(282) Kittel, C. *Introduction to solid state physics / Charles Kittel*, 8th ed.

(283) *Light scattering in solids. VIII, Fullerenes, semiconductor surfaces, coherent phonons* Cardona, M.; Güntherodt, G., Eds.; Springer: Berlin, New York, 2000.

(284) Long, D. A. *Raman spectroscopy* McGraw-Hill: New York, 1977.

(285) Verma, P.; Cordts, W.; Irmer, G.; Monecke, J. *Physical Review B* **1999**, *60*, 5778.

(286) Duval, E. *Physical Review B* **1992**, *46*, 5795.

(287) Arora, A. K.; Rajalakshmi, M.; Ravindran, T. R.; Sivasubramanian, V. *Journal of Raman Spectroscopy* **2007**, *38*, 604.

(288) Rodden, W. S. O.; Torres, C. M. S.; Ironside, C. N. *Semiconductor Science and Technology* **1995**, *10*, 807.

(289) Campbell, I. H.; Fauchet, P. M. *Solid State Communications* **1986**, *58*, 739.

(290) Fauchet, P. M.; Campbell, I. H. *Crc Critical Reviews in Solid State and Materials Sciences* **1988**, *14*, S79.

(291) Gonzalez-Hernandez, J.; Azarbayejani, G. H.; Tsu, R.; Pollak, F. H. *Applied Physics Letters* **1985**, *47*, 1350.

(292) Braunstein, G.; Tuschel, D.; Chen, S.; Lee, S. T. *Journal of Applied Physics* **1989**, *66*, 3515.

(293) Tiong, K. K.; Amirtharaj, P. M.; Pollak, F. H.; Aspnes, D. E. *Applied Physics Letters* **1984**, *44*, 122.

(294) Boppart, H.; van Straaten, J.; Silvera, I. F. *Physical Review B* **1985**, *32*, 1423.

(295) Mitra, S. S.; Brafman, O.; Daniels, W. B.; Crawford, R. K. *Physical Review* **1969**, *186*, 942.

(296) Tan, P. H.; Dimovski, S.; Y., G. *Philosophical Transactions of the Royal Society of London Series A* **2004**, *362*, 2289.

(297) Reich, S.; Thomsen, C. *Philosophical Transactions of the Royal Society of London Series a-Mathematical Physical and Engineering Sciences* **2004**, *362*, 2271.

(298) Mykhaylyk, O. O.; Solonin, Y. M.; Batchelder, D. N.; Brydson, R. *Journal of Applied Physics* **2005**, *97*.

(299) Aleksenskii, A. E.; Osipov, V. Y.; Vul, A. Y.; Ber, B. Y.; Smirnov, A. B.; Melekhin, V. G.; Adriaenssens, G. J.; Iakoubovskii, K. *Physics of the Solid State* **2001**, *43*, 145.

(300) Jawhari, T.; Roid, A.; Casado, J. *Carbon* **1995**, *33*, 1561.

(301) Shimodaira, N.; Masui, A. *Journal of Applied Physics* **2002**, *92*, 902.

(302) Dillon, R. O.; Woollam, J. A.; Katkanant, V. *Physical Review B* **1984**, *29*, 3482.

(303) Bourrat, X. *Carbon* **1993**, *31*, 287.

(304) Wada, N.; Solin, S. A. *Physica B & C* **1981**, *105*, 353.

(305) Ferrari, A. C.; Robertson, J. *Physical Review B* **2001**, *64*, 075414.

(306) Reich, S.; Thomsen, C. *Philosophical Transactions of the Royal Society of London Series A* **2004**, *362*, 2271.

(307) Yushin, G.; Gogotsi, Y.; Nikitin, A. *Nanomaterial Handbook* **1999**, *Chapter 8*, 237.

(308) Dash, R. K.; Yushin, G.; Gogotsi, Y. *Microporous and Mesoporous Materials* **2005**, *86*, 50.

(309) Urbonaite, S.; Juárez-Galán, J. M.; Leis, J.; Rodríguez-Reinoso, F.; Svensson, G. *Microporous and Mesoporous Materials* **2008**, *113*, 14.

(310) Bronikowski, M. J.; Willis, P. A.; Colbert, D. T.; Smith, K. A.; Smalley, R. E. *Journal Of Vacuum Science and Technology A-Vacuum Surfaces And Films* **2001**, *19*, 1800.

(311) Portet, C.; Yushin, G.; Gogotsi, Y. *Carbon* **2007**, *45*, 2511.

(312) Osswald, S.; Behler, K.; Gogotsi, Y. *Journal of Applied Physics* **2008**, *104*.

(313) Chang, H.; Charalampopoulos, T. T. *Phil. Trans. R. Soc. Lond. A* **1990**, *430*, 577.

(314) Keyvan, S.; Rossow, R.; Romero, C. *Fuel* **2006**, *85*, 796.

(315) Rohlfing, E. A. *Journal of Chemical Physics* **1988**, *89*, 6103.

(316) Qiao, Z. J.; Li, J. J.; Zhao, N. Q.; Shi, C. S.; Nash, P. *Scripta Materialia* **2006**, *54*, 225.

(317) Mochalin, V.; Osswald, S.; Gogotsi, Y. *Chem. Mater.* **2009**, *In press*, *Available online,* DOI: 10.1021/cm802057q

(318) Ferraro, J. R.; Nakamoto, K. *Introductory Raman Spectroscopy*; Academic Press, 2003.

(319) Ravikovitch, P. I.; Neimark, A. V. *Coll. Surf. A* **2001**, *187–188*, 11.

(320) Osswald, S.; Flahaut, E.; Ye, H.; Gogotsi, Y. *Chem. Phys. Lett.* **2005**, *402*, 422.

(321) Jorio, A.; Filho, A. G. S.; Dresselhaus, G.; Dresselhaus, M. S.; Swan, A. K.; Unlu, M. S.; Goldberg, B. B.; Pimenta, M. A.; Hafner, J. H.; Lieber, C. M.; Saito, R. *Physical Review B (Condensed Matter and Materials Physics)* **2002**, *65*, 155412.

(322) Osswald, S.; Flahaut, E.; Gogotsi, Y. *Chem. Mater.* **2006**, *18*, 1525.

(323) Ci, L. J.; Zhou, Z. P.; Yan, X. Q.; Liu, D. F.; Yuan, H. J.; Song, L.; Gao, Y.; Wang, J. X.; Liu, L. F.; Zhou, W. Y.; Wang, G.; Xie, S. S.; Tan, P. H. *Journal of Applied Physics* **2003**, *94*, 5715.

(324) Henrard, L.; Hernandez, E.; Bernier, P.; Rubio, A. *Physical Review B* **1999**, *60*, R8521.

(325) Ci, L. J.; Zhou, Z. P.; Song, L.; Yan, X. Q.; Liu, D. F.; Yuan, H. J.; Gao, Y.; Wang, J. X.; Liu, L. F.; Zhou, W. Y.; Wang, G.; Xie, S. S. *Applied Physics Letters* **2003**, *82*, 3098.

(326) Huang, F. M.; Yue, K. T.; Tan, P. H.; Zhang, S. L.; Shi, Z. J.; Zhou, X. H.; Gu, Z. N. *Journal Of Applied Physics* **1998**, *84*, 4022.

(327) Osswald, S.; Havel, M.; Gogotsi, Y. *Journal of Raman Spectroscopy* **2007**, *38*, 728.

(328) McKee, D. W. *Carbon* **1970**, *8*, 623.

(329) Walker, P. L.; Rusinko, F.; Austin, L. G. *Chem. Phys. Carbon* **1968**, *4*, 287.

(330) Fanning, P. E.; Vannice, M. A. *Carbon* **1993**, *31*, 721.

(331) Kuhlmann, U.; Jantoljak, H.; Pfander, N.; Bernier, P.; Journet, C.; Thomsen, C. *Chem. Phys. Lett.* **1998**, *294*, 237.

(332) Zawadzki, J. *Carbon* **1980**, *18*, 281.

(333) Kastner, J.; Pichler, T.; Kuzmany, H.; Curran, S.; Blau, W.; Weldon, D. N.; Delamesiere, M.; Draper, S.; Zandbergen, H. *Chem. Phys. Lett.* **1994**, *221*, 53.

(334) Liu, M.; Yang, Y.; Zhu, T.; Liu, Z. *Carbon* **2005**, *43*, 1470.

(335) Chen, X.-H.; Chen, C.-S.; Xiao, H.-N.; Chen, X.-H.; Li, W.-H.; Xu, L.-S. *Carbon* **2005**, *43*, 1800.

(336) Zawadzki, J. *Chem. Phys. Carbon* **1989**, *21*, 147.

(337) Aleksenskii, A. E.; Osipov, V. Y.; Vul', A. Y.; Ber, B. Y.; Smirnov, A. B.; Melekhin, V. G.; Adriaenssens, G. J.; Iakoubovskii, K. *Physics of the Solid State* **2001**, *43*, 145.

(338) Khasawinah, S. A.; Popovici, G.; Farmer, J.; Sung, T.; Prelas, M. A.; Chamberlain, J.; White, H. *Journal of Materials Research* **1995**, *10*, 2523.

(339) Ferrari, A. C.; Robertson, J. *Philosophical Transactions of the Royal Society of London Series a-Mathematical Physical and Engineering Sciences* **2004**, *362*, 2477.

(340) Stöhr, J. *NEXAFS Spectroscopy* Springer: Berlin, 2003.

(341) Jaouen, M.; Tourillon, G.; Delafond, J.; Junqua, N.; Hug, G. *Diam. Related Mater.* **1995**, *4*, 200.

(342) Huang, F.; Tong, Y.; Yun, S. *Physics of the Solid State* **2004**, *46*, 616.

(343) Eidelman, E. D.; Siklitsky, V. I.; Sharonova, L. V.; Yagovkina, M. A.; Vul, A. Y.; Takahashi, M.; Inakuma, M.; Ozawa, M.; Osawa, E. *Diamond and Related Materials* **2005**, *14*, 1765.

(344) Shenderova, O.; Grichko, V.; Hens, S.; Walch, J. *Diamond and Related Materials* **2007**, *16*, 2003.

(345) Osswald, S.; Portet, C.; Gogotsi, Y.; Laudisio, G.; Singer, J. P.; Fischer, J. E. *Microporous and Mesoporous Materials* **2009**, *In press*.

(346) Wei, S.; Li, Z.; Yaping, Z. *Chinese J. Chem. Eng.* **2006**, *14*, 266.

(347) San Miguel, G.; Fowler, G. D.; Sollars, C. J. *Carbon* **2003**, *41*, 1009.

(348) Mozammel, H. M.; Masahiro, O.; Sc, B. *Biomass and Bioenergy* **2002**, *22*, 397.

(349) Chmiola, J.; Largeot, C.; Taberna, P. L.; Simon, P.; Gogotsi, Y. *Angewandte Chemie-International Edition* **2008**, *47*, 3392.

(350) Schwan, J.; Ulrich, S.; Batori, V.; Ehrhardt, H.; Silva, S. R. P. *Journal of Applied Physics* **1996**, *80*, 440.

(351) Palmer, J. C.; Jain, S. J.; Gubbins, K. E.; Cohaut, N.; Fischer, J. E.; Dash, R. K.; Gogotsi, Y. *J. Mater. Chem. (in press)* **2009**.

(352) Yushin, G.; Hoffman, E. N.; Barsoum, M. W.; Gogotsi, Y.; Howell, C. A.; Sandeman, S. R.; Phillips, G. J.; Lloyd, A. W.; Mikhalovsky, S. V. *Biomaterials* **2006**, *27*, 5755.

(353) Cambaz, Z. G.; Yushin, G. N.; Gogotsi, Y.; Vyshnyakova, K. L.; Pereselentseva, L. N. *Journal of the American Ceramic Society* **2006**, *89*, 509.

(354) Achar, B. N.; Brindley, G. W.; Sharp, J. H. "Kinetics and mechanism of dehydroxylation process. III. Applications and limitations of dynamic methods"; International Clay Conference, 1966, Jerusalem.

(355) Sharp, J. H.; Wentworth, S. A. *Anal. Chem.* **1969**, *41*, 2060.

(356) Tonglai, Z.; Rongzu, H.; Fuping, L. *Thermochimica Acta* **1994**, *244*, 177.

(357) Hu, R. Z.; Yang, Z. Q.; Liang, Y. J. *Thermochimica Acta* **1988**, *123*, 135.

(358) Phadnis, A. B.; Deshpande, V. V. *Thermochimica Acta* **1983**, *62*, 361.

(359) Yang, Y.; He, F.; Wang, M. *Tansu* **1998**, *1*, 2.

(360) Pichot, V.; Comet, M.; Fousson, E.; Baras, C.; Senger, A.; Le Normand, F.; Spitzer, D. *Diamond and Related Materials* **2008**, *17*, 13.

(361) Ji, S. F.; Jiang, T. L.; Xu, K.; Li, S. B. *Applied Surface Science* **1998**, *133*, 231.

(362) Jiang, T.; Xu, K. *Carbon* **1995**, *33*, 1663.

(363) Kuznetsov, V. L.; Aleksandrov, M. N.; Zagoruiko, I. V.; Chuvilin, A. L.; Moroz, E. M.; Kolomichuk, V. N.; Likholobov, V. A.; Brylyakov, P. M.; Sakovitch, G. V. *Carbon* **1991**, *29*, 665.

(364) Osswald, S.; Flahaut, E.; Gogotsi, Y. *Chemistry of Materials* **2006**, *18*, 1525.

(365) Mochalin, V. N.; Osswald, S.; Portet, C.; Yushin, G.; Hobson, C.; Havel, M.; Y., G. *Mater. Res. Soc. Symp. Proc.* **2008**, *1039*, 1039.

(366) Kalish, R.; Reznik, A.; Prawer, S.; Saada, D.; Adler, J. *Physica Status Solidi A* **1999**, *174*, 83.

(367) *Lange's Handbook of Chemistry*; 16th ed.; Speight, J. G., Ed.; McGraw-Hill, 2005, pp 1572.

(368) Osswald, S.; Yushin, G.; Mochalin, V.; Kucheyev, S. O.; Gogotsi, Y. *Journal of the American Chemical Society* **2006**, *128*, 11635.

(369) Mann, D. J.; Halls, M. D. *Physical Review Letters* **2003**, *90*.

(370) Marti, J.; Gordillo, M. C. *Physical Review B* **2001**, *63*.

(371) Korobov, M. V.; Avramenko, N. V.; Bogachev, A. G.; Rozhkova, N. N.; Osawa, E. *Journal of Physical Chemistry C* **2007**, *111*, 7330.

(372) Danilenko, V. V. *Combustion Explosion and Shock Waves* **2005**, *41*, 577.

(373) Yushin, G. N.; Osswald, S.; Padalko, V. I.; Bogatyreva, G. P.; Gogotsi, Y. *Diamond and Related Materials* **2005**, *14*, 1721.

(374) Osswald, S.; Gurga, A.; Kellogg, F.; Cho, K.; Yushin, G.; Gogotsi, Y. *Diamond and Related Materials* **2007**, *16*, 1967.

(375) Gordeev, S. *Journal of Superhard Materials* **2004**, 34.

(376) Gordeev, S. K. "Carbon Composites Based Nanodiamonds"; NanoCarbon and NanoDiamond, 2006, St. Petersburg, Russia.

(377) Osswald, S.; Havel, M.; Mochalin, V.; Yushin, G.; Gogotsi, Y. "Increase of nanodiamond crystal size by selective oxidation", 2008.

(378) Zhang, Z.; Zhou, F.; Lavernia, E. J. *Metallurgical and Materials Transactions A* **2003**, *34A*, 1349.

(379) Williamson, G. K.; Hall, W. H. *Acta Metallurgica* **1953**, *1*, 22.

(380) Tomita, S.; Burian, A.; Dore, J. C.; LeBolloch, D.; Fujii, M.; Hayashi, S. *Carbon* **2002**, *40*, 1469.

(381) Mykhaylyk, O. O.; Solonin, Y. M.; Batchelder, D. N.; Brydson, R. *Journal of Applied Physics* **2005**, *97*, 074302.

(382) Palosz, B. Structure of nano-crystals: the key to understanding the unique properties of nano-materials. In *Nanodiam*; Mitura, S., Niedzielski, P., Walkowiak, B., Eds.; Wydawnictwo Naukowe: Warszawa, 2006; pp 129.

(383) Yoshikawa, M.; Mori, Y.; Maegawa, M.; Katagiri, G.; Ishida, H.; Ishitani, A. *Applied Physics Letters* **1993**, *62*, 3114.

(384) Herchen, H.; Cappelli, M. A. *Physical Review B* **1991**, *43*, 11740.

(385) Sun, Z.; Shi, J. R.; Tay, B. K.; Lau, S. P. *Diamond and Related Materials* **2000**, *9*, 1979.

(386) Warren, J. L.; Yarnell, J. L.; Dolling, G.; Cowley, R. A. *Physical Review* **1967**, *158*, 805.

(387) Warren, J. L.; Wenzel, R. G.; Yarnell, J. L. "Dispersion curves for phonons in diamond"; Inelastic Scattering of Neutrons (International Atomic Energy Agency), 1965, Vienna.

(388) Alcaniz-Monge, J.; Linares-Solano, A.; Rand, B. *Journal of Physical Chemistry B* **2002**, *106*, 3209.

APPENDIX A: LIST ABBREVIATIONS

ABSW	Achar-Brindley-Sharp-Wendeworth
AFM	Atomic force microscopy
BET	Brunauer-Emmett-Teller
BZ	Brillouin zone
CDC	Carbide-derived carbon
CNT	Carbon nanotube
CVD	Chemical vapor deposition
DOS	Density of states
DSC	Differential scanning calorimetry
DWCNT	Double-walled carbon nanotube
EDS	Energy-dispersive X-ray spectroscopy
EELS	Electron energy loss spectroscopy
ERM	Eley-Rideal mechanism
EXAFS	Extended X-ray absorption fine structure
FTIR	Fourier-transform infrared spectroscopy
FWHM	Full width at half maximum
HRTEM	High resolution transmission electron microscopy
ICP	Inductively coupled plasma
LHM	Langmuir-Hinshelwood mechanism
MWCNT	Multi-walled carbon nanotube
ND	Nanodiamond

PCM	Phonon confinement model
PSD	Pore size distribution
RBM	Radial breathing mode
RRS	Resonant Raman spectroscopy
SSA	Specific surface area
STM	Scanning tunneling microscopy
SWCNT	Single-walled carbon nanotube
TGA	Thermogravimetric analysis
XRD	X-ray diffraction
WHA	Williamson-Hall analysis

VITA

Education

Ph.D. in Materials Science and Engineering, Drexel University (USA)	Dec. 2008
Dr. rer. nat. in Physics (Dual Ph.D.), TU Ilmenau (Germany)	Dec. 2008
MBA, Drexel University (USA)	Dec. 2008
MS (Diplom) in Technical Physics, TU Ilmenau (Germany)	Dec. 2005

Honors and Fellowships

- 2005 DAAD Fellowship (German Academic Exchange Service)
- 2005 Ernest-Solvay-Foundation Fellowship
- 2006-2007 Arkema PhD Fellowship
- 2006 1st place award (in the Combined Techniques category) at the American Ceramic
- Society's annual Ceramographic Competition
- 2008 George Hill, Jr. Fellowship and Award for excellence in graduate career

Publications

- V. Mochalin, **S. Osswald**, Y. Gogotsi, Contribution of functional groups to the Raman spectrum of nanodiamond, *Chem. Mat.*, In press, DOI:10.1021/cm802057q
- **S. Osswald**, Y. Gogotsi, Laser-induced light emission from carbon nanoparticles, *J. Appl. Phys.*, 104, 2008, 074308
- **S. Osswald**, M. Havel, V. Mochalin, G. Yushin, Y. Gogotsi, Increase of nanodiamond crystal size by selective oxidation, *Diam. Relat. Mat.*, 17,(7-10), 2008, 1122-1126
- Z. Cambaz, G. Yushin, **S. Osswald**, V. Mochalin, Y. Gogotsi, Noncatalytic synthesis of carbon nanotubes, graphene and graphite on SiC, *Carbon*, 46 (6), 2008, 841-849.
- V. Mochalin, **S. Osswald**, C. Portet, G. Yushin, C. Hobson, M.Havel, Y.Gogotsi, High temperature functionalization and surface modification of nanodiamond powders, MRS Proc. 1039, 2007, 1039-P11-03
- **S. Osswald**, A. Gurga, F. Kellogg, K. Cho, G. Yushin, Y. Gogotsi, Plasma pressure compaction of nanodiamond, *Diam. Relat. Mater.*, 16 (11), 2007, 1967-1973.
- **S. Osswald**, M. Havel, Y. Gogotsi, Monitoring oxidation of multiwalled carbon nanotubes by Raman spectroscopy, *J. Raman Spectrosc.*, 38 (6), 2007, 728-736.
- K. Behler, **S. Osswald**, S. Dimovski, Y. Gogotsi, Effect of thermal treatment on the structure of multi-walled carbon nanotubes, *J. Nanopart. Res.*, 8(5), 2006, 615-625.
- **S. Osswald**, G. Yushin, V. Mochalin, S. Kucheyev, Y. Gogotsi, Control of sp(2)/sp(3) carbon ratio and surface chemistry of nanodiamond powders by selective oxidation in air, *J. Am. Chem. Soc*, 128 (35), 2006, 11635-11642.
- **S. Osswald**, E. Flahaut, Y. Gogotsi, In Situ Raman spectroscopy study of oxidation of double- and single-wall carbon nanotubes, *Chem. Mat.* 18(6); 2006, 1525-1533.
- G.N. Yushin, **S. Osswald**, V.I. Padalko, G.P. Bogatyreva, Y. Gogotsi, Effect of sintering on structure of nanodiamond, *Diam. Relat. Mater.*, 14 (10), 2005, 1721-1729.
- **S. Osswald**, E. Flahaut, H.Ye, et al., Elimination of D-band in Raman spectra of double-wall carbon nanotubes by oxidation, *Chem. Phys. Lett.* 402 (4-6), 2005, 422-427.